Loughborough University

This item was submitted to Loughborough University as a PhD thesis by the author and is made available in the Institutional Repository (https://dspace.lboro.ac.uk/) under the following Creative Commons Licence conditions.

creative commons

COMMONS DEED

Attribution-NonCommercial-NoDerivs 2.5

You are free:

- to copy, distribute, display, and perform the work

Under the following conditions:

Attribution. You must attribute the work in the manner specified by the author or licensor.

Noncommercial. You may not use this work for commercial purposes.

No Derivative Works. You may not alter, transform, or build upon this work.

- For any reuse or distribution, you must make clear to others the license terms of this work.
- Any of these conditions can be waived if you get permission from the copyright holder.

Your fair use and other rights are in no way affected by the above.

This is a human-readable summary of the Legal Code (the full license).

Disclaimer

For the full text of this licence, please go to:
http://creativecommons.org/licenses/by-nc-nd/2.5/

COMBINED PIV/PLIF MEASUREMENTS IN A HIGH-SWIRL FUEL INJECTOR FLOWFIELD

Liangta Cheng

Submitted in partial fulfillment of the requirements for the award of
Doctor of Philosophy of Loughborough University
Department of Aeronautical and Automotive Engineering
October 2012
© L Cheng, 2012

Abstract

Current lean-premixed fuel injector designs have shown great potential in terms of reducing emissions of pollutants, but such designs are susceptible to combustion instabilities in which aerodynamic instability plays a major role and also has an effect on mixing of air and fuel. In comparison to prototype testing with combustors running in operating conditions, computational approaches such as Large Eddy Simulations (LES) offer a much more cost-effective alternative in the design stage. However, computational models employed by LES require validation by experimental data. This is one of the main motivations behind the present experimental study.

Combined particle image velocimetry (PIV) and planar laser induced fluorescence (PLIF) instrumentation allowed simultaneous measurements of velocity vector and a conserved scalar introduced into the fuel stream. The results show that the inner swirl shear layer features two pairs of vortices, which draw high concentration fuel mixture from the central jet into the swirl stream and causes it to rotate in their wakes. Such periodic entrainment also occurs with the characteristic frequencies of the vortices. This has clear implications for temporal variations in fuel/air ratio in a combusting flow; these ‘bursts’ of mixing, and hence heat release, could be a possible cause of mixing-induced pressure oscillation in combusting tests.

For the first time in such a flow, all 3 components of the turbulent scalar flux were available for validation of LES-based predictions. A careful assessment of experimental errors, particularly the error associated with spatial filtering, was carried out. Comparison of LES predictions with experimental data showed very good agreement for both 1st and 2nd moment statistics, as well as spectra and scalar pdfs. It is particularly noteworthy that comparison between LES computed and measured scalar fluxes was very good; this represents successful validation of the simple (constant Schmidt number) SGS model used for this complex and practically important fuel injector flow.

In addition to providing benchmark data for the validation of LES predictions, a new experimental technique has been developed that is capable of providing spatially resolved residence time data. Residence times of combustors have commonly been

used to help understand NO_x emissions and can also contribute to combustion instabilities. Both the time mean velocity and turbulence fields are important to the residence time, but determining the residence time via analysis of a measured velocity field is difficult due to the inherent unsteadiness and the three dimensional nature of a high-Re swirling flow. A more direct approach to measure residence time is reported here that examines the dynamic response of fuel concentration to a sudden cutoff in the fuel injection. Residence time measurement was mainly taken using a time-resolved PLIF technique, but a second camera for PIV was added to check that the step change does not alter the velocity field and the spectral content of the coherent structures. Characteristic timescales evaluated from the measurements are referred to as convection and half-life times: The former describes the time delay from a fuel injector exit reference point to a downstream point of interest, and the latter describes the rate of decay once the effect of the reduced scalar concentration at the injection source has been transported to the point of interest. Residence time is often defined as the time taken for a conserved scalar to reduce to half its initial value after injection is stopped: this is equivalent to the sum of the convection time and the half-life values. The technique was applied to a high-swirl fuel injector typical of that found in combustor applications. Two test cases have been studied: with central jet (with-jet) and without central jet (no-jet). It was found that the relatively unstable central recirculation zone of the no-jet case resulted in increased transport of fuel into the central region that is dominated by a precessing vortex core, where long half-life times are also found. Based on this, it was inferred that the no-jet case may be more prone to NO_x production. The technique is described here for a single-phase isothermal flow field, but with consideration, it could be extended to studying reacting flows to provide more insight into important mixing phenomena and relevant timescales.

Keywords: Particle Image Velocimetry, Planar Laser-Induced Fluorescence, Gas Turbine Fuel Injectors, Aerodynamic Instabilities**,** Vortices, Coherent Structures, Scalar Mixing, Precessing Vortex Core, Residence Time Measurement, Convection Time, Halflife Time, NO_x Production

Acknowledgements

I would like to express my sincere gratitude to the entire Rolls-Royce UTC applied aerodynamics research team, including all the RAs and technicians, for their technical assistance and moral support. I would like to extend my deepest appreciation to my supervisor, Dr. Adrian Spencer, for giving me the opportunity to work on the project and providing me with all the support I needed throughout the years. I would also like to thank Dr. Jim McGuirk for his co-supervision and effort in getting the work published.

Most of the analysis presented in this thesis would not have been possible without Dr. Mark Robinson's help in Matlab coding and Dr. David Dunham's extremely valuable input and discussions. The two have been instrumental in my learning process.

Finally, I would like to thank my wife, Jennifer, for her loving care and support. When the writing got tough, she was always there for me – telling me to be patient and helping me to regain focus. This thesis is dedicated to her.

Table of Contents

Abstract……..…i
Acknowledgements…….iii
Table of Contents……iv
List of Figure……...ix
List of Table…….xvii
Nomenclature……..xviii

Chapter 1 1

1. INTRODUCTION 1

1.1 Gas turbine combustor 2
1.1.1 Gas turbine emissions 3
1.1.2 Regulations 4
1.1.4 Emission Reduction Techniques 5
1.2 Fuel Injector 6
1.2.1 Swirlers 7
1.2.2 Physics of fuel injector swirling flow 8
1.2.3 LPP fuel injector instabilities 11
1.3 Computational fluid dynamics 13
1.3.1 Large eddy simulation 14
1.3.2 Validation of scalar mixing 15
1.4 Mixture residence time 16
1.4.1 Residence time estimation methods 19
1.5 Review of experimental techniques 20
1.5.1 SPIV 21
1.5.2 Review of combined PIV-PLIF 23
1.6 Objectives 24
1.7 Thesis Structure 25

Chapter 2 27

2. EXPERIMENTAL FACILITIES.....27

2.1 Water Analogy Facility 27
2.1.1 Closed-loop system 28

2.1.2 Modifications 29
2.1.3 Pipe flow calibration 30
2.1.4 Annulus flow calibration 31
2.1.5 BS1042 manometer calibration 33
2.1.6 Uncertainty of BS1042 mass flow rate measurements 34
2.2 Dye injection system 35
2.2.1 Flow calibration 36
2.3 Fuel injector configurations and test section 37
2.3.1 Non-premixed (main) configuration 38
2.3.2 Premixed configurations 39
2.3.3 Vertical test section 40
2.4 Test conditions 41
2.4.1 Premixed 43
2.4.2 Validation of the mass flux ratio 44
2.5 Sign convention 45
2.6 Chapter summary 46
Chapter 3 47
3. MEASUREMENT TECHNIQUES 47
3.1 Light sheet imaging technique (LSI) 47
3.2 Particle image velocimetry 48
3.2.1 Errors in PIV 50
3.2.2 Stereoscopic PIV 53
3.3 Planar laser induced fluorescence (PLIF) 55
3.3.1 PLIF: background subtraction 58
3.3.2 PLIF: sheet correction 59
3.3.3 PLIF: absorption correction 61
3.3.4 PLIF: concentration calibration 63
3.3.5 PLIF: pulse-to-pulse energy variation 64
3.3.6 Total error estimate 66
3.4 Optical arrangements and instrumentation 66
3.4.1 2C-PIV/PLIF 66
3.4.2 SPIV/PLIF setup 68
3.4.3 Instrumentation 68

3.4.4 Instrument synchronisation 70
3.4.5 SPIV/LIF system communication 72
3.5 Residence time measurement technique 73
3.5.1 Effect of dye injection system response time 77
3.5.2 Effect of impulse on velocity time history 78
3.5.3 Effect of impulse on the spectral content 79
3.6 Data structure 80
3.6.1 Low-speed data 80
3.6.2 High-speed data 82
3.7 Chapter summary 83
Chapter 4 85
4. DATA REDUCTION 85
4.1 Single point statistics 85
4.1.1 Extraction of scalar data 85
4.1.2 Reynolds decomposition 86
4.1.3 Probability density function 88
4.1.4 Integral timescales and power spectral density 89
4.2 Scales of turbulent fluid flow 91
4.2.1 Computation of Kolmogorov length scale 92
4.2.2 Discussion of Batchelor length scale 95
4.2.3 Computation of integral length scale 96
4.3 Spatial filtering error 99
4.3.1 Velocity 100
4.3.2 Scalar 101
4.3.3 Effect of spatial averaging on scalar flux 102
4.3.4 Length scale informed filtering of scalar 103
4.4 Validation of methods 105
4.4.1 Synthetic data generation 105
4.4.2 Validation of error estimation method 106
4.4.3 Effect of adaptive filtering of scalar on synthetic scalar flux 108
4.4.4 Scalar flux correction 109
4.5 Statistical convergence 111
4.5.1 Theoretical formula 111

4.5.2 Observation from synthetic data 112
4.5.3 Observation from experimental data 114
4.6 Computation of time-mean pressure fields 116
4.6.1 Mathematical formulations 116
4.6.2 Validation on a simple flow case 120
4.7 Coherent structure identification 121
4.7.1 Conditional averaging 121
4.7.2 Proper Orthogonal Decomposition 122
4.8 Chapter summary 125
Chapter 5 126
5. RESULTS: NON-PREMIXED TEST 126
5.1 Time mean flowfield characteristics 127
5.1.1 Time-mean flow field characteristics 127
5.1.2 Time-mean velocity profiles 131
5.1.3 Shear stresses and turbulent kinetic energy 137
5.1.4 Time mean pressure field 140
5.1.5 Instantaneous flow field visualisation 142
5.2 Mixing field characteristics 144
5.2.1 Time mean scalar field 144
5.2.2 Data validation 146
5.2.3 Instantaneous scalar fields 148
5.2.4 Scalar fluxes 152
5.3 Coherent structure and spectral analysis 160
5.3.1 Single point statistics 160
5.3.2 Temporal characteristics 162
5.3.3 Conditional averaging 171
5.3.4 Proper orthogonal decomposition 174
5.4 Reference to LES predictions 178
5.4.1 LES results 178
5.4.2 Validation of LES predictions 180
5.5 Chapter summary 187
Chapter 6 190
6. RESULTS: PREMIXED TEST 190

6.1 Flow field characteristics of premixed configuration 191
6.1.1 Time averaged flow field 191
6.1.2 Temporal characteristics 194
6.2 Mixing field characteristics of premixed configuration 198
6.2.1 Time mean mixing field 199
6.2.2 Instantaneous scalar fields 201
6.2.3 Turbulent scalar fluxes 205
6.2.4 Coherent scalar structure 207
6.3 Residence times 211
6.3.1 Point histories 212
6.3.2 Convection time 217
6.3.3 Half-life time 218
6.3.4 Total residence time 220
6.3.5 Repeatability 221
6.4 Reference to combustion data 225
6.4.1 Main flame zone 225
6.4.2. Effect of helical vortex structure 227
6.5 Chapter summary 227
Chapter 7 230
7. CONCLUSIONS AND RECOMMENDATIONS 230
7.1 Conclusions 230
7.2 Recommendations for future work 233
REFERENCES 235
Appendix 248

List of Figures

Fig. 1.1 Combustor operation and zones (Rolls-Royce, 1995) 2
Fig. 1.2 Schematic of Combustion Products and Their Scale (IPCC) 3
Fig. 1.3 Pre-film airblast fuel injector (Lefebvre, 1998) 6
Fig. 1.4 Axial swirler and radial swirler (Lefebvre, 1998) 7
Fig. 1.5 Tangential velocity distributions of forced vortex and free vortex (Muson et al 2004) 8
Fig. 1.6 Tangential velocity profile of a Rankine vortex (Gupta, 1984) 9
Fig. 1.7 Streamlines of recirculation bubble in Swirling jet, S=1.57 (Chigier and Beer, 1972) 11
Fig. 1.8 3D reconstruction of vortex structures in a partially-premixed flow field (Stohr et al, 2012) 12
Fig. 1.9 Illustration of combustion instability feedback loop (Lieuwen, 2001) 13
Fig. 1.10 Time evolution of disturbances responsible for combustion instability (Lieuwen, 2001) 18
Fig. 1.11 Perspective Error (based on Raffel, 2007) 22
Fig. 1.12 Typical SPIV Setup 22

Fig. 2.1 Closed-loop water analogy rig 28
Fig. 2.2 Measurement locations for pipe flow calibration: (a) x-r view and (b) r-θ view 30
Fig. 2.3 Pipe flow inlet profile 31
Fig. 2.4 Measurement locations for annulus flow calibration: x-r view (left), r-θ view (right) 32
Fig. 2.5 Annulus mean and rms velocity profiles 32
Fig. 2.6 Axial variation of mass flow rate 33
Fig. 2.7 BS1042 (a) mass flow rate as a function of dP, (b) uncertainty as a function of mass flow rate 35
Fig. 2.8 Dye injection system 35
Fig. 2.9 Calibration of central jet flow meter 36
Fig. 2.10 Turbomeca low emissions fuel injector (MOLECULES, 2004) 37
Fig. 2.11 Fuel Injector used for combusting test case in MOLECULES (2004) 38
Fig. 2.12 Fuel injector design 39

Fig. 2.13 Fuel injector in the premixed configuration 40
Fig. 2.14 Fuel injector test cases: (left) without central jet, (right) with central jet 40
Fig. 2.15 Vertical water flow facility 41
Fig. 2.16 Contours of mean axial velocity: (a) current data and (b) Midgley (2005) .. 45
Fig. 2.17 Axial velocity profiles at (left) x/D_s=0.02, (right) x/D_s=0.5 45

Fig. 3.1 Light sheet imaging system 48
Fig. 3.2 Calculation of displacement vector in an interrogation window using CCF (DaVis, 2009) 49
Fig. 3.3 SPIV setup for x-r plane measurement: 3D view (left), calibration (right) 53
Fig. 3.4 Absorption/Emission wavelength spectra for Rhodamine B, Kemnitz et al (1986), Du et al (1998) 55
Fig. 3.5 Background subtraction: instantaneous raw image (left), after background subtraction (right) 58
Fig. 3.6 Sheet correction: sheet correction image (left), normalised sheet correction image (right) 60
Fig. 3.7 Typical measurement image: before correction (left) after correction (right) 61
Fig. 3.8 Light sheet geometry: (a) ray path determination technique, and (b) sheet geometry 62
Fig. 3.9 Attenuation behaviour of increasing concentration levels: (a) sheet corrected and normalised by the mean intensity at C=100%, (b) sheet corrected and normalised by the profile of C=100% 63
Fig. 3.10 Normalised intensity as a function of normalised concentration 64
Fig. 3.11 rms scalar field as a percentage of the mean 65
Fig. 3.12 Intensity variation: time history (left), histogram (right) 65
Fig. 3.13 Optical apparatus for a combined 2C-PIV-PLIF: top view (Left) photo (Right) 67
Fig. 3.14 Combined SPIV-PLIF setup on x-r plane: picture (left), side view (right) .. 68
Fig. 3.15 Synchronisation of laser and cameras 71
Fig. 3.16 Schematic of Combined SPIV-PLIF Instrument Arrangement 72
Fig. 3.17 Sequence of concentration images and time history at a point in the swirler exit 74
Fig. 3.18 Illustration of the reference point location in the flow field 74

Fig. 3.19 Illustration of convection time: (top) time history at reference point in the swirler passage exit, (bottom) time history at a point located in the corner recirculation 75
Fig. 3.20 Flow without recirculation; (left) flow with gradual area increase, (right) time history of the impulse and response at points A and B 76
Fig. 3.21 Two-dimensional flow with recirculation; (a) simple flow geometry, (b) time history of a switch-on impulse at point A and response at point C, (c) time history of a switch-off impulse and its response at point C 76
Fig. 3.22 Two configurations at which response time was evaluated: (a) premixed configuration, and (b) non-premixed, directed injected through central jet 77
Fig. 3.23 Time histories of axial velocity and intensity in a region within the potential core 78
Fig. 3.24 Time histories of axial velocity 79
Fig. 3.25 PSD of fluctuating axial velocity at r/D_s=0.27, x/D_s=0.04 of (a) with-jet and (b) no-jet test cases 79
Fig. 3.26 Scalar flux: axial scalar flux with locations of 2C-PIV-PLIF and SPIV in the rθ plane 81
Fig. 3.27 2C-PIV/PLIF data (taken at the USF lab) for scalar flux reduction, recorded at 2.2Hz 81
Fig. 3.28 SPIV/PLIF data (taken at the AAE lab) for scalar flux reduction, recorded at 1.7Hz 81
Fig. 3.29 SPIV data (taken at the AAE lab) for pressure reduction, recorded at 1.7Hz 82
Fig. 3.30 High-speed measurement FOV locations 82
Fig. 3.31 High-speed data in x-r plane (taken at USF lab) 83
Fig. 3.32 High-speed data in r-θ plane (taken at USF lab) 83

Fig. 4.1 Scalar nearest-point finding relative to position of vector 86
Fig. 4.2 Schematic diagram of the energy cascade at very high Reynolds number 92
Fig. 4.3 Kolmogorov length scales (μm): radial (left), axial (right) 95
Fig. 4.4 Treatment of the Missing SSC Curve Due to Curtailment 98
Fig. 4.5 Subgrid filtering effect on (a) rms velocity and (b) integral lengthscale 100
Fig. 4.6 Error due to spatial filtering: (a) $Err(\Delta x_{PIV}/{}^{1}L_{11})$ and (b) $Err(\Delta x_{PIV}/{}^{2}L_{22})$ 101

Fig. 4.7 Error (%) Due to Spatial filtering: radial direction (left); axial direction (right) 102
Fig. 4.8 Effect of spatial filtering of scalar on the scalar flux at 6 axial stations..... 103
Fig. 4.9 Spatially varying filter widths 104
Fig. 4.10 Effect of spatial filtering on fluctuating scalar (Exp is an abbreviation for experimental and the Synthetic Integral is obtained from the exercise described in the previous section) 107
Fig. 4.11 Effect of spatial filtering on scalar flux (synthetic data) 109
Fig. 4.12 Original and corrected scalar flux profiles in the radial (left) and axial (right) directions at x/Ds=0.13 110
Fig. 4.13 Statistical convergence of scalar flux, calculated from synthetically generated data with the prescribed parameters selected from experimental data at r/Ds=0.06, x/Ds=0.13, ρ_{ucuc}=0.46 113
Fig. 4.14 Statistical convergence of scalar flux, calculated from synthetically generated data with the prescribed parameters selected from experimental data at r/Ds=0.09, x/Ds=0.13, ρ_{ucuc}=0.56 114
Fig. 4.15 Statistical convergence of scalar flux, calculated from experimental data at r/Ds=0.1, x/Ds=0.13, with a correlation coefficient of 0.50 115
Fig. 4.16 Statistical convergence of scalar flux, calculated from experimental data at r/Ds=0.1, x/Ds=0.08, with a correlation coefficient of 0.22 115
Fig. 4.17 Pressure on a rectangular grid segment 118
Fig. 4.18 Boundaries of the computational domain 119
Fig. 4.19 Static pressure (left) Fluent, (right) calculated using the VVB method 121
Fig. 4.20 Conditional averaging of a pdf distribution 121

Fig. 5.1 Stream traces on mean axial velocity contour 128
Fig. 5.2 Axial velocity contour near-field of the fuel injector exit 129
Fig. 5.3 Time-mean velocity contours at x/Ds=0.02: (a) axial velocity, (b) radial velocity, (c) tangential velocity 130
Fig. 5.4 Contours of RMS (a) axial, (b) radial, (c) tangential velocities 131
Fig. 5.5 Mean axial velocity profiles at 4 axial stations 133
Fig. 5.6 Mean radial velocity profiles at 4 axial stations 134
Fig. 5.7 Mean tangential velocity profiles at 4 axial stations 134
Fig. 5.8 RMS axial velocity profiles at 4 axial stations 136

Fig. 5.9 RMS radial velocity profiles at 4 axial stations 136
Fig. 5.10 RMS tangential velocity profiles at 4 axial stations 137
Fig. 5.11 Shear stresses: (a) axial-radial, and (b) axial-tangential 139
Fig. 5.12 Turbulent kinetic energy 140
Fig. 5.13 Contours of (a) static pressure, (b) swirl-induced pressure, and (c) non-swirl-induced pressure 141
Fig. 5.14 Contours of (a) dynamic pressure and (b) total pressure 142
Fig. 5.15 Contours of (a) axial velocity superimposed with arbitrarily plotted stream traces and (b) tangential velocity with superimposed U and V vectors 143
Fig. 5.16 Contours of axial velocity in the r-θ plane at (a)x/D_s=0.02, and (b) x/D_s=0.27 144
Fig. 5.17 Time-mean concentration field 145
Fig. 5.18 Time-mean concentration field at the exit plane at (a) x/D_s=0.02 and (b) x/D_s=0.27 146
Fig. 5.19 RMS concentration 146
Fig. 5.20 Comparison of time-mean concentration profiles at (a) x/D_s=0.02, (b) x/D_s=0.27, (c) x/D_s=0.53, and (d) x/D_s=1.06 147
Fig. 5.21 Comparison of RMS concentration profiles at (a) x/D_s=0.02, (b) x/D_s=0.27, (c) x/D_s=0.53, and (d) x/D_s=1.06 148
Fig. 5.22 Sequence of snapshots of scalar fields with overlaid velocity vectors 149
Fig. 5.23 Examples of shear layer vortices 150
Fig. 5.24 Snapshots of fluctuating scalar with superimposed streamlines at x/D_s=0.27 151
Fig. 5.25 Jet shear vortices and mixing 152
Fig. 5.26 Instantaneous snapshots of (a) fluctuating scalar, (b) axial scalar flux, and (c) radial scalar flux 154
Fig. 5.27 Instantaneous snapshot of (a) fluctuating scalar, (b) axial scalar flux, and (c) radial scalar flux 155
Fig. 5.28 Point histories of turbulent scalar flux at x/D_s=0.15, r/D_s=0.15 in the inner swirl shear 156
Fig. 5.29 Point histories of turbulent scalar flux at x/D_s=0.27, r/D_s=0.27 in the inner swirl shear 156
Fig. 5.30 Time-mean axial scalar flux, $\langle uc \rangle / U_s^2$ 158
Fig. 5.31 Time-mean radial scalar flux, $\langle vc \rangle / U_s^2$ 158

Fig. 5.32 Time-mean tangential scalar flux, $\langle wc \rangle / U_s^2$ 159
Fig. 5.33 Cross correlation of uc and vc of a point in the (a) jet shear, and (b) inner swirl shear 160
Fig. 5.34 Normalised pdf of (a) axial velocity, (b) radial velocity, (c) tangential velocity, and (d) scalar at $r/D_s=0.18$, $x/D_s=0.02$ 161
Fig. 5.35 Normalised pdf of (a) axial velocity, (b) radial velocity, (c) tangential velocity, and (d) scalar at $r/D_s=0.30$, $x/D_s=0.27$ 162
Fig. 5.36 PSDs of (a) u and v, (b) c, (c) uc, and (d) vc of a point in the inner swirl shear 163
Fig. 5.37 ACF of u, v and c of a point in the inner swirl shear 164
Fig. 5.38 PSDs of (a) u and v, (b) c, (c) uc, and (d) vc of a point in the jet shear 165
Fig. 5.39 PSDs of (a)u and v, (b) c, (c) uc, and (d) vc of a point in the swirl stream 166
Fig. 5.40 PSDs of (a) u and v, and (b) c of a point in the downstream jet spread 167
Fig. 5.41 PSDs of (a)u and v, and (b) c of a point in the free stagnation region 167
Fig. 5.42 PSDs of (a)u and v, and (b) c of a point at $x/D_s=1.5$, $r/D_s=0$ 168
Fig. 5.43 Amplitude of the primary PSD spike at $S_t=1.19$: (a) E_{uu}, (b) E_{vv}, and (c) E_{cc} 169
Fig. 5.44 Amplitude of the secondary PSD spike at $S_t=2.38$: (a) E_{uu}, (b) E_{vv}, and (c) E_{cc} 169
Fig. 5.45 Amplitude of the secondary PSD spike at $S_t=1.22$: (a) E_{ucuc} and (b) E_{vcvc} . 170
Fig. 5.46 Amplitude of the secondary PSD spike at $S_t=2.42$: (a) E_{ucuc} and (b) E_{vcvc} . 170
Fig. 5.47 Contours of SVC(u) with superimposed stream traces of radial-tangential velocity, averaged conditionally upon axial velocity at (a) $x/D_s=0.02$ and (b) $x/D_s=0.27$ 172
Fig. 5.48 SSC contours of concentration with superimposed stream traces of radial-tangential velocity, averaged conditionally upon concentration at (a) $x/D_s=0.02$, and (b) $x/D_s=0.27$ 172
Fig. 5.49 Stream traces of conditionally averaged fluctuating velocity superimposed on (a) radial scalar flux and (b) axial scalar flux contours 173
Fig. 5.50 First POD mode (a) in the x-r plane, and (b) in the r-θ plane at $x/D_s=0$ 174
Fig. 5.51 Contours of (a) First and (b) second POD modes of axial velocity with superimposed radial-tangential stream traces at $x/D_s=0.02$ 175
Fig. 5.52 (a) Contours of (a) First and (b) second POD modes of concentration with superimposed radial-tangential stream traces at $x/D_s=0.02$ 176

Fig. 5.53 Cumulative distribution of energies across the first 50 POD modes of (a) 3C velocity and (b) concentration 177
Fig. 5.54 1st POD mode of (a) axial velocity and (b) concentration with superimposed radial tangential stream traces at x/D_s=0.27 177
Fig. 5. 55 Instantaneous (a) velocity and (b) concentration at t=I 179
Fig. 5.56 Instantaneous (a) velocity and (b) concentration at t=II 179
Fig. 5.57 Iso-surface of correlation of axial velocity 180
Fig. 5.58 Profiles of $<U>U_s$ at (a) x/D_s=0.27 and (b) x/D_s=1.06 181
Fig. 5.59 Profiles of <C> at (a) x/D_s=0.27 and (b) x/D_s=1.06 182
Fig. 5.60 RMS velocity and scalar profiles at x/D_s=0.02 182
Fig. 5.61 Scalar flux contours, LES versus experiment: (a) $<uc>/U_s$, (b) $<vc>/U_s$, and (c) $<wc>/U_s$ 184
Fig. 5.62 Turbulent scalar flux profiles at two locations, x/DS = 0.13 (*left*) and x/DS = 0.53 (*right*) 185
Fig. 5.63 pdf's of (a) axial, (b) radial, (c) tangential velocities, and (d) scalar concentration 187

Fig. 6.1 Mean velocity vectors with cone angles in the x-r plane: (a) with-jet, and (b) no-jet (Midgley, 2005) 191
Fig. 6.2 Mean tangential velocity contours in the x-r plane: (a) with-jet, and (b) no-jet 192
Fig. 6.3 RMS velocity contours of no-jet test case: (a) axial, (b) radial, and (c) tangential velocity 193
Fig. 6.4 PSD estimates at four point locations 195
Fig. 6.5 PSD amplitude of primary peak, S_t=0.60, of (a) axial, and (b) radial velocity 196
Fig. 6.6 PSD amplitude of secondary peak, S_t=1.20, of (a) axial, and (b) radial velocity 197
Fig. 6.7 pdf of spatial attachment point of swirl cone (Midgley, 2005) 197
Fig. 6.8 Time-mean scalar field normalised by maxima of (a) with-jet and (b) no jet 199
Fig. 6.9 RMS scalar field normalised by maxima of (a) with-jet and (b) no jet 200
Fig. 6.10 RMS scalar profiles along the centreline 201

Fig. 6.11 Reynolds decomposed instantaneous scalar fields with superimposed stream traces of Reynolds decomposed axial-radial velocity vectors, with-jet test case 202
Fig. 6.12 Reynolds decomposed instantaneous scalar fields with superimposed stream traces of Reynolds decomposed axial-radial velocity vectors, no-jet test case 204
Fig. 6.13 Axial scalar flux of (a) with-jet and (b) no-jet.....206
Fig. 6.14 Radial scalar flux of (a) with-jet and (b) no-jet.....206
Fig. 6.15 Spatial scalar correlation (R_{cc}) contours of the with-jet case with reference point at (x/D_s=0.09, r/D_s=0.34) with superimposed stream traces of conditionally averaged axial-radial velocity.....209
Fig. 6.16 Spatial scalar correlation (R_{cc}) contours of the no-jet case with reference point at (x/D_s=0.09, r/D_s=0.34) with superimposed stream traces of conditionally averaged axial-radial velocity.....209
Fig. 6.17 Spatial scalar correlation (R_{cc}) contours with reference point at (x/D_s=1.12, r/D_s=0).....210
Fig. 6.18 PSD amplitudes of a) primary and b) secondary peaks of the with-jet test case, at S_t=1.2 and S_t=2.4, respectively 210
Fig. 6.19 PSD amplitudes of a) primary and b) secondary peaks of the no-jet test case, at S_t=0.6 and S_t=1.2, respectively 211
Fig. 6.20 Examples of point histories and decay fits (x/D_s<=0.4).....214
Fig. 6.21 Examples of point histories and decay fits (x/D_s>=0.9).....216
Fig. 6.22 Normalised convection times 218
Fig. 6.23 Normalised halflife times 220
Fig. 6.24 Normalised total residence times.....221
Fig. 6.25 Total residence time, τ_{res}, taken at two different FOVs (a) main test, (b) repeat test 222
Fig. 6.26 Centreline profiles of (a) convection time, (b) half life time, and (c) total residence time 223
Fig. 6.27 Measurements of residence times in the r-θ plane at x/Ds=0.13 (with-jet case) 224
Fig. 6.28 With-jet residence times in the r-θ plane at x/Ds=0.13: (a) convection time, (b) half-life time, and (c) residence time 224
Fig. 6.29 Iso-surfaces of mean concentration ($<C>/C_{max}$>0.55) and an arbitrarily drawn PVC.....229

List of Tables

Table 2.1 Fuel Injector Dimensions 39
Table 2.2 Comparison of test conditions 42
Table 2.3 Swirl stream mass flow rates 43
Table 2.4 Comparison of isothermal experimental test conditions with reacting cases 43
Table 2.5 Test Conditions 44

Table 3.1 SPIV errors and minimisation strategy 54
Table 3.2 Rhodamine B properties 56
Table 3.3 PLIF errors 66
Table 3.4 2C-PIV/PLIF recording devices 69
Table 3.5 SPIV/PLIF recording devices 70
Table 3.6 High-speed recording devices 70

Table 4.1 Methods of Calculating Dissipation Rate from PIV Data 93
Table 4.2 Summary of Type 1 Methods of Kolmogorov Length Scale Estimation 94

Nomenclature

Symbols

a_k	uncorrelated temporal coefficient
A	Absorption factor
b	exponential coefficient
c	fluctuating concentration
C	instantaneous concentration
Cs	Smagorinsky constant
d	distance
Da	Damköhler number
D_{mol}	molecular diffusivity
D_s	swirler diameter
E_{cc}	spectral energy of scalar
f_{coll}	Fluorescence collected
G	filter kernel
I	intensity
k	constant used in conditional averaging
k_1, k_2	constants
${}^kL_{ij}$	integral lengthscale of i and j component of velocity in k direction
L_{meas}	measure integral lengthscale
L_{true}	true integral lengthscale
N_p	width of filter window in number of pixels
N_s	number of samples
P	Pressure
r	radial location
R	radius
Re	Reynolds number
R_{ii}	Correlation
S	Signal
S_c	Schmidt number
S_{ij}	strain rate
S_L	flame laminar speed
S_n	swirl number

S_t	Strouhal number
t_n	time instant
u	fluctuating axial velocity
U	instantaneous axial velocity
u_ic	velocity-scalar covariance
U_s	bulk swirl stream velocity
v	fluctuating radial velocity
V	instantaneous radial velocity
w	fluctuating tangential velocity
W	instantaneous tangential velocity
x	axial location
X_{PLIF}	optical distance from PLIF camera to target
α_d	thermal diffusivity
γ_1	skewness
γ_2	kurtosis
Δ	cube root of local cell volume
Δx_{PIV}	PIV grid size
Δx_{PLIF}	PLIF grid size
ε_D	dissipation rate
ε_{EC}	extinction coefficient
ε_N	sample size error
η	Kolmogorov lengthscale
θ	circumferential location
κ	wavenumber
λ_{abs}	peak absorption wavelength
λ_{em}	Batchelor lengthscale
λ_{em}	peak emission wavelength
μ	viscosity
ν	kinematic viscosity
ξ	methane mixture fraction
ρ	density
ρ_{cc}	correlation coefficient of concentration
$\tau_{1/2}$	halflife time
τ_{chem}	chemical reaction time

τ_{conv}	convection time
τ_{res}	total residence time
φ_k	spatial functions
Φ_{QE}	Quantum efficiency

Operators

< >	time averaging
˜	explicit filtering of measured scalar
¯	implicit filtering in LES

Abbreviations

2C	2-component
3C	3-component
2D2C	2-dimensional 2-component
2D3C	2-dimensional 3-component
AAE	aeronautical and automotive engineering
ANTLE	affordable near term low emissions
AOI	area of interest
BS1042	British Standard 1042
CAEP	Committee on Aviation Environmental Protection
CCD	clear crystal display
CCF	cross-correlation function
CFD	computational fluid dynamics
CO	carbon monoxide
CO_2	carbon dioxide
CTRZ	central toroidal recirculation zone
CRZ	corner recirculation zones
CW	continuous-wave
DC	direct current
DFFT	digital fast fourier transform
DNS	direct numerical simulations
EPA	Environmental Protection Agency
FAR	fuel air ratios
FFT	Fast Fourier transform

FoV	field of view
HS	high-speed
ICAO	International Civil Aviation Organization
ID	inner diameter
LDA	laser Doppler anemometry
LES	Large Eddy Simulation
LIF	laser induced fluorescence
LPP	lean premixed prevaporized
LS	low-speed
LSI	Light Sheet Imaging
NACA	National advisory committee for aeronautics
Nd:YAG	neodymium-doped yttrium aluminum garnet
NO_{EI}	NO emission index
NO_x	nitric oxide, nitrogen dioxide
OD	outer diameter
OH-LIF	hydroxyl radical laser induced fluorescence
pdf	probability density function
PIV	Particle Image Velocimetry
PLIF	Planar Laser Induced Fluorescence
POD	proper orthogonal decomposition
PPM	parts per million
PSD	power spectral density
PTU	programmable timing unit
PVC	precessing vortex core
RhB	Rhodamine B
RQL	Rich-burn, Quick-quench, Lean-burn
SC	Sheet correction
SGS	sub-grid scale
SO_x	sulphur oxides
SPIV	stereoscopic PIV
UHC	unburned hydrocarbons
URANS	unsteady Reynolds-averaged Navier-Stokes

Chapter 1

1. INTRODUCTION

Growing concerns of global warming, coupled with the surging costs of fuel, have put immense pressure on gas turbine manufacturers to come up with design improvements to reduce fuel consumption and emission of pollutants. Although there have been incremental improvements over the past decades to reduce emissions, conventional combustor designs have been unable to meet any further emission reduction targets. Fortunately, development of a new breed of low-emissions type fuel injectors has proven to be promising, but the fundamental flow physics, which dictates efficiency and performance of combustion, is not fully understood. In order to understand the combustion aerodynamics of such new fuel injector design, prototype testing in real operating conditions is beneficial but often not feasible due to the cost and time required. For this reason, gas turbine engineers turn to computational predictions as a much cheaper means to resolve design and operational issues. Among the most popular computational fluid dynamics (CFD) methods today is Large Eddy Simulation (LES), which, according to many published researches on jet flow in particular, provides fairly accurate and reliable predictions when validated against experimental data. For the new class of low-emissions fuel injectors, however, there still lacks high-quality experimental data for the validation of LES predictions.

One of the main areas of interest when it comes to studying the performance of fuel injectors is to understand how the aerodynamics affects the mixing of fuel and air characteristics in the combustor. This project therefore sets out to combine otherwise now standardised experimental techniques of Particle Image Velocimetry (PIV) and Planar Laser Induced Fluorescence (PLIF) for the study of passive scalar mixing and validation of the LES prediction of air-fuel mixing in the combustor. The limitations of combining these techniques have also been investigated. Furthermore, a novel experimental technique was developed alongside to characterise spatially-resolved fuel mixture residence time.

1.1 Gas turbine combustor

The operation of a gas turbine engine consists of air intake, compression, combustion, and exhaust. Air at ambient pressure and temperature is drawn into the compressor, where it is compressed and heated before entering the combustor. In diffusion flame combustors such as the one shown in Fig. 1.1, air and fuel are supplied into the primary zone where mixing and chemical reaction take place. As the heated gases expand and exit the combustor, part of its energy is extracted by the turbine such that the mechanical power is used to drive the compressor and the shaft while the remainder discharges through the exit nozzle into the atmosphere, thereby producing propulsion. These four stages happen continuously in a gas turbine – thus eliminating the three idle strokes in a piston engine and as a consequence producing a greater power output for a given size of engine (Rolls Royce, 1995).

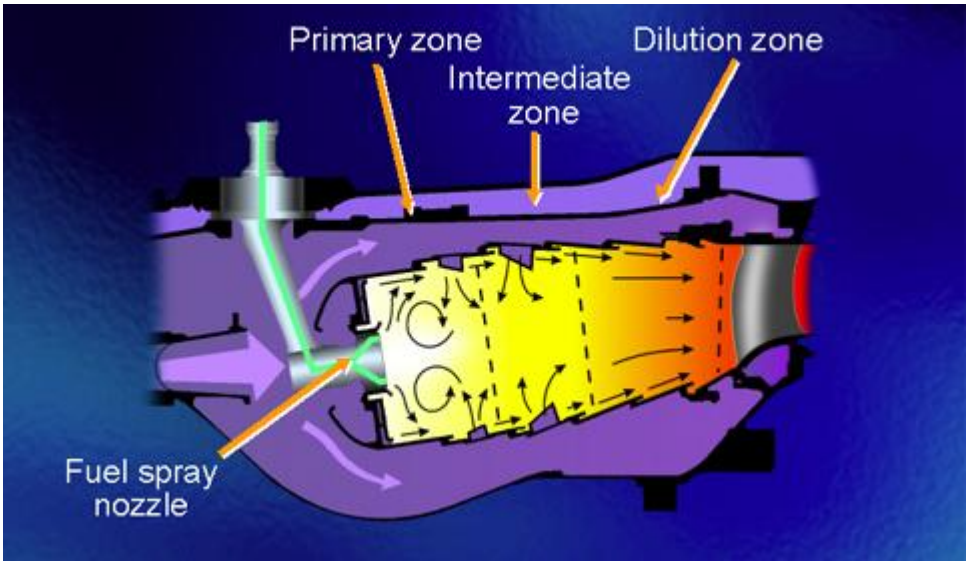

Fig. 1.1 Combustor operation and zones (Rolls-Royce, 1995)

Fig. 1.1 shows a typical single-annular combustor configuration. Since velocity of the air exiting the compressor is too high for stable flame holding, it is decelerated first by a pre-diffuser, followed by a dump diffuser before entering the combustor. In conventional designs, about 20% of the total mass flow enters the combustor through the fuel injector while the remaining 80% flows around the flame tube head and into the annular gap between the liner and combustor casing. About three quarters of this remaining 80% air mass flow is introduced into the flame tube through ports along the primary, intermediate, and dilution zones. The present experimental study focuses on

fluid mechanics and mixing properties in the primary zone, where a central toroidal recirculation zone (CTRZ) exists as an aerodynamic blockage. The CTRZ entrains a portion of hot combustion products and transports it upstream to provide continuous ignition of the incoming air and fuel. Temperatures of the hot combusted gases are subsequently dropped by the cooling air entering through the secondary and dilution zones such that a favourable temperature profile can be generated for the nozzle guide vanes and turbine rotors. The modern combustor achieves virtually 100% combustion of fuel and stable operation over a wide range of fuel air ratios (FAR).

1.1.1 Gas turbine emissions

Gas turbine combustion results in emissions including water vapour, carbon dioxide (CO_2), unburned hydrocarbons (UHC), carbon deposits or soot (C), sulphur oxides (SO_x), nitrogen oxides (NO_x) and carbon monoxide (CO). The reactions producing these chemicals are summarized in Fig. 1.2.

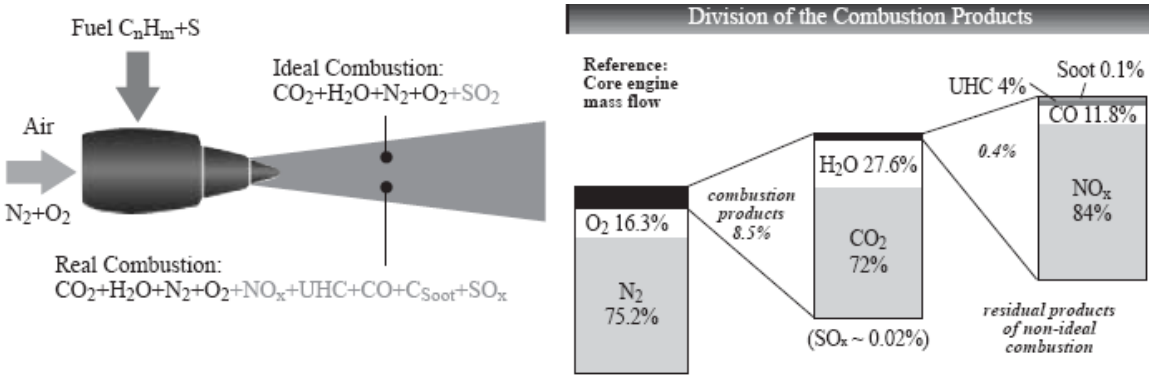

Fig. 1.2 Schematic of Combustion Products and Their Scale (IPCC, 1999)

As shown in Fig. 1.2, majority of the non-ideal combustion products is NO_x. In the context of industrial gas turbines, emissions of NO_x at the ground level present health hazards on respiratory system and lung function (WHO, 2003). NO_x also increases the ozone amount in the upper and lower troposphere by reacting with CO and volatile organic compounds in the presence of sunlight. Tropospheric ozone also causes respiratory ailments such as lung diseases and asthma (WHO, 2003). Two types of NO_x can be formed in a gas turbine combustor: organic NO_x and thermal NO_x. The former is produced by the oxidization of fuel-bound nitrogen, which is more abundant in crude and residual oils; the latter is a result of the dissociation of nitrogen and

oxygen in air and the subsequent oxidisation of free nitrogen to form NO_x. The series of chemical reactions leading to the formation of thermal NO_x follows the extended Zeldovich mechanism (Heyward, 1970). In general, NO_x formation in combustors can be abated by reducing: (1) FAR, (2) flame temperature, (3) inlet air temperature, (4) inlet pressure, and (5) residence time in the flame zone (General Electric, 2001). It is important to note that each of the five variables has an optimum range, under or beyond which other types of pollutants or undesired combustion behaviours could be induced. For example, stoichiometric flame temperatures (above T~1900K) give rise to the formation of NO_x while incomplete combustion at low temperatures (below T~1670K) leads to the formation of CO and UHC. Another example is the residence time of fuel mixtures in the flame zone: while low residence time is preferable in terms of thermal NO_x reduction, it must be long enough to allow chemical reaction and flame holding and to prevent flame blow-out. Hence, although this section and much of this work may make direct or indirect references to the production of NO_x, the formation of other types of pollutants or unwanted combustion effects should not be overlooked.

1.1.2 Regulations

Unlike the regulations on aircraft emissions enforced by the Committee on Aviation Environmental Protection (CAEP), which is a branch of the International Civil Aviation Organization (ICAO)[1], NO_x emissions by existing industrial gas turbines are regulated with various standards in different geographies and countries. Despite this, ever more stringent regulations are being enforced on newly manufactured gas turbines. For example, the US Environmental Protection Agency (EPA, 2012) has recently updated the NO_x emission limit on new stationary gas turbines (with combustion heat input of >15MW and using gaseous fuel) to 25 parts per million (PPM)[2], as compared to the current limit of 42ppm on existing ones. Following this trend, single-digit PPM regulations on new gas turbines can be expected before the end of this decade.

[1] The CAEP/8 NO_x stringency options (to come to effect in 2016) range from 5% to 20% stringency increases for 10 aircraft engine scenarios relative to the current CAEP/6 Standards (ICAO, 2010).

[2] This is corrected to 15% O_2 per unit volume (US EPA, 2012).

1.1.4 Emission Reduction Techniques

Recent efforts (past 15 years) to reduce NO_x emission include flame cooling, variable geometries, staged combustion, Rich-burn, Quick-quench, Lean-burn (RQL), and lean premixed prevaporized (LPP) combustion. These are briefly described here. An effective method of flame cooling is to inject water into the combustor to act as a heat sink, but the technique requires a water-feed passage to be designed into the fuel injector, which means there is a cost penalty. The method also causes decreased thermodynamic and operational efficiencies; and it leads to significant pressure fluctuations in the primary zone. Variable geometry of primary port or fuel injector controls the FAR and thus the equivalence ratio by altering the mass flows of air. However, weight penalties and unsatisfactory reliability when operating such complex system under high temperatures have prevented further development in this area. Staged combustion typically separates combustion into stages using "pilot" and "main" zones: the former is used at low loads while the latter is initiated as the power is increased. In practice, the concept requires double annular configuration to accommodate to the conflicting requirements of both high-power and low-power operations. However, because such design requires extra cooling air and other compromises, the concept was eventually dropped from the Rolls-Royce ANTLE[3] project (Ruffles, 2003). The RQL combustor design utilizes a three stage geometry system in which the fuel is burned in controlled fuel-rich and fuel-lean environments. This technique takes advantage of the low NO_x production in the initial rich burn condition and subsequently completes the combustion in the lean zone, in which temperatures are lowered by air quenching. One of the major difficulties in this technique is maintaining the correct flow split between rich and lean burn zones for the whole range of engine power settings. Also, the rich burn zone needs special cooling techniques; film cooling cannot be used as it would produce locally stoichiometric conditions that increase flame temperatures and stimulate NO_x production. Finally, in the LPP design, fuel is premixed and pre-vaporised with air in a fuel injector before exiting into the combustor. In the literature, the term "partially premixed" may also be used to refer to high levels of mixing prior to ignition even if the first instance of mixing occurs in the combustor (e.g. Stohr et al (2012)). The

[3] ANTLE – affordable near term low emissions

objective of premixing air and fuel is to create a lean homogenous mixture in the combustor so that local hot spots, which are favourable to NO_x production, are avoided. The typical lean FAR in an LPP system translates to about half to three quarters of the equivalence ratio; for example, a derivative of the Turbomeca fuel injector that is studied in this thesis has been operated at an equivalence ratio of 0.70 (Meier et al, 2010). Although LPP combustion appears to be the most effective and economically feasible solution as it is relatively cheaper to retrofit LPP fuel injectors in existing gas turbines, current LPP designs are vulnerable to risks of auto-ignition in the premix passage, flashback, and combustion instabilities. For example, because the Turbomeca fuel injector had been identified to be prone to flashbacks at higher pressure ratios, it was no longer considered suitable for aero applications. The above-mentioned undesired effects may be related to the aerodynamics under isothermal, non-reacting conditions, which is the focus of the present study.

1.2 Fuel Injector

A fuel injection system consists of fuel control, electronic engine control, fuel pumps, fuel atomizer and swirlers. Fuel is first delivered to the fuel injector by one or more pumps, which controls the flow rate to maintain a constant desirable engine speed or pressure ratio. Typical non-LPP liquid fuel injectors in service today incorporate a fuel spray nozzle and one or more sets of annular swirlers. A popular fuel spray design is the prefilm airblast atomiser, which spreads out liquid fuel into a thin conic sheet sandwiched by high velocity swirling air streams.

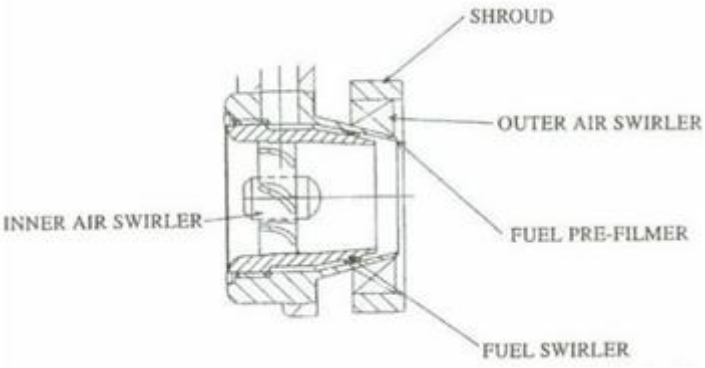

Fig. 1.3 Pre-film airblast fuel injector (Lefebvre, 1998)

The swirling air streams are generated by an inner swirler and an outer one, as shown in Fig. 1.3. The shearing action of high velocity air surrounding the thin cone-shaped fuel sheet helps disintegrate fuel into dispersed smaller droplets, which are more conducive to uniform mixing (Lefebvre, 1998).

1.2.1 Swirlers

In addition to imparting high velocity swirling air into the combustor for the purpose of fuel liquid disintegration, swirling flows also promote the formation CTRZ. CTRZ acts as an aerodynamic blockage, thereby minimising impingement on solid surfaces. Another advantage of the CTRZ is stable flame holding in the swirl cone, which is achieved by the recirculation of active chemical species and heat to the flame base, where the flow and turbulent flame velocity can be matched (Gupta, 1984). Typical swirlers in service today are comprised of angled vanes mounted annularly around a central dome. There are two main types of swirlers commonly found in gas turbines: axial and radial, as shown in Fig. 1.4.

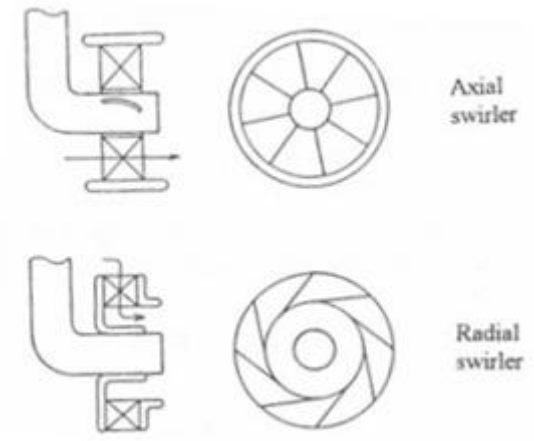

Fig. 1.4 Axial swirler and radial swirler (Lefebvre, 1998)

Only single swirlers are shown in Fig. 1.4, but many fuel injector designs that are being developed or are already in service today may contain more than one swirler. In the case of a double-swirl fuel injector, the swirl vanes may be arranged so that the two swirling jets either co-rotate or counter-rotate. Effects of the co-swirl or count-swirl arrangement have been studied experimentally. For example, Gupta et al (2001) find that the counter-swirl arrangement causes an asymmetrical flame, in which

higher temperature fluctuations are found in localised regions in the flame, whereas co-swirling flame extends to a wider area with lower temperature fluctuations. The authors argue that the counter-swirl arrangement is expected to cause increased NO_x emission. In an experimental study of an airblast fuel injector, Merkle (2003) shows that the counter-swirl arrangement results in a stronger and more compact CTRZ. These studies have therefore highlighted the effects the swirlers have on the flow fields in the combustor. Obviously, single or double swirler designs can also be incorporated into LPP-type fuel injectors; examples include fuel injectors with single swirler (e.g. current work, see Chapter 2) and dual swirlers (e.g. Capena et al (2006) and Stohr et al (2012)).

1.2.2 Physics of fuel injector swirling flow

The central core of a swirling flow is dominated by solid body (forced vortex) rotation and outside this region free vortex conditions may prevail (Gupta, 1984). The demarcation between the central forced vortex and the outer free vortex is the characteristic radius, R. In the rigid body rotation the tangential velocity increases with radial distance from the centre, but in the outer irrotational region the tangential velocity decreases with radial distance. The tangential velocity (W) distributions of both types of vortex are shown in Fig. 1.5, in which both k_1 and k_2 are constants dependent on the flow.

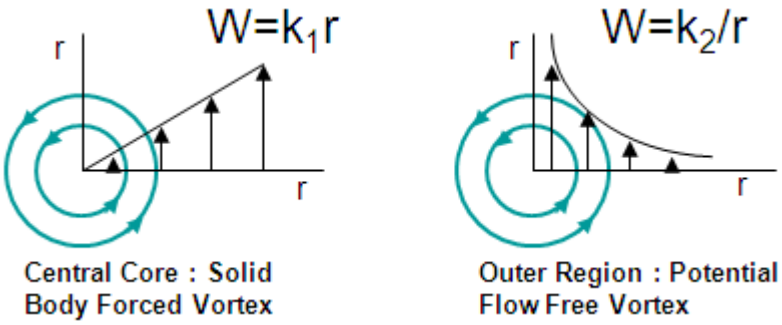

Fig. 1.5 Tangential velocity distributions of forced vortex and free vortex (Muson et al 2004)

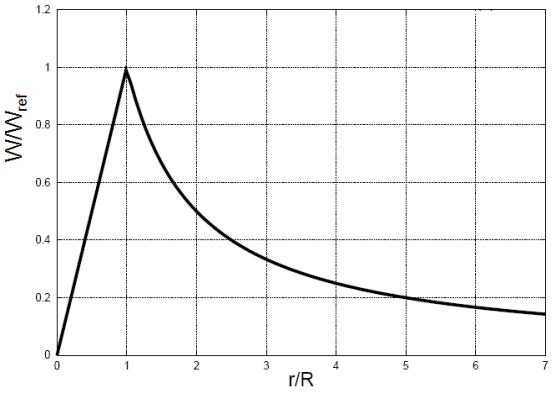

Fig. 1.6 Tangential velocity profile of a Rankine vortex (Gupta, 1984)

A swirling flow having both central forced vortex and outer free vortex may be represented as a function of radius by a combined vortex relationship, which is known as "Rankine" vortex; its tangential velocity profile is shown in Fig. 1.6.

In order to quantify the strength of a swirling flow, the Swirl number is introduced. It is the ratio of the axial flux of swirl momentum and the axial flux of axial momentum times a characteristic radius (Kerr and Fraser, 1965):

$$S_n = \frac{\int_0^R < U >< W > r^2 dr}{R\int_0^R < U^2 > r dr} \tag{1.1}$$

Where <U> is the time-mean axial velocity and '< >' denotes the time-average. At low swirl numbers (S_n<~0.6), an adverse axial pressure gradient may be present but is not enough to cause axial recirculation. At higher swirl numbers (S_n~>0.6), strong coupling is developed between tangential and axial components, both of which decay as the swirl cone spreads downstream. Swirling flow generates a natural radial pressure gradient due to the term W^2/r (Gupta, 1984); as W decreases axially, so does the radial pressure gradient.

$$\frac{dp}{dr} = -\rho \frac{W^2}{r} \tag{1.2}$$

This subsequently produces an axial pressure gradient which cannot be overcome by the forward momentum of the flow, resulting in the formation of CTRZ, which is an aerodynamic phenomenon called vortex breakdown. Vortex breakdown may be most aptly defined by the this statement (Wang and Rusak, 1997): "*an abrupt and drastic change in flow structure which is characterised by a sudden axial deceleration that occurs above a certain level of swirl, leading to the formation of a free stagnation point followed by a separation region with turbulence behind it.*" Although there are seven distinct modes of vortex breakdown observed experimentally (Leibovich, 1978), only the spiral and bubble modes have been observed in turbulent flows. As the swirl number is increased there is a progression of breakdown types such that the bubble mode always evolves from the spiral mode (Sarpkaya, 1972). Further increases in the swirl could move the breakdown further upstream until the boundary of the equipment. Indeed, in the experimental study of Midgley (2005), it is postulated that bubble type is the 'primary' breakdown, which extends backwards into the fuel injector and initiates a 'secondary' breakdown in the form of a helical instability. A series of snapshots showing the evolution of a vortex breakdown with increasing swirl number is shown in Appendix 1.1; these are believed to be representative of the superposition of the two breakdown modes reported in Midgley (2005). Further readings of vortex breakdown can be found in Escudier (1988) and Lucca-Negro and O'Doherty (2001). As shown in Fig. 1.7, a stable recirculation bubble (CTRZ) is generated at a swirl number of S=1.57 and at a Reynolds Number greater than 1.8×10^4, beyond which there is no significant change to the flow field (Gupta, 1984). The Reynolds number is defined as:

$$\mathrm{Re} = \frac{\rho U_{ref} D_{ref}}{\mu} \tag{1.3}$$

Where D_{ref} is the swirler diameter, U_{ref} is the bulk average axial velocity, and μ is the fluid density.

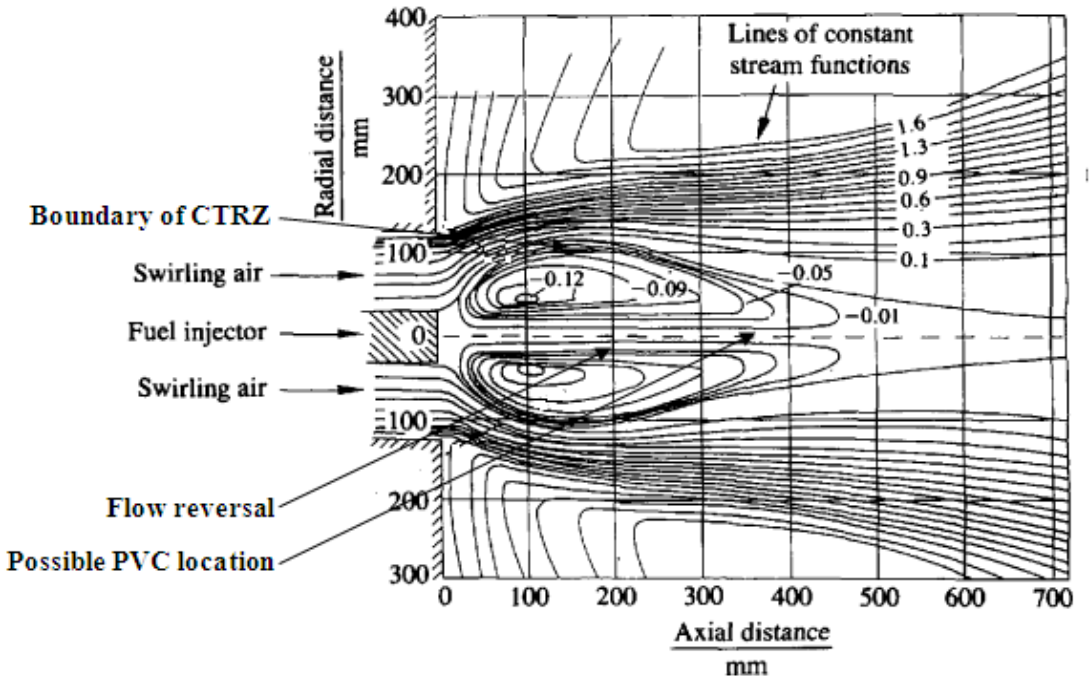

Fig. 1.7 Streamlines of recirculation bubble in Swirling jet, S=1.57 (Chigier and Beer, 1972)

Vortex breakdown can also display strong time-dependent characteristics, whereby the recirculation zone itself becomes unstable, non axis-symmetric and precessses about its own axis (Syred, 2006). This occurs when the central forced vortex becomes unstable and starts to precess about the geometric centre, forming a precessing vortex core (PVC). Rankine-type vortices are particularly prone to the formation of PVC (Syred, 2006). Several experimental studies on swirling flows show that PVC tends to have a regular frequency that is considerably lower than the helical instability, Grosjean (1997), Midgley (2005), Syred (2006), Janus (2007), and Dunham (2010).

1.2.3 LPP fuel injector instabilities

The helical-type instability mentioned earlier is a hydrodynamic instability that is commonly seen across various LPP-type fuel injectors. This instability exists in the form of temporally coherent vortices that follow a helical path in the vicinity of the boundary of the CTRZ, as indicated in Fig. 1.7. For the present work, a distinction is to be made between the helical type instability and the PVC: the former exists in the near field of the fuel injector as the result of secondary vortex breakdown (Midgley, 2005) while the latter is found in the wake of the recirculation bubble, as indicated in Fig. 1.8.

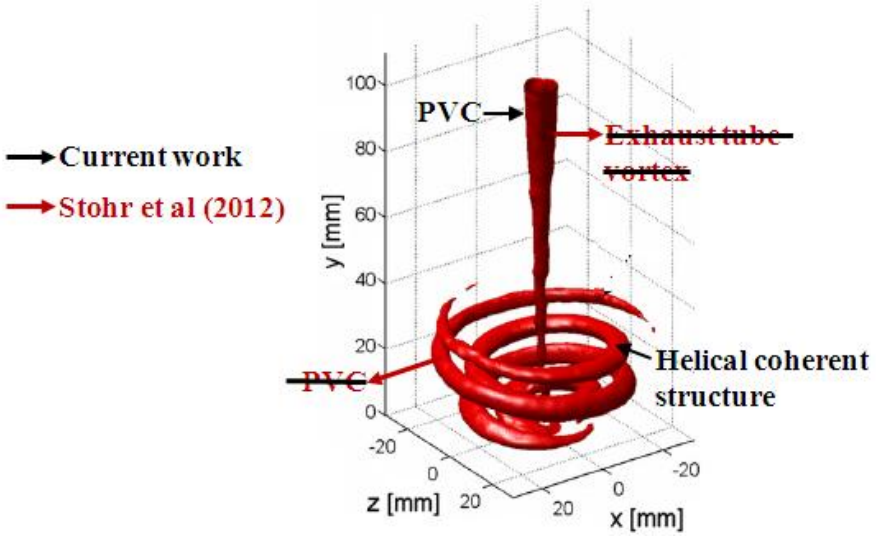

Fig. 1.8 3D reconstruction of vortex structures in a partially-premixed flow field (Stohr et al, 2012)[4]

To avoid confusion, it should be noted that what is referred to as PVC in this study is referred to as "exhaust tube vortex" in Stohr et al (2012); and the same authors, along with Meier et al (2010) and Wegner et al (2007), among others, actually refer to the helical type instability as 'PVC'. Fig. 1.8 helps to clarify this important distinction. Experimental studies thus far have not shown that the PVC is a substantial contributor to combustion instability, Janus et al (2007) and Stohr et al (2012).

The helical coherent structure, on the other hand, has been shown to couple with other types of instabilities to complete a feedback loop (Meier et al, 2007, 2010), as illustrated in Fig. 1.9. A hypothetical sequence of events is described here:

i) Bursts of combustion in the inner swirl shear lead to pressure oscillation at the fuel injector.

ii) Swirl stream air mass flow modulates as a result of the pressure oscillation.

iii) The mass flow of the fuel feed is unaffected due to a much higher injection pressure, e.g. Meier (2007, 2010). This results in oscillation of the equivalence ratio.

iv) The rise in equivalence ratio is transported to the flame base or inner swirl shear with a time delay (convection time) from the fuel feed port.

[4] References to the respective vortex structures by Stohr et al (2012) have been crossed out and replaced with the nomenclature convention of the current work for clarity.

v) A certain period (associated with the chemical reaction time) after the arrival of the rise in equivalence ratio, combustion occurs resulting in a burst of heat release. If the heat release is in phase with the pressure oscillation, then combustion instability can be sustained via the Rayleigh criterion (Putnam, 1971).

A detailed schematic showing the time revolutions necessary for completion of the feedback loop is shown in Fig. 1.10 (Lieuwen, 2001). LPP fuel injectors are notorious for such feedback mechanism between instability types, in which the source of disturbance in step i) can potentially be hydrodynamic in the form of periodic vortices. One such example is the periodic vortex system in the inner swirl shear of the LPP Turbomeca fuel injector flow field, where the vortex system has been identified in both isothermal, non-reaction test (Midgley, 2005) and in reacting test (Janus et al, 2007). Therefore, this suggests that the vortices are hydrodynamic in nature and are independent of combustion.

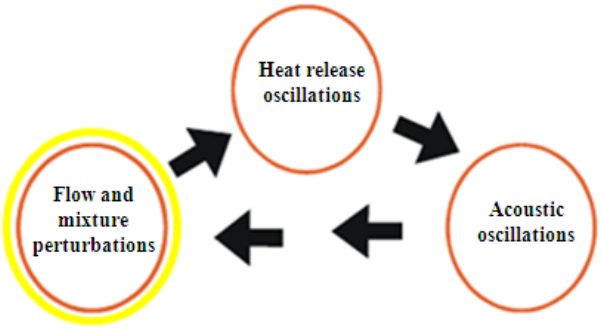

Fig. 1.9 Illustration of combustion instability feedback loop (Lieuwen, 2001)

1.3 Computational fluid dynamics

There are three popular CFD methodologies when it comes to modelling a fuel injector flow field (James et al, 2006): unsteady Reynolds-averaged Navier-Stokes (URANS), large eddy simulation (LES), and direct numerical simulations (DNS). URANS assumes a turbulence model, based on which phase-averaged fluctuating motions are computed. LES resolves large-scale structures and uses algebraic models to solve for sub-grid scale (SGS) motions. DNS does not require modelling for SGS turbulence as all spatial and temporal scales of turbulence are resolved; such

requirement on grid resolution – down to the dissipative range (Kolmogorov length scale for turbulent motions and Batchelor length scale for scalar dissipation) – makes DNS very expensive for high Reynolds number applications. Hence, URANS and LES remain to be the more attractive options from a cost point of view. Dunham et al (2009) is among the first computational fluid dynamicists to show that modelling using unsteady URANS fails to capture the spectral characteristics of the helical instabilities emanating from the swirler, whereas LES reproduces the frequencies of the helical coherent structures and the PVC accurately. Based on these findings, the authors recommend that only LES-based CFD be used for fuel injector flows. Indeed, LES has had reasonable success in predicting time-mean and time-dependent flow structures in fuel injector flows as complex as the present one, examples can be found in Huang and Yang (2005), Wegner et al (2007), Garcia-Villalba et al (2007), Frohlich et al (2008), Dunham et al (2009), and Cheng et al (2012).

1.3.1 Large eddy simulation

In the LES treatment of a fuel injector flow field, three sets of spatially filtered and temporally discretised equations have to be solved. Details of the first two sets of equations, namely the continuity and the Navier-Stokes equations, can be found in Dianat et al (2006). The last one, which governs mixing of passive scalar, is the scalar transport equation (Dianat, 2006):

$$\frac{\partial \rho \overline{C}}{\partial t} + \frac{\partial}{\partial x_k}\left(\rho \overline{U}_k \overline{C}\right) = \frac{\partial}{\partial x_k}\left(\frac{\mu}{Sc}\frac{\partial \overline{C}}{\partial x_k}\right) - \frac{\partial J_k}{\partial x_k} \tag{1.4}$$

Where the over bar denotes a spatially filtered quantity, C is the passive scalar, μ is the molecular viscosity, Sc is the molecular Schmidt number, and J_k is the subgrid flux of the passive scalar C. J_k is defined as:-

$$J_k = \rho\left(\overline{U_k C} - \overline{U}_k \overline{C}\right) \tag{1.5}$$

Where $\overline{U_k C}$ is the resolved turbulent scalar flux and J_k is modelled using the scalar gradient hypothesis:-

$$\mu_{SGS} = \rho l_s^2 S \quad S = \left(2\overline{S}_{ij}\overline{S}_{ij}\right)^{\frac{1}{2}} \quad J_k = -\frac{\mu_{SGS}}{Sc_{SGS}}\frac{\partial \overline{C}}{\partial x_k} \tag{1.6}$$

Where μ_{SGS} is the constant SGS turbulent viscosity, S_{ij} is the resolved strain rate tensor, and Sc_{SGS} is the constant SGS Schmidt number set to 0.7. A standard Smagorinsky SGS model was used in both scalar and momentum equations: $ls = Cs\Delta$, CS=0.1, and Δ is based on the cube root of local cell volume. In the present LES predictions (performed by Dianat, Dianat (2007), Dunham (2009) and Cheng et al (2012)), the spatial filtering operation is not explicitly performed. The discretisation of computational space into a finite number of grids mimics the filtering operation (James et al, 2006), which is also referred to as 'implicit' filtering, where the local filter width is represented by Δ. Although the above scalar gradient model with a constant S_{SGS} is preferred due to its simplicity, methods that incorporate spatially varying S_{SGS} have also been developed (e.g. Brun et al (2008) and Hassan et al (2011)), but these have not been investigated in fuel injector flows relevant to the current one to the author's knowledge.

1.3.2 Validation of scalar mixing

Despite recent advances in experimental techniques, a review of which is provided in Section 1.5, measurements that have focused on the validation of LES-predicted passive scalar mixing, particularly the SGS model J_k via direct comparisons of scalar fluxes, for example, remain unexpectedly rare for fuel injector flow fields. Similar to implicit filtering in LES, popular experimental methods applied to the diagnostics of fuel injector flow and mixing, such as PIV and PLIF, are also subject some form of filtering, as will be discussed throughout Chapters 3 and 4. Therefore, it is just as important to assess the errors associated with implicit spatial filtering in the measured data. In a similar study that focused on the validation of LES-predicted velocities and passive scalar (Frohlich et al, 2008), no effort was made to quantify errors associated with spatial filtering in the predicted or the measured data. Hence, in regions where large discrepancies between predicted and measured data are present, there is

practically no discussion regarding the confidence in the respective datasets from a spatial resolution point of view. Indeed, Kempf (2008) rightfully argues that because it is often too difficult to quantify errors in experimental data, the value in validating LES predictions against measured data becomes questionable. For this reason, much of the effort in the current work has been devoted into the estimation of errors in the turbulent scalar fluxes.

1.4 Mixture residence time

As mentioned earlier, swirl-induced CTRZ acts as a downstream blockage that anchors and stabilises flame in the combustor primary zone. However, LPP-type fuel injector flow fields are susceptible to certain conditions that could serve to destabilise the flame; these conditions are associated with the following phenomena, which may be related to one another (Lieuwen et al, 2008):-

1. Blowout – flame *blowout* refers to the destabilising of the flame to the point where it is no longer anchored in the desired region and "blows out" of the combustor.
2. Flashback – flame *flashback* refers to propagation of the flame in the primary zone upstream into the fuel injector, which may not be designed to withstand combustion temperatures.
3. Auto-ignition – *auto-ignition* refers to the spontaneous ignition of premixed fuel mixture within the premixer (prior to exiting the fuel injector).
4. NO_x emission – as discussed in Section 1.1.1, NO_x emission increases with residence time in the flame zone.
5. Combustion instabilities – the major combustion instability refers to coupling between pressure oscillation and heat release such that the feedback loop in Fig. 1.9 is sustained via the Rayleigh criterion (Lieuwen, 2001).

In the quest to predicting these five phenomena (perhaps with the exception of flashback), the ability to characterise spatially resolved residence times has remained the missing link. The following discussions highlight the importance of residence time in this regard.

Blowout

The Damköhler number, a ratio of the empirically measured chemical reaction time and residence time, has been widely used to correlate with blowout behaviour as a means to predict its occurrence, Driscoll et al, (1992), Noble et al (2006), and Lieuwen (2006). The Damköhler number is expressed as:

$$Da = \frac{\tau_{res}}{\tau_{chem}} = \frac{S_L d}{\alpha_d U_{ref}} \tag{1.7}$$

where τ_{res} is the mixture residence time, τ_{chem} is the chemical reaction time, S_L is the laminar flame speed, α_d is the thermal diffusivity, U_{ref} is the reference velocity (e.g., temperature scaled fuel mixture velocity), and d is typically taken to be the length of the combustor or recirculation zone (Lieuwen, 2006). Hence, residence time under this definition ($\tau_{res} = d/U_{ref}$) simply refers to the convective time it takes to complete one through flow or recirculation in the case of a flame holder. Such estimates of τ_{res} are questionable because there are many routes via which fluid could travel through the combustor, and the length of recirculation zone from the swirler exit to the flame could also be subject to inconsistencies in interpretation.

Auto-ignition

To avoid auto-ignition, residence time in the premixing passage must be shorter than the characteristic auto-ignition delay of fuel mixture (Boyce, 2006). The characteristic auto-ignition delay time can be estimated from the chemical properties of fuel and air with known pressure and temperature, but spatial characterisation of residence times in the geometries of a swirler passage remains a challenge for experimentalists.

NO_x emission

As discussed throughout Section 1.1, NO_x emission from LPP combustion is what motivates much of the recent research effort. It has long been known that thermal NO_x emission increases with residence time in the flame zone, Nicol (1995) and GE (2001). Roffe and Venkataramani (1978) show that for a propane flame, the NO emission index, NO_{EI}, is described well by the empirical expression:-

$$\ln(NO_{EI}/t_G) = -72.28 + 2.80\sqrt{T_{AF}} - T_{AF}/38 \qquad (1.8)$$

Where T_{AF} is the adiabatic flame temperature (Kelvin), t_G is the characteristic combustor residence time (ms), and numerical constants have units consistent with the equation. The residence time only becomes insignificant for very lean mixtures (equivalence ratios below ~0.4) because the temperature, which determines the equilibrium point of the dissociation reaction (e.g., NO production from O_2 and N_2 in the Zeldovich chain mechanism (Heywood et al. 1970)), is then very low. A somewhat similar empirical relationship between NO_x emission and residence time of a methane flame can be found in Rutar and Malte (2001). Although such global measures of residence time allow correlations of emissions to be made and hence allow combustor scaling to be done, they do not help identify the regions of emission production.

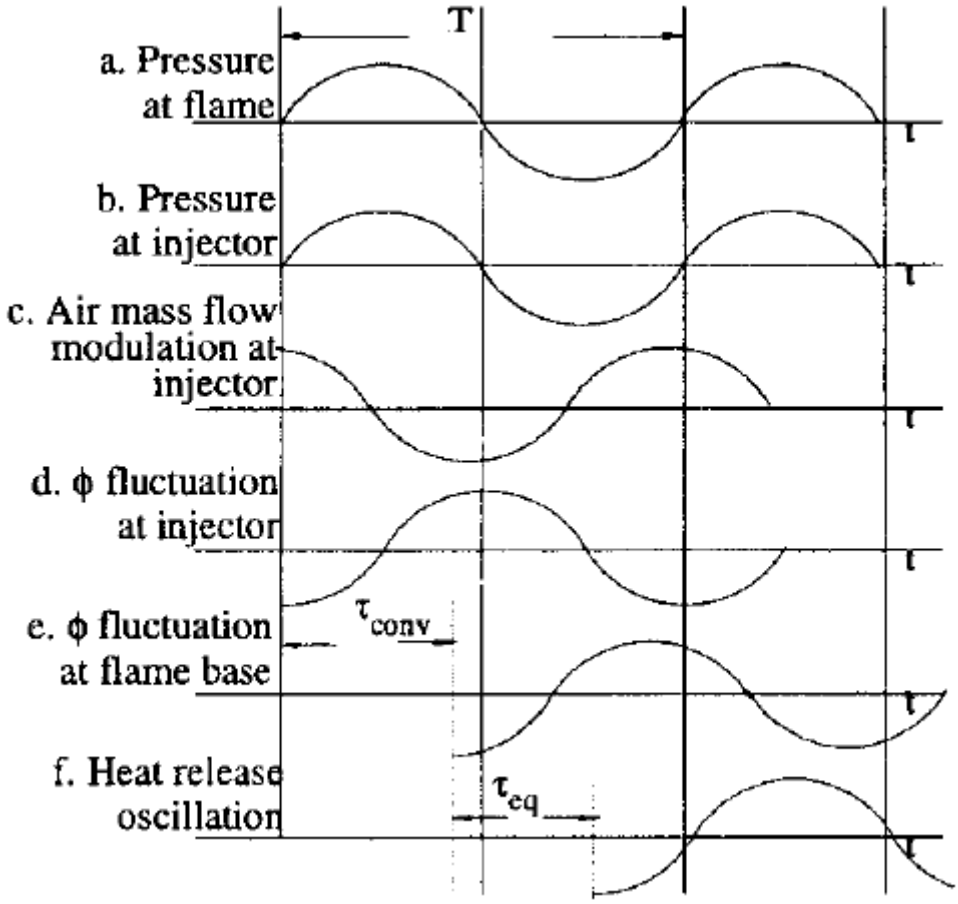

Fig. 1.10 Time evolution of disturbances responsible for combustion instability (Lieuwen, 2001)

Combustion instability

Finally, as discussed in Section 1.2.3, the convection time of equivalence ratio perturbation from the fuel injector exit to the flame base is a crucial parameter in the completion of the insatiability feedback loop. This is clearly illustrated in Fig. 1.10. In order for heat release oscillation to become in phase with pressure oscillation, the sum of τ_{conv} and τ_{eq} must be around 3/4 of a period of the pressure oscillation at the flame base. Here, τ_{conv} refers to the convection time from the fuel injector to the flame base and τ_{eq} refers to a time delay between fuel mixture's arrival and the subsequent reaction (Lieuwen, 2001). When the flame becomes unstable and the location of the flame base becomes phase dependent, then the ability to measure spatially-resolved τ_{conv} would be required.

1.4.1 Residence time estimation methods

Residence time can be inferred from tracing particles through a measured (Giordano et al. 2001) or CFD-predicted velocity fields (Di Nardo et al. 2009). Ozdemir and Peters (2001) used TiO_2 as a particulate passive tracer in the mild combustion reaction zone of a combustor. Concentration was measured at a point via Mie-scattering in response to ceasing the tracer injection and referred to as a ''step-down'' procedure. Highly skewed residence time distributions were observed with the pdf biased strongly toward long residence times. First- through fourth-order statistics of residence time distributions were calculated and discussed in the context of NO_x emissions. The long time average of the residence time was shown to be a misleading quantity when strongly skewed distributions were observed. This is particularly true if the tail of the pdf has timescales associated with it that are significantly longer than the chemical kinetic timescales when the average or global residence time is not. However, these methods can be questioned due to the differences between the equations governing the transport of momentum and of a conserved scalar: The former is influenced by the pressure field, while the latter is not; turbulent diffusion rates of the two quantities will therefore be different (Pantano et al, 2003). The estimation of residence time from conserved scalar tracking, on the other hand, has also been reported. For example, Arai et al. (1998), followed by similar work of van der Lans et al (1997), used helium as a tracer and injected it into a swirl-stabilized combustion chamber with and without reaction. The helium injection was stopped

suddenly, and the attenuation curves (helium concentration decay) at various locations were studied in response. The authors observed slightly shorter residence times due to heat release as would be expected due to flow acceleration caused by density reduction. Accuracy of the absolute concentration measurement was relatively poor in absolute terms (~20%), but it is the rate of concentration change, which was found to be of importance to the technique. Despite these findings, the two aforementioned techniques are single-point-based measurements that do not help identify the possible region of NO_x production.

A simple and efficient technique is developed in this work to provide spatially resolved estimates of residence time using temporally resolved PLIF. This measurement approach, applied to a representative high-swirl combustor flow, examines the dynamic response of non-reacting and isothermal fuel concentration after the injection of fuel is suddenly switched off. To the author's knowledge, this is the first time that planar LIF has been used in this step-down approach, particularly for a combustion-related flow. With careful considerations, the technique could be applied to combusting and reacting tests to help predict the 4 undesired combustion phenomena described above.

1.5 Review of experimental techniques

This brief review focuses mainly on PIV and PLIF, which were already a standard and accepted methodology at the commencement of this work. The development of 2-component PIV (2C-PIV) commenced in the late 1970's (Adrian, 2005), roughly 10 years after Yeh and Cummins (1964) invented the non-intrusive, single-point laser Doppler anemometry (LDA) technique. In the early 1990s, stereoscopic PIV was developed as an extension from conventional 2C-PIV to measure the third component (through-plane) velocity vector on a 2-dimensional plane (Arroyo and Greated, 1991). The main advantages of stereoscopic PIV (SPIV) over 2C-PIV are discussed in Section 1.5.1. A review of the development of PIV till the commencement of this work can be found in Adrian (2005). Due to the non-intrusive and multi-point measurement nature of PIV, it has been the preferred choice of technique for the study of gas turbine combustor flows. Recent development in PIV includes tomographic PIV (tomo-PIV), which uses a number of algorithms to reconstruct 3D volumetric

velocity field from four or more camera views; a most recent application of the technique can be found in Novara and Scarano (2012).

Pioneering studies using LIF were reported by Dewey (1976) and Owen (1976). Dam and Dimotakis (1990) were among the first researchers to demonstrate 2D planar-LIF, or PLIF. Since then, PLIF has traditionally been used to study the mixing of passive scalar, but in the past 10 years the technique has been extended to measurements of temperature, density, mixing rates, and scalar fluxes (Crimaldi, 2008). As discussed in Section 1.3.2, the measurement of scalar fluxes is of particular interest in the present study. A review of the experimental techniques involving combined PIV and PLIF is presented in Section 1.5.2.

1.5.1 SPIV

Conventional 2C-PIV can only resolve two velocity components and turbulence data simultaneously. The inability to simultaneously resolve rms velocities in the 3rd component means that 5 out of 9 terms in the Reynolds stress tensor are missing. Therefore, it is also not possible to obtain quantities such as turbulent kinetic energy from 2C-PIV. 2C-PIV's inability to resolve the 3rd component also leads to another deficiency: the in-plane component measurement is subject to a certain degree of error due to the nature of perspective projection. Fig. 1.11 shows a displacement of the particle within the confines of the laser sheet. The true displacement between X_1 and X_2 is indicated by the dashed arrow, which can be broken into ΔX and ΔZ, respectively. Because of perspective projection, by which the position of the particle is viewed in the perspective of the image plane, the spatial shift between x_1 and x_2 does not represent the true ΔX. Instead, the displacement seen by the image plane is $\Delta X'$, which represents a larger displacement. Raffel (2007) shows that $\Delta X'$, the measure displacement, can be more than 15% larger than the true displacement, ΔX. This error ($\Delta X'$-ΔX) is proportional to the relative magnitude of the out-of-plane component to the in-plane component ($\Delta z/\Delta x$) and the off-axis angle θ (Prasad and Jensen, 1995).

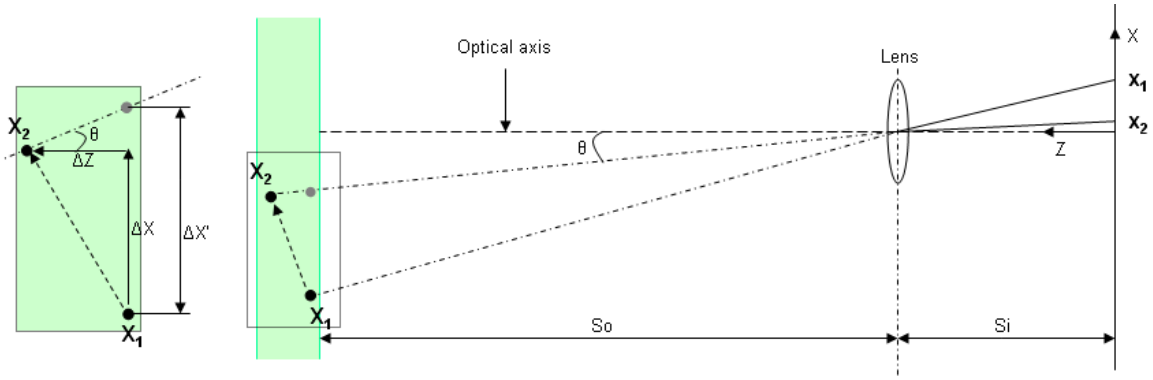

Fig. 1.11 Perspective Error (based on Raffel, 2007)

SPIV eliminates the above-mentioned systematic uncertainty by simultaneously viewing from two different off-axis directions. A typical SPIV setup is shown in Fig. 1.12. The blue vector represents the true displacement of the particle. Each of the left and right cameras sees a displacement. With knowledge of these two displacements and a z-component scaling via 3D calibration, the true displacement can be calculated. The 3C displacement field is constructed from the two planar displacement fields. The equations used for this construction is discussed in Raffel (2007). A comprehensive review of the measurement error in SPIV and the calibration technique can be found in Lawson and Wu (1997), Wienke (2005), and Willert (2006). Optical arrangements and error minimisation strategy are discussed in Chapter 3.

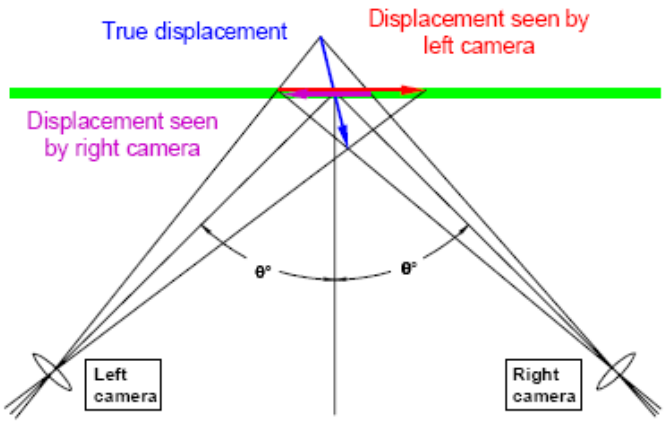

Fig. 1.12 Typical SPIV Setup

1.5.2 Review of combined PIV-PLIF

Passive scalar mixing

Fukushima et al (2000) was among the first researchers to report an experimental study of passive scalar mixing in an axis-symmetric turbulent jet (Re~2000), utilising combined PIV and PLIF. The scalar flux data was compared to LDA-LIF results by other researchers and acceptable agreement was reported. Hu et al (2002) also reported a combined PIV-PLIF study on a turbulent jet (Re~6000): the results were for visualisation only and neither meaningful discussion into the mixing behaviour nor error analysis was provided. Borg (2001) compared the measured the scalar fluxes downstream of a round jet (Re~6000) using combined PIV-PLIF to those predicted by LES; large discrepancies were found between the predicted and measured scalar fluxes. The authors concluded that their measured data suffered from too small sample size to be statistically accurate. Feng et al (2007) applied combined PIV-PLIF to the study of a rectangular jet (Re~50000); the authors used their scalar flux data to reduce a globally averaged turbulent Schmidt number of 0.8, which is consistent with the existing body of experimental data for rectangular jet flows. Zarruk and Cowen (2008) used combined PIV-PLIF to investigate the effect of Re (1500 and 4000) on the scalar variance and scalar fluxes in the far field. Löffler et al (2008) applied the technique to a coaxial jet study for the assessment of LES SGS model, although no LES predictions were presented. The authors addressed the important issue that the velocity and scalar needed to evaluate the scalar flux are measured on different spatial grids, and some form of interpolation/filtering of scalar data to velocity locations is required. Varying the filter size showed notable differences in the resultant measured scalar flux, but no attempt was made to quantify the error due to spatial filtering (for either scalar *or* velocity field).

Reacting flows

In addition to studies of passive scalar mixing, combined PIV-PLIF has also been applied to a number of reacting tests. For example, in the study of flashback driven by combustion induced vortex breakdown reported by Konle et al (2008), the authors used OH-LIF to illustrate and to determine the position of the top flame front relative to the tip of the recirculation bubble, which is calculated from the PIV vector field. Sadanadan et al. (2008) also applied combined PIV and OH-PLIF in a gas turbine

model combustor; the authors examined several instantaneous vector fields and concentration images, from which they observed that localised regions of ignition and flame extinction are related to small vortical structures near the shear layer. The above studies utilise the detection of OH radicals in reacting tests because they appear in high concentrations in burned gas, thereby enabling the determination of flame front by separating burned and unburned gases. Pfadler et al (2009) were the first authors to report a combined SPIV-OHPLIF (dual-plane) study on the evaluation of SGS several models in a v-shaped flame. Meier et al (2010) also applied the technique to two fuel injector flows: temporal variation in methane mixture fraction was found to be related to combustion and aerodynamic instability in the Turbomeca fuel injector, and the dual-swirl fuel injector's strong phase-dependent flow field was shown to alter the flame structure. In a similar study, Stohr et al (2012) applied POD and phase averaging to their combined PIV-OHLIF data; the authors found that the vortices in the inner swirl shear cause a regular sequence of flame roll-up, mixing of burned and unburned gases, and subsequent ignition.

The above-mentioned examples of successful tests in reacting combustor flows do not necessarily eliminate the need for isothermal, non-reacting tests. This is because the flow or mixing phenomenon of interest may be hydrodynamic in nature and are only slightly modified in combusting environments. Careful comparison of cold flow and reacting data can lead to the simplification of further experiments for cost and time considerations.

1.6 Objectives

- ✓ Improve fundamental understanding of single stream radial swirler by enabling simultaneous planar measurement of all 3 velocity components, as well as passive scalar concentration.
- ✓ Deliver an accurate benchmark dataset of turbulent scalar transport for LES validation and understanding of scalar mixing processes.
- ✓ Develop appropriate error assessment techniques, which are to be applied to the experimental data.
- ✓ In addition to identifying the coherent structures in the flow field, apply quantitative techniques to study their effect on the passive scalar.

- ✓ Expand on the previous experimental data by Midgley (2005) and Dunham (2010) on the Turbomeca fuel injector by enabling isothermal tests with the fuel injector operating in premixed configurations.
- ✓ Demonstrate a new residence time measurement technique utilising PLIF and discuss its relevance to NO_x emission and other combustion phenomena.

1.7 Thesis Structure

There are 7 chapters in this thesis and they are arranged as follows:-

Chapter 1 – This chapter starts with an introduction to the motivation behind the present experimental investigation. A brief overview of gas turbine, LPP fuel injector, and its aerodynamic instabilities has been provided. The chapter ends with a review of the most current experimental studies relevant to the present interest.

Chapter 2 – This chapter describes the water flow facility where all experimental data is acquired. Emphasis of the first half of the chapter is on the pipe flow calibration and uncertainty analysis of mass flow measurement apparatus. Detailed descriptions of the fuel injector geometry and test conditions have been provided. The chapter concludes with a validation of the desired test conditions.

Chapter 3 – This chapter deals with instrumentation and minimisation of systematic errors in the measurement. It starts with a general description of the light imaging technique before going into details about the guidelines employed to minimise PIV errors. This is followed by a step-by-step description of PLIF calibration techniques, in which an experimental error estimate has been provided. The optical arrangement involving up to three cameras is described, followed by a description of the residence time measurement technique. The chapter concludes with a listing of the data structure.

Chapter 4 – This chapter explains the data reduction methods used throughout the thesis, including single-point and multi-point data analyses techniques. An individual section has been devoted to the discussion of the current measurement's spatial resolution relative to turbulence length scales. Then detailed error analysis is applied to velocity, scalar, and scalar flux data. The chapter ends with discussions of a new

technique to reduce the static pressure from SPIV data and two established techniques for coherent structure identification.

Chapter 5 – This chapter presents results of the non-premixed fuel injector flow and mixing fields. The ability to characterise all three velocity components provides new understandings into the fuel injector flow fields. All three turbulent scalar fluxes have been discussed and their time-dependent behaviours analysed. For the first time, coherent structure analysis is performed on all three velocity components and scalar simultaneously. The chapter concludes with direct comparisons of scalar mixing with LES predictions.

Chapter 6 – This chapter presents the results of the premixed fuel injector flow and mixing fields. Two test cases have been examined: with central jet and without central jet. Meaningful comparisons in terms of turbulent mixing and vortex behaviour have been provided. The characteristic residence time data has also been compared and discussed with regard to combustion instability and NO_x production with references to combusting data in the literature.

Chapter 7 – This chapter provides conclusions and recommendations for future work.

Chapter 2

2. EXPERIMENTAL FACILITIES

The experimental facility, along with its modifications and calibration work, is described in Section 2.1. The dye injection system and its calibration are described in Section 2.2. For all of the measurements reported in this thesis, the 'datum' fuel injector previously reported in Midgley (2005) has been used. Measurements taken with the fuel injector operating in the non-premixed mode will be used for CFD validation, while those taken in the premixed mode will be used for the extraction of residence time data. These different configurations are elaborated in Section 2.3. The main test conditions and their validations are detailed in Section 2.4.

It may be noted that the measurements were made in two facilities of the same design: one is located in the AAE Department's Water Lab and the other is located in the Unsteady Fluids (USF) Lab near the Hollywell Science Park. For simplicity of referencing, the former is referred to as 'AAE Lab' and the latter is referred to as 'USF Lab' hereon. Experiments were conducted at two facilities because this project had to share the same optical and light sheet instruments with another project in the USF lab. Extensive rig calibration works have been conducted in both facilities, only a generic description of the calibration work based on the USF facility is reported to avoid repetition.

2.1 Water Analogy Facility

The water analogy rig is based on an established vertical tunnel design that utilises gravity as the driving force, thereby eliminating fluctuations in the pump delivery rate. The rig was initially designed by Spencer (1998) in the experimental study of port flows and has been modified in two successive projects; details of the modifications made can be found in the respective PhD theses of Hollis (2004) and Midgley (2005). Water was chosen as the working fluid because it has several advantages over air. First, it is relatively easier to seed water with neutrally buoyant particles than doing so in air. Indeed, when comparing airflow data with water flow data, differences were mostly due to slippage of seeded particles in air (Spencer and Cheng, 2010). Second,

using water as the working fluid has around a 15 to 1 advantage in temporal resolution when scaling through the Strouhal number after matching Reynolds number for the same geometry scale. This helps the identification of high-frequency hydrodynamic instabilities with instruments of limited temporal resolution. Given these advantages, water analogy rig has been widely adopted as a useful tool in understanding isothermal, non-reacting combustor flow, examples of which can be found in Koutmos and McGuirk (1989), Coupland and Priddin (1986), among many others. Previous water flow results on the fuel injector being investigated also showed good agreements with those obtained in air flow (Lartigue et al, 2004), and the Strouhal numbers of the periodic structures also matched well with those found in a combusting test (Janus et al, 2007).

2.1.1 Closed-loop system

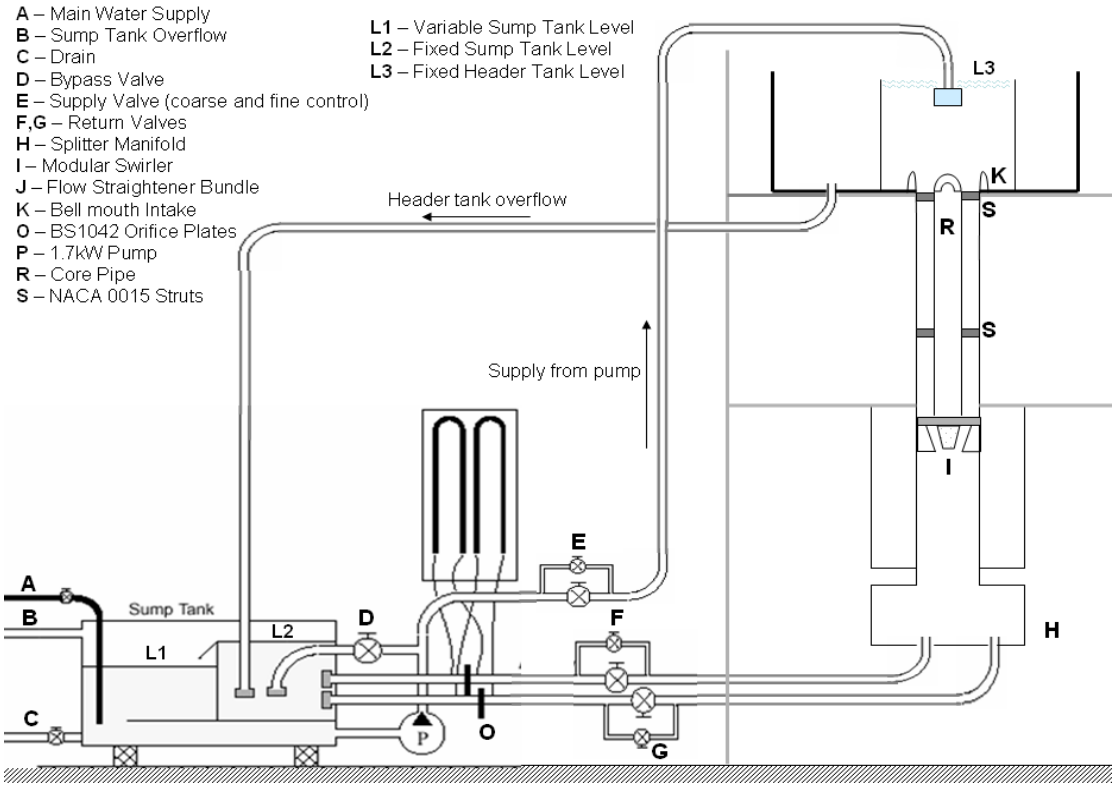

Fig. 2.1 Closed-loop water analogy rig

As shown in Fig. 2.1, water in the sump tank is pumped by one or two pumps (P) into the header tank and is then kept at a constant head level (L3). Any overflow spills into the outer tank and is then returned to the sump tank via the tank overflow pipe. The

mass flow rate through the test section is controlled by the two return valves (F) and (G). The bulk mass flow through the test section is indicated by two inverted manometer connected to the two orifice plates (O) of BS1042 standard. The British Standard Association provides a series of equations to convert a pressure differential to a mass flow rate. Using a series of incremental pressure differentials, the mass flow rate can be plotted as a function of the pressure differential. This procedure was first employed by Spencer (1998) and its accuracy was qualitatively discussed in Hollis (2004). The assessment of its uncertainty is detailed in Section 2.1.5. Stable and evenly distributed annulus flow is created by installing a core pipe (R) of 90mm ID and 100mm OD, held concentrically within the annulus pipe of 140mm ID by two sets of NACA 0015 struts at the pipe inlet and in the mid-section. The installation of a bell mouth at the annulus pipe inlet and the fitting of a bullet shaped cap at the tip of the core pipe prevented the formation of vena contracta and minimised turbulence at the pipe inlet.

2.1.2 Modifications

The main modifications made to the rig included a significant increase of the capacity of the working fluid in the closed-loop system: the capacity of the sump tank has been increased to 2700 litres from the previous capacity of 200 litres; the capacity of the header tank has also been increased to 800 litres from the previous capacity of 50 litres. The length of pipe, measured from bottom of the header tank to exit plane of the fuel injector, has also been increased to 4 meters, which is equivalent to about 200 annulus heights. This is sufficient for the fuel injector inlet flow to be considered fully developed, as confirmed by Midgely (2005), showing that the flow is fully developed at mass flow rates above 1.13kg/s (Re >3000) for the pipe length of 75 annulus heights. Another major benefit brought about by making these modifications is an increase of the residence time of the re-circulating fluid, thereby allowing more data acquisition time for low-speed PLIF before the water contaminated with dye completes one recirculation.

2.1.3 Pipe flow calibration

In addition to checking if the flow is fully developed at the swirler inlet, it was also important to check the circumferential uniformity of the pipe flow. Circumferential bias, which could be caused by possible pipe manufacturing defects and rig installation errors, could result in circumferentially non-uniform distribution of mass flux, hence affecting the symmetry of the fuel injector flow field. Therefore, careful pipe flow calibration work was performed by making PIV measurements in two orthogonal x-r planes, as shown in Fig. 2.2.

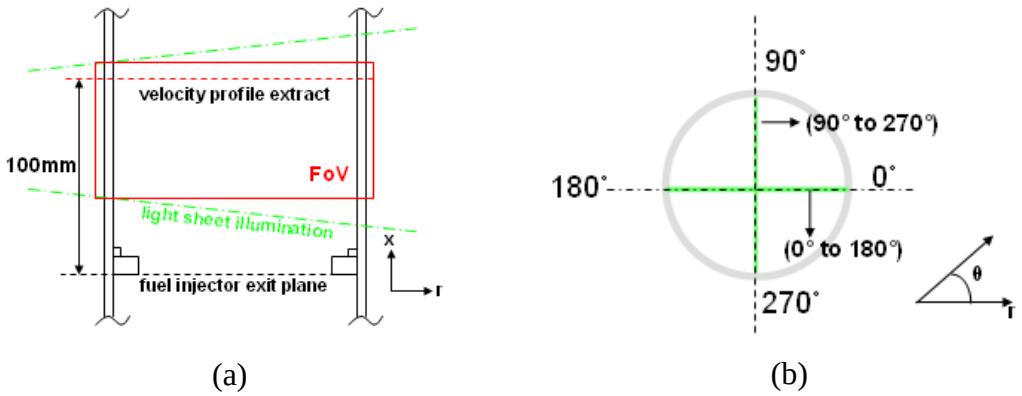

Fig. 2.2 Measurement locations for pipe flow calibration: (a) x-r view and (b) r-θ view

Axial velocity profiles at 4 quadrants have been extracted from 2C-PIV data at 100mm upstream of the fuel injector's exit station, as shown in Fig. 2.2(a). The four quadrants are separated by θ=90°, as shown in Fig. 2.2(b). Each of the four axial velocity profiles is normalized by the centerline axial velocity and the radial locations have been normalized the inner radius of the pipe. Then the profiles are overlaid onto one another, as shown in Fig. 2.3. The good overlap among the profiles confirms the circumferential uniformity. Also, good agreement between the measured profiles and the one-seventh power law (Schlichting and Gersten, 1975) proves that the inlet flow is fully developed.

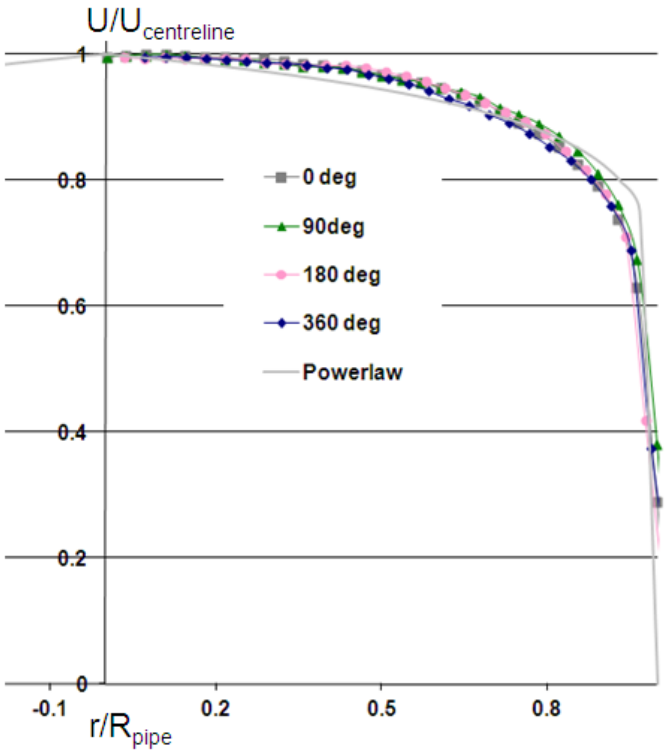

Fig. 2.3 Pipe flow inlet profile

2.1.4 Annulus flow calibration

As mentioned in section 2.1.1, the annulus flow was created by the insertion of the core pipe. The location of the NACA airfoil struts, which help fix the core pipe concentrically, is at about 75 annulus height. At this height, the turbulent wake flows are expected to have dissipated by the time the flow enters the radial swirler. This can be verified by looking at the turbulence intensity profile. Also, to check if the annulus flow is fully developed, the time-averaged axial velocity profiles have been compared against the previous annulus flow data of Hollis (2004), as well as the power law. Again, the level of circumferential variation in the fuel injector inlet has also been assessed with PIV measurements taken at four quadrants that are separated by 90 degrees, as shown in Fig. 2.4. The four velocity profiles extracted at x=80mm above the fuel injector's exit plane are shown in Fig. 2.5. Again there is good agreement among the profiles; differences are within ±5% of the mean with the exception of near-wall regions. The high levels of discrepancy at 2mm near the walls are due to strong image distortion and glare. According to the rms profiles, the turbulence intensity is generally low except for the near wall region, where it may reach up to 23% of the mean.

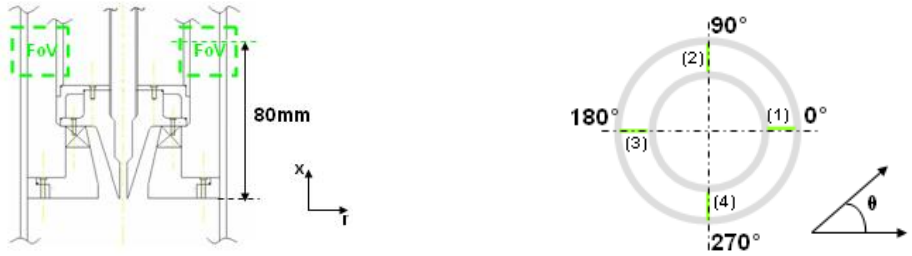

Fig. 2.4 Measurement locations for annulus flow calibration: x-r view (left), r-θ view (right)

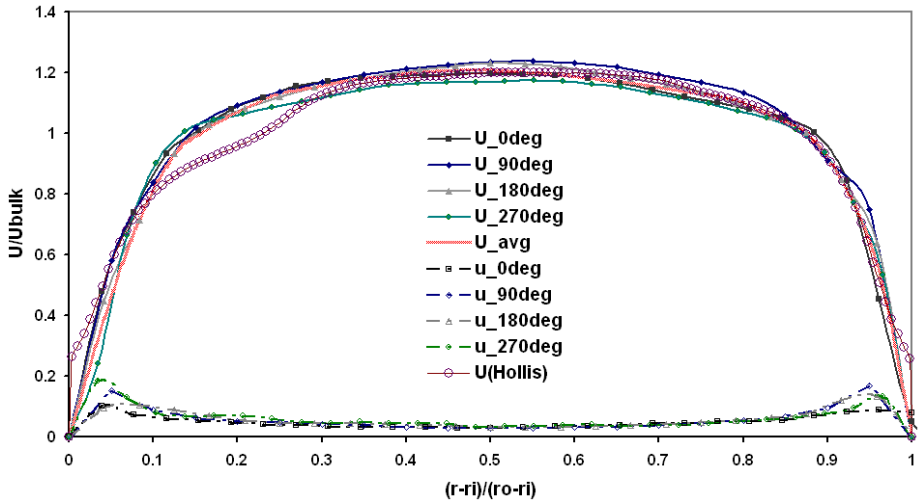

Fig. 2.5 Annulus mean and rms velocity profiles

The comparison with Hollis' data shows acceptable agreement for the most part. In the region where the main discrepancy is found, it can be explained by the lack of symmetry in Hollis' data. The profiles presented in Fig. 2.5 verify the followings:

1. The flow is fully developed at the swirler inlet.
2. The wake turbulence below the six struts and/or possible steps in the pipes' joining sections do not propagate downstream to the fuel injector inlet (also verified by examination of the instantaneous velocity profiles).
3. The level of circumferential uniformity is acceptable and is better than that shown in the previous data.

2.1.5 BS1042 manometer calibration

As the inlet mass flow through the test section is adjusted by the two return valves (F and G in Fig. 2.1), it is important to calibrate the readouts of the two manometers. They are connected to the tappings of two orifice plates that are inserted further downstream (>50 pipe diameters) in the return pipes. A detailed description of the orifice plates and the calibration of the manometer readouts (converted from inches H_2O to kg/s using the BS1042 standard) can be found in Appendix 2.1. As discussed in the Appendix 2.1, because there are several inconsistencies between the orifice plates dimensions and the BS1042 specifications, the manometer-measured mass flow rate had to be calibrated against and corrected by that computed from the PIV data using the following equation:-

$$\dot{m} = \rho\pi\int_{r=r_1}^{r=R} U(r)rdr \tag{2.1}$$

where U(r) is the time-averaged axial velocity as a function of radius, r. The mass flow rate is computed in Matlab, which performed numerical integration of Eq. 2.1 on a best-fitted interpolant function with zero sum-of-squares errors. Uncertainty in the PIV-measured mass flow rate can be quantified as the standard deviation of the mass flow rates at different axial stations, as shown in Fig. 2.6.

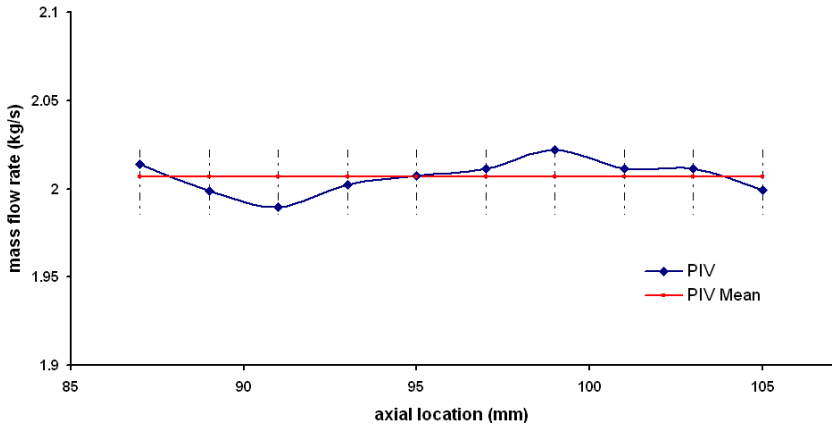

Fig. 2.6 Axial variation of mass flow rate

The mass flow rates calculated from PIV data at 10 axial stations should ideally be the same but instead there is an rms of 0.8% of the mean. But this uncertainty is much lower than that of the water manometer measurements (~5%, see Fig. 2.7(b)), as

discussed in the next section. Since PIV has a significantly lower uncertainty, it was used to calibrate the manometer measurements. Details of the calibration and correction for the manometer readouts are again shown in Appendix 2.2.

2.1.6 Uncertainty of BS1042 mass flow rate measurements

The British Standard provides a series of equations that converts pressure differentials across an orifice plate to a mass flow rates – starting with a Reynolds number estimate based on a typical mass flow rate, a new mass flow rate can be calculated using the given equations; this new mass flow rate in turn provides a more accurate Reynolds number. This procedure is repeated until the difference in mass flow rate with the previous calculation is less than 10^{-6} kg/s. The calculated mass flow rates can then be plotted over a range of pressure drops; a curve can be fitted, from which an equation describing mass flow as a function of pressure differential can be deduced, as shown in of Fig. 2.7(a). However, many variables used in the BS1042 equations have notable uncertainties which may affect the accuracy of the calculated mass flow rate. More specifically, the equations use an approximation of the contraction coefficient; it is an empirical function of β, which is itself a function of the orifice and pipe diameters. It is straight-forward to assess how uncertainty in one variable affects the uncertainty of the calculated mass flow rate. For example, given that the measured orifice throat diameter (nominal at 39mm) is accurate to ±0.5mm while all other measured variables are 100% accurate, the mass flow rate calculated for a pressure differential of 6 inches of water has an uncertainty of ±0.7%. However, because it is more time-consuming to carry out the same analysis for all variables over a range of pressures, a theoretical uncertainty assessment method detailed in Kline and McClintock (1953) serves as a convenient alternative. This method (derived in Appendix 2.3) effectively combines uncertainties in the independent variables, namely manometer water level differential and orifice throat and pipe diameters, to estimate an uncertainty for the dependent variable – mass flow rate. The uncertainty calculated using this method has been added to the uncertainty in the correction method to give an overall uncertainty estimate, as shown in Fig. 2.7(b).

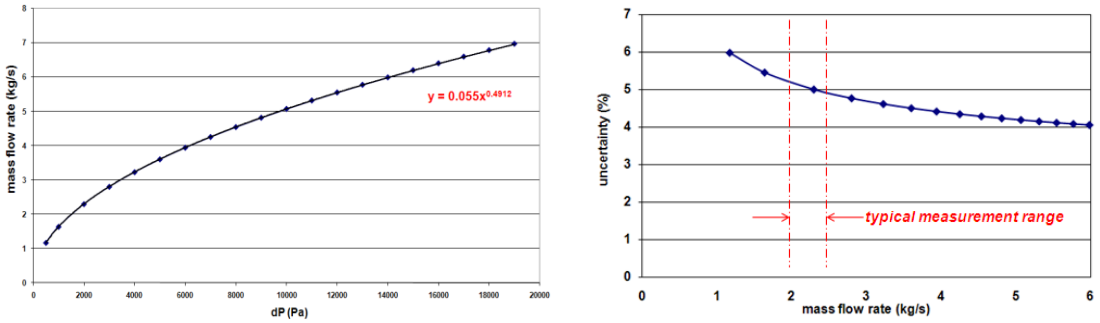

(a) (b)

Fig. 2.7 BS1042 (a) mass flow rate as a function of dP, (b) uncertainty as a function of mass flow rate

The level of uncertainties decays exponentially as the mass flow rate increases. This coincides with the fact that the gradient $\partial \dot{m} / \partial dP$ is larger at smaller pressure drops – meaning that the estimated mass flow rate is more sensitive at lower manometer pressure readings (in inches of water) – thus the mass flow rates estimated there have a higher fractional uncertainty. Based on this analysis, the typical range of swirl stream mass flow rates (~2kg/s to ~3kg/s) has an uncertainty ranging from about 4.8% to 5.3%. This is the uncertainty in the swirl-stream mass flow rate, and it can also be used to represent uncertainty in the swirl stream to jet stream mass flow ratio.

2.2 Dye injection system

To seed the central jet or the premixer with a fluorescent tracer fluid, a dedicated dye injection system was used. The system, shown in Fig. 2.8, is placed next to the header tank at roughly the same height so that the high head pressure keeps the injection rate constant, unaffected by the downstream pressure fluctuations.

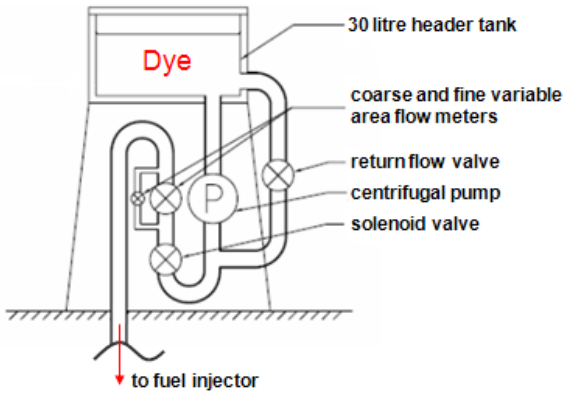

Fig. 2.8 Dye injection system

Fuel, as discussed in Section 2.3, is modelled using a fluorescent dye solution contained in the 30 litre header tank. The dye is injected into the hose pipe that can be connected to the fuel injector's central jet or to the premixing cavity. A 60W DC centrifugal pump provides a constant delivery through the 12mm ID pipe network. The solenoid valve acts as an on-off switch for the dye injection system: when it is closed, flow is only allowed through the return pipe; when it is open, flow is allowed through both the return pipe and the feed hose pipe. The solenoid valve is controlled by a mechanical switch at the ground level. The mass flow rate was controlled by two flowmeters with variable area valves operating in parallel: a "coarse" flow-meter has measurable increments of 3.33×10^{-3} kg/s and a "fine" control has incremental steps of 4.16×10^{-4} kg/s.

2.2.1 Flow calibration

Calibration of the variable flow meters was done by exhausting the flow into a jug over 30 seconds. The amount of water collected by the jug during the time period (converted to litres per minute) is compared to the flow rate read on the flow-meter. This comparison is shown in Fig. 2.9. The good agreement (slope of the line is near unity) confirms that the volumetric flow rate measured by the flow meter could be used directly for setting the dye mass flow.

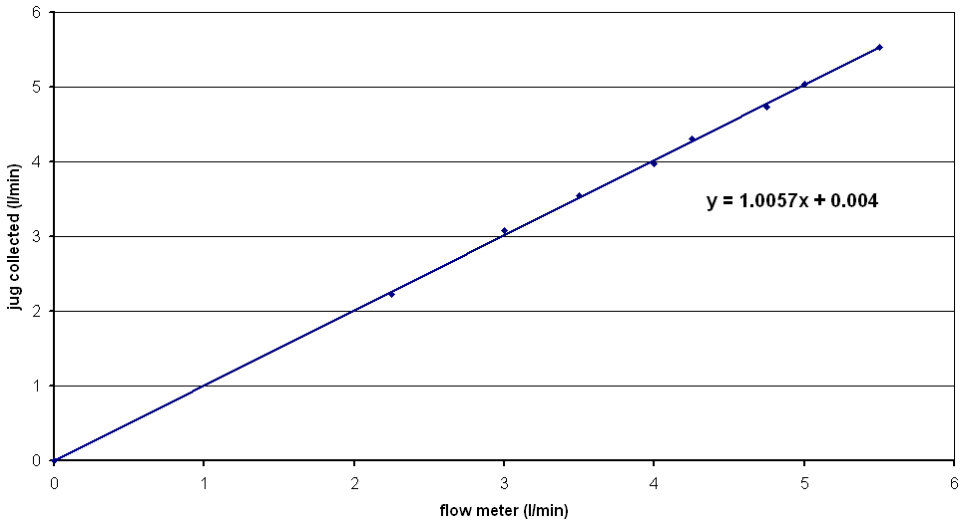

Fig. 2.9 Calibration of central jet flow meter

2.3 Fuel injector configurations and test section

The fuel injector under investigation in this project was based on the Turbomeca lean premix design, which is still of great current interest due to its compact nature and its less-researched radially-fed swirler geometry. As discussed in Chapter 1, the strong shear layer turbulence also makes this fuel injector an interesting case study in terms of the aerodynamic instability and its effect on scalar mixing. The original fuel injector design shown on the left of Fig. 2.10 had been subject to the 4 modifications listed below; these simplifications were made to allow for easier construction of computational meshes (MOLECULES[5], 2004). No changes had been made to the twelve 30-degree radial swirl slots shown on the right of Fig. 2.10, which also shows a central jet that injects air directly into the combustor for control of the primary zone recirculation.

1. The curvature of the inner wall was replaced with a constant angle (17°) tapered slope from the height of the swirl slots to the exit plane.
2. The flare at the exit of the outer wall was removed so that the central jet and the swirler exit are co-planar.
3. The radius of the swirler from the exit plane to 10mm upstream of it was made constant.
4. The curvature or the outer wall had also been removed in favour of a constant angle tapered slope of a 12.5° angle.

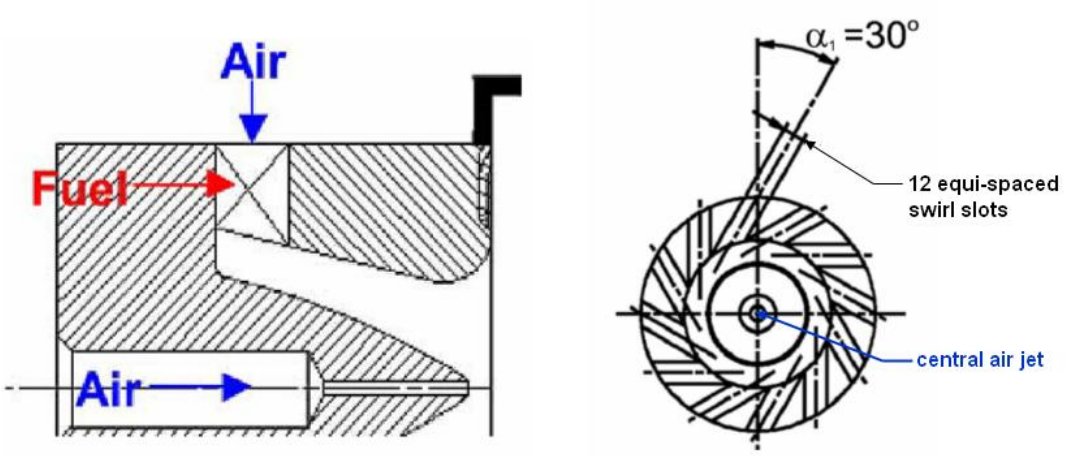

Fig. 2.10 Turbomeca low emissions fuel injector (MOLECULES, 2004)

[5] MOLECULES – Modelling of low emissions combustor using large eddy simulation, an EU project (Contract No. – G4RD-CT-2000-00402) coordinated by Rols-Royce Deutschland. See Report WP3-Lough-15M.

2.3.1 Non-premixed (main) configuration

The new design with the four above-mentioned modifications is shown in Fig. 2.11. Three other key changes that were made with the agreement of the MOLECULES team (MOLECULES, 2002) are listed below:

1. The central jet of air stream was replaced by fuel.
2. No fuel was injected through the premixing swirl slots.
3. The fuel injector was scaled up by a factor of 1.35 to maintain a similar ratio of swirl stream exit area to dump expansion area.

This configuration, with the fuel injector operating in the non-premixed mode, is referred to as the "main" configuration. The gaseous fuel shown on the left of Fig. 2.11 is simulated by a fluorescent dye solution, which is injected directly into the combustor through the central feed pipe. A detailed side-view of the fuel injector geometry is shown in Fig. 2.12. The relevant dimensions are listed in Table 2.1. It may be noted that the swirl stream diameter, D_s, has been used as the normalisation diameter throughout this thesis.

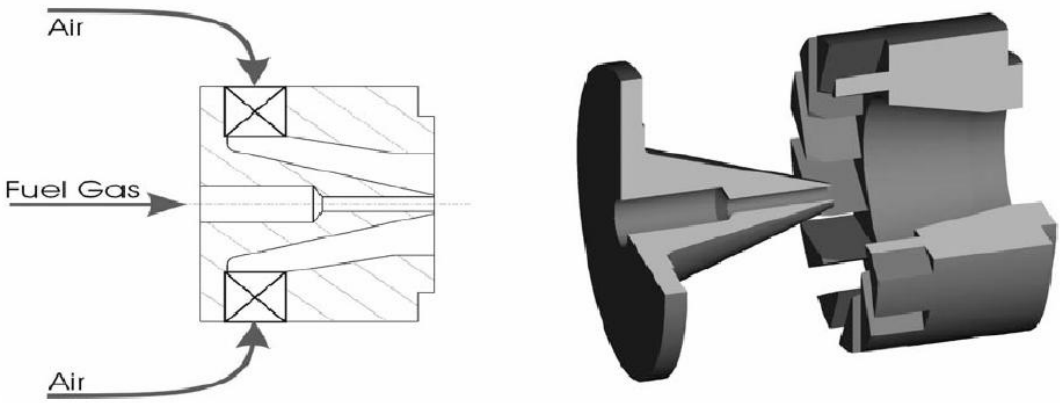

Fig. 2.11 Fuel Injector used for combusting test case in MOLECULES (2004)

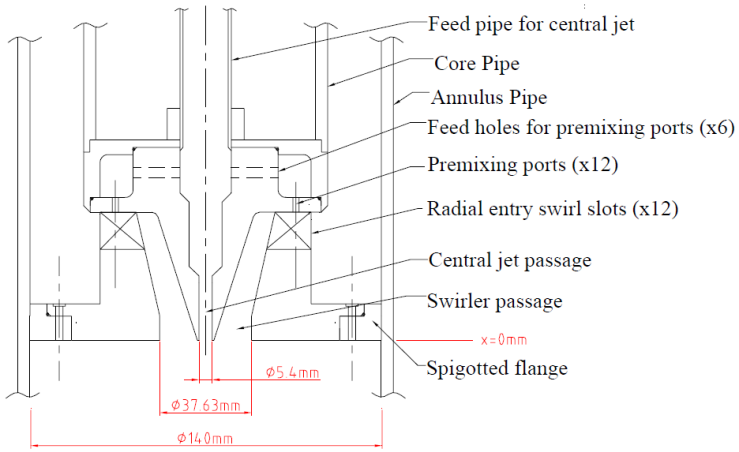

Fig. 2.12 Fuel injector design

Swirl stream outer diameter, D_s	37.63×10^{-3} m
Swirl stream inner diameter	6.76×10^{-3} m
Swirl stream geometrical area, A_s	1.08×10^{-3} m^2
Central jet diameter, D_j	5.40×10^{-3} m
Central jet geometrical area, A_j	2.29×10^{-5} m^2
Dump expansion chamber diameter, D_{ex}	1.40×10^{-2} m^2

Table 2.1 Fuel Injector Dimensions

2.3.2 Premixed configurations

Instead of injecting dye through the central jet and directly into the cylindrical dump expansion chamber, the fuel injector can also be operated in two premixed conditions, where a hose pipe extending from the dye injection system is connected to the premixer. The dye feed to the premixing cavity is indicated by the red arrow shown in Fig. 2.13. After filling up the premixing cavity, the dye exits through 12 ports into the radial entry slots, where premixing takes place before exiting the swirl passage. Two premixed configurations have been tested: with central jet (with jet in Fig. 2.14(b)), and without central jet (no-jet in Fig. 2.14(a)). In the with-jet case, water is fed into the central jet with the same test condition as that used in the non-premixed tests, as summarised in Section 2.4. In the no-jet test case, the central jet hose pipe was removed and it was instead blocked off at the inlet. The dye (RhB) mass flow rate was controlled by the dye injection system described previously.

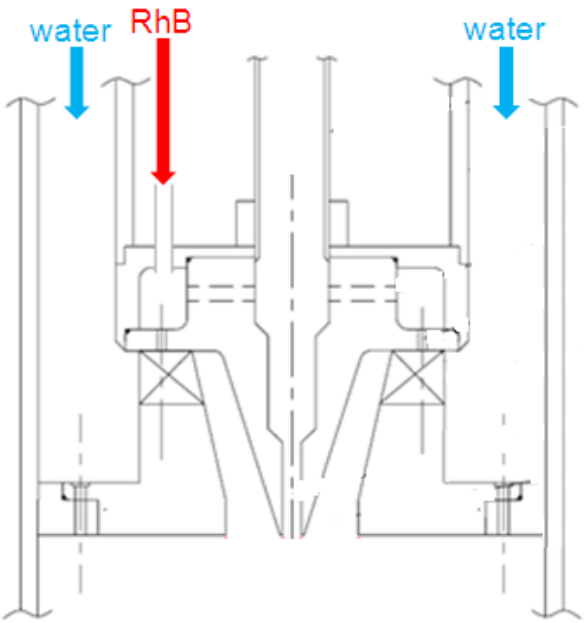

Fig. 2.13 Fuel injector in the premixed configuration

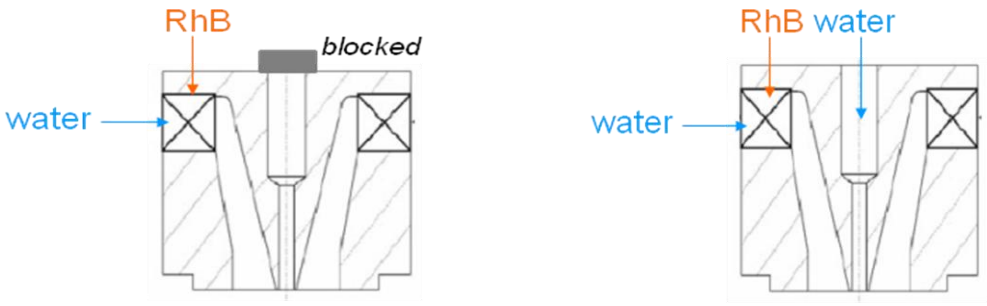

(a) (b)

Fig. 2.14 Fuel injector test cases: (left) without central jet, (right) with central jet

2.3.3 Vertical test section

Downstream of the fuel injector is a cylindrical dump expansion chamber (D_{ex}=140mm), in which all measurements were made. A central blockage was placed 160mm (4.25 swirl diameters) downstream of the injector exit plane to prevent an unduly long CTRZ. This blockage has the same effect as the impinging ports along a combustor's primary-zone liner, which act as an aerodynamic blockage and stabilises the swirl. As shown in Fig. 2.15, the blockage is a hollow round-shaped tube that is inserted concentrically from beneath the exhaust.

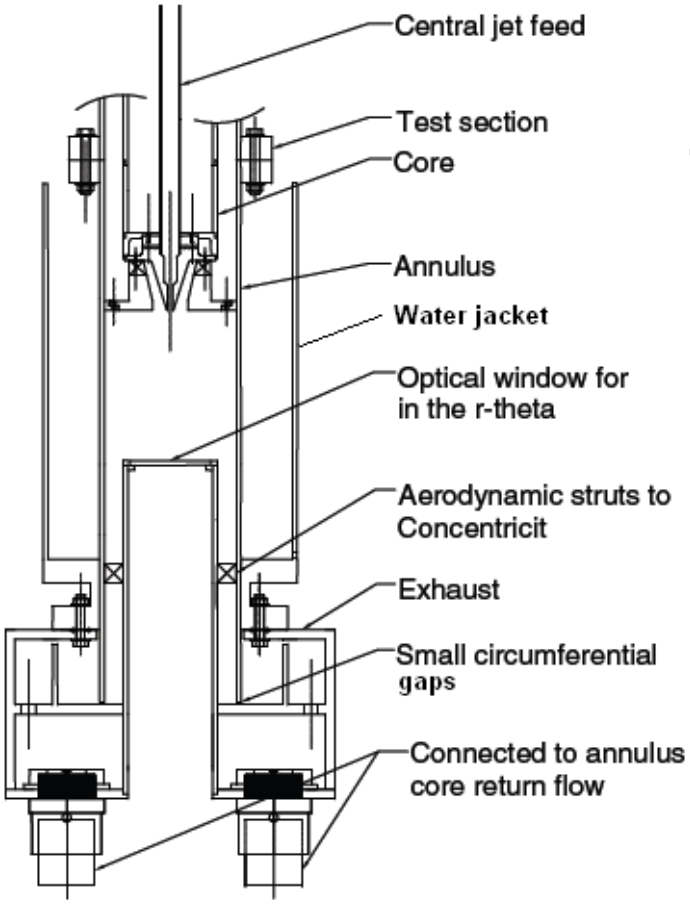

Fig. 2.15 Vertical water flow facility

A similar strategy was employed by Khezzar (1997), who placed a baffle plate 5.4 swirl passage diameters downstream of a radially fed swirler. This blockage also allows for optical access in the r-θ plane; the optical arrangements will be discussed in Chapter 3. The flow exits the test section through the annular gap between the blockage tube and the outer wall before it enters the exhaust through a series of circumferential gaps. These have been designed to ensure that the exhaust is circumferentially uniform, unaffected by downstream pressure variations.

2.4 Test conditions

The test conditions of the non-premixed configuration in this project are similar to the 'main test conditions' reported in Midgley (2005), who calculated the reference jet and swirl stream velocities from the swirl stream mass flow rate and the FAR used in Darmstadt's combusting experiments (Meier et al 2007). Although it was feasible to match the swirl-to-jet velocity ratio, it was instead decided to match the axial

momentum flow rate ratio, $M_{x,j}/M_{x,s}$, to ensure a similar central jet penetration and mixing properties.

Mass flow rate	Combusting (Darmstadt)	Isothermal Air (Loughborough)	Isothermal Water (Loughborough)
Central jet stream (kg/s)	1.38×10^{-3}	17.90×10^{-4}	0.11
Swirl stream (kg/s)	25.0×10^{-3}	34.81×10^{-3}	2.14
Ratio	5.52×10^{-2}	5.14×10^{-2}	5.14×10^{-2}
Reference velocity			
Jet stream (m/s)	84.91	65.58	4.81
Swirl stream (m/s)	37.86	27.19	1.99
Ratio	2.24	2.41	2.41
Reynolds number			
Jet stream (m/s)	3.33×10^{4}	2.34×10^{4}	2.59×10^{4}
Swirl stream (m/s)	2.91×10^{4}	5.79×10^{4}	7.48×10^{4}
Axial momentum flux			
Central Jet stream ($kg\cdot ms^{-2}$)	1.17×10^{-1}	1.17×10^{-1}	5.29×10^{-1}
Swirl stream ($kg\cdot ms^{-2}$)	9.46×10^{-1}	9.46×10^{-1}	4.26
Ratio	1.24×10^{-1}	1.24×10^{-1}	1.24×10^{-1}

Table 2.2 Comparison of test conditions

Table 2.2 shows a comparison of the test conditions used in Darmstadt's combusting tests and Midgley's isothermal airflow and water flow tests. Midgley (2005) showed that variation of the Reynolds numbers did not have an effect on the flow field. This is consistent with the observation of Gupta (1984) that beyond a critical nozzle exit Reynolds number (~1.80×10^{4}), a swirler flow field remains largely independent of the Reynolds number. Since $M_{x,s} = \dot{m}U_s$, the momentum flux ratio can be matched by setting the ratio of mass flow rates at 5.14×10^{-2}. When setting this ratio, adjustment of the mass flow rate in the dye injection system affected the total mass flow rate through the test section, which then increased the pressure differential on the manometer. Hence, an iterative approach was needed to ensure that the desired mass flow rates were met. The swirling flow field generated at the main test condition has a swirl number of around 0.74.

2.4.1 Premixed

Two premixed configurations have been described in Section 2.3.2. The mass flow split between the dye feed and the swirl stream are listed in Table 2.3. For the with-jet case,

The with-jet test case adopts the same momentum flux ratio as that of the main test conditions (but the central jet was injected with water instead). To achieve this, a second dye injection system of the same design was used to inject the dye solution into the premixing cavity at a fixed mass flow rate.

Dye feed (kg/s)	Swirl stream (kg/s)	Ratio
0.12	2.41	0.05

Table 2.3 Swirl stream mass flow rates

Comparisons of the current test conditions with those of the combusting tests by Janus et al (2007) for the with-jet test case and Meier et al (2007) for the no-jet test case are presented in Table 2.4. Because the axial momentum flux ratio ($M_{x,j}/M_{x,s}$) has been matched, the velocity ratio and mass flow rate ratios (m_j/m_s) for the with-jet condition are slightly different than the engine condition as the latter has a density difference between the jet (methane) and swirl streams (air). Obviously, such a difference is not present in water flow. Because the Reynolds numbers used in the combusting experiments are both above 1.80×10^4, the difference in Re has negligible effect on the velocity field.

Conditions	U_s (m/s)	U_j/U_s	$Re_s \times10^4$	$Re_j\times10^4$	m_j/m_s	$M_{x,j}/M_{x,s}$
Janus et al (2007)	37.9	2.24	2.9	3.3	0.053	0.124
Meier et al (2007)	~24	0	3.5	0	0	0
With-jet	1.99	2.41	7.48	2.63	0.0514	0.124
No-jet	1.99	0	7.48	0	0	0

Table 2.4 Comparison of isothermal experimental test conditions with reacting cases

2.4.2 Validation of the mass flux ratio

Since both the 'main' test in the non-premixed configuration and the 'with-jet' test in the premixed configuration involve setting the desired mass flux ratio between the jet and the swirl stream, validation of the ability to control the return valves and the variable area valves on the dye injection is required. Some tests have also been performed at higher Re_s because uncertainty in the manometer pressure differential is lower (Fig 2.7(b)) at higher mass flow rates. The test conditions of an example with elevated Re's are listed in Table 2.5.

	U_s (m/s)	$\dot{m}$ (kg/s)	Re
Central Jet Stream	5.48	0.13	$2.95x10^4$
Swirl Stream	2.35	2.54	$8.88x10^4$
Ratio	2.46	$5.12x10^{-2}$	

Table 2.5 Test Conditions

Because the PIV data reported in Midgley (2005) had been validated against an independently acquired LDA dataset and excellent agreement was found, the former also serves as a valuable benchmark dataset for the present validation. To determine if the main test conditions were correctly set, contours of the mean axial velocity are compared. As shown in Fig. 2.16, the two contours are very similar in terms of the jet penetration distance and distributions of the colour bands. One of the key improvements in the present work is the camera resolution and CCD size: while it required Midgley (2005) to patch together data captured on 4 FoVs, the upgraded cameras (described in Chapter 3) allow the same spatial resolution to be recorded in a single FoV. This essentially avoided the need to patch FoVs, which results in discontinuities in the contour.

A more accurate validation can be done by comparing the profiles directly, as shown in Fig 2.17. The profiles of mean axial velocity extracted at $x/D_s=0.02$ and at $x/D_s=0.5$ have been normalised by the swirl stream's bulk axial velocity, U_s, which is listed in Table 2.5. As shown in Fig. 2.17, good agreements between the profiles at both axial stations support the fact that the desired mass flux ratio can be reproduced in the present work with confidence.

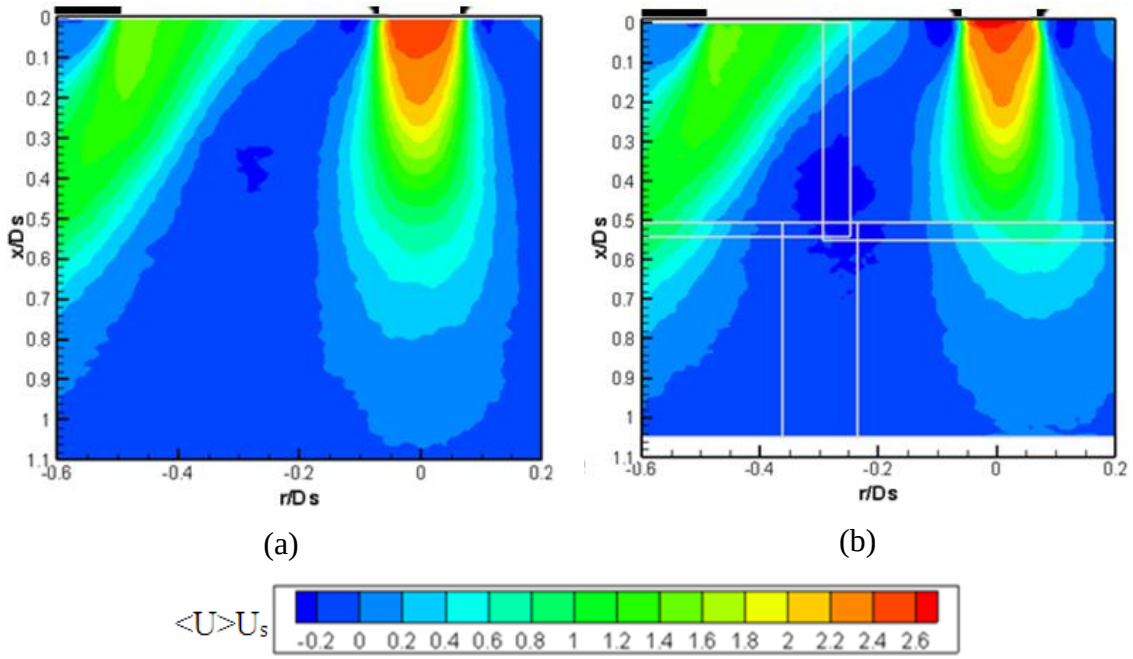

Fig. 2.16 Contours of mean axial velocity: (a) current data and (b) Midgley (2005)

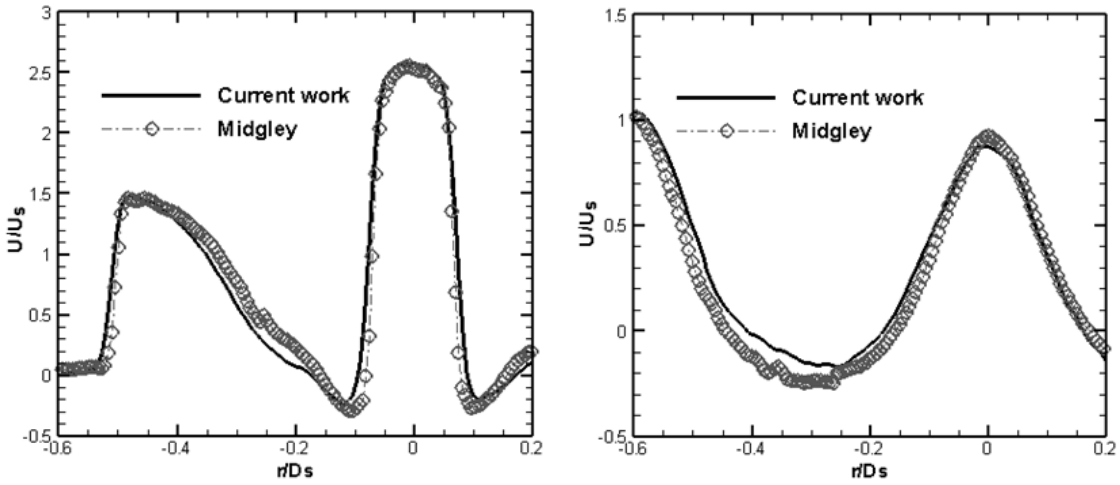

Fig. 2.17 Axial velocity profiles at (left) x/D_s=0.02, (right) x/D_s=0.5

2.5 Sign convention

The positive time-mean axial velocity, $<U>/U_s$, shown in Fig. 2.17 indicates that streamwise flow in the direction away from the fuel injector is positive. Therefore, the right-hand rule is adopted for the sign convention, as illustrated in Fig. 2.18. With the thumb pointing in the positive direction, the palm and the remaining four fingers are curled in the anti-clockwise direction. Thus, when interpreting SPIV data in the x-r plane on the right side of the geometric centreline, positive tangential velocity indicates out-of-page flow. The sign convention for the radial direction is such that it

is positive if the flow direction is away from the geometric streamwise centreline and negative if otherwise.

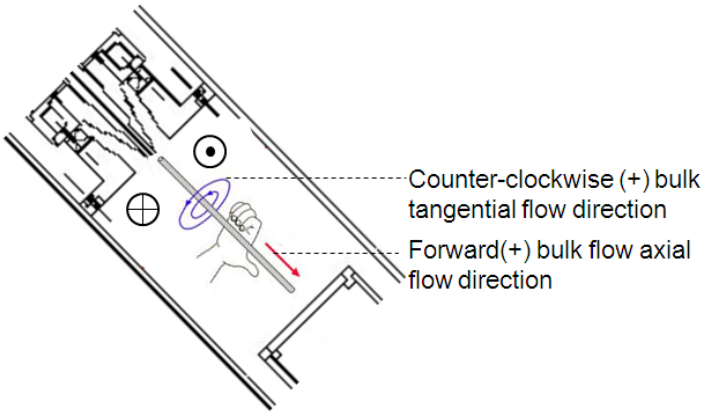

Fig. 2.18 Sign convention adopted for presentation of experimental data

2.6 Chapter summary

This chapter starts with a brief description of the water flow facility and the modifications made to improve the existing design. This is followed by a detailed account of the calibration works done in the rig commissioning stages, including pipe flow calibration and annulus flow calibration. In addition, the manometers, which were used to adjust the mass flow rate through the test section to set the desired test conditions, have been calibrated against the more accurate PIV-measured data. An uncertainty analysis was performed; the results showed that the manometer reading, hence the mass flow rate through the test section, had an uncertainty of around 5% for the typical range of mass flow rates tested. A model relating mass flow rate to pressure differential had also been built based on the BS1042 instructions. The facility commissioning work was concluded with the description of the dye injection system and the calibration of its mass flow rates. The dye injection system was used to feed the fuel injector's central jet or the premixer with a dye solution. The 'main' test conditions had been determined so that the jet stream to swirl stream momentum flux ratio match that of the combustion tests. Although the Reynolds numbers of the water flow tests differ from those of the combusting tests, it has been shown that Re's do not have an effect on the flow field as long as they are larger than 1.8×10^4. Validation of the momentum flux ratio had been completed by directly comparing the current data with the previous data, and good agreement was found.

Chapter 3

3. MEASUREMENT TECHNIQUES

Both PIV and PLIF, which were used here to acquire velocity and scalar fields respectively, can be collectively described as Light Sheet Imaging (LSI) techniques; this approach is introduced in Section 3.1. Planar PIV techniques, including both 2-dimensional 2-component (2D2C) PIV and 2-dimensional 3-component (2D3C) SPIV, are covered in Section 3.2, with emphasis on error minimisation strategies. Section 3.3 follows with an introduction to the PLIF technique, including an in-depth description of the correction steps that were performed to arrive at the final scalar fields. Having described PIV and PLIF, Section 3.4 illustrates the optical arrangements adopted to combine the two techniques to provide simultaneous velocity and scalar measurements, requiring a multi-camera synchronisation strategy. Section 3.5 shows preliminary, large-FoV scalar flux measurements, which were used to highlight the regions of interest and to guide selections of an optimum structure. Finally, Section 3.6 describes a novel residence time measurement technique, which utilises the combined 2D2C-PIV-PLIF technique.

3.1 Light sheet imaging technique (LSI)

Fig. 3.1 shows a typical arrangement of an LSI system. In short, LSI is a non-intrusive technique that involves illuminating the flow area of interest (AOI) with a divergent light sheet, the thickness of which is generally kept as low as possible with the light beam waist generally positioned in the middle of the camera's FoV. In PIV, light scattered by seeding particles are recorded by one or more cameras; the particle image(s) are then subject to image analysis to produce the final velocity vector fields. PLIF, on the other hand, works by capturing the intensity of a fluorescent dye introduced into the flow with an excitation wavelength that is similar to that of the light sheet. A programmable timing unit (PTU) is often included in systems to synchronise the pulsed laser light sources with the recording devices.

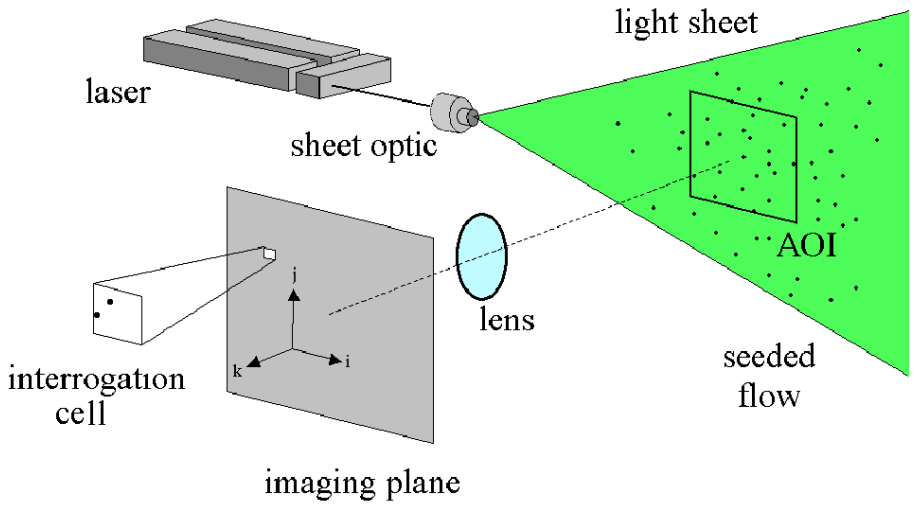

Fig. 3.1 Light sheet imaging system

In this project, pulsed light sources were used instead of a continuous-wave (CW) laser because the former increases the scattering efficiency by packing the available laser energy into a shorter time duration. The recording devices were also operated in a similar pulsed mode and were synchronised with the light source, as elaborated in Section 3.4.

3.2 Particle image velocimetry

Two images, or an image pair, of the illuminated particles are typically needed for a PIV analysis. The image pair is separated by a time interval, known as the interframe time. Locally averaged seeding particle displacements between the first image and the second images can be computed using an algorithm, a generic version of which is briefly described as follows. First, the particle-scattered light within the FoV of a typical image pair are divided into a number of interrogation windows (for example, 64×64 windows with an interrogation window size of 16×16 pixels for a recording device with an overall 1024×1024 pixel field). Then, the intensity field of the interrogation window with second image is convolved with that of the first image using the direct cross-correlation function (CCF):-

$$\mathrm{CCF}(m,n) = \sum_{i}^{M}\sum_{j}^{N} f(a,b) \times g(c+m, d+n) \tag{3.1}$$

Where f(a,b) is the intensity distribution of the interrogation window in the first frame and g(c,d) is that in the second frame. Cross correlation of the two yields a correlation peak within each interrogation window, the location of which relative to the centroid of the interrogation window represents the displacement vector.

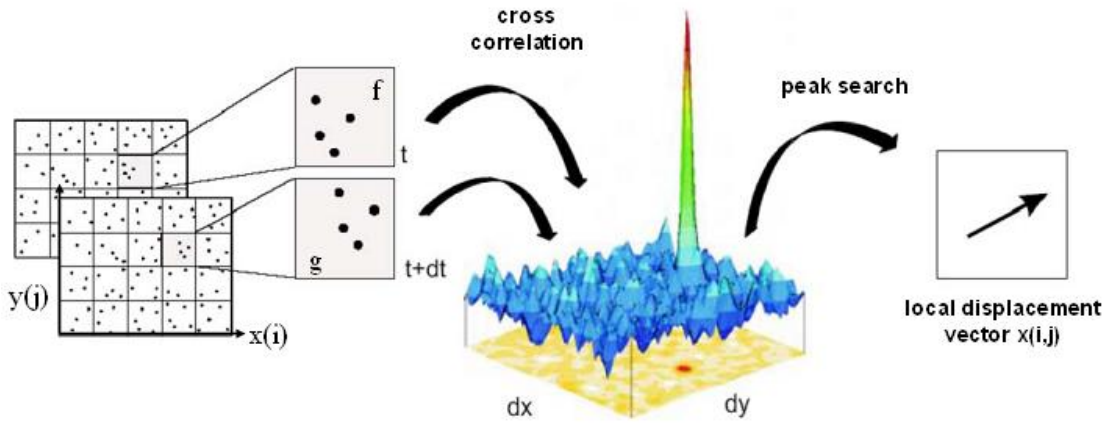

Fig. 3.2 Calculation of displacement vector in an interrogation window using CCF (DaVis, 2009)

The displacement vectors are simply divided by the inter-frame time to produce the corresponding velocity vector components:-

$$U(i,j) = \frac{\Delta x(i,j)}{\Delta t} \qquad V(i,j) = \frac{\Delta r(i,j)}{\Delta t} \tag{3.2}$$

Calculating velocity vectors for a typical image that may contain thousands of interrogation windows using the CCF function as described is computationally expensive: it requires a large number of operations of the order N^4, where N is the length of the FoV in pixels. This number would be increased if a 50% window overlap as usually used was adopted along with a multi-pass algorithm with decreasing window sizes. In order to reduce the computational cost, commercial PIV software such as DaVis (2009) computes the CCF using the fast Fourier transform technique (FFT). This is done by taking advantage of the fact that the cross correlation of two functions is equivalent to a complex conjugate multiplication of their Fourier transforms (Raffel, 2007):-

$$\Phi_{fg} \Leftrightarrow F \bullet G^{*} \tag{3.3}$$

Where F and G^* are the Fourier transforms of the 1^{st} frame intensity field and the complex conjugate of the Fourier transform of the 2^{nd} frame intensity field, respectively, and Φ_{fg} is the resulting Fourier coefficient, which has to be inversely transformed to produce the final cross correlation plane. The FFT is performed more efficiently on windows whose size is a power of 2, and this effectively reduces the computational cost from N^4 to $N^2\log_2 N$. Although a correlation peak is always found on one specific pixel within the interrogation window, as shown in Fig. 3.2, the displacement shift can be calculated to sub-pixel accuracy (up to $1/64^{th}$ of a pixel) by applying a three-point Gaussian fit to the correlation map and interpolating for the point location of the peak (DaVis, 2009). The displacement shift can be interpreted as an average particle displacement between the two laser pulses.

In recent years, researchers have made significant progress to improve the accuracy of PIV; a comprehensive review of its current stages of developments can be found in Adrian (2005).

3.2.1 Errors in PIV

Despite the fact that PIV is a well-established technique, there are several errors which can only be minimised by taking precautions and making right optimisations of user-available parameters. To help understand these errors, it is helpful to divide them into two categories: random errors and bias errors. The former are a result of unpredictable random fluctuations in PIV system hardware operational features, which may include camera noise, variance in the size of seeded particles, and the density of seeded particles. Bias errors in PIV, on the other hand, are a result of systematic errors; these include image distortion and unduly long or short interframe time, among several others. In general, random errors in PIV are very difficult to quantify while bias errors can often be corrected for by use of appropriate correction methods. Researchers have quantified a number of bias errors with the aid of synthetic turbulence data of known characteristics. The quantification of these errors has then enabled the development of a best-practice error minimisation or correction strategy. The following list summarises the common error sources in PIV, with the main emphasis placed on how such errors were avoided/minimised/corrected in this project.

1. Image capture (bias) - Systematic errors associated with image distortion were minimised by enclosing the test section in a square water jacket and inspecting the level of radial distortion of an imaged calibration target containing arrays of 3mm-equi-spaced crosses.
2. Background noise (random) - High background noise intensity could result in errors in correlation peak detection. In addition to enclosing the measurement volume and the optical path to the camera with non-reflective surfaces to block out ambient or stray light, the Q-factor (Raffel, 2007), which is the ratio between the highest and the second highest correlation peaks, was at least 2 for a measurement to be accepted.
3. Particle diameter (bias/random) - Particle image diameters that are smaller than 1.5 pixels may cause peak locking, whereby the measured displacements tend to be biased towards integer values. Particle image diameters that are too large, however, may result in a poor sampling size and a higher rms; this is because large-diameter particles may occupy a large area of the interrogation window and reduce the intensity contrast between particles and background fluid. Simulation data reported by Adrian (1991) suggests that a particle diameter of 2.5 pixels is optimal for an interrogation window size of 32×32 pixels. In this project, the particle image diameter was nominally between 2 and 3 pixels. This was achieved by adjustments of the optical distances and selection of lenses.
4. Particle density (random) – In practice, it is computationally too expensive to monitor the number of particles per interrogation window, however, assuming no in-plane or out-of-plane loss of particles, the synthetic data analysis of Keane and Adrian (1990) shows that the probability of valid displacement detection approaches 100% if the particle density is at least 10 per interrogation window for a 32×32 sized interrogation window. This was achieved by incrementally increasing seeding particles in the sump tank with the rig running in normal test conditions until the desired optimal number was reached.
5. Loss of particle pairs (random) - Although Adrian (1991) recommends that the inter-frame time be optimised such that the out-of-plane movement is less than one quarter of the light sheet thickness, it is in practice difficult to follow this rule as one does not have prior knowledge of the magnitude of out-of-plane

displacement. As a result of this limitation, this rule was not observed in experiments performed in this project.

6. Displacement range (bias) - Selecting a maximum displacement range that is too large increases the likelihood of loss of particles, while a range that is too small makes measurements more sensitive to errors in sub-pixel interpolation and low SNR (Adrian, 1991). The inter-frame time for each test was therefore carefully selected such that the maximum displacement shift in the region of interest was a quarter of the width of the interrogation window (Adrian, 1991).
7. Fluid tracking (bias) - Tracking errors occur when the seeding particles do not follow or lag the fluid movement. These errors are minimised by selecting seeding particles that have similar density as the working fluid and conducting a Stokes analysis to determine the response time (Davis, 2009). The seeding particles selected were made of polyamide with a diameter of 20μm and density of 1.03g/cm^3.
8. Acceleration errors (bias) - PIV uses a Eulerian approximation of displacement rather than the true particle displacement following the Langrangian motion by assuming zero acceleration of a particle captured in the two images. This error is negligible for the present fuel injector flowfield since the inter-frame time is lower than or similar to the Kolmogorov timescale (Midgley, 2005) for the majority of area of interest, as discussed in Section 4.3.
9. Displacement gradient (bias/random) - The lack of homogeneity in the movements of the fluid particles within an interrogation window results in the broadening of the correlation peak, thereby decreasing the accuracy of sub-pixel interpolation. This error effectively results in a low-pass filtering of the displacement vector and causes a loss of the sub-grid fluctuating turbulence information. This error, often referred to as sub-grid filtering, was minimised by selecting as small an FoV as possible. A correction methodology for sub-grid filtering of turbulence data has also been adopted (Spencer and Hollis, 2005); further details of it are presided in Section 4.3.
10. Parallax (bias) – this is a perspective error associated with the through-plane movement of the particles. It could affect the accuracy of the vectors located away from the centre of the image FOV. SPIV is often cited in the literature as the ideal method to address this issue (Raffel, 2007).

It should be noted that with the exception of point 10, the error minimisation strategies in the list are equally applicable to both 2C-PIV and SPIV.

3.2.2 Stereoscopic PIV

Since the basic theories of SPIV were outlined in Section 1.5.1, this section focuses on the apparatus setup and the calibration procedure. Shown in Fig. 3.3 is an example of the SPIV optical setup in the x-r plane of the current experiment.

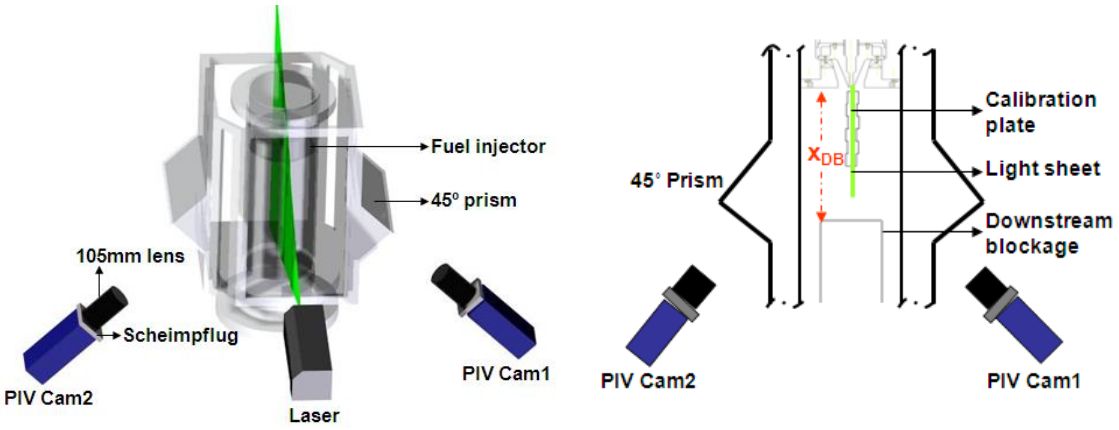

Fig. 3.3 SPIV setup for x-r plane measurement: 3D view (left), calibration (right)

For measurements in the x-r plane, two cameras were placed on either side of the measurement plane which contains the calibration plate. This setup enabled both camera views to be stretched identically, making the orientations of the images more intuitively comprehensible. Measurements in the r-θ plane utilise a different setup, in which the two cameras view the same side of the calibration plate (shown below in Fig. 3.14). The calibration of geometry and orientation was done using a black 2-level calibration plate with equi-spaced white dots, the recorded images of which were fitted using a pinhole mapping function with second order radial distortion correction (DaVis, 2009). Pinhole fit was selected in Davis to fit the image of the calibration plate (whose dot sizes and distances change due to varying magnification, translation and rotation of the calibration plate relative to the camera). Subsequently, a geometric model that maps the positions of each camera's pixels to those defined on the calibration plate was constructed. Finally, the geometric model of the second camera was mapped onto that of the first camera to identify the region of overlap. Since SPIV computes displacement of the through-plane component based on the disparity of the

in-plane components, only the overlapped region could be used for the calculation of displacement vectors. Thus, the cameras were carefully adjusted to achieve a maximum overlap.

Source of Error	**Type**	**What is it and how to minimise?**
Image mapping	Bias	The pinhole model is the mapping function used for all SPIV tests because it has been shown to be highly accurate (Willert, 2006) and its computed geometric projection parameters also allow for the triangulation analysis used in the light-sheet misalignment correction (DaVis, 2009). The error in the mapping procedure is displayed by Davis as the fit rms (DaVis, 2009), which was roughly 0.7 pixels for either camera in the main condition validation test.
Misalignment of calibration plate	Bias/random	Misalignment of the light sheet relative to the centre-plane of the calibration plate is often present. This error can be corrected for by Davis' self-calibration procedure, in which a disparity map is calculated by cross correlation of the two cameras' particle images. Wienke (2005) states that a 9-pixel disparity has an error of 0.44 pixels, which is the maximum disparity vector allowable. The triangulation of the disparity map allowed for a corrected plane that is within 0.1 pixels of the centreline of the light sheet.
Reconstruction of velocity	Bias	Since a 3-component velocity vector is constructed from a total of 4 components, two from each camera, spurious or erroneous vectors present in either camera view would result in a false construction of the final 3-C vector. This error is minimised by specifying a maximum deviation of 3 pixels for either component (Raffel, 2007).

Table 3.1 SPIV errors and minimisation strategy

The prism's inclined angle was designed to reduce the refractive effects due to the camera's oblique viewing angle of 45°, which was chosen to balance the out-of-plane to in-plane error ratio to unity (Lawson and Wu, 1997). A ratio of unity was desired because previous PIV data (Midgley, 2005) showed that the magnitude of the average peak in-plane velocity was somewhat similar to that of the out-of-plane velocity. A Scheimpflug adapter was mounted on each camera to tilt the 105mm Nikon lens as a means to balance the varying optical path lengths from top to bottom of the

calibration plate. It was found that uniform focus throughout a FoV of 50mm×50mm was obtained using a Scheimpflug angle of roughly 15º. The F number of the lens was adjusted to 5.6, which provided a depth of field that entailed the depth of the 2-level calibration plate. In addition to the errors listed in the previous section, SPIV is prone to three additional errors, as summarised in Table 3.1.

3.3 Planar laser induced fluorescence (PLIF)

PLIF is a popular technique used to measure the planar distribution of scalar properties such as species concentration (passive) or flame front locations (reactive). For typical concentration measurements such as those in the current project, only a single fluorescent dye (as opposed to two or more dyes) is needed. The fluorescence light emitted by the dye molecules upon excitation can be related to the dye concentration. The dye tracer used in this project was Rhodamine B ($C_{27}H_{31}ClN_2O_3$). This chemical's absorption and emission wavelengths are shown in Fig. 3.4.

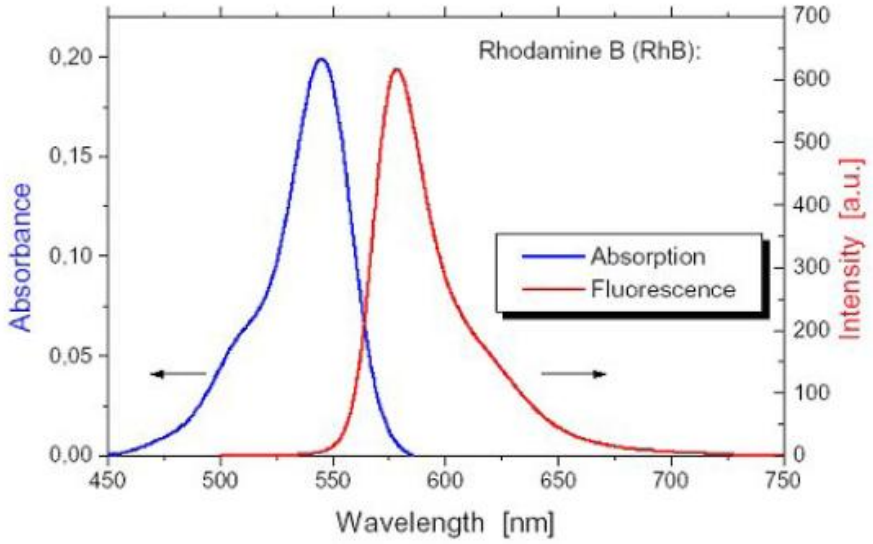

Fig. 3.4 Absorption/Emission wavelength spectra for Rhodamine B, Kemnitz et al (1986), Du et al (1998)

Rhodamine B (abbreviated as RhB) has a high solubility. Its low molecular diffusivity, D_{mol}, means it has a high Schmidt number ($Sc=\upsilon/D_{mol}$) of nearly 2740 in water (Du, 1998); hence its transport is dominated by momentum diffusivity and turbulent velocity fluctuations rather than mass diffusivity, making it a suitable tracer for studies of scalar transport by turbulence. Table 3.2 summarises the relevant properties

of RhB: the peak wavelengths (λ_{sbs} and λ_{em}), the extinction coefficient (ε_{EC}) at the light sheet wavelength of 532nm (Coppeta and Rogers, 1998), and the molecular diffusivity (Rani et al, 2005).

Peak absorption (λ_{sbs})	*Peak emission (λ_{em})*	*Extinction Coefficient (ε_{EC}) at 532mm*	*Molecular diffusivity (D_{mol})*	*Solubility (sol)*
555nm	580nm	81954$cm^{-1}Mol^{-1}$	3.7E-6 cm^2/s	~50g/L

Table 3.2 Rhodamine B properties

RhB is also temperature sensitive: fluorescence decreases linearly with temperature, as demonstrated by Lemoine et al (1999). Because all experiments were conducted in isothermal conditions, temperature variations were negligible and were therefore not considered in the calibration. The relationship between local fluorescence signal (S_{fsc}) of RhB upon excitation by a light sheet with a local intensity (I_L) and local concentration (C) can be written as (Crimaldi, 2008):-

$$S_{fsc} \propto \frac{I_L}{1 + I_L/I_{sat}} C \tag{3.4}$$

where I_{sat} is the saturation intensity of RhB. Saturation occurs when the time rate of excitation exceeds the time rate at which absorbed energy is converted into fluorescence. Pulsed Nd:YAG laser is susceptible to saturation because a significant amount of energy is packed within a short time duration (~ 8×10^7W for a maximum input energy of 40mJ over a pulse duration of 5ns, (DaVis, 2009)), resulting in a fast rate of excitation. Therefore, it is important to ensure that I_L be sufficiently small compared to I_{sat}, so that the term I_L/I_{sat} becomes negligible, thereby reducing Eq. 3.4 to:-

$$S_{fsc} \propto I_L C \tag{3.5}$$

Provided that the local intensity remains constant, S_{fsc} becomes a simple linear function of C. The validity of Eq. 3.5 was verified for every experiment performed in the current work by plotting the recorded fluorescence with respect to concentration, an example of which is elaborated in Section 3.3.4. Eq. 3.5, however, does not relate a

camera's recorded intensity to concentration, nor does it address spatial variations in the light sheet over the area of interest. There are two causes for spatial variations in a light sheet: the first is due to attenuation as energy is absorbed along the ray path and the second is associated with beam shape and sheet-generating optics. Taking these variables into account, the relationship between the fluorescence intensity imaged at any given camera pixel and concentration can be written as:-

$$I_F(i, j) = \alpha(i, j)A(r, \theta)C(i, j) \tag{3.6}$$

where $I_F(i,j)$ is the fluorescence intensity imaged at the ith and jth pixel, (r,θ) takes into account the divergence of the light sheet, as shown in Fig. 3.8(b), $A(r,\theta)$ is a non-dimensional absorption factor and is a function of concentration, $C(r,\theta)$, and $\alpha(i,j)$ is a group of concentration-independent constants that collectively affect how light is imaged onto and recorded by a camera:-

$$\alpha(i, j) = f_{coll}(i, j)\Phi_{QE}\varepsilon_{EC}P_{IB}F_L(r, \theta) \tag{3.7}$$

where f_{coll} accounts for the ratio of fluorescence received by the camera pixel (i,j) to that being emitted at (r,θ) and the subsequent conversion into photo counts, Φ_{QE} is quantum efficiency, which is the ratio of light emitted to that absorbed, ε_{EC} is the extinction coefficient, P_{IB} is the power of the incoming beam, and $F_L(r,\theta)$ is a non-dimensional factor that describes the intensity distribution of the sheet and should integrate to unity if all of the light were contained within the FoV.

Assuming an 'optically thin' system (Melton and Lipp, 2003) in which the absorption term in Eq. 3.6 equals unity, then concentration can be obtained by simply dividing I_F by α, yielding an intensity-corrected concentration value relative to α. Section 3.3.2 describes how the correction for intensity variation was performed, as instructed by Davis (2009). The analysis methods employed to assess whether the measurement system was optically thin are presented in Section 3.3.3, followed by a discussion on how measured and corrected intensities were normalised to obtain concentrations in percentage values in Section 3.3.4. Finally, Section 3.3.5 evaluates the temporal variation of P_{IB}.

3.3.1 PLIF: background subtraction

An instantaneous fluorescence signal recorded by a camera for an arbitrary concentration field consists of two sources: the fluorescence signal itself due to the laser illumination and a signal due to background illumination:-

$$I_{Rec}(i,j) = I_F(\alpha(i,j), C(i,j)) + I_B(i,j) \tag{3.8}$$

where I_{Rec} is the recorded intensity field. The signal response is dominated by the two following sources which determine the spatial variation of I_B.

1. The camera's dark image intensity.
2. Background noise and non-fluorescence light that bleeds through the filtering lens.

To determine I_B the test section was filled with pure water (no dye) and 20 laser-illuminated images were recorded. These images were then averaged to produce one single image – the background image. The fluorescence signal of interest (S_{RhB}) is computed by a simple subtraction for all experimentally captured images:-

$$I_F(i,j) = I_{Rec}(i,j) - I_B(i,j) \tag{3.9}$$

An example of the effect of background subtraction for a typical raw image captured during an experiment is shown in Fig. 3.5.

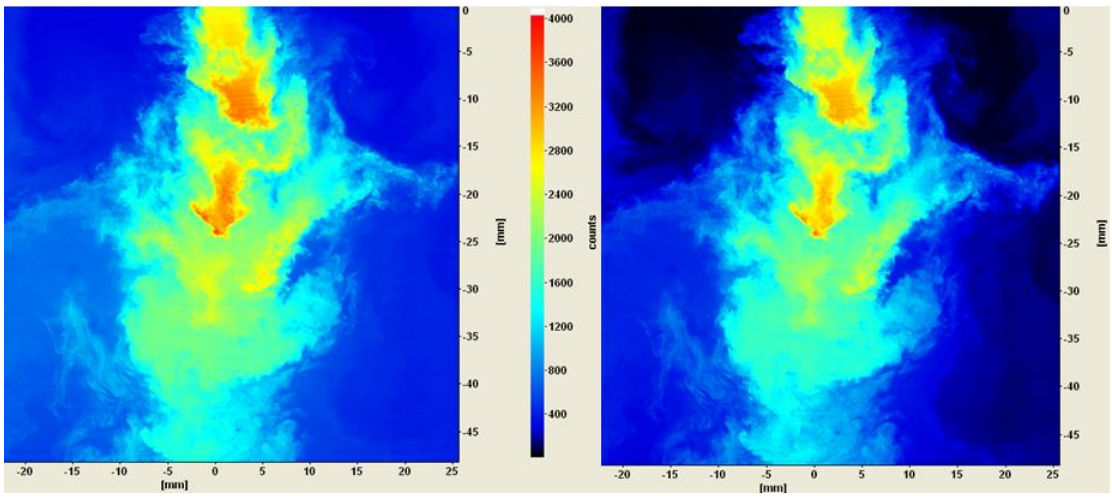

Fig. 3.5 Background subtraction: instantaneous raw image (left), after background subtraction (right)

3.3.2 PLIF: sheet correction

Assuming an optically thin system, the concentration, $C(\alpha(i,j), I_F(i,j))$, as stated in Eq. 3.6 and 3.7, can be obtained by dividing I_F by α, where I_F is the background-subtracted intensity and a robust way to determine α uses a reference image of a uniform, known concentration (Crimaldi, 2008). Instead of using a reference 'sheet correction' image, a spatially distributed sheet correction factor is used by Davis (2009). Therefore, to determine the C(i,j) relative to a known reference concentration, Eq. 3.6 can be re-written as:-

$$I_F(i,j) = I_{ref}(C_{Ref}(i,j))F_{SC}(i,j)C(i,j) \tag{3.10}$$

Where I_{ref} is the uniform intensity field of a known concentration and the term $F_{SC}(i,j)$ is a unit-less factor that corrects for the intensity variation in I_F, which are caused by the beam shape and the use of cylindrical lens to form a sheet. Because the cross-sectional energy distribution of a light beam is typically Gaussian shaped, intensity distribution also appears Gaussian-like in the j direction. The position and choice of cylindrical lens, on the other hand, results in varying thickness of the light sheet in the through-plane direction, particularly affecting planar measurements with low depths of field. $F_{SC}(i,j)$ is obtained by first recording 10 laser-illuminated images of a low-concentration solution and averaging them to produce a single standard 'sheet correction' image, which is then divided by its spatially averaged intensity ($F_{SC}(i,j)=I_{SC}(i,j)/I_{SC,avg}$). There are several criteria suggested by Davis (2009) for this step:

1. The solution must be homogeneous.
2. The laser power and optical setup must be identical to those of the final test.
3. The concentration should be strong enough such that there is sufficient signal strength from RhB fluorescence.
4. A low concentration should be chosen so that the decrease in intensity in the horizontal direction can be assumed to be independent of attenuation due to absorption.

The solution selected for sheet correction image has intensity counts between 50 and 100 (roughly 1% to 2% of the maximum concentration in the example shown here)

after background subtraction (Hollis, 2008). After averaging and background subtraction, Davis' (2009) sheet smoothing step was applied to filter out particulate structures and to smooth the entire sheet correction image with a Gaussian 9×9 filter. This step was applied to remove localised or single-pixel noise that is present in the sheet correction image but absent in final tests.

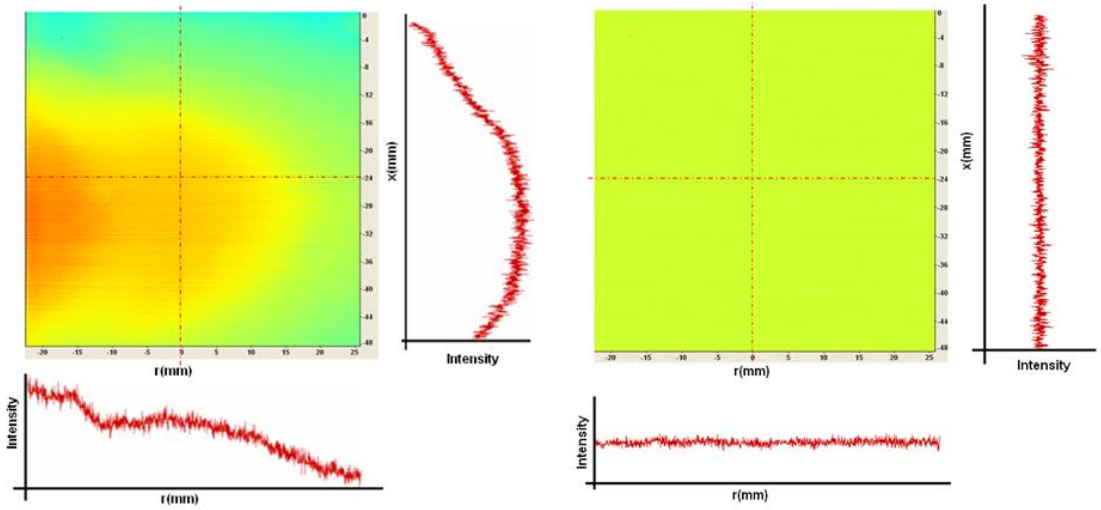

Fig. 3.6 Sheet correction: sheet correction image (left), normalised sheet correction image (right)

Fig. 3.6 (left) shows the raw sheet correction image obtained using the method described, in which the light sheet intensity decreases in the i direction and a roughly Gaussian-like distribution in the j direction, as shown in the intensity profiles extracted along the dashed lines. When this image is normalised by the sheet-smoothed version of itself, the right of Fig. 3.6 shows that the local variations are removed and the intensity profiles become flat in both directions, although low levels of noise-induced fluctuations are still present.

Assuming that the spatial variations of the light sheet intensity remains the same during the experiment, the final images were 'sheet corrected' by normalising them against the image shown on the left of Fig. 3.6. An example of the 'sheet correction' changes that are introduced with a final image is shown in Fig. 3.7.

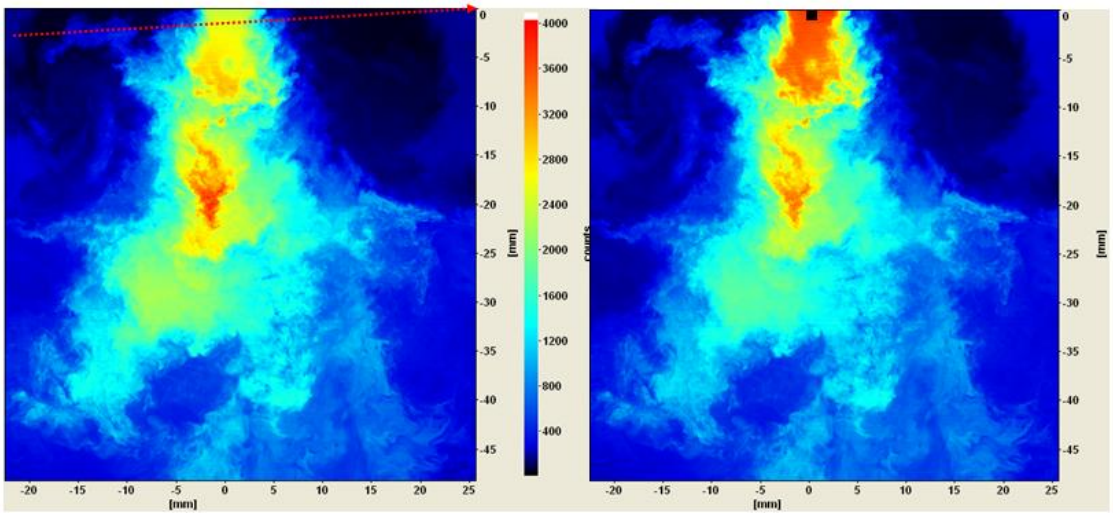

Fig. 3.7 Typical measurement image: before correction (left) after correction (right)

3.3.3 PLIF: absorption correction

As stated in Eq. 3.6, attenuation of the light sheet intensity may also occur due to the extinction of photons after they have been absorbed by RhB molecules. The absorption factor, A(r,θ), that describes the decrease of intensity along the propagation path follows the Beer-Lambert's law:-

$$A(r,\theta) = e^{-\int_0^{\delta} \varepsilon C(\delta) d\delta} \tag{3.11}$$

Where ε is the extinction coefficient of the dye, δ is the beam propagation distance and is a function of r and the sheet divergent angle θ, C(δ) is the concentration at δ, and dδ is the distance between the centres of two pixels. The light sheet's divergent angle was made visible and measured by attaching an opaque object with an aperture on the water jacket's outer wall so that only a portion of the light sheet is allowed into the test section, as shown in Fig. 3.8(b). In order to determine A(r,θ) accurately, the calibration vessel is filled with dye of maximum concentration, such that the absorption correction factor can be empirically determined and subsequently applied from the light sheet entry to any location of interest in a final test image:-

$$I(\delta) = I_0 e^{-\int_0^{\delta} \varepsilon C(\delta) d\delta} \tag{3.12}$$

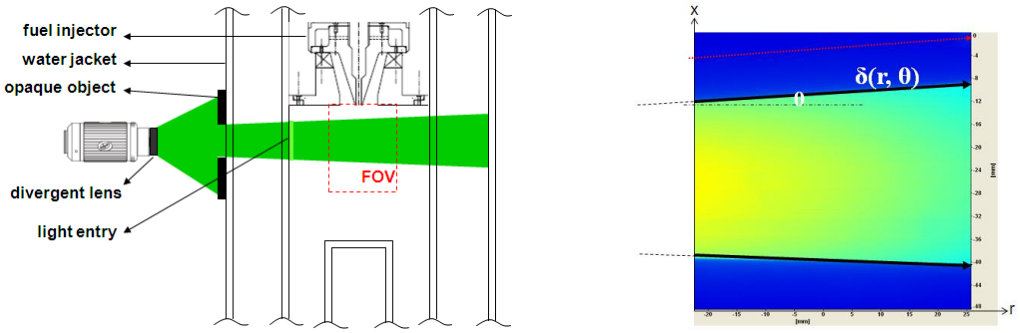

(a) (b)

Fig. 3.8 Light sheet geometry: (a) ray path determination technique, and (b) sheet geometry

The above-mentioned absorption correction could not be applied with accuracy because all of the measurements were made in FoVs that were positioned about the geometric centre, away from the light sheet entry, in order to optimise spatial resolution and to capture fuel injector exit turbulence mixing. Therefore, it is important to examine the attenuation behaviour with respect to two factors – (1) incremental concentration levels up to C=100% and (2) ray path (δ) – these are shown in Fig. 3.9. The ray path along which the intensity profiles were extracted is indicated by the red dashed line in Fig. 3.8(b). All profiles in Fig. 3.9(a) are normalised by the mean intensity value of the 100% concentration, while all profiles in Fig. 3.9(b) are normalised by the intensity profile of the 100% concentration along the ray path. The initial rise in intensity (less visible for C=0.6, C=0.4, and C=0.2 due to scaling) seen in Fig. 3.9(a) is also observed in Karasso and Mungal (1997), Melton and Lipp (2003), and Crimaldi (2008) and their causes are still unknown. The initial rise in intensity reaches a peak at about δ=15mm, followed by a decrease to the furthest edge of the FoV. The range of the rise and the fall is ±8% of the mean value and the RMS of the entire profile is 2.3% of the mean. This attenuation behaviour is also independent of the concentration levels, as Fig. 3.9(b) shows that the 4 other profiles become flat after normalising by I (δ,C=100%). In other words, Fig. 3.9(a) shows that attenuation is indeed present after sheet correction, and Fig. 3.9(b) shows that the attenuation behaviour is the same along the ray path for all levels of concentrations used in the experiments.

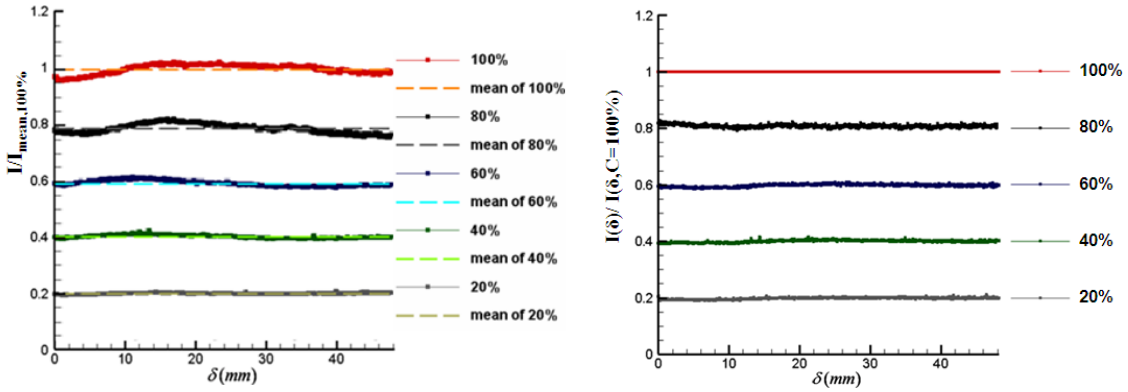

(a) (b)

Fig. 3.9 Attenuation behaviour of increasing concentration levels: (a) sheet corrected and normalised by the mean intensity at C=100%, (b) sheet corrected and normalised by the profile of C=100%

3.3.4 PLIF: concentration calibration

Assuming negligible absorption, Eq. 3.10 can be re-arranged:-

$$C(i,j) = \frac{I_F(i,j)/F_{SC}(i,j)}{I_{ref}(C_{Ref}(i,j))} \tag{3.13}$$

where I_{Ref} is the intensity of the maximum concentration. To show that Eq. 3.5 is valid and that I_F/I_{sat} is much smaller than 1, the intensities of four levels of concentrations below the maximum have been recorded in Davis. An example of the relationship between C and I_F/I_{Ref} is shown in Fig. 3.10. The five known levels of concentrations are each separated by 20%. As shown in Fig. 3.10, the fluorescence intensity is proportional to the RhB concentration and the slope is near unity. C_{Ref} is the same concentration as that at the immediate central jet exit, the location of which is indicated by the small square on the right of Fig. 3.7. Because each intensity recording contains 2048×2048 pixels while the processed vector fields are of 128×128 interrogation cells, the concentration fields would require a further spatial averaging; this will be discussed in details in Chapter 4. Hence, it should be noted that it was the intensity that was first spatially averaged, followed by conversion to C by dividing it by I_{Ref}, which is the spatially averaged intensity at the jet exit. Similar approaches, whereby an instantaneous intensity field is normalised by reference intensity at the injection source, can be found in Feng et al. (2007) and Meyer et al. (2000).

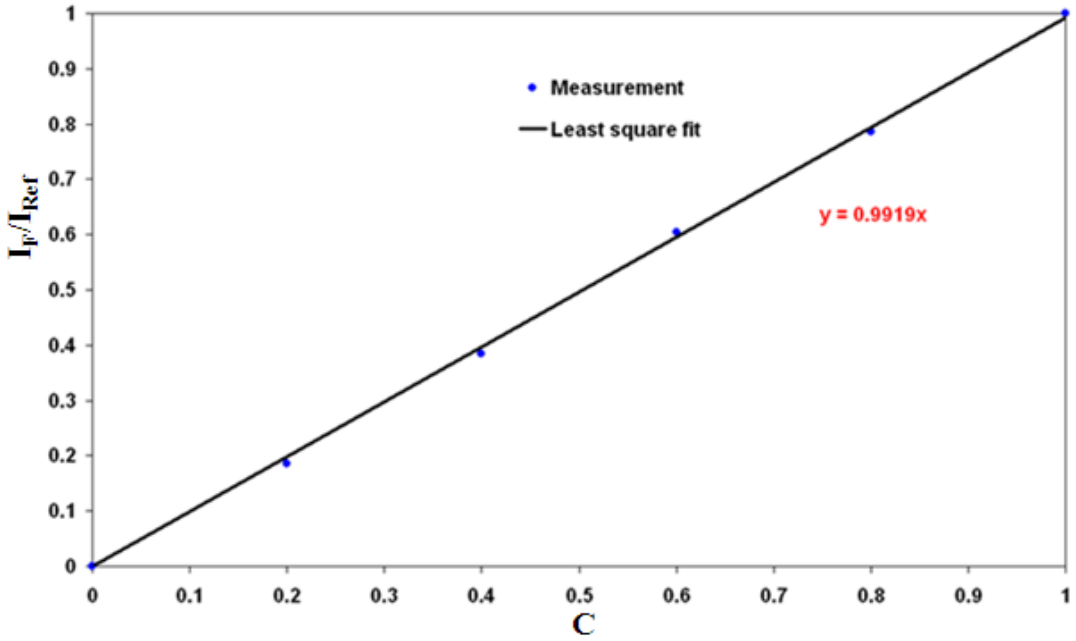

Fig. 3.10 Normalised intensity as a function of normalised concentration

3.3.5 PLIF: pulse-to-pulse energy variation

Pulse-to-pulse energy (P_{IB} in Eq. 3.7) variation could undermine the accuracy of the scalar data, especially for the fluctuating component. Ideally, the energy output of every pulse could be measured and recorded either by installing an energy monitor on the laser head (Lehwald et al, 2010) or deflecting part of the pulsed light into a separate enclosed volume to be imaged by a dedicated camera (Gnirs et al, 2008). However, it was decided not to use such an approach. Instead of measuring the energy output of each pulse, it is possible to evaluate the energy fluctuation statistically and to assign an error to this. This is done by recording 100 images of a homogeneous RhB solution and dividing the rms scalar field by the mean scalar field. As shown in Fig. 3.11, using a uniform solution, it is evident that the pulse-to-pulse energy also varies spatially: temporal fluctuation is higher in the outer, divergent regions of the sheet. This is likely due to variations in the beam shape from pulse to pulse: some might appear spherical while others more elliptical (Raffel, 2007). The overall rms as a percentage of the mean, nevertheless, does not exceed 2.4% in the majority of the FoV. This is consistent with the laser manufacturer's stated energy stability of 2% (NewWave, 2005); such a level of energy variation is generally regarded as acceptable, Borg et al (2001) and Ritchie (2008).

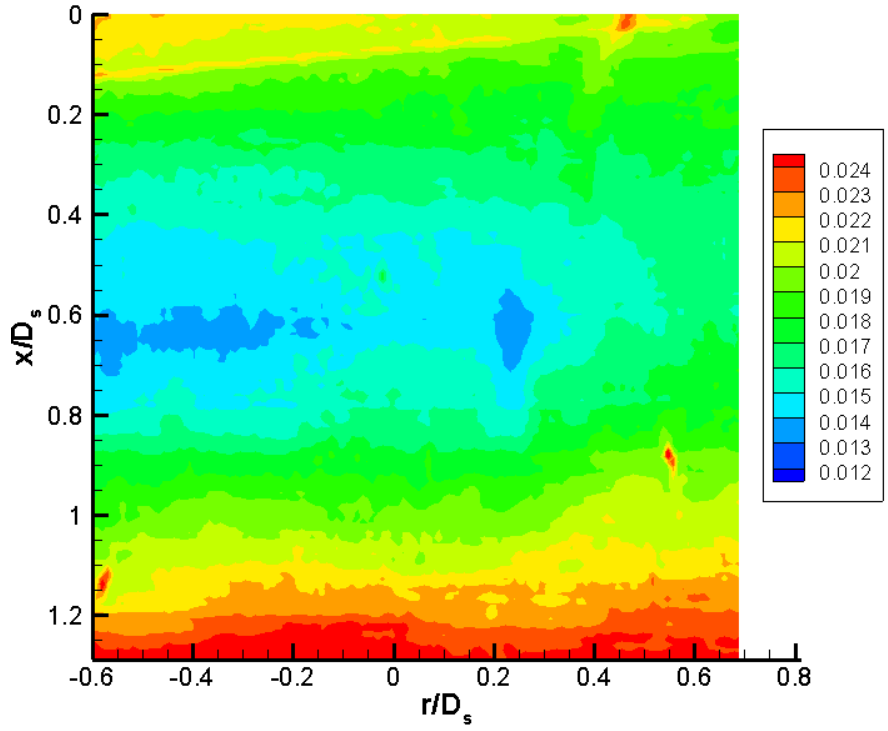

Fig. 3.11 rms scalar field as a percentage of the mean

This error could also be quantified for a final test in the following manner. Time-history of the scalar value averaged within a region of 20×20 pixels (equivalent to 1mm^2), located just downstream of the central jet exit (see right of Fig. 3.7). The instantaneous fluorescent light intensity in this region for each laser pulse was non-dimensionalised by the time-averaged value of the intensity.

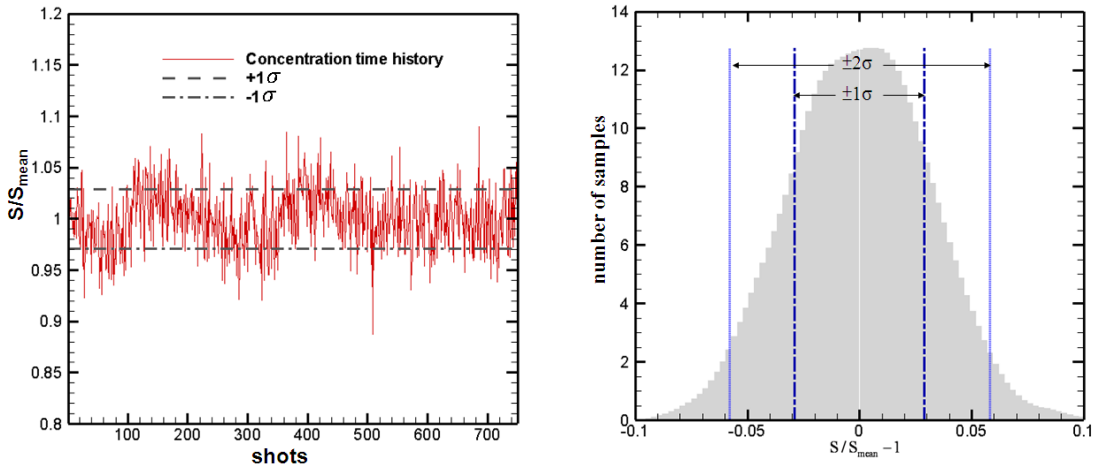

Fig. 3.12 Intensity variation: time history (left), histogram (right)

Fig 3.12 shows that from a dataset containing 750 samples, the standard deviation is about 2.9% of the mean and the probability density function was skewed to the left

with a factor of 0.034. The distribution resembles a standard normal one: about 68% of the samples fall within one standard deviation (1σ) about the mean, and 96% within two standard deviations (2σ), or ±5.8%, of the mean.

3.3.6 Total error estimate

The fact that corrections for absorption and pulse-to-pulse energy variation were not applied meant each had a bias error associated with it. These errors have been estimated with emphasis on the immediate jet exit, where the pulse-to-pulse variation and RhB absorption effects are known be strongest. These errors, along with a combined estimate using quadrature addition, are summarised in Table 3.3.

Error Source	Absorption	Pulse-to-pulse	Total estimate
% magnitude	2.3%	2.9%	3.7%

Table 3.3 PLIF errors

Assuming that the errors take on a standard normal distribution and that they are independent of one another, the PLIF technique used in this project has a total error of 3.7% for a confidence level of 95%.

3.4 Optical arrangements and instrumentation

Both 2C-PIV/PLIF and SPIV/PLIF techniques have been employed in this project. Their respective optical arrangements and synchronisation strategies are described in the following sections.

3.4.1 2C-PIV/PLIF

In order to capture velocity field and concentration images instantaneously using two cameras, the light scattered by seeding particles must first be separated from the RhB fluorescent light and subsequently focused onto PIV and PLIF cameras respectively. Splitting of the planar light signal was achieved by use of a dichroic mirror, which was set at a 45° angle relative to the light sheet plane. The dichroic mirror deflects light with a wavelength that is smaller than 550nm and allows it to pass otherwise.

Hence, it may also be referred to as an "image splitter". This particular setup is shown in Fig. 3.13.

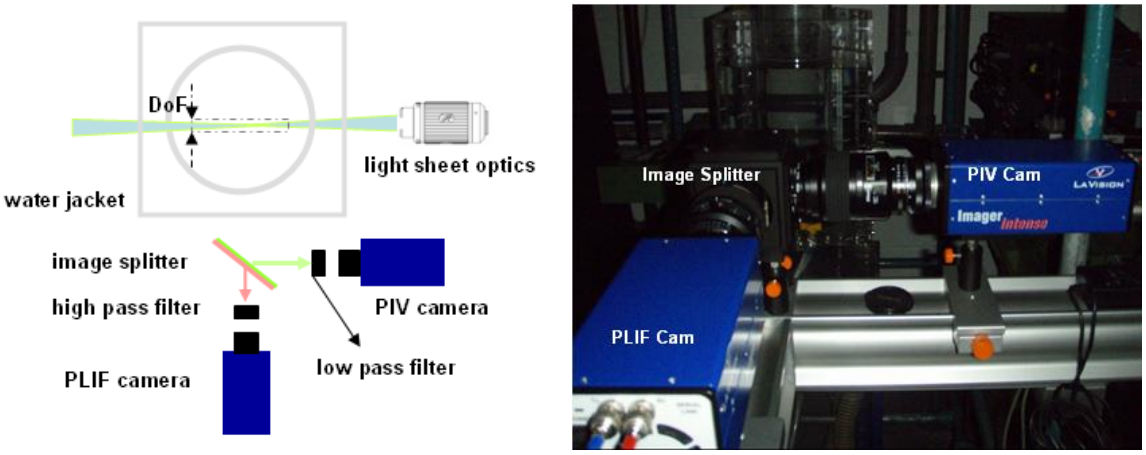

Fig. 3.13 Optical apparatus for a combined 2C-PIV-PLIF: top view (Left) photo (Right)

The PLIF and PIV cameras were positioned perpendicular to each other and their distances from the dichroic mirror were adjusted so that they view the same area. In order to minimise the detection of reflected light, a 560nm high-pass optical filter was mounted on the lens of the PLIF camera. Similarly, a 532nm low-pass optical filter was attached to the lens of the PIV camera to filter out the fluorescence signal and any reflection. In the geometry calibration, because the image of the PIV camera was flipped in the horizontal direction, a consistent right-hand rule was applied in the selection of the three position-defining marks to establish the coordinate system (DaVis, 2009). A third-order polynomial model was then used in Davis (2009) to map the world coordinates (in mm) to the image coordinates (in pixels). The mapping function was carried out separately for each camera, and the grid points of the PIV camera were interpolated onto those of the PLIF camera such that the two overlap. Despite having applied this method, some coordinate mismatch was still found because of small downward and sideway shifts of the rig as water from the 4m-high top tank impacted the test section; hence a further coordinate correction and scalar extraction algorithm were developed, as discussed in Chapter 4.

When spatial resolution can be maximized by decreasing the optical path length, this setup is expected to produce the most accurate velocity measurement because the FoV can be zoomed-in to smaller regions of interest, thus allowing better optimisation of

the interframe time and reducing the probability of sub-filter averaging. However, this optimisation was not possible for the r-θ plane measurements due to the long optical path length (see X_{PLIF} on the right of Fig. 3.14).

3.4.2 SPIV/PLIF setup

The SPIV arrangement offers an effective alternative to cope with the 2C-PIV/PLIF system's poor spatial resolution in the r-θ plan because the SPIV cameras could be brought as close to the measurement plane as permitted by the distance to the prisms. A third camera (for PLIF) was added just beneath the downstream blockage tube such that the focusing lens extended slightly inside the tube, as shown in Fig. 3.14.

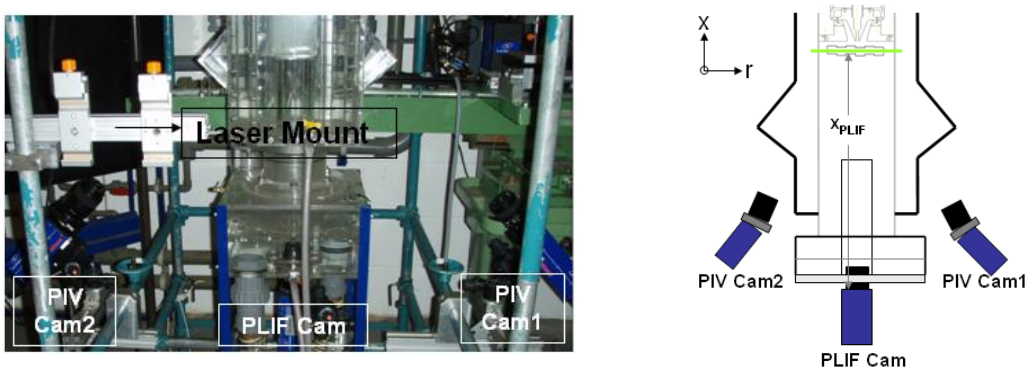

Fig. 3.14 Combined SPIV-PLIF setup on x-r plane: picture (left), side view (right)

The lenses on the SPIV cameras were fitted with Scheimpflug adapters that were tilted with angles of roughly 10º. The optical distance (x_{PLIF}) between the PLIF camera and the light sheet was limited by the height of the rig because it was not possible to insert the PLIF camera into the downstream blockage tube. The coordinates of the PLIF camera and SPIV cameras were calibrated separately but were all in accordance with a right-handed coordinate orientation.

3.4.3 Instrumentation

In total, three different sets of instruments were used. These and the main measurements gathered for each particular instrument configuration are summarised in this section.

2C-PIV/PLIF system (low-speed)

The light source was the low-speed ND:YAG Litron Laser with a maximum repetition rate of 10Hz, an energy of 120mJ at 532mm, and an energy stability of ±2%. Two cameras of the same specifications and model were used for the PIV and PLIF image recording, as listed in Table 3.4.

	ImagerProX 4M × 2
Dynamic range	13-bit (8192 gray levels)
Pixel size	7.4 μm × 7.4 μm
Resolution	2048 × 2048 pixels
CCD size	15.2mm × 15.2mm
Max. Frame Rate	14.7 frames/s
Min. inter-frame time	1μs
Camera RAM	1GB

Table 3.4 2C-PIV/PLIF recording devices

As stated in Table 3.4, there are some 4 million pixels packed within a 15.2mm-squared CCD area. This enabled high spatial resolution measurements even in the larger FoV s.

SPIV/PLIF system (low-speed)

The light source used here was the low-speed ND:YAG NewWave Solo XT120 Laser with a maximum repetition rate of 30Hz, an energy of 120mJ at 532mm, and an energy stability of ±4%. Two cameras of the same specifications and model were used for the SPIV, while for PLIF image recording the Imager ProX 4M was used; these are listed in Table 3.5. This system was used for all 3C-PIV data gathering in all x-r and r-θ planes.

	LaVision Imager Intense × 2 SPIV	**LaVision ImagerProX 4M** PLIF
Dynamic range	12-bit (4096 gray levels)	13-bit (8192 gray levels)
Pixel size	6.45μm × 6.45μm	7.4 μm × 7.4 μm
Resolution	1376 × 1040 pixels	2048 × 2048 pixels
CCD Size	8.875mm × 6.7mm	15.2mm × 15.2mm
Max. Frame Rate	10 frames/s	14.7 frames/s
Interframe Time	1μs to 1000μs	1μs
Camera RAM	None	1GB

Table 3.5 SPIV/PLIF recording devices

2C-PIV/PLIF system (high-speed)

For high-speed measurements, the light source used was a Quantronix Darwin Duo ND:YLF laser with maximum repetition rate of 10KHz, an energy of 15mJ at 532nm, and an energy stability of ±1%. The two cameras used for PIV and PLIF measurements were of the same model, as listed in Table 3.6. This system was used for all measurements that required temporal resolutions.

Highspeed Star6 × 2	
Dynamic range	10-bit (1024 gray levels)
Pixel size	20 μm × 20 μm
Resolution	1024 × 1024 pixels
CCD size	20.5mm × 20.5mm
Max. Frame Rate	5400 frames/s
Min. inter-frame time	1μs
Camera RAM	2GB

Table 3.6 High-speed recording devices

3.4.4 Instrument synchronisation

Both high-speed and low-speed systems share a similar sequence of events; hence only a generic illustration of the synchronisation process is shown in Fig. 3.15. It should be noted that Fig. 3.15 is not drawn to scale and the readout time of the high-speed camera is significantly shorter (on the order of one hundred times) than that of

the low-speed camera. The exposure time of the first frame for both cameras is usually 10μs, after which the image is transferred into a non-light-sensitive memory on the CCD. A user-adjusted delay of camera shutter is often required such that the peaks of the two pulses occur within the exposure time of the first and second frames; this is also related to the software's default setting of device offset, which is the time delay between the Q-switch trigger and the peak of the pulse. These time offsets were set to ensure that the first pulse falls within the camera's first exposure and the second falls in the camera's second exposure.

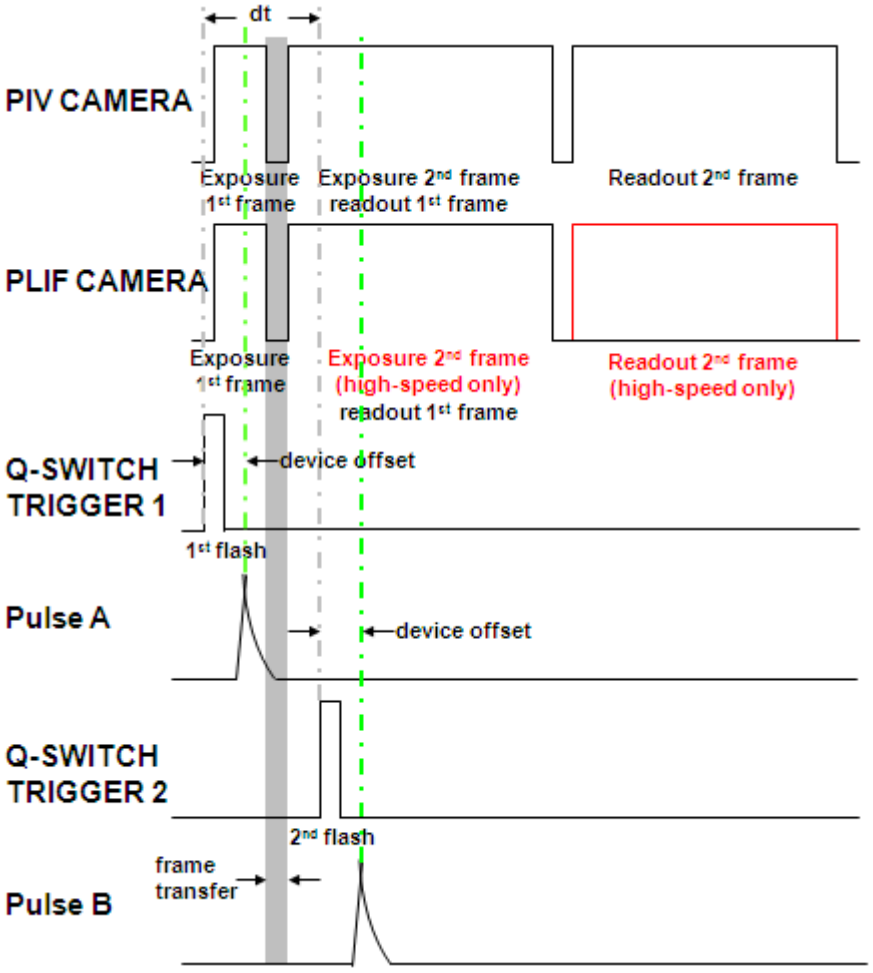

Fig. 3.15 Synchronisation of laser and cameras

Since the PLIF camera's exposure time of 10μs is smaller than the smallest Kolmogorov timescale of 40μs (Midgley, 2005) in the flow field being investigated, it can be assumed that dynamic averaging of the scalar transport is negligible on a single-fame basis. However, this may not always be the case if one takes the inter-frame time into consideration. For example, if the first exposure lasted 10μs and an

inter-frame time of 100μs was used between PIV's double exposures, the total time elapsed would be 110μs, which is almost 3 times the smallest Kolmogorov timescale. Therefore, although researchers often claim to have captured "simultaneous" velocity and scalar data using PIV and PLIF, most fell short of noting the fact that the level of "simultaneity" is actually subject to the time-scale of interest.

3.4.5 SPIV/LIF system communication

The setup of computer control and data acquisition in SPIV/PLIF tests was considerably more complicated because the two PCs had to be linked to enable the synchronisation of a third camera. Hence, the communication between the two systems may be of interest. A schematic showing these connections is shown in Fig. 3.16.

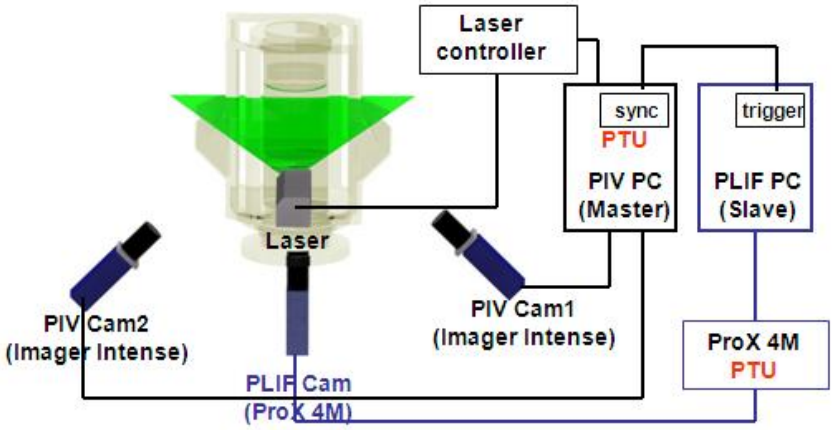

Fig. 3.16 Schematic of Combined SPIV-PLIF Instrument Arrangement

The synchronisation strategy was specified as the following: after the first Q-switch was triggered by the PTU of the Master PC, a signal was sent to the Slave PC, whose mode was set to "external cyclic trigger" with zero time delay. This effectively triggered the PLIF camera's exposure of the first frame immediately after the falling edge of the first Q-switch trigger by the Master PC. Since it was not possible to set a negative delay time after the first Q-switch trigger, the first exposure of the PLIF camera consistently lagged behind that of the PIV camera by 10μs. As a consequence, it was more straight-forward to capture the second light pulse, which meant that the

"instantaneous" scalar field was captured in the second frame rather than the first. The exposure time of the second frame was again set to 10μs.

3.5 Residence time measurement technique

The residence time measurement technique adapted within present experiments involved studying transient concentration response following a sudden reduction of dyed fluid feed. The 2C-PIV/PLIF technique has been employed for this measurement, utilizing the high-speed laser and camera system.

The technique is illustrated in Fig. 3.17. The rig was set running with the required test conditions for a few seconds until a statistically steady condition is reached (t_1), at time t_1 the data recording sequence was started with the pulsed laser and cameras operating at 500Hz (for a recording time of 6.144 seconds – generating 3072 image pairs). Then, at time t_2, the switch connected to the solenoid valve described earlier was flipped to shut off the dye fluid feed to the test section. A switch-triggered laser pointer was turned on which projected a beam onto the light sheet, causing slight brightening in a spot near the edge of the FoV. The appearance of this bright spot marked the time instant (t_2) at which the dye flow was shut off. However, even after the dye was shut off, the dye continued to leak through the fuel injector at a reduced mass flow rate for some time, referred to here as the response time, $t_{response}$, of the dye injection system. After time t_3, the concentration started to decay very rapidly near the fuel injector exit but a significantly longer time was required to achieve near-zero concentration in other parts the FoV. This is demonstrated in the concentration field at time t_4. The concentration field at time t_5 shows a particular region which took longest to mix out with the surrounding zero-concentration fluid. Examples of concentration point histories, detections of t_d, and exponential curve fits can be found in Section 6.3.1.

The concentration drops by around 33% almost immediately after the switch is flipped (t_2), but the final rapid decay does not start until some 3.08s later (t_3). The time lag between the switch-off instant and the instant at which the decay starts ($t_{response}$) is far longer than the estimated 0.07s of residence time within the swirler passage. Although the long response time is not clearly understood, it is independent

of fuel injector configurations, which is to be elaborated in Section 3.5.1. Instead of quantifying the convective time from the dye feed ports to any given point in the FoV, which would require sudden shut-off of the premixing ports, it is possible to estimate the convective time delay from a reference point location in the swirler exit to other point locations. An example of the convective time delay between the reference point location and a point location in the corner recirculation is shown in Figs. 3.18 and 3.19.

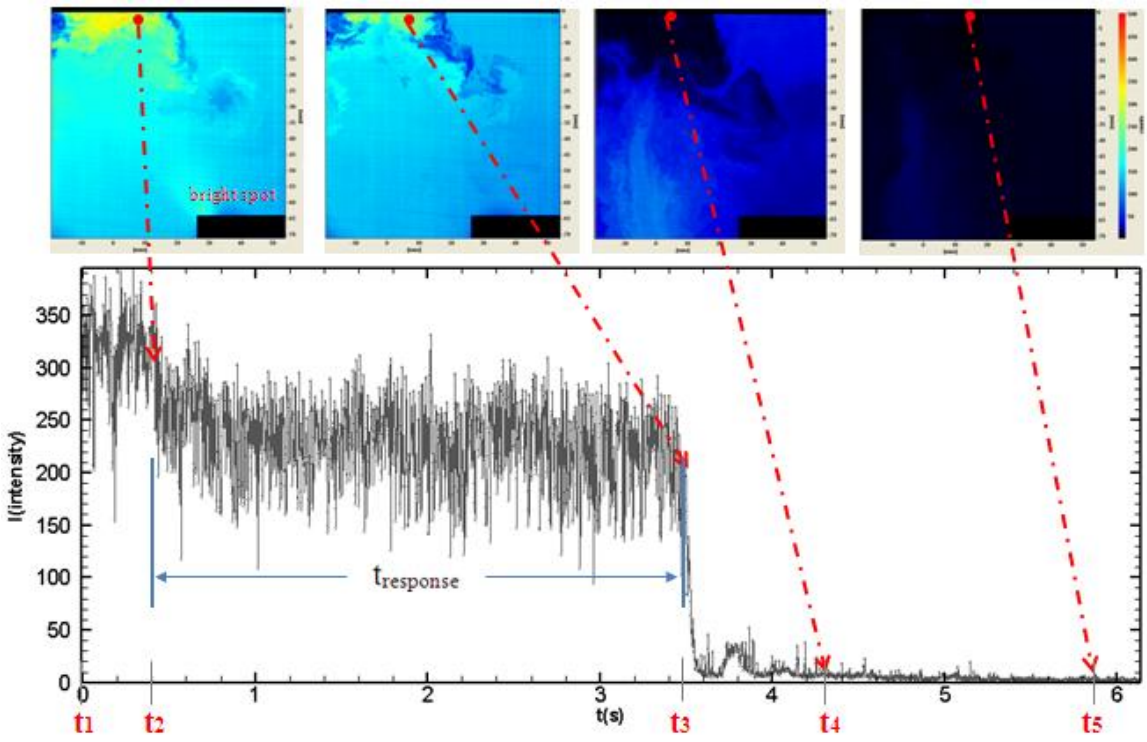

Fig. 3.17 Sequence of concentration images and time history at a point in the swirler exit

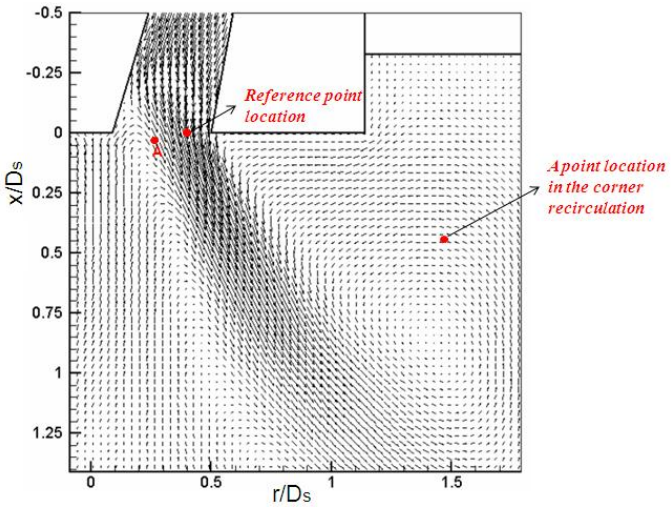

Fig. 3.18 Illustration of the reference point location in the flow field

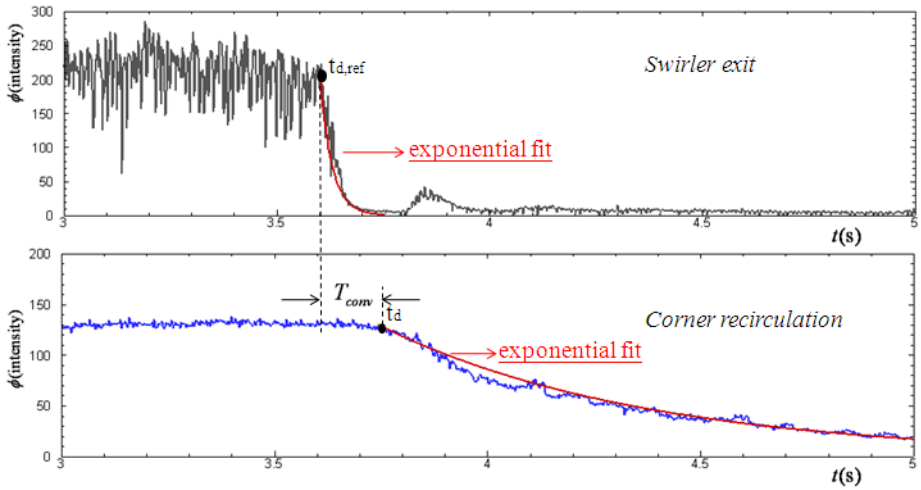

Fig. 3.19 Illustration of convection time: (top) time history at reference point in the swirler passage exit, (bottom) time history at a point located in the corner recirculation

The time instant at which the decay starts at the swirler passage exit, $t_{d,ref}$, is identified using an algorithm developed in Spencer and Cheng (2010, 2012). It first identifies when the concentration last drops–and remains–below one standard deviation of the mean value after $t_{d,ref}$, and then, an exponential fit is applied to the data after this point. The fit coefficients of this exponential curve provide the location in time at which the model curve intercepts the steady time average intensity. The curve originating from this crossing point is then fitted again to the concentration decay signal, producing a second set of curve fit coefficients. This step is iterated until the location of the intercept point of the time mean and exponential curve converges, typically in less than 10 iterations. The difference between $t_{d,ref}$ and the starting decay instant of a point located in the corner recirculation, t_d, for example, is referred to as the convection time, t_{conv}, as indicated in Fig. 3.19. Therefore, the convection time, t_{conv}, is the time delay by which a disturbance observed at the swirl stream exit is transported to any other point of interest in the FoV. In addition to t_{conv}, a second characteristic residence time scale – the half life time ($t_{1/2}$) – is defined as the time it takes for the concentration at any point in the flow to decay to half of its time mean value, see Fig. 3.19. The half life time is determined by fitting an exponential curve to the concentration decay (red fitted line in Fig. 3.19).

It has been found that the exponential fit best describes the concentration decay following the upstream cut-off. Similar observations have been made by Read and Hochgreb (2010), and Arai et. al (1998). A theoretical background for this is provided

here. For a flow with gradual area increase, it may be expected that the arrival time at point B of the impulse of a tracer released at point A would have a near Gaussian distribution, as shown on the right of Fig. 3.20. If the flow deceleration is instead performed suddenly, then recirculations will be formed as in Fig. 3.21. Now the impulse released at A may become entrained in to the recirculations and the transport time to the exit plane of some of the tracer will be considerably increased, particularly at C where the streamlines interact strongly with the recirculation. This will skew the arrival time distribution at the exit plane as shown. If a steady input followed by a step reduction of trace gas is used at A rather than an impulse then the response at the exit plane will be (one minus) the cumulative arrival time distribution derived from the impulse. Thus at B and C the tracer concentration will remain high until the step has been transported to that location. Because of mixing however there will be a characteristic decay curve dependent upon how the history of the flow has affected its transit time. For typical combustor swirling flows, it would be expected that recirculations feature strongly. Here, scalar responses were found to be well approximated by an exponential decay for most of the measurement points. This supported the findings of Ozdemir and Peters (2001) as discussed in the introduction.

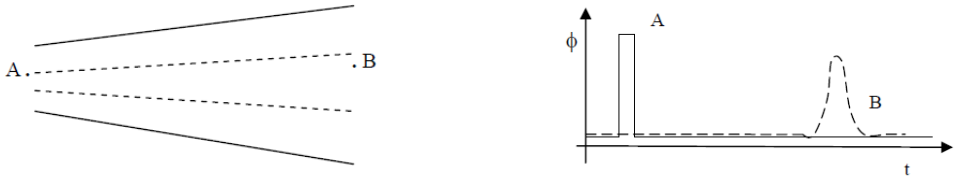

Fig. 3.20 Flow without recirculation; (left) flow with gradual area increase, (right) time history of the impulse and response at points A and B

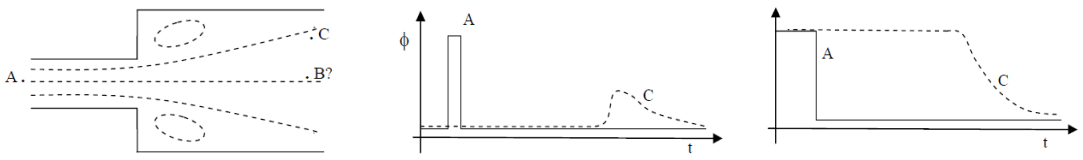

(a) (b) (c)

Fig. 3.21 Two-dimensional flow with recirculation; (a) simple flow geometry, (b) time history of a switch-on impulse at point A and response at point C, (c) time history of a switch-off impulse and its response at point C

3.5.1 Effect of dye injection system response time

Although the exact mechanism causing the long system response time is unknown, it is possible to alter the test case, thereby checking whether the response time is sensitive to variation in the test operating conditions. To achieve this, the dye fluid feed hose pipe is connected to the central jet instead of the premixing cavity and the rig is set running at the main test condition detailed in Chapter 2. The difference between the two flow configurations is illustrated in Fig. 3.22.

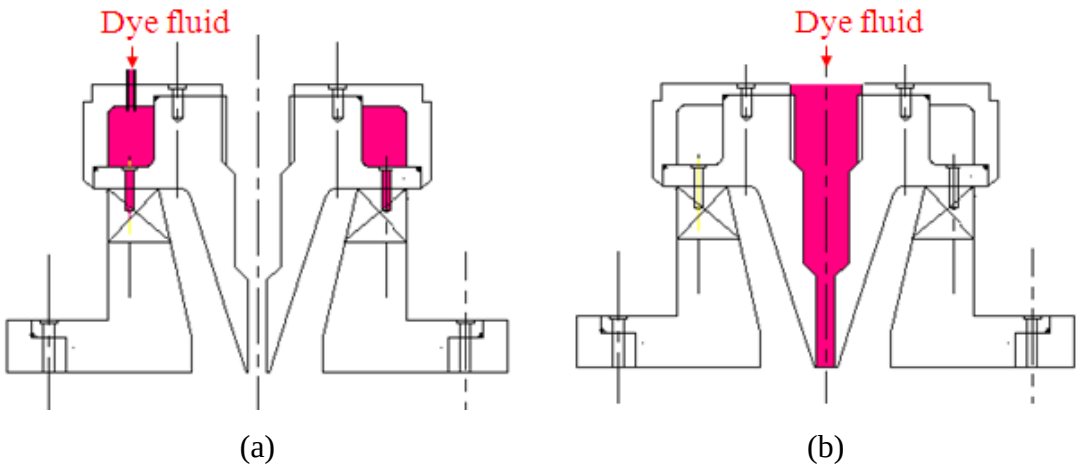

Fig. 3.22 Two configurations at which response time was evaluated: (a) premixed configuration, and (b) non-premixed, directed injected through central jet

As shown in Fig. 3.22(a), after the dye fluid enters into and fills the premixing cavity, it exits into the swirler passage through radial swirl slots and eventually into the dump expansion chamber. The non-premix configuration shown in Fig. 3.22(b), on the other hand, has the dye fluid hose pipe directly connected to the central jet, through which the dye fluid is directly injected into the test section.

Using the same procedure described in the previous section, the rig was set running for a few seconds before the switch-off was made. The time histories of velocity and intensity near the central jet exit measured with the set up shown in Fig. 3.22(b) are plotted in Fig. 3.23. As shown in Fig. 3.23, despite running with a different dyed fluid feed arrangement, the response time of the dye injection system is only about 1% higher than that of the previous case. Based on this finding, it is inferred that the long response time is associated with mechanisms inherent to the dye injection system (valve response and flow paths) and the influence of the downstream feed system

disturbances are negligible. From the velocity time history in Fig. 3.23, it can be seen that the mass flow rate of the fuel feed is also reduced by 33%, which is consistent with the reduction in concentration from time t_2, as shown in Fig. 3.17. This suggests that the reduction of mass flow rate during the response time period is also due to mechanisms inherent to the injection system.

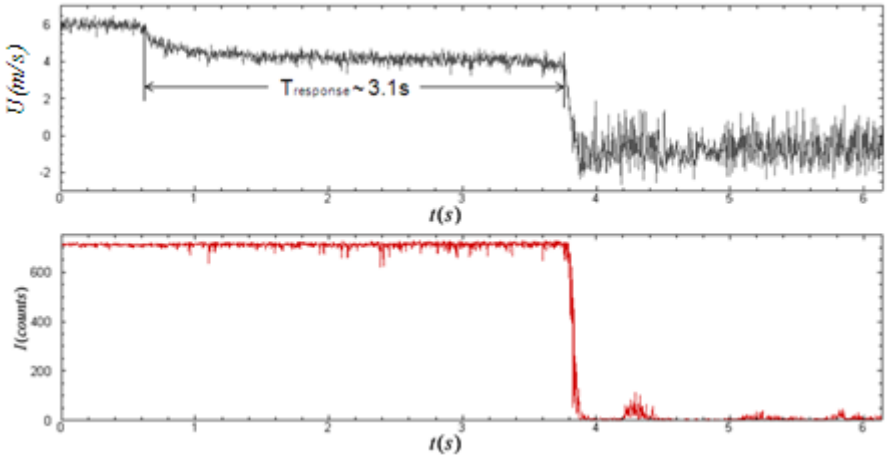

Fig. 3.23 Time histories of axial velocity and intensity in a region within the potential core

3.5.2 Effect of impulse on velocity time history

The residence times measured via scalar tracking are only valid under the condition that the sudden upstream impulse does not alter the downstream velocity field and its strong features which are responsible for scalar transport. Therefore, it is important to inspect the long time history of the velocity in both test cases at various locations.

The axial velocity time histories at a point in the swirler exit and another point further downstream in the swirl stream have been selected for illustration in Fig. 3.24. As shown in Fig. 3.24, the dye-shut impulse does not have an observable effect on the time history as there is no step change in the velocity after t_{shut}. The mean and rms velocities before and after t_{shut} also agree well, to within ±5%.

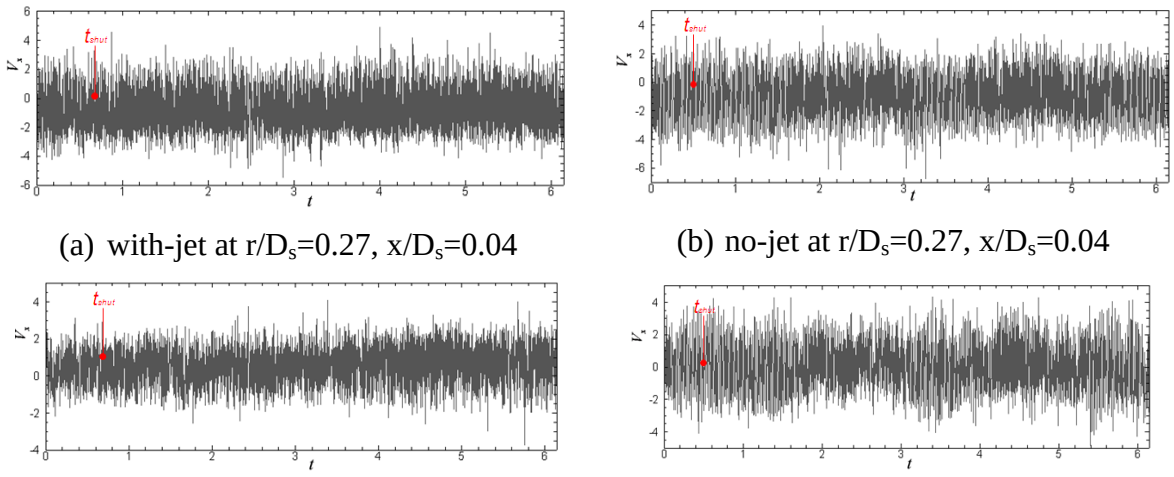

(a) with-jet at $r/D_s=0.27$, $x/D_s=0.04$ (b) no-jet at $r/D_s=0.27$, $x/D_s=0.04$

(c) with-jet at $r/D_s=0.27$, $x/D_s=0.27$ (d) no-jet at $r/D_s=0.27$, $x/D_s=0.27$

Fig. 3.24 Time histories of axial velocity

3.5.3 Effect of impulse on the spectral content

In addition to the time mean, it is important to ensure that the impulse does not have an effect on the spectral content of the coherent structures because these are responsible for much of the scalar entrainment and recirculatory flows. This is checked by computing the power spectral density (PSD) of the fluctuating component of the axial velocity signal at various point locations after t_{shut}. The resultant PSD plot is then directly compared against the same spectral analysis carried out on the time history prior to dye shut-off. The PSD plots of both cases at a point in the inner swirl shear are shown in Fig. 3.25.

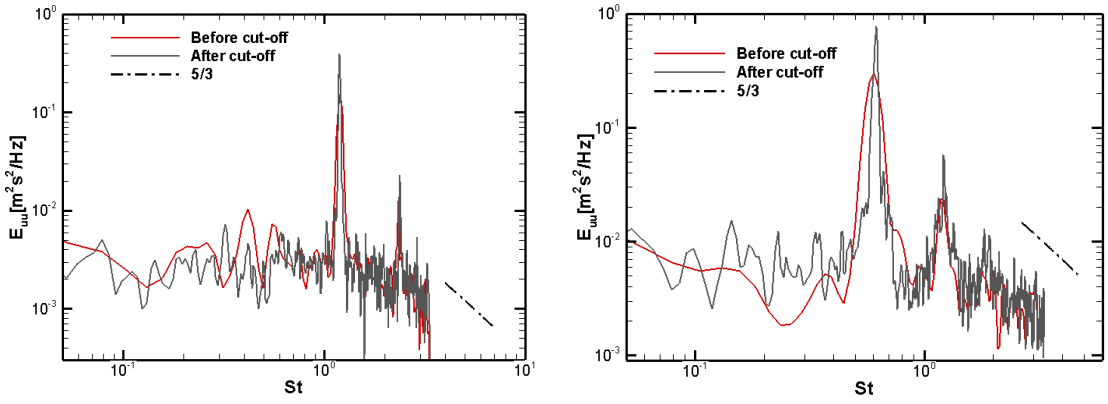

(a) (b)

Fig. 3.25 PSD of fluctuating axial velocity at $r/D_s=0.27$, $x/D_s=0.04$ of (a) with-jet and (b) no-jet test cases

As shown in Fig. 3.25, there is good agreement in the Strouhal numbers of the peak power spectral densities between the before and after shut-off data for both test cases. This validates the assumption that the sudden reduction of the dyed fluid feed does not alter the spectral content of the coherent structures.

3.6 Data structure

The data collected using the low-speed systems was in general more appropriate for validation of CFD predictions of scalar mixing because of its high spatial resolution. Moreover, at low capture rates, the time interval between two successive recordings is larger than the integral timescale. Data collected using the high-speed data, on the other hand, was used for extractions of temporal information, such as residence time and periodicity of vortices. The data structure adopted is best summarised by division into these two categories.

3.6.1 Low-speed data

A large-FoV measurement using the low-speed 2C-PIV/PLIF system was carried out initially to help locate the main regions of scalar mixing. The scalar flux contours show that most of the mixing takes place within $\pm 0.5D_s$ in the radial direction and to $1.2D_s$ in the axial direction. Hence, it was decided that the x-r plane measurement be zoomed-in to the region referred to as *xr1*, bounded within the red box in Fig. 3.26. Two separate sets of measurement at this particular location provide the definitive experimental data in the x-r plane for the validation of CFD predictions. The dataset referred to as *xr2* was taken to check the repeatability and consistency of the measurements. the axial stations of the SPIV data are shown on the right of Fig. 3.26. These SPIV/PLIF r-θ plane measurements, referred to as rθ1, rθ2, rθ3, and rθ4, provide the definitive simultaneous 3-component velocity and scalar data. One SPIV/PLIF measurement was also taken in the xr plane in the same area bounded by xr1, although it is not indicated in Fig. 3.26. Fig. 3.27 and Fig. 3.28 summarise the 2C-PIV/PLIF and SPIV/PLIF datasets, respectively, with the datasets selected for the final CFD validation boxed in red.

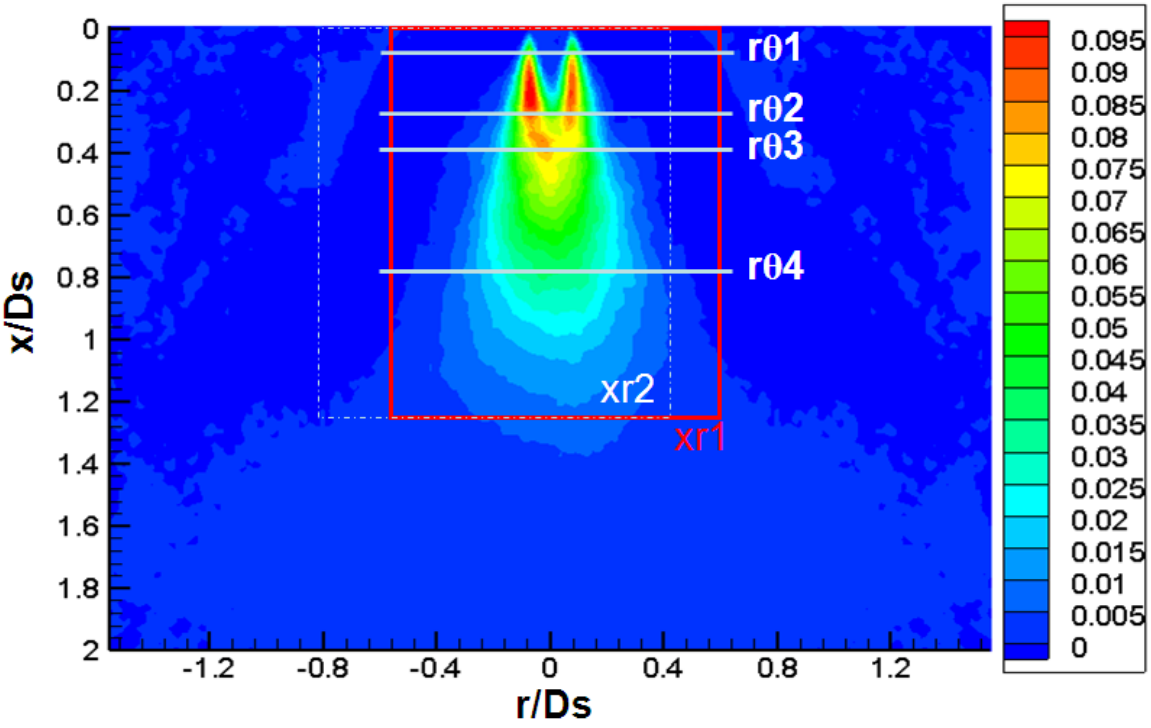

Fig. 3.26 Scalar flux: axial scalar flux with locations of 2C-PIV-PLIF and SPIV in the rθ plane

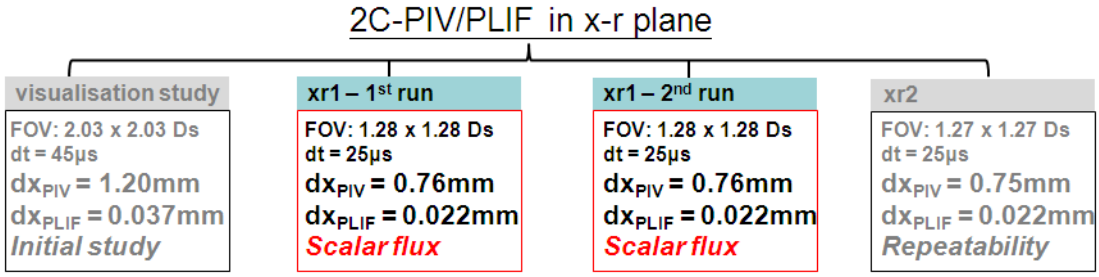

Fig. 3.27 2C-PIV/PLIF data (taken at the USF lab), recorded at 2.2Hz

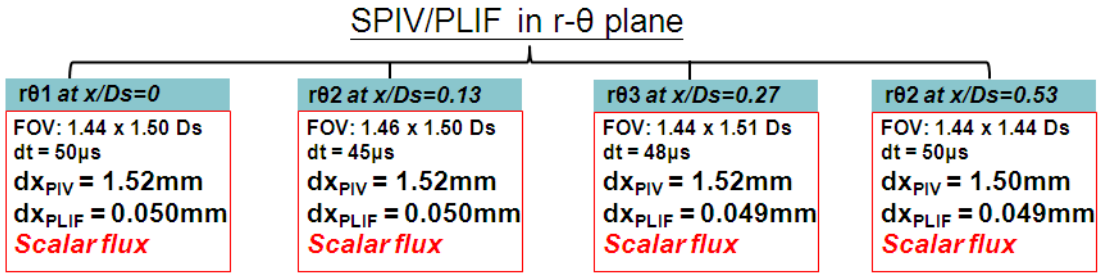

Fig. 3.28 SPIV/PLIF data (taken at the AAE lab) recorded at 1.7Hz

SPIV taken in the xr plane is summarised in Fig. 3.29. This dataset was used for the computations of shear stresses, turbulent kinetic energy, and time-mean pressure fields. Instantaneous snapshots of through-plane flow in the x-r plane are also quite beneficial for visualisation.

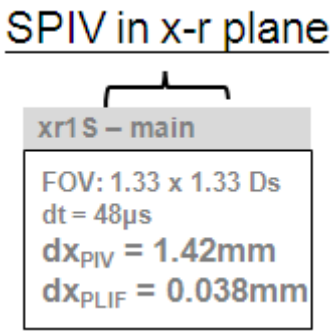

Fig. 3.29 SPIV/PLIF data in the x-r plane, recorded at 1.7Hz

3.6.2 High-speed data

For high-speed measurements, only 2C-PIV-PLIF data has been acquired (no SPIV). The locations of the FoVs are shown in Fig. 3.30.

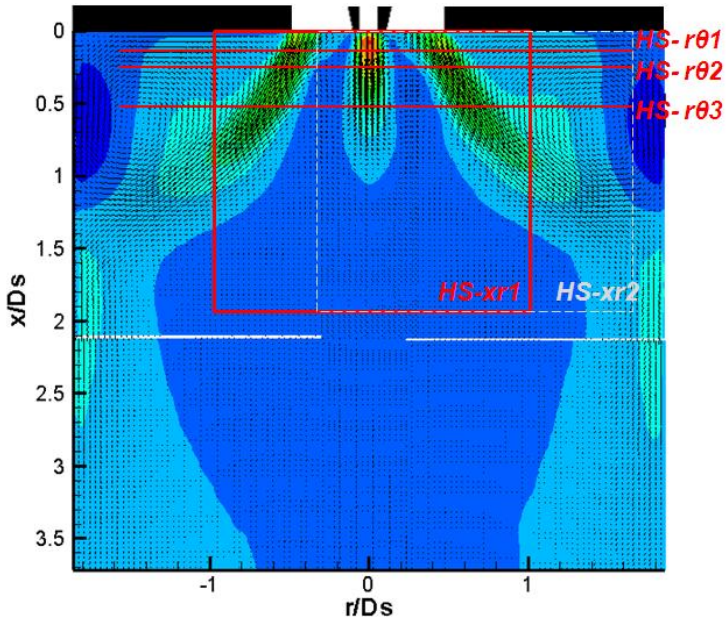

Fig. 3.30 High-speed measurement FOV locations

Other than the main test condition (non-premixed), the fuel injector has also been operated in the premixed configurations for analysis of time-dependent flow features, as well as for residence time measurements, the FoV locations of which are the same as those shown in Fig. 3.30. Details pertaining to the x-r and r-θ plane FOVs are shown in Fig. 3.31 and Fig. 3.32, respectively.

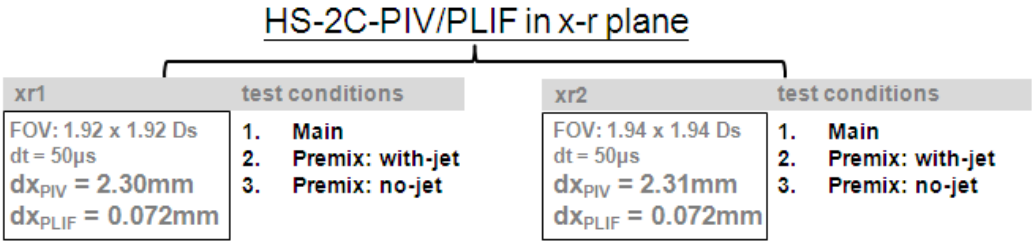

Fig. 3.31 High-speed data in x-r plane (taken at USF lab)

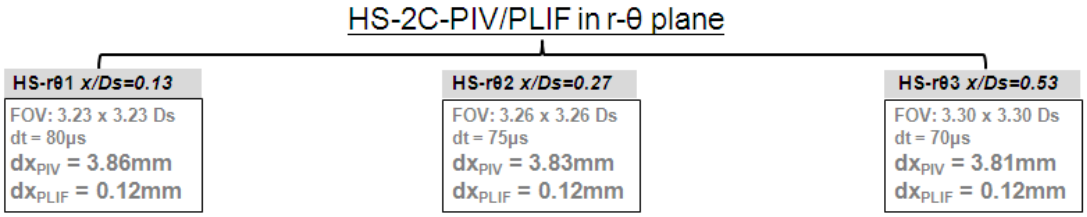

Fig. 3.32 High-speed data in r-θ plane (taken at USF lab)

3.7 Chapter summary

This chapter starts with an introduction to LSI technique, followed by a description of 2C-PIV and SPIV, in which a list of errors was provided with emphasis on the minimisation strategies. Then, a brief review of the PLIF technique is provided, followed by descriptions of the calibration procedure and examples. It was found that the absorption effect during the final tests could be corrected by the sheet correction step alone and no further absorption correction was necessary. Errors in PLIF, including sheet correction uncertainty and pulse-to-pulse energy variation, were individually quantified. The total error was shown to be around ±3.7% considering a confidence level of 95%.

PIV and PLIF were combined in a dual-camera setup to provide simultaneous 2C-velocity and scalar data. The optical setup, along with the use of a dichroic mirror to separate the signal wavelengths, was illustrated. The spatial resolution of the 2C-PIV/PLIF in the r-θ was poor due to the long optical path length (height of the rig and vertical distance to downstream optical access). Hence, SPIV/PLIF was employed to decrease the optical distance, which was enabled by placing the cameras on the sides of the test section instead of beneath it. The specifications of the instruments used in each setup have been summarised, followed by a description of the synchronisation strategy for the light source and cameras. Because the SPIV/PLIF setup required a

more complicated system communication, involving two PC systems, one PTU, and 3 cameras, a schematic showing the system communication has been provided.

The residence time measurement technique developed in this project utilises the high-speed 2C-PIV/PLIF setup. The technique involves quantifying the scalar response following a sudden shut-off of the fuel feed. The response time of the dye injection system has been quantified and it remained constant despite making significant changes to the operating condition. Inspection of the velocity time history showed that the step-change in fuel feed has no effect on it. In addition, FFT analysis on the fluctuating velocity time history also showed no change in the spectral content of the coherent structures after fuel cut-off. Therefore, the residence time measured using the technique is expected to be characteristic of the flow fields in the operating conditions.

Finally, the chapter ends with a detailed depiction of the data structure, which was divided into two categories: low-speed (LS) data and high-speed (HS) data. LS data was mainly used for reductions of scalar flux for validations of CFD predictions due to its high spatial resolution, while HS data was used for extractions of temporal information, such as velocity-scalar co-spectra and residence time.

Chapter 4

4. DATA REDUCTION

This chapter focuses on the data reduction techniques that have been used throughout the thesis to i) describe the flow fields, ii) to estimate and to correct for errors associated with spatial averaging in the 2^{nd} order statistics, with an emphasis on scalar flux, and iii) to identify the unsteady flow features. Section 4.1 describes the data reduction of the single-statistics, introducing methods such as time-averaging, probability density function (pdf), auto-correlation, and its conversion of time-series into frequency-domain representation. Section 4.2 provides a theoretical overview of the scales of turbulent flow, with the emphasis on describing the experimental spatial resolution relative to the smallest length scales of turbulence and scalar fluctuations. Then Section 4.3 goes into details about the error estimation and correction method for both velocity and scalar, and the validation of the method is provided in Section 4.4. Section 4.5 deals with the error associated with a limited sample size, where the main focus is on quantifying its effect on the velocity-scalar covariance statistics. Section 4.6 describes a computation technique to reduce mean static pressure from SPIV data. Finally, Section 4.7 discusses two very effective techniques that have been used to identify coherent structures.

4.1 Single point statistics

This section discusses the processing and data reduction of single-point statistics, which is commonly used throughout the thesis.

4.1.1 Extraction of scalar data

While the computation of velocity was done in interrogation windows, the size of which are 128×128 (an interrogation window width of 32 pixels), the concentration was recorded on single pixels (e.g. 2048 pixels by 2048 pixels for a typical FoV). Other than the different density, there is usually a slight positional shift between PIV and PLIF images due to slight movement of the rig as the falling water impacts the fuel injector. This shift required a scheme to locate a scalar coordinate position to

correspond to the position of each vector interrogation window, as illustrated in Figure 4.1.

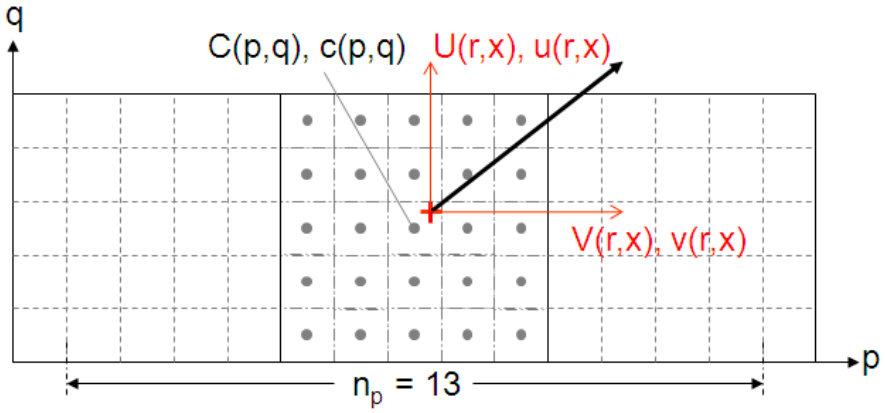

Fig. 4.1 Scalar nearest-point finding relative to position of vector

As pictured in Fig. 4.1, an instantaneous velocity vector in the x-r plane, with components of U and V, is located at world coordinate position of (r,x), which is an interpolated value of the centre position of the vector's interrogation window. The pixel location whose mapped world coordinate that is nearest to (r,x) is (p,q), and the instantaneous concentration value on that pixel is C. The search for the nearest point was done in Matlab using an algorithm that detects the nearest (p,q) to (r,x).

4.1.2 Reynolds decomposition

As shown in Fig. 4.1, the upper case U and V are the instantaneous axial and radial velocities, and next to them are u and v, which are the fluctuating components at a given time instant, t_n. Not shown in Fig. 4.1 is the through-plane velocity, or the tangential velocity, which is denoted as W. In the equations of this chapter, U_i is used to describe any one of the three instantaneous velocities and U_1, U_2, and U_3 can be used interchangeably with U, V, and W, respectively. The fluctuating components are computed using Reynolds decomposition:-

$$u_i(t_n) = U_i(t_n) - < U_i > \tag{4.1}$$

$$c(t_n) = C(t_n) - < C > \tag{4.2}$$

Where u_i and c are the fluctuating components of velocity and concentration respectively, the bracket '< >' denotes a time-average of the discrete number of measured samples, N_s. The time-mean quantities of $<U_i>$ and <C> are calculated as follows:

$$< U_i >= \frac{1}{N_s}\sum_{n=1}^{N_s} U_i(t_n) \tag{4.3}$$

$$< C >= \frac{1}{N_s}\sum_{n=1}^{N_s} C(t_n) \tag{4.4}$$

From the fluctuating components, the velocity and concentration variances ($<u_i^2>$ and $<c^2>$) and their root mean squares (RMS) can be calculated as follows:-

$$< u_i^{\,2} >= \frac{1}{N_s}\sum_{n=1}^{N_s}\left(u_i(t_n)\right)^2 \qquad < u_i >=< u_i^{\,2} >^{1/2} \tag{4.5}$$

$$< c^2 >= \frac{1}{N_s}\sum_{n=1}^{N_s}\left(c(t_n)\right)^2 \qquad < c >=< c^2 >^{1/2} \tag{4.6}$$

Where $<u_i>$ and <c> are the RMS velocity and concentration, respectively. From the fluctuating velocity components, the Reynolds stresses can be calculated as follows:-

$$< u_i u_j >= \frac{1}{N_s}\sum_{n=1}^{N_s} u_i(t_n)u_j(t_n) \tag{4.7}$$

Similarly, scalar fluxes are then calculated as follows:-

$$< u_i c >= \frac{1}{N_s}\sum_{n=1}^{N_s} u_i(t_n)\tilde{c}(t_n) \tag{4.8}$$

where $\tilde{c}$ is the spatially filtered fluctuating scalar. Of the three types of filters experimented (e.g. box, Gaussian, and median), the box filter is found to be effective for the current work, as will be discussed later in this chapter. Computation of $\tilde{c}$ follows:

$$\tilde{c}' = \frac{\sum_{p-\frac{1}{2}N_p}^{p+\frac{1}{2}N_p} \sum_{p-\frac{1}{2}N_p}^{q+\frac{1}{2}N_p} c'(p,q)}{N_p^{\,2}} \tag{4.9}$$

where N_p is the pixel width (see Fig. 4.1) of the filter window, or simply the number of pixels, it must be an odd number because the centre pixel is the point location that is nearest to the velocity location. The choice of N_p is quite important, as will be discussed in the remainder of this chapter.

4.1.3 Probability density function

From the time-averaged quantities that have been introduced in the previous section, it is not possible to tell whether dominant trends or strong intermittency exist. Trends (of moving average, for example) that exhibit notable increases or decreases in time mean that the time series is non-stationary and must be caused by systematic errors. The scalar time histories of the low-speed datasets, for example, have been examined for trends to ensure that it is not contaminated by recirculation fluid (leading to an increasing background concentration over time). Intermittency is defined as the frequent transition between turbulent and non-turbulent flows (Pope, 2003). Therefore, in locations where strong intermittencies are present, the flow may exist in more than one state. Conversion of the time series into a pdf can provide evidence of such flow transitions. The pdf's of velocity or scalar can be calculated by dividing N_s into a series of bins within specific limits, or bin width. The equation described in Libby (1996) has been adopted:-

$$P(\tilde{a}) = \lim_{(\tilde{a}_2 - \tilde{a}_1)\to 0} \frac{1}{(\tilde{a}_2 - \tilde{a}_1)} \left[\lim_{N_{samp}\to\infty} \frac{N_{\tilde{a}}}{N_s} \right] \tag{4.10}$$

where $\tilde{a}$ is a bin that is within the range of $\tilde{a}_1$ and $\tilde{a}_2$, $N_{\tilde{a}}$ is the number of samples that fall within this range, and N_s is the total number of samples. The pdf of any given time history from the experimental data can be obtained by using the 'hist' function in Matlab, which has been used for much of the data reduction. With a finite sample size,

a suitable bin width must be chosen. There are a number of bin width optimisation choices in literature, for example (Scott, 1979). In this work the number of bins was chosen to best represent the shapes of each PDF. Previous discussion of a normal pdf (Fig. 3.12(b)) involved the use a skewness estimate, which was used to indicate the pdf's bias towards one side about the mean. The Skewness (γ_1), which is a third-order statistic, is defined in Eq. 4.11. In Section 4.5.1, Kurtosis (γ_2), which is the fourth moment about the mean and indicates a pdf's peakedness, is used to model distribution of turbulent scalar flux; it is defined in Eq. 4.12.

$$\gamma_1(U_i)=\frac{\frac{1}{N_s}\sum_{n=1}^{N_s}\left(U_i(t_n)-<U_i>\right)^3}{\sigma^3} \tag{4.11}$$

$$\gamma_2(U_i)=\frac{\frac{1}{N_s}\sum_{n=1}^{N_s}\left(U_i(t_n)-<U_i>\right)^4}{\sigma^4} \tag{4.12}$$

4.1.4 Integral timescales and power spectral density

A technique that is widely used to compute multi-time statistics is the autocovariance. When the autovariance of a scalar time series, for example, is normalised, it becomes the autocorrelation function (ACF), which yields the correlation coefficient, $\rho_{cc}(s)$, between times t and t+s:-

$$\rho_{cc}(s)=\frac{<c(t)c(t+s)>}{<c^2>} \tag{4.13}$$

Where s is the time separation, and <c(t)c(t+s)> is the autocovariance, $R_{cc}(s)$. Obviously, ρ_{cc} is used as an example only and the same equation can be applied to u_i, example results of which can be found in Fig. 5.37. The integration of the ACF gives the integral time scale.

$$\tau_{cc}=\int_0^{\infty}\rho_{cc}(s)ds \tag{4.14}$$

Where τ_{cc} is the integral time scale of the scalar time series. Evaluation of the integral with experimental data is done by summing the individual discretised area ($\rho\Delta s$) below the curve from $\rho_{cc}(s=0)=1$ to the first s-axis crossing point of $\rho_{cc}(s)=0$. The integral timescale may be considered as the characteristic timescale of an eddy, but it provides no information on how energy is distributed across the resolvable range of spectra, or frequency bands. To analyze the spectra, or PSD, the correlation function must be converted from time domain to frequency domain; this is done by evaluating the Fourier transform of the $R_{cc}(s)$.

$$E_{cc}(\omega)=\frac{2}{\pi}\int_0^{\infty} R_{cc}(s)\cos(\omega s)\,ds \tag{4.15}$$

Where $E_{cc}(\omega)$ is the energy spectrum across a range of frequencies, ω. Instead of the continuous integral, finite sample size and discretised sampling of experimental data requires the discretised Fourier transform (DFFT) to be evaluated, as defined in Eqs. 4.16 and 4.17.

$$E_{k+1}=\sum_{j=0}^{N_s-1}\omega^{jk}R_{j+1} \tag{4.16}$$

$$\omega=e^{-2\pi i/N_s} \tag{4.17}$$

Where k and j denote indices of E and R that run from 0 to N_s-1, and *i* is the imaginary unit, the subscripts "cc" have been omitted for simplicity. E is complex-valued, but its absolute value at k+1 shows the amount of frequency $f=P(f_s/N_s)$ at each frequency interval f(k) in the data (Matlab 2010). A number of PSD estimation methods had been applied to the study of turbulent flow (e.g. Raja and Mumukutla (1992)); the current study adopted the Welch periodogram method (Welch, 1967), coded using a built-in Matlab function (Matlab, 2010).

4.2 Scales of turbulent fluid flow

One of the fundamental challenges in experimental fluid mechanics is the selection of the most practical probe resolution relative to the length scales of the flow features of interest. Because it is not always possible to resolve the smallest length scale, it is important to estimate how much of the turbulent energy can be captured with the measurement resolution. Classical turbulence theory provides a good guideline in this respect. It is in this spirit that an overview of the scales of turbulence is provided here.

In an isothermal non-reacting flow (as in this project), in which heat transfer and chemical reaction are non-existent, the fluid has only one contribution to its energy – the total kinetic energy – a sum of the energy in random molecular motion and the kinetic energy of the moving fluid. As the total kinetic energy enters the large motions of the flow, i.e. the confined swirling flow in the dump expansion chamber, turbulence kinetic energy is produced in motions whose sizes may be characterised by the length scale L_c (the subscript 'c' here denotes energy 'containing' range). These eddies may be coherent and localised within characteristic sizes, ℓ. They may contain any number of small eddies, onto which the incoming kinetic energy is cascaded until it is finally dissipated by viscosity of the smallest eddies at the Kolmogorov length scale, η:

$$\eta = \left(\frac{\upsilon^3}{\varepsilon_D} \right)^{1/4} \tag{4.18}$$

Where ε_D is the dissipation rate. The concept of energy cascade, first introduced by Richardson (1922), was supported by the famous Kolmogorov's hypotheses that small-scale turbulence at very high Reynolds number is statistically isotropic within the universal equilibrium range and is uniquely determined by the energy dissipation rate and the kinematic viscosity, υ. Therefore, at the smallest, dissipative eddies, the sizes of which are characterised by the Kolmogorov's length scale, energy is dissipated by the viscous force. The different ranges of scales of turbulent flow and the length scales associated with them are shown in Figure 4.2 (Pope, 2003).

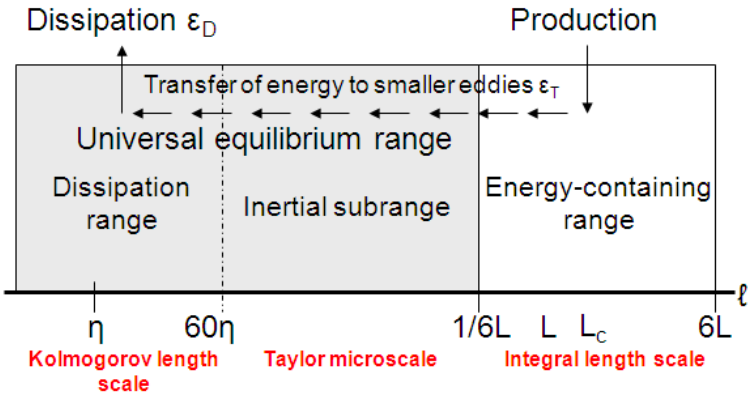

Fig. 4.2 Schematic diagram of the energy cascade at very high Reynolds number

The demarcations among the different characteristic lengths were proposed by Pope (2003). Turbulent kinetic energy (TKE) that is produced at L_c is progressive cascaded down and is therefore distributed across a wavenumber spectrum, κ, of eddy sizes (i.e. $\kappa=2\pi/\ell$). For homogeneous turbulence, the energy contained within a range of length scales, or wavenumber, can be calculated by integrating over the wavenumber spectrum:-

$$k(\kappa_a,\kappa_b)=\int_{\kappa_a}^{\kappa_b}E(\kappa)d\kappa \tag{4.19}$$

Where k is the turbulent kinetic energy contained within the wavenumber range of κ_a and κ_b. Theoretical derivations and empirical data have shown that around 80% of the energy is contained within the production range ($L/6 < \ell < 6L$). But in order to obtain all of the net energy received by the smallest dissipative eddies, the measurement must be sampled at a wavenumber that is equivalent to or higher than $2\pi/\eta$, or a spatial resolution of $\Delta x<\eta$. Until recently, only micro-PIV has been proven to achieve such fine spatial resolution in measurements of high Reynolds number flows (Rafael et al, 2007). In most conventional planar PIV studies, interrogation cell sizes are considerably larger than the Kolmogorov length scale.

4.2.1 Computation of Kolmogorov length scale

The evaluation of Kolmogorov length scale using Eq. 4.18 remains difficult because the evaluation of dissipation rate from PIV data relies on a spatial derivative method - thus making the calculated values highly sensitive to the spatial resolution. Indeed,

Tanaka and Eaton (2007) demonstrated that in order to obtain the correct dissipation rate, the PIV interrogation cell size has to be smaller than one fifth of the Kolmogorov length scale ($\Delta x<0.5\eta$). Due to such stringent requirement on spatial resolution, researchers in recent years have come up with several ways by which the dissipation rate can be estimated from non-Kolmogorov resolution PIV data. Two of these methods are summarised in Table 4.1. The Sharp and Adrian (2001) method was devised for 2C-PIV data with the assumption of isotropy and meaningful results could be obtained only if the measurement grid size is on the order of the Kolmogorov length scale. Sheng et al. (2000) used the Smagorinsky SGS model to account for dissipation rate associated with the SGS stresses, for which dynamic equilibrium is assumed. Gabriele et al (2009) applied both methods in the study of a motor-stirred tank and found that they overestimate the known energy input by a factor of 5 and 2, respectively. Robinson (2009) also questioned the method by showing that its derived final stress term was incorrect. Thus far, there has yet been a fully validated PIV-based method that provides accurate dissipation rate measurement (Jong et al, 2009).

Approximation of ε_D		
Methods	**Notation**	**Recent applications**
Sharp and Adrian (2001) $\varepsilon_D = 2\nu\langle s_{ij}s_{ij}\rangle = \frac{\upsilon}{2}\left\langle\left(\frac{\partial u_i}{\partial x_j}+\frac{\partial u_j}{\partial x_i}\right)^2\right\rangle$	S_{ij} – strain rate x_i – grid in i direction	Sharp and Adrian (2001) computed ε_D in a stirred tank using 2C-PIV data with isotropy assumption. Huchet et al. (2009) used the same method in evaluation of local ε_D in a Rushton turbine.
Sheng et al. (2000) $\varepsilon_D = \langle\varepsilon_{SGS}\rangle = 2\nu\langle\tau_{ij}s_{ij}\rangle$ Smagorinsky SGS model $\tau_{ij} = -C_s^2\Delta^2\lvert S\rvert\langle S_{ij}\rangle$	ε_{SGS} – SGS dissipation rate τ_{ij} – SGS stress tensor C_s – Smagorinsky constant equal to 0.17 Δ – resolved grid length	Sheng et al (2000) used the method they developed to estimate ε_D in an impeller-stirred vessel and found good agreement with that calculated from dimensional scaling. Robinson (2009) used this method to compute ε_D from single-plane SPIV data; it was fed into Eq. 4.18 to calculate η. Gabriele et al (2009) also used the method to compute ε_D in a stirred tank from 2C-PIV data.

Table 4.1 Methods of Calculating Dissipation Rate from PIV Data

Therefore, instead of calculating ε_D, the older method that relies on dimensional scaling may be more appropriate. Examples of this type of method are summarised in Table 4.2.

Estimation of η or ε_D by dimensional scaling		
Methods	**Notation**	**Recent applications**
Antonia et al (1993) $\varepsilon_D \approx 1.3(U_0^3/h)(y/h)^{-5/2}$ $\eta \approx 2.7\delta Re_\delta^{-3/4}$	U_0 – jet exit velocity h – jet nozzle width y – streamwise direction δ – jet full width	Su and Clemens (2003) calculated η using this method to estimate the Batchelor scale in a combined Rayleigh scattering and PLIF study of scalar mixing in gas-phase planar turbulent jets.
Tennekes and Lumley (1972) $Re_{Lx} = uL_X/\nu$ $\eta \approx L_X Re^{-3/4}$	u – axial fluctuating velocity L_X – axial integral length scale	Pfadler et al (2009) calculated η using this method to show that the "largest part" of the turbulent kinetic energy spectrum could be resolved in a dual-plane stereo-PIV study of turbulent premixed flames.
Piirto et al (2001) $\varepsilon_D = A(u^3/L)$ $Re_{Lc} = k^2/(\varepsilon_D/\nu)$ $\eta \approx L_i Re^{-3/4}$	A – unity in isotropic flows L – characteristic length in the flow (e.g. jet diameter) $u' - (2/3k)^{1/2}$ k – turbulent kinetic energy	Hollis (2004) calculated η using this method in the 2C-PIV studies of a combustor port flow. Midgley (2005) applied the same method to the same fuel injector flow field that is under investigation in this project.

Table 4.2 Summary of Type 1 Methods of Kolmogorov Length Scale Estimation

The method invokes the ratio between the large scale and small scale eddies:-

$$\eta / \ell = \mathrm{Re}_L^{-3/4} \tag{4.20}$$

Where ℓ is the length scale of the large eddies and Re_L is the Reynolds number associated with them. All three methods listed in Table 4.2 are very similar with the Piirto (2001) method involved iterations, examples of which can be found in Hollis (2004). In the current study, the Tennekes and Lumley (1976) method has been adopted, as shown in Fig. 4.3. L_x in the notation column denotes the axial integral

length scale, which is evaluated along the axial direction and is equivalent to ${}^{1}L_{11}$ (to be explained in Section 4.2.3).

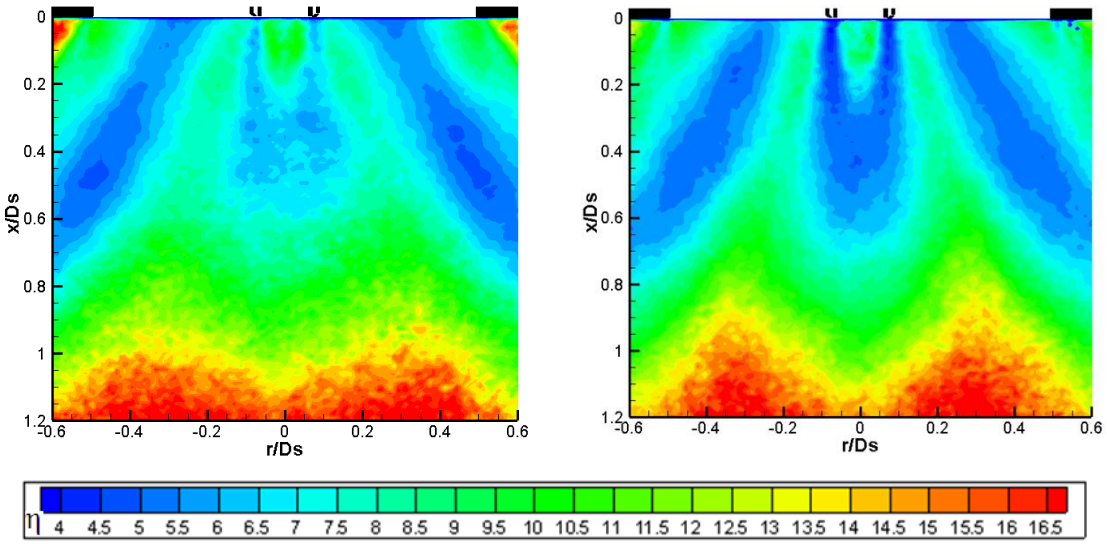

Fig. 4.3 Kolmogorov length scales (μm): radial (left), axial (right)

The smallest Kolmogorov length scales are found near the outer radii of the central jet and at the immediate exit, where they can be as low as 4μm, or about 180 times smaller than the interrogation cell size. Even the largest Kolmogorov length scale in the presented FoV is roughly 40 times smaller than the interrogation cell size. Therefore, the PIV measurements reported in this study are unable to capture turbulent energy in the dissipation range.

4.2.2 Discussion of Batchelor length scale

Similar to the concept of energy dissipation rate – and equally important in studies of turbulent mixing in combustors – is scalar dissipation rate, which is a measure of the time rate at which the smallest scalar fluctuation is destroyed at the finest length scale, or the Batchelor scale (Batchelor, 1959). Estimation of scalar dissipation rate is important in combustion research because it serves as a characteristic diffusion timescale: a diffusion time scale that is smaller than the chemical time scale of the flame structure could lead to local extinction and result in poor flame anchoring (Sutton and Driscoll, 2007). Because the goal of the present work is to capture the large-scale energy containing fluctuations under isothermal, non-reacting conditions, the characterisation of dissipation rate is not relevant. Nevertheless, the Batchelor

length scale is introduced here of purpose of describing PLIF's spatial resolution relative to the smallest lengthscale of scalar mixing. The Batchelor length scale, λ_B, is related to the Kolmogorov length scale by:-

$$\lambda_B = \eta Sc^{-1/2} \tag{4.21}$$

The high Schmidt number (Sc_{RhB} = 2740, see Section 3.3) of Rhodamine B in water means that the spatial resolution required to measure the scalar dissipation rate is nearly 1/50 of the Kolmogorov scale. Therefore, the smallest η of 4μm (Fig. 4.3) would result in a λ_B of 0.077μm (recall that the finest PLIF spatial resolution per Section 3.6.1 was Δx_{PLIF}=0.022mm). Achieving Batchelor resolution for the current project would require a further ~10^5 magnification, which is not possible with the optical arrangement used in the conventional PLIF configurations (Crimaldi, 2008). Mi and Nathan (2003) and Bilger (2004) note that the difficulty is further exacerbated if one considers light sheet thickness, which may result in spatial filtering in the through-plane direction, given the complexity of setting a depth of field that is similar to or thinner than the Batchelor lengthscale. Therefore, based on this discussion alone, it is clear that the current PLIF measurement was not able to resolve the smallest scalar dissipation lengthscale.

4.2.3 Computation of integral length scale

The previous discussion explained the limits of the measurement technique in terms of its non-Kolmogorov resolution for velocity and non-Batchelor resolution for scalar. This part describes the data reduction of the integral length scales, which are in the energy containing range, as shown in Fig. 4.2. The calculated integral length scales will be used for error estimates throughout this work. Integral lengthscales can be directly calculated from spatial velocity correlation (SVC), or cross-correlation functions, which yield normalised two-point covariance at the same point in time:-

$$\mathrm{SVC} = R_{ij} = \frac{< u_i(\mathbf{x},t) u_j(\mathbf{x}+\mathbf{r},t) >}{\sqrt{< u_i(\mathbf{x},t)^2 >}\sqrt{< u_j(\mathbf{x}+\mathbf{r},t)^2 >}} \tag{4.22}$$

Where $u_i(\vec{x},t)$ is the i-component fluctuating velocity at fixed point, and $u_j(\vec{x}+\vec{r},t)$ is the j-component velocity located at a point separated by r. In this project, SVC is evaluated along the axial or radial directions (lines) and only for the same velocity component (i=j), which can also be referred to as autocorrelation in space. The notation of the integral length scale and its mathematical definition are as follows:-

$$^{k}L_{ii} = \int_{0}^{\infty} R_{ii}(\mathbf{x},\mathbf{r})d\mathbf{r} \tag{4.23}$$

Where i may be any of the three velocity components (k=1-3) or the scalar (k=4), while k is restricted to either of the two in-plane components (k=1,2). Thus, from an xr-plane dataset, integral length scales of $^{1}L_{11}$, $^{1}L_{22}$, $^{2}L_{11}$, $^{2}L_{22}$, $^{1}L_{44}$, and $^{2}L_{44}$, can be calculated. The computation of integral length scales from PIV data followed the same procedure as that described in Hollis (2004), using an in-house Matlab code developed by Robinson (2009).

The scalar integral length scales were calculated from PLIF data using a slightly different algorithm. Since SSC calculation on the entire raw scalar field (2048×2048 pixels) was computationally expensive (on the order of 10^{14} operations), it was decided to perform the computation only at the PIV grid points. Hence, the nearest-point finding algorithm described in Section 4.1 was employed, followed by extraction of the axial and radial line data. This procedure effectively enables the computation of the scalar integral length scale in the PIV coordinate presentation but with the original PLIF spatial resolution. Similar to Eq. 4.22, the SSC is defined as:-

$$\mathrm{SSC} = R_{ij} = \frac{< c(\mathbf{x},t)c(\mathbf{x}+\mathbf{r},t) >}{\sqrt{< c(\mathbf{x},t)^2 >}\sqrt{< c(\mathbf{x}+\mathbf{r},t)^2 >}} \tag{4.24}$$

Scalar integral length scales, namely $^{4}L_{11}$, and $^{4}L_{22}$, were obtained by integration of the SSC function, the missing part of which due to curtailment at the domain edge was filled by extrapolating the least-square exponential fit of the existing part of the curve. An example of this is shown in Figure 4.4.

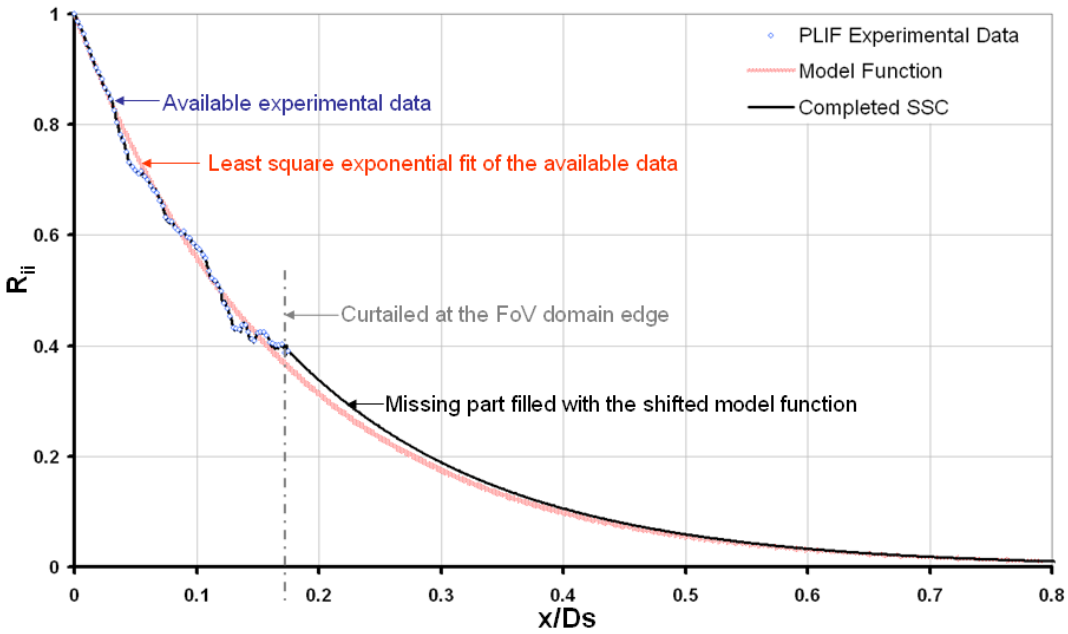

Fig. 4.4 Treatment of the Missing SSC Curve Due to Curtailment

Wygnanski and Fiedler (1969) showed that $R_{ii}=e^{-x}$ could be used as a reasonable generic model for a given SVC function. Hollis (2004) used the model for treatment of the missing curve by shifting the model horizontally to match the point of curtailment (Hollis 2004). The curtailed SSC curve treatment routine shown in Figure 4.4, on the other hand, does not use the simple exponential function to complete the SSC curve in cases of curtailment, neither is it based entirely on a fitted model, such as that reported by Bridges and Wernet (2002). Instead, the model was constructed by fitting a simple exponential equation in the form of $R_{44}=e^{-bx}$ to the available part of the SSC curve. Based on the least-square fitted *b*, the exponential coefficient, a model was constructed and shifted horizontally to "fill" the missing part of SSC curve till $R_{44}\leq 0.001$. Therefore, the completed SSC curve is the sum of the available portion and the shifted exponential least-square-fit model. This way the SSC curve is constructed with reference to the available data points rather than being based solely on a generic model. In order to account for asymmetry of the SSC curve due to curtailment in either streamwise or spanwise directions, a confidence weighting method developed by Hollis (2004) was adopted (the method is described in Appendix 4.1). The errors associated with the computation of integral length scales are discussed in the next section.

4.3 Spatial filtering error

As discussed in Section 4.1, as long as the PIV interrogation cell size is not equal to or smaller than the Kolmogorov scale, sub-grid scale velocity gradients may be present in a turbulent flow. As discussed in Table 2.3, this leads to broadening of the correlation peak, which in turn results in a low-pass filtered version of the true displacement and its higher-order statistics. This contamination of the velocity statistics due to spatial averaging is similar to implicit filtering in LES:-

$$\tilde{U}(\mathbf{x},t) = \int_D G(\mathbf{r},\mathbf{x})U(\mathbf{x}-\mathbf{r},t)dr \tag{4.25}$$

Where $\tilde{U}(\mathbf{x},t)$ is the velocity vector field convolved with the filter kernel $G(\mathbf{r},\mathbf{x})$, most popular types of which include: top-hat or box, Gaussian, and sharp cut-off filters. Hoest and Madsen (1995), abbreviated as HMN from here on, and Spencer and Hollis (2005) show that for PIV data, the box filter most aptly represents the effect of spatial averaging. The authors then validated the HMN integral curve with synthetic and experimental data, as shown in Fig. 4.5(a).

Instead of using the HMN curve, a best-fit polynomial was generated to characterise the portion of the curve at $\Delta x/L_{true} < 1$ (Eq. 4.26) and a logarithmic function to the portion at $\Delta x/L_{true} > 1$ (Eq. 4.27).

$$u_{i,meas}/u_{i,true}(\Delta x/{}^{i}L_{ii}) = 0.2381(\Delta x/{}^{i}L_{ii})^3 - 0.395(\Delta x/{}^{i}L_{ii})^2 - 0.1155(\Delta x/{}^{i}L_{ii}) + 1 \tag{4.26}$$

$$u_{i,meas}/u_{i,true}(\Delta x/{}^{i}L_{ii}) = -0.2181\,Ln(\Delta x/{}^{i}L_{ii}) + 0.7501 \tag{4.27}$$

Where $u_{i,meas}$ and $u_{i,true}$ are the measured and the true velocities. From Eq. 4.26 and 4.27, theoretical error estimates can be obtained:

$$Err(\Delta x/{}^{i}L_{ii}) = 1 - u_{i,meas}/u_{i,true}(\Delta x/{}^{i}L_{ii}) \tag{4.28}$$

Where $Err(\Delta x/{}^{i}L_{ii})$ provides a percentage error estimation for the given grid size, Δx, relative to the true integral length scale, ${}^{i}L_{ii}$ at a given point in the flow. Computing

the true value of ${}^{i}L_{ii}$, or simply L_{true} for easier referencing, would require measurement grid size to be considerably smaller than L_{true} in the first place, as shown in Fig. 4.5(b). If such requirement on spatial resolution cannot be met or is not known a priori, Hollis (2004) and Spencer and Hollis (2005) developed an iterative algorithm that involves the use of Eq. 4.29, which is an empirical best-fit of the data points in Fig. 4.5(b).

$$L_{meas} / L_{true}(\Delta x/L_{true}) = e^{-0.4001(\Delta x/L_{true})} \tag{4.29}$$

Where L_{meas} and L_{true} are the measured and the true integral lengthscales, respectively. The correction algorithm has been used for all integral length scale computations in this work.

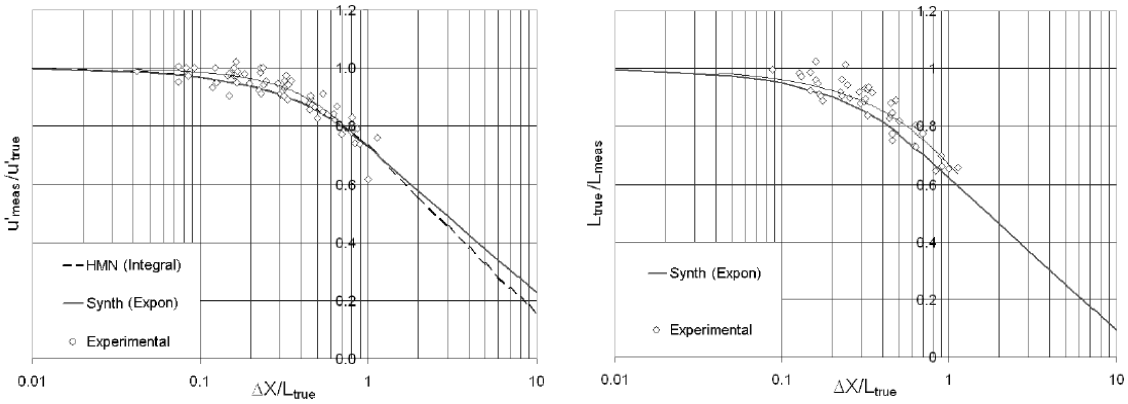

(a) (b)

Fig. 4.5 Subgrid filtering effect on (a) rms velocity and (b) integral lengthscale

4.3.1 Velocity

Using the method described in the previous section, spatial averaging errors of fluctuating velocity can be estimated. The errors in percentage values shown in Fig. 4.6 are calculated with respect to the integral length scale in the radial and axial directions, i.e. $\Delta x_{PIV}/{}^{2}L_{22}$ and $\Delta x_{PIV}/{}^{1}L_{11}$, respectively.

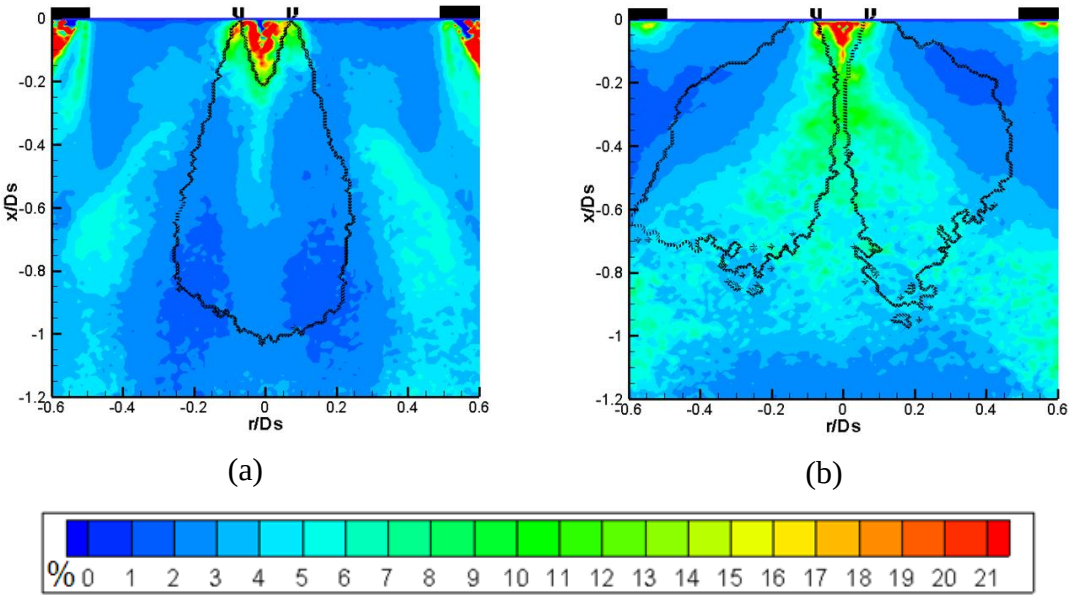

Fig. 4.6 Error due to spatial filtering: (a) Err($\Delta x_{PIV}/^{1}L_{11}$) and (b) Err($\Delta x_{PIV}/^{2}L_{22}$)

The lines shown in Fig. 4.6 are drawn to mark the boundaries in which the scalar flux is larger than a threshold value (e.g. $uc>0.05uc_{max}$). This is done to highlight the scalar mixing regions that are particular prone to errors due to spatial filtering and will be referred to in Chapter 5, further details can be found in Cheng et al (2012). In both Err($\Delta x_{PIV}/^{1}L_{11}$) and Err($\Delta x_{PIV}/^{2}L_{22}$), spatial filtering errors up to ~20% are found in the jet's potential core and these can slightly spill over into the bounded regions at the immediate exit ($x/D_s<0.1$). Err($\Delta x_{PIV}/^{2}L_{22}$) of around 12% are found along the jet spread while Err($\Delta x_{PIV}/^{1}L_{11}$) of similar magnitudes are seen surrounding the jet's potential core.

4.3.2 Scalar

Eqs. 4.26 and 4.27 have also been employed to estimate errors in <c> because spatial averaging of <c> follows the same exponential decay trend shown in Fig. 4.5(a); the validation of this will be discussed in Section 4.4. The ratio of the pixel image width and the calculated scalar integral lengthscale can be used to estimate spatial filtering errors in two directions: Err($\Delta x_{PLIF}/^{1}L_{44}$) and Err($\Delta x_{PLIF}/^{2}L_{44}$). As shown in Fig. 4.7, the overall error magnitudes are much lower than Err($\Delta x_{PIV}/^{1}L_{44}$) and Err($\Delta x_{PIV}/^{2}L_{44}$). The highest errors – Err($\Delta x_{PLIF}/^{2}L_{44}$)~5% – are found along the centreline of the jet penetration because spanwise SSC in that region is very low, resulting in a higher

$\Delta x_{PLIF}/^2L_{44}$. Errors of ~1.3% are found in the jet shear; with tiny red spots of $Err(\Delta x_{PLIF}/^2L_{44})$~2% spiller over to into the jet shear just beneath the jet lips.

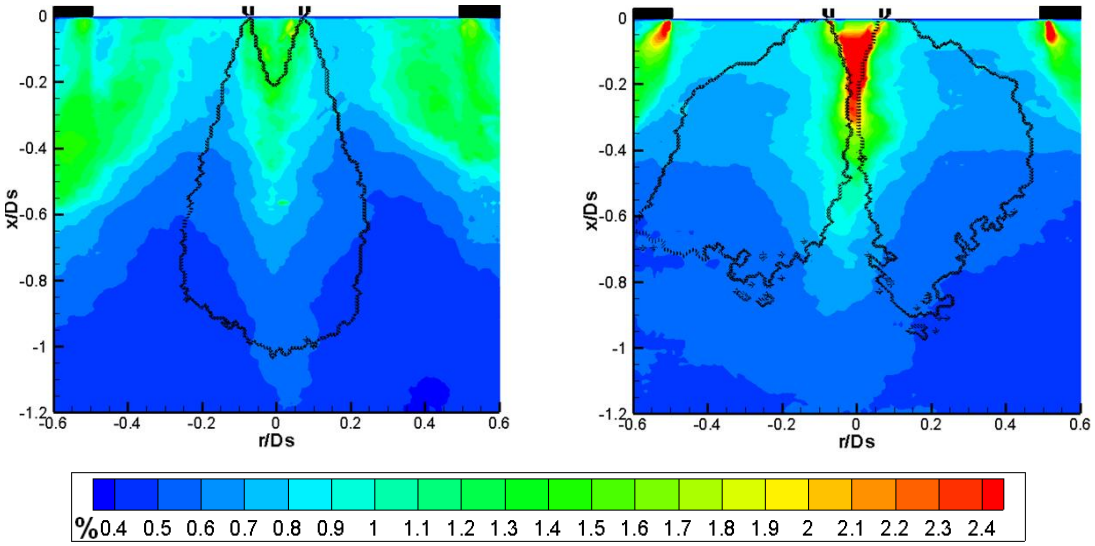

Fig. 4.7 Error (%) Due to Spatial filtering: radial direction (left); axial direction (right)

4.3.3 Effect of spatial averaging on scalar flux

The effect of spatial filtering on the scalar variance has been demonstrated by Barlow and Karpetis (2004), in which the authors showed that the scalar variance tends to decrease linearly with increasing filter widths. Loffler et al (2008) also showed that different scalar filter widths resulted in different scalar fluxes. Here an analysis is presented that examines how the scalar flux varies with different scalar filter sizes, the scalar flux has been calculated with successive spatial filter widths (n_p=1, n_p =3…n_p =61, recall that n_p denotes 'number of pixels', as shown in Fig. 4.1). Profiles were extracted at several axial stations, six of which, zoomed in on their peak values, are selected for demonstration here. As shown in Fig. 4.8, the sensitivity of scalar flux to varying scalar filter widths is dependent on locations, with the largest difference of 32% (between n_p =1 and n_p =61) found at x/D_s=0.02 and gradually decreasing towards 4% at x/D_s=0.8. This trend is consistent with the scalar error contour shown in Figure 4.7, in which the error is significantly reduced further away from the jet shear layer or areas surrounding the jet potential core.

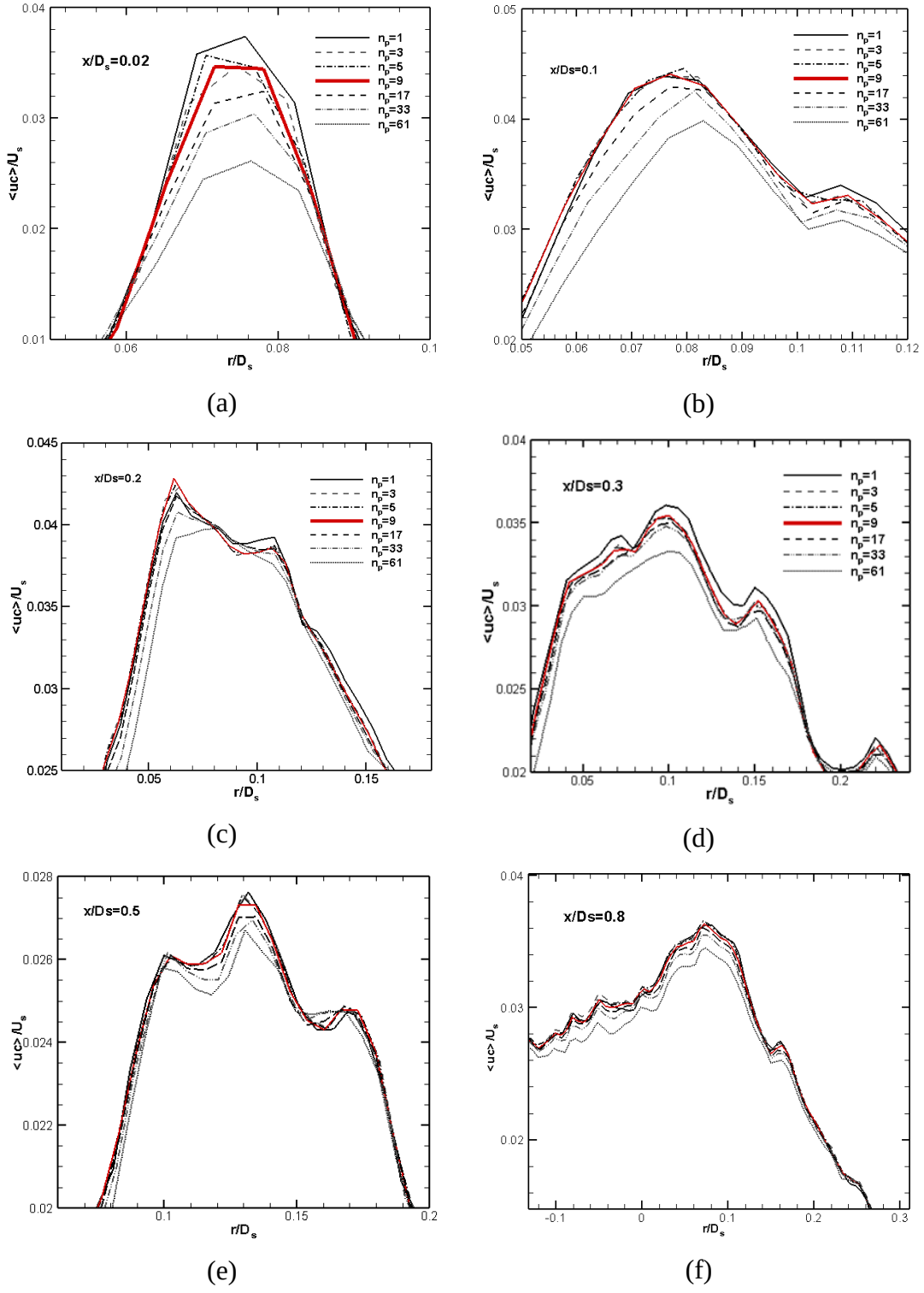

Fig. 4.8 Effect of spatial filtering of scalar on the scalar flux at 6 axial stations

4.3.4 Length scale informed filtering of scalar

Upon examination of Fig. 4.8, it appears that the 'best' filter size changes in location and the use of n_p=1 should be limited to the most sensitive regions, for example Fig.

4.8(a), while n_p =9 may be ideal for Fig. 4.8(c). This calls for the need to develop a method to adapt to the spatial dependence and the spatially varying sensitivity to filtering. However, applying filtering to raw data theoretically leads to an increase in error (HMN 1995), hence it is necessary to assign an artificial error threshold. Instead of using a constant filter width, n_p, it is varied locally to achieve an optimum value that is informed by the scalar integral length scale. The method to determine the length scale informed filter width is described here:

1. Calculate the scalar filtering error $Err(\Delta x_{PLIF}/{}^4L_{ii})$.
2. Assign a 0.5% threshold to allow for errors due to filtering, then compute n_p such that $Err(n_p \times \Delta x_{PLIF}/{}^4L_{ii}) = Err(\Delta x_{PLIF}/{}^4L_{ii})+0.5\%$.
3. If $Err(\Delta x_{PLIF}/{}^4L_{ii})+0.5\%$ at a point is larger than 2%, then the unfiltered scalar (n_p=1) should be used.

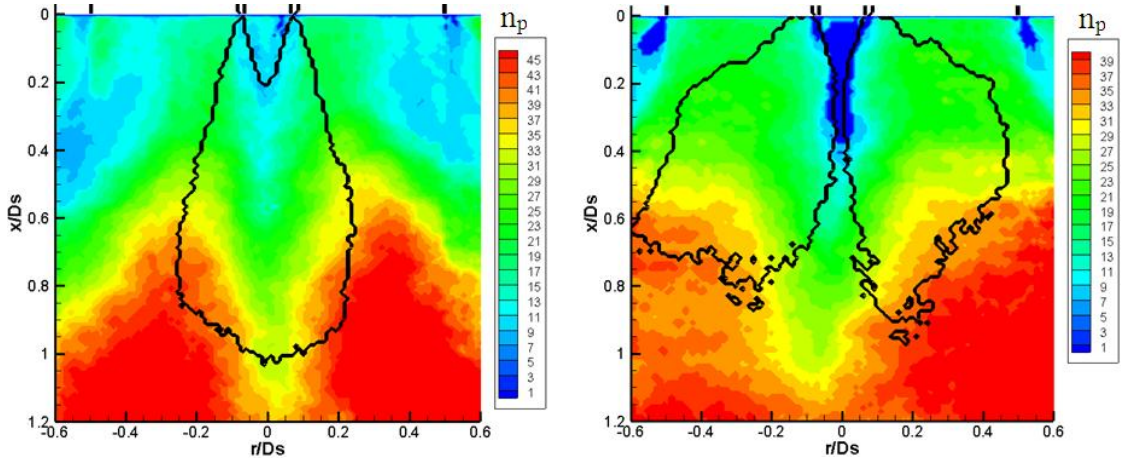

(a) $n_p(\Delta x_{PLIF}/{}^4L_{11})$ (b) $n_p(\Delta x_{PLIF}/{}^4L_{22})$

Fig. 4.9 Spatially varying filter widths

As expected, the spatial variation of colour contours of n_p shown in Fig. 4.9 is extremely similar to those shown in Figure 4.7. The finest filter widths are distributed along areas previously identified to be sensitive to filtering errors, while larger filter widths are assigned to areas that are less so. In the example shown in Fig. 4.8(a), a globally constant filter width of n_p=9 would have introduced to an error as high as ~12% at r/D_s=0.081. Thus, applying the spatially adaptive filter widths would have avoided this error while keeping the less sensitive regions free from single-pixel noise. In the validation of LES predictions in Chapter 5, it will become clear as to why such error minimisation is benefitial. The adaptive filtering method resulted in two

different scalar datasets; for simplicity, it was decided that the lower filter width of the two at each point location be selected.

4.4 Validation of methods

The adaptive filtering method relies on the assumption that Spencer and Hollis' error estimation method could be applied to scalar data. This is validated in the current section using a combination of synthetic and experimental data.

4.4.1 Synthetic data generation

The well-established software developed by Klein et al (2003) was chosen for the generation of synthetic data because it allows for the specification of single-point first and second order statistics, as well as integral lengths scales. These in turn allow for the experimentation with varying filter widths and quantifying their effect on the fluctuating scalar and scalar flux. The method was mainly designed for generation of inlet turbulence data and has been applied successfully in a large number of studies (e.g. Keimpf (2005) and Veloudis et al (2007)). Spencer and Hollis (2005) modified the software to generate fluctuating velocity data and subsequently applied different spatial averaging filters to assess their effect on turbulence intensity. For the present work, a slight modification was made to generate fluctuating scalar with prescribed grid size and scalar integral lengthscale. Only a brief description of the method is described here; the reader is advised to refer to Lund et al (1998) and Klein et al (2003) for more detailed mathematical derivations.

The modified algorithm for generating fluctuating velocity and scalar follows the steps below:-

1. Specify n_{p1} and n_{p2} based on length scales in each of the coordinate directions such that ${}^4L_{11}= n_{p1}\Delta x_{PLIF}$ and ${}^4L_{22}= n_{p2}\Delta x_{PLIF}$. Also initialise a filter F_B with a width that is at least two times the size of n_{pi} ($N_i >= 2n_{pi}$). Note that ${}^4L_{11}$ and ${}^4L_{22}$ have been selected in order to evaluate spatial filtering error with respect to scalar length scales.
2. Specify the size, M_i, of the outputted planar turbulence field (e.g. 61×61) and initialise three random fields R_i (i=1,2,3) of the dimensions ($-n_{p1}$-1: $n_{p1}+M_1$, -

n_{p2}-1: n_{p2}+M_2). The random fields are specified to take on a normal distribution (pdf) with a mean of zero and a standard deviation of unity.

3. Calculate the filter coefficients b(i,j) to store in F_B based on the correlation model of homogeneous, isotropic turbulence: $b(i,j)=\exp(-\Delta x_{PLIF}/{}^{4}L_{ii})$. Derivations of the model can be found in Hinze (1959).
4. Convolve the R_i with F_B to yield two-dimensional arrays of spatially correlated data. To expedite the processing time, the convolution was carried out in Fourier space via DFFT and subsequently inverted back to physical space.
5. Repeat steps 1 to 4 for N_s times until the desired sample size is reached and store the series of data planes.

4.4.2 Validation of error estimation method

Although Spencer and Hollis (2005) have supported the HMN model with ample velocity data, both experimental and synthetic, the question still remains as to whether the model could be aptly adopted for the estimation of spatial filtering error of scalar. For this reason, the model has been checked against a new set of synthetic scalar data, the experimental scalar data of this work, and a set of scalar data acquired from literature.

The experimental scalar data was extracted at various point locations, six of which have been selected for demonstration in Fig. 4.10. From the scalar data, the integral length scales in the dominant flow direction were calculated. The ratio of the unfiltered grid size and the integral length scale, $\Delta x_{PLIF}/{}^{i}L_{44}$, helps determine the first point on the y-axis using the HMN model. Then the scalar field is filtered with incremental widths (i.e. n_{pi}=1,3….21), and their results are plotted. All data-points except those extracted at P4 fall well between the HMN integral and the Hollis experimental models. The discrepancy at P4 may be explained by the fact that scalar fluctuation is very low in the potential core; spatial averages are likely contaminated by neighbouring values. For all other extracted points, the level of agreement is generally very good, particularly at $\Delta x_f/L<0.15$, where $\Delta x_f=n_{pi}\Delta x_{PLIF}$.

In validation against synthetic data, the ratio between the generated unfiltered fluctuating scalar and the specified one provides the location on the y axis and the

$\Delta x_{PLIF}/{}^{i}L_{44}$ provides the location on the x axis. The stored scalar field was then subject to the same spatial filtering routine with incremental filter widths. As shown in Fig. 4.10, there is excellent agreement between the synthetic scalar data and the HMN model, particularly at $\Delta x_f/L<0.2$.

The data obtained by Barlow and Karpetis (2004) in turbulent piloted methane/air jet flames provides further possibility to validate the error estimation method, as well as the filtering algorithm. The authors measured scalar variance using a combination of imaging techniques including Raman scattering, Rayleigh scattering, and laser induced CO fluorescence. From the measured instantaneous fluctuating scalar data, quantities such as scalar variance, scalar dissipation rate, and integral length scales were calculated. Of particular relevance to the present interest is the scalar variance, to which the authors applied a very similar spatial averaging algorithm to the one used here.

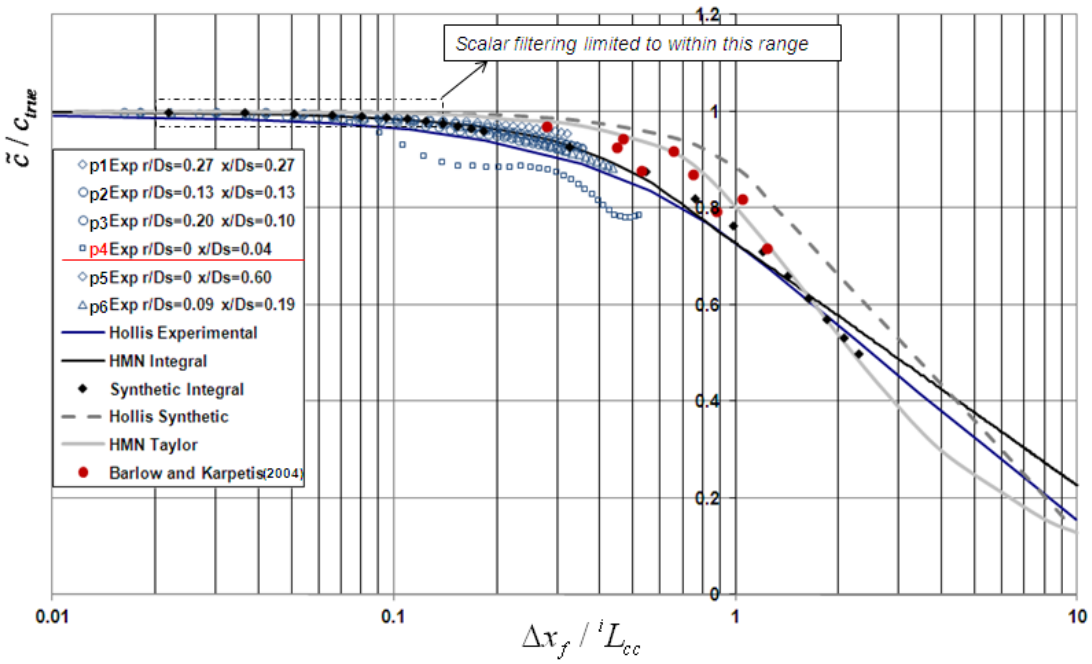

Fig. 4.10 Effect of spatial filtering on fluctuating scalar (Exp is an abbreviation for experimental and the Synthetic Integral is obtained from the exercise described in the previous section)

The scalar variance was directly converted to fluctuating scalar, and based on information of the filter width to length scale ratio provided by the authors at three point locations, the filtered points with increasing filter widths (3, 5, and 7) can be plotted relative to what the authors referred to as ‘super-resolution’ values. It should

be noted that 'super-resolution' scalar fluctuation was obtained by extrapolating the value to a zero pixel, which is taken to be the true value in this case. As shown in Figure 4.10, there is some scatter among the data points and the HMN integral curve also tends to underestimate the decay. This could be explained by the fact that the correlation functions of this set of scalar data may deviate from that of the exponential model. Despite the scatter, the average deviation from the HMN integral is about 6%, and all data points fall within the HMN integral and the HMN Taylor models.

4.4.3 Effect of adaptive filtering of scalar on synthetic scalar flux

With the velocity unfiltered, it is possible to study the effect of spatial filtering of the scalar on the scalar flux independently. This is valid as long as the velocity converges towards the specified value, typically at a sample size of 15000 or larger. Synthetic data was generated on various point locations, six of which have been selected for illustration. Again, the strategy employed to filter the data with incremental window sizes is very similar to that reported in Hollis (2004):

1. Carry out spatial averaging on each stored synthetic data plane (in a time series of N_s samples) by applying a local $n_p \times n_p$ matrix averaging algorithm, thus creating a filtered velocity field $\tilde{c}\,(x_1,x_2)$ at each cell using Eq. 4.9.
2. Generate a random 1-D time series that has a mean of unity and a standard deviation of 0.028, and multiply this time series with the N_s samples generated above to simulate the effect of shot-to-shot energy variation (Section 3.3.5).
3. Calculate the ensemble-averaged scalar flux with varying n_p using Eq. 4.9, where n_p ranges from 1 to 41.
4. Divide the spatial-filtered scalar flux ($u\tilde{c}(n_p)$) by the specified one (uc_{sp}).

The results are plotted in Figure 4.11, which shows that the synthetically generated scalar fluxes converge towards the specified values with decreasing filter widths. The plotted synthetic data exhibits a similar behaviour as Fig. 4.8: the slopes tend to decrease as the location is further away from the exit plane. Also, the filter widths above the 0.05% threshold agree well with those shown in Fig. 4.9. This verifies the ability of the method to limit spatial filtering error to 0.5%.

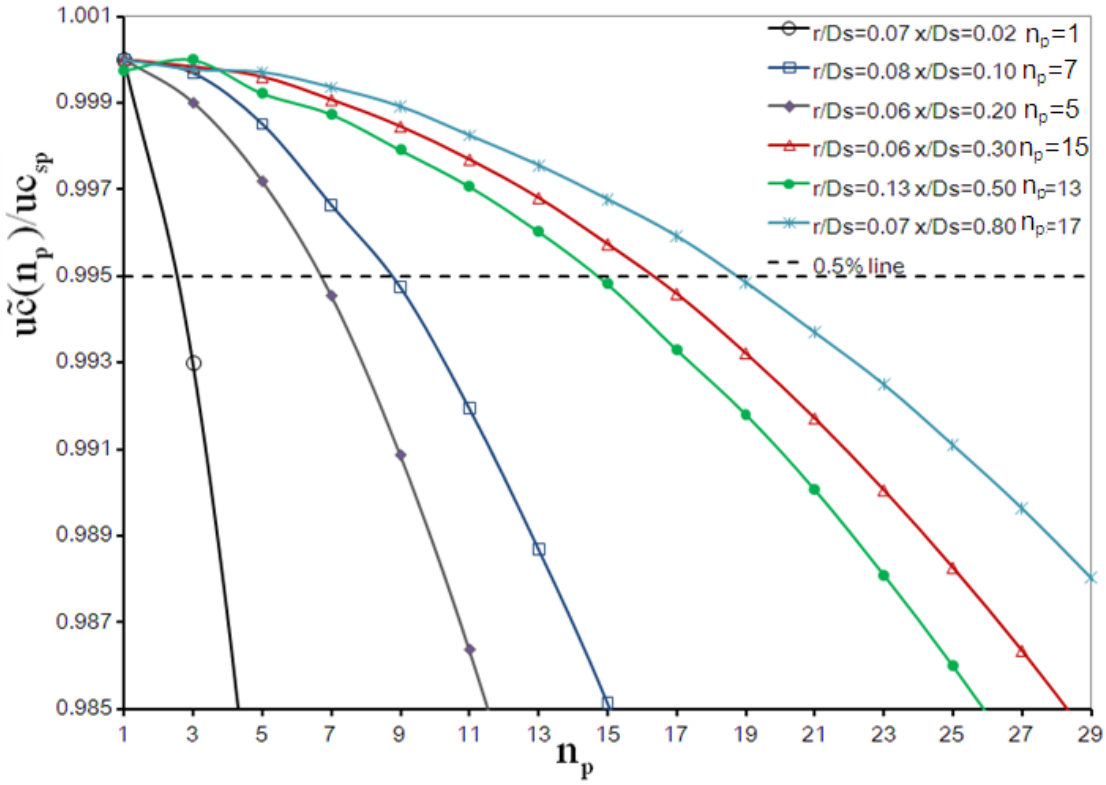

Fig. 4.11 Effect of spatial filtering on scalar flux (synthetic data)

4.4.4 Scalar flux correction

Using the method developed and validated in the previous sections, adaptive spatial filtering error of the scalar with respect to the integral length scale can be controlled to about 0.5% throughout the x-r measurement plane. It is important to recall that this error is independent from the errors that already exist in the unfiltered data, as shown in Fig. 4.7. As discussed in Section 4.3.2, $Err(\Delta x_{PLIF}/^{2}L_{44})$ reaches a maximum of about 2% just downstream of the jet lip, where no additional filtering was applied (n_p=1). In majority of the FoV, the scalar error magnitude is rather insignificant when combining with the much larger velocity errors via the quadrature addition. Therefore, the strategy employed in terms of error management is to minimise scalar filtering errors $Err(\Delta x_{PLIF}/^{i}L_{44})$, while using the velocity spatial filtering error, $Err(\Delta x_{PIV}/^{k}L_{ii})$ to correct for time-mean scalar fluxes. In other words, correction of the spatial filtering error for scalar fluxes could be solely based on the evaluation of Eqs. 4.26 and 4.27 with respect to $\Delta x_{PIV}/^{1}L_{11}$ and $\Delta x_{PIV}/^{2}L_{22}$.

$$\langle u_i c_{corr} \rangle = \frac{\langle u_i c_{meas} \rangle}{1\text{-}Err(\Delta x_{PIV} / {}^{i}L_{ii})} \tag{4.30}$$

An example of the correction is shown in Fig. 4.12.

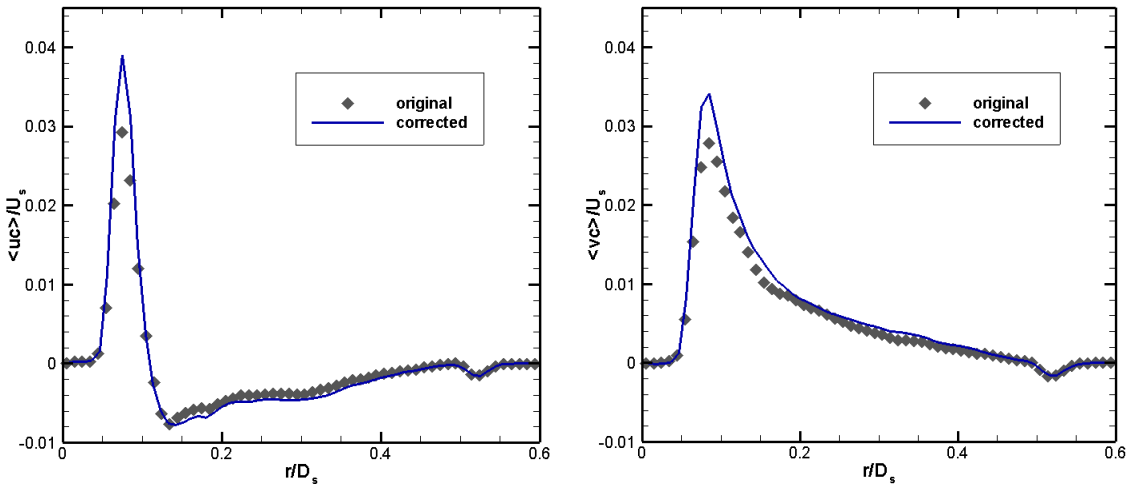

Fig. 4.12 Original and corrected scalar flux profiles in the radial (left) and axial (right) directions at x/Ds=0.13

Previous discussions on spatial filtering have largely neglected tangential velocity due to two major difficulties in the characterisation of circumferential velocities as well as integral lengthscales, ${}^{3}L_{33}$:

1. The instantaneous, hence Reynolds decomposed, tangential velocity in an r-θ plane is not directly measured; it is converted from the two in-plane Cartesian components. Thus, errors that are present in the two Cartesian components can propagate into W without being accounted for.
2. The converted tangential velocities are still stored on Cartesian coordinates, which need to be interpolated onto a polar mesh with denser grids about the geometric centre. In the jet shear region, which is important for turbulent mixing, the coarser Cartesian mesh would be interpolated onto a finer polar one. Doing so would introduce errors to the computation of ${}^{3}L_{33}$ because there are not enough grid points in the centre region for an accurate integration of SVC(w).

For these reasons, corrections for <w> and <wc> have been omitted.

4.5 Statistical convergence

The uncertainty due to limited sample size (a random error) in separate velocity and scalar measurements is quite straight-forward. Provided that the rms is known or can be inferred with confidence from measured data and that the normal distribution can be assumed, statistical errors of the mean and rms velocities, as well as the variance, can be evaluated using Eq. 4.31, Eq. 4.32, and Eq. 4.33, respectively.

$$\varepsilon_{U_i} = z\sigma\sqrt{\frac{1}{N}} \tag{4.31}$$

$$\varepsilon_{u_i} = z\sigma\sqrt{\frac{1}{2N}} \tag{4.32}$$

$$\varepsilon_{u_i u_i} = z\sigma^2\sqrt{\frac{2}{N-1}} \tag{4.33}$$

Where σ is the rms velocity, z is the confidence level, and N is the sample size. Hence, the errors are also a function of the turbulence intensity. These equations can be found in most standard statistics textbooks, i.e. Bendat and Pierso (1986); the applications of these equations in the study of turbulence intensity with PIV data can be found in Uzol and Camsi (2001).

4.5.1 Theoretical formula

The error estimate of covariance statistics is less documented in literature. In fact, detailed discussions on sample size effects are lacking even in studies associated with the reductions of scalar fluxes. For examples, Loffler et al (2008) used a sample size of 512 in an experimental determination of subgrid scale scalar flux without quantifications of the error. Borg et al (2001) used a sample size of only 320, but the author was able to quantify the error via evaluation of a theoretical formula provided by Bendat and Piersol (1986):

$$\varepsilon_N\left(\rho_{ucuc}, N_s\right) = \sqrt{\frac{1}{N_s}\left(\frac{1}{\rho_{ucuc}^{\,2}} + 1\right)} \tag{4.34}$$

where ε_N is the error estimate as a function of the correlation coefficient, ρ_{ucuc}, and the sample size, N_s. Eq. 4.34 is valid under the assumption that the pdfs of both velocity and scalar fluctuations are Gaussian. If the distributions were to deviate from perfect Gaussian, then the following formula by Mirskii (1981) may be considered.

$$\varepsilon_N\left(\rho_{ucuc},N_s\right)=\sqrt{\frac{1}{N_s}\left(\frac{1}{\rho_{ucuc}^{\ 2}}+1+\left[\sqrt{\left(\gamma_2(u)+2\right)\left(\gamma_2(c)+2\right)}-2\right]\right)} \tag{4.35}$$

where $\gamma_2(u)$ and $\gamma_2(c)$ are the kurtosis of the velocity and the scalar distributions respectively. The kurtosis is added into the equation to account for the shapes of the respective distributions of u and c. In general, an increasingly positive kurtosis means the distribution is dominated by a certain range of values, while a negative kurtosis means that the distribution is flatter. In the present study, sample size effects will be discussed with observations from both synthetic and experimental data, as presented in the two following sections.

4.5.2 Observation from synthetic data

To test Eq. 4.34, the synthetic data generation method described in the previous section was used. The u_i and c matrices of random numbers (step 2 in Section 4.4.1) were generated with a mean of zero and a standard deviation of unity, again with a normal distribution. Hence, from the 15,000 synthetic datasets, Eq. 4.34 can be tested by calculating the scalar flux with incremental sample sizes (for example, 100, 200, 1000, to 10000), without applying any filtering. As shown in Figure 4.13, the scalar flux does converge towards the specified value with increasing sample sizes. The error estimate using Eq. 4.34 presented by Borg et al (2001) assumed a z-score of one (a 68% confidence level), hence the 12% error estimate for their sample size of 320 was underestimated by roughly a factor of 1.96 should the 95% confidence level be considered. As shown in Fig. 4.13, Eq. 4.34 predicts the statistical convergence of the synthetic scalar flux data with good accuracy.

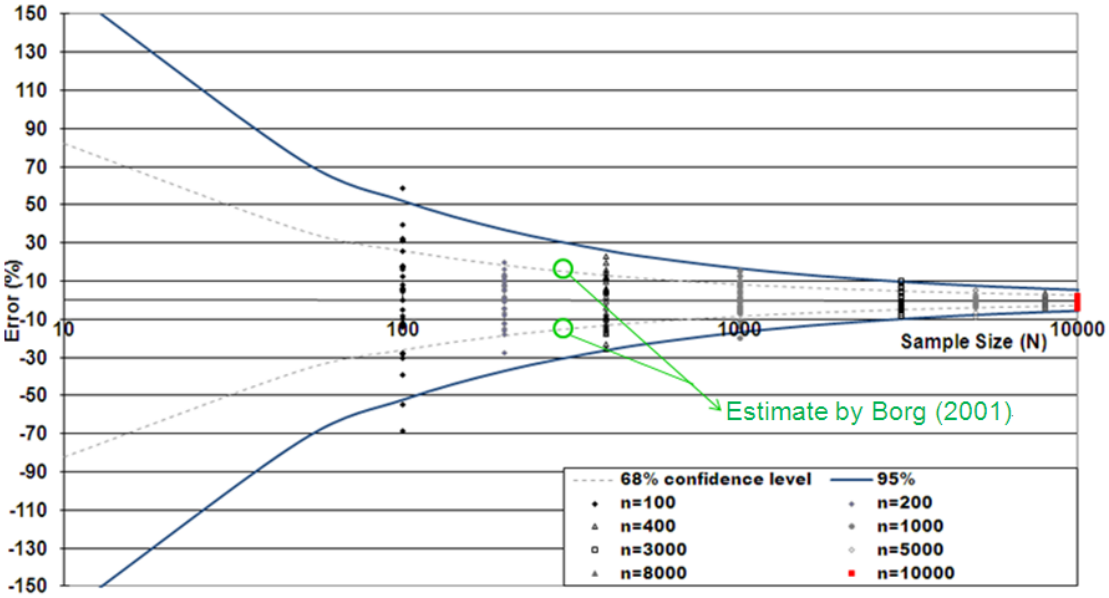

Fig. 4.13 Statistical convergence of scalar flux, calculated from synthetically generated data with the prescribed parameters selected from experimental data at r/Ds=0.06, x/Ds=0.13, ρ_{ucuc}=0.46

To account for variations in pdf shapes, Miirski's formula (Eq. 4.35) is also tested. Eq. 4.35 states that the uncertainty is not only dependent on the sample size and the correlation coefficient, but also the shapes of the pdfs, which are not known a priori. Hence, the synthetic data once again serves as a powerful tool validation because it allows the user to specify a known correlation coefficient, as well as kurtosis for both velocity and scalar (to allow some deviations from the Gaussian distribution). The Pearson method of random number generation allows the inputs of kurtosis (Matlab, 2010). The synthetic data shown in Fig. 4.14 has been generated with negative kurotsis (γ_2(u) =-1 and γ_2(c) =-1), which were calculated from the experimental data at the point location. The statistical convergence of the synthetic data, bounded by the theoretical estimates by Eq. 4.35, is shown in Fig. 4.14. As expected from Eq. 4.35, the negative kurtosis has the effect of increasing the slopes of the convergence. As shown in Fig. 4.14, the convergence trend of the normal distribution (based on Eq. 4.34) only slightly overestimates the theoretical error with the prescribed Kurtosis in this important region of scalar mixing.

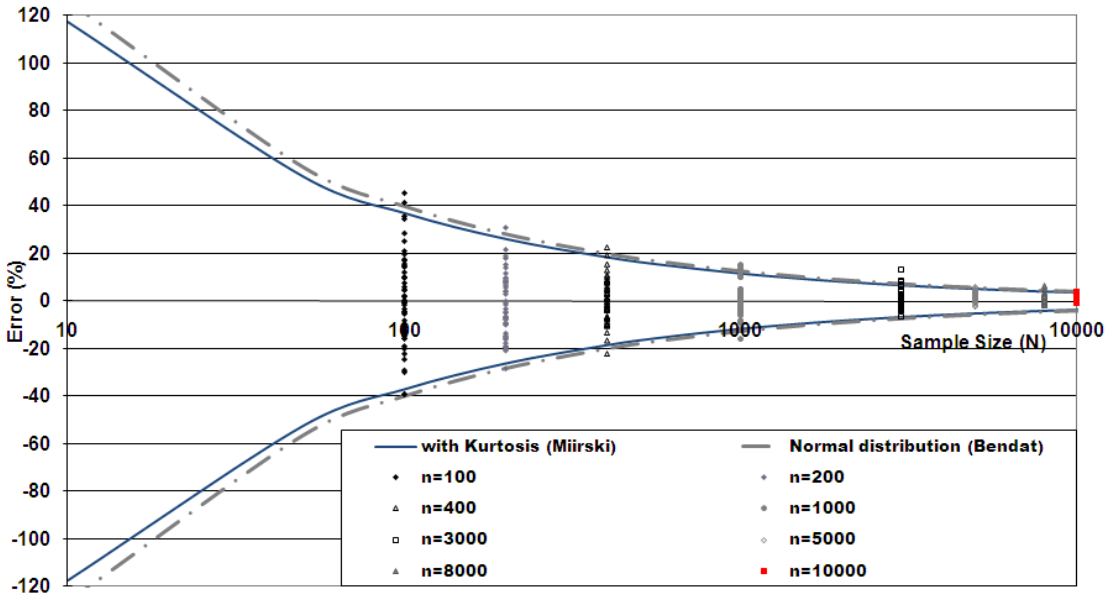

Fig. 4.14 Statistical convergence of scalar flux, calculated from synthetically generated data with the prescribed parameters selected from experimental data at r/Ds=0.09, x/Ds=0.13, ρ_{ucuc}=0.56

4.5.3 Observation from experimental data

Despite the fact that Eq. 4.34 requires sample sizes on the order of 10^4 for the error to be reduced to below 5% for a typical range of correlation coefficient ($0.2<\rho_{uc}<0.5$), observation from the experimental data actually shows that Eq. 4.34 overestimates the statistical spread by a factor of around 2. A possible explanation for this has to do with the fact that velocity and scalar have already been group averaged when spatial filters were applied. Examples of the convergences of experimental data, extracted from a total sample size of 1500, are shown in Fig. 4.15 and Fig. 4.16. The statistical convergence study has been conducted on two scalar fluxes with two different correlation coefficients; this is done to highlight the effect of the correlation coefficient, as predicted by Eq. 4.34. The definitive x-r plane measurement has a combined sample size of 1500, thus the error estimates at N=1250 may be considered a reasonable estimation of the spread. Based on Fig. 4.15 and Fig. 4.16, the errors are roughly 5% and 10%, respectively. Thus, this may be considered to be the statistical convergence error associated with the x-r plane data. The r-θ plane data, on the other hand, typically has a sample size of 1000, equating to errors of roughly 10% and 20%, respectively, although error in the circumferentially averaged profiles are expected to be reduced considerably.

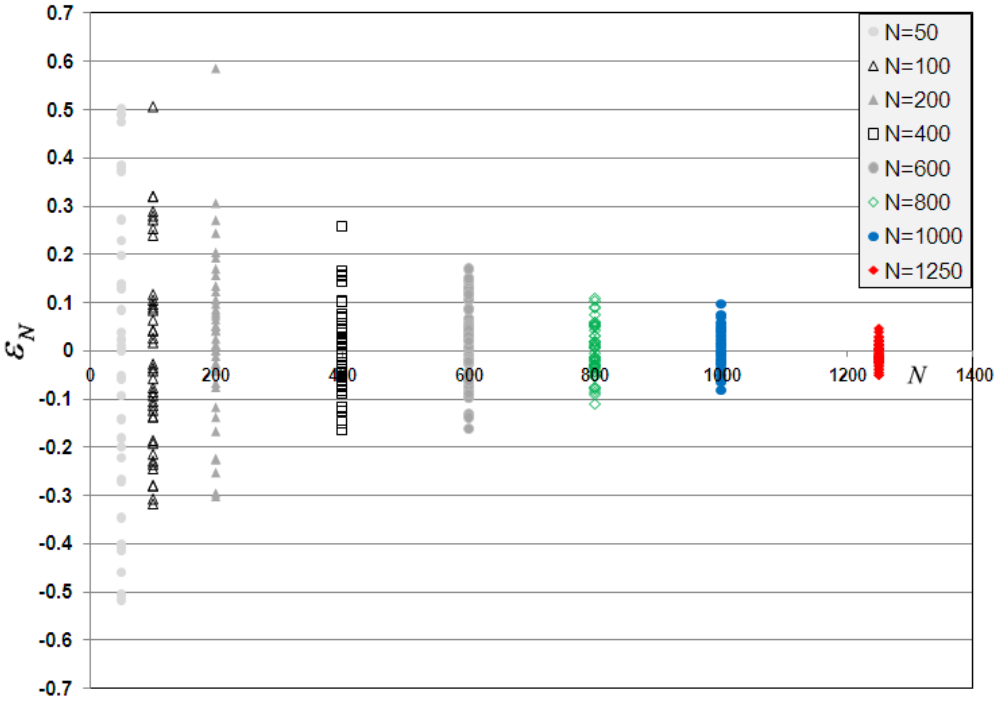

Fig. 4.15 Statistical convergence of scalar flux, calculated from experimental data at r/Ds=0.1, x/Ds=0.13, with a correlation coefficient of 0.50

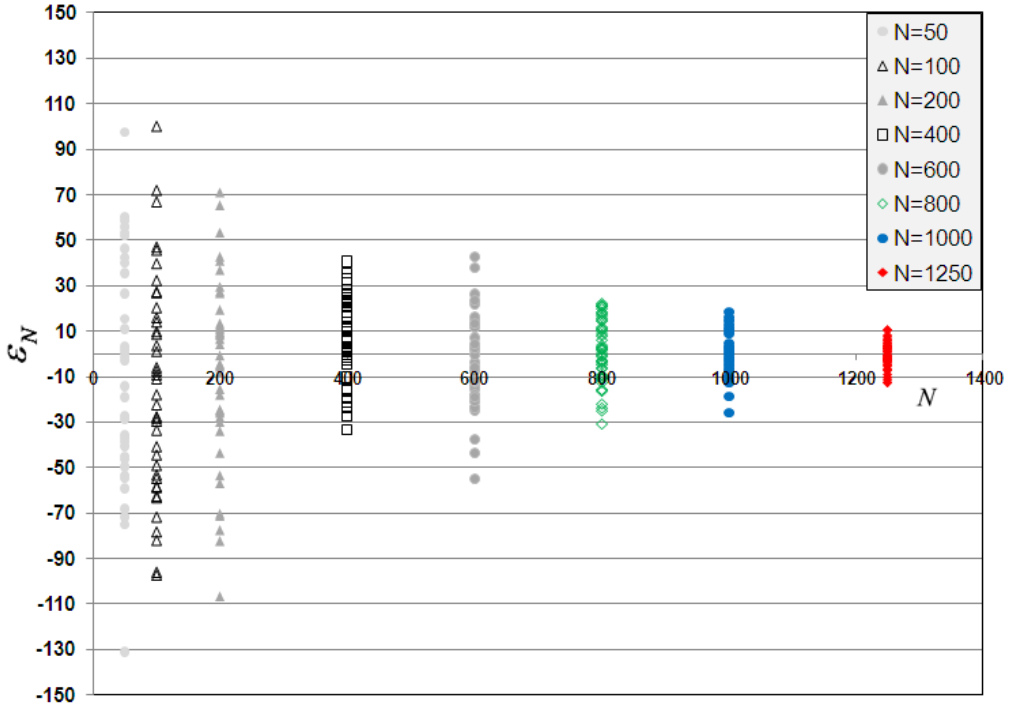

Fig. 4.16 Statistical convergence of scalar flux, calculated from experimental data at r/Ds=0.1, x/Ds=0.08, with a correlation coefficient of 0.22

4.6 Computation of time-mean pressure fields

Vanierschot and Van den Bulck (2008) developed a method to compute the mean static pressure distribution from spatially resolved planar SPIV data. The method is referred to as "VVB" from this point for simplicity. The authors applied the method to three axially imparted swirling flow cases of different swirl numbers – S_n=0.18, S_n=0.37, and S_n=0.74. By decomposing the static pressure field into a swirl-induced one and a non-swirl-induced one, it was found that the former becomes more dominant as the swirl number increases. Here, the data reduction method, including the theoretical framework, assumptions, and the specifications of boundary conditions, is described.

4.6.1 Mathematical formulations

In accordance with the cylindrical coordinate system that has been used throughout the study,the divergence of Reynolds averaged velocity is written as:-

$$\nabla\cdot<\bar{\mathrm{U}}>=\frac{\partial<\mathrm{U}>}{\partial \mathrm{x}}+\frac{1}{\mathrm{r}}\frac{\partial \mathrm{r}<\mathrm{V}>}{\partial \mathrm{r}}+\frac{1}{\mathrm{r}}\frac{\partial<\mathrm{W}>}{\partial\theta} \tag{4.36}$$

Where $<\bar{\mathrm{U}}>$ is the mean velocity vector, and as a reminder, <U>, <V>, and <W> denote the mean axial, radial, and tangential components. The Reynolds averaged momentum equation can therefore also be broken into the three components:-

$$\frac{\bar{\mathrm{D}}<\mathrm{U}>}{\bar{\mathrm{D}}\mathrm{t}}=\upsilon\nabla^2<\mathrm{U}>-\frac{1}{\rho}\frac{\partial<\mathrm{p}>}{\partial \mathrm{x}}-\frac{\partial<\mathrm{u}^2>}{\partial \mathrm{x}}-\frac{1}{\mathrm{r}}\frac{\partial \mathrm{r}<\mathrm{uv}>}{\partial \mathrm{r}}-\frac{1}{\mathrm{r}}\frac{\partial<\mathrm{uw}>}{\partial\theta} \tag{4.37}$$

$$\frac{\bar{\mathrm{D}}<\mathrm{V}>}{\bar{\mathrm{D}}\mathrm{t}}=\upsilon\nabla^2<\mathrm{V}>-\frac{1}{\rho}\frac{\partial<\mathrm{p}>}{\partial \mathrm{r}}-\frac{\partial<\mathrm{uv}>}{\partial \mathrm{x}}-\frac{1}{\mathrm{r}}\frac{\partial \mathrm{r}<\mathrm{v}^2>}{\partial \mathrm{r}}-\frac{1}{\mathrm{r}}\frac{\partial<\mathrm{vw}>}{\partial\theta}+\frac{<\mathrm{w}^2>}{\mathrm{r}} \tag{4.38}$$

$$\frac{\bar{\mathrm{D}}<\mathrm{W}>}{\bar{\mathrm{D}}\mathrm{t}}=\upsilon\nabla^2<\mathrm{W}>-\frac{1}{\rho\mathrm{r}}\frac{\partial<\mathrm{p}>}{\partial\theta}-\frac{\partial<\mathrm{uw}>}{\partial \mathrm{x}}-\frac{1}{\mathrm{r}}\frac{\partial \mathrm{r}<\mathrm{vw}>}{\partial \mathrm{r}}-\frac{1}{\mathrm{r}}\frac{\partial<\mathrm{w}^2>}{\partial\theta}+\frac{<\mathrm{vw}>}{\mathrm{r}} \tag{4.39}$$

Where ρ is the density, υ is the kinematic viscosity of water, <P> is the time-mean static pressure, and $\bar{D}/\bar{D}t$ is the mean substantial derivative, its definition can be found in the Appendix 4.2. Summation of the three pressure terms is effectively the gradient of P:-

$$\nabla < P >= \frac{\partial < P >}{\partial x} + \frac{\partial < P >}{\partial r} + \frac{1}{r}\frac{\partial < P >}{\partial \theta} \tag{4.40}$$

Then, VVB made the following assumptions, which have also been adopted in the current work. A description of them is provided here (details of the omitted terms in fully expanded equations can be found in Appendix 4.2:

1. The through-plane (xr plane), or tangential, derivatives ($\partial/\partial\theta$) of the mean momentum equation and of the mean material derivative equation are assumed to be negligible in accordance with the 2D3C nature of planar SPIV measurement.
2. The transient terms of the mean substantial derivative are assumed negligible.
3. The viscous terms (υ) are also neglected as they are several orders of magnitude smaller than the others in the mean momentum equations, as confirmed by VVB's measurements. This is also considered valid under the current experiment as water has a lower kinematic viscosity than air and the Reynolds number of this work is about 1.7 times higher that of VVB's experiment.

After these negligible terms are eliminated, the term $-1/\rho\nabla < P >$ can be rearranged to the left-hand-side (LHS), and rest of the terms to the right-hand-side (RHS). By taking a divergence and taking into account the continuity equation, then expression of the Laplacian of the mean pressure can be obtained:-

$$-\frac{1}{\rho}\nabla^2 < P >= \left(\frac{\partial < U >}{\partial x}\right)^2 + \left(\frac{\partial < V >}{\partial r}\right)^2 + 2\frac{\partial < U >}{\partial r}\frac{\partial < V >}{\partial x} + \frac{< V^2 >}{r^2} + \frac{\partial^2 < uu >}{\partial x^2}$$
$$+ \frac{2}{r}\frac{\partial^2 r < uv >}{\partial r \partial x} + \frac{1}{r}\frac{\partial^2 r < v^2 >}{\partial r^2} - \frac{1}{r}\frac{\partial}{\partial r}\left(< W^2 > + < w^2 >\right) \tag{4.41}$$

The Laplacian of P, without the tangential contribution is given by:-

$$\nabla^2 < \mathrm{P} >= \frac{\partial^2 < \mathrm{P} >}{\partial \mathrm{x}^2} + \frac{1}{\mathrm{r}} \frac{\partial < \mathrm{P} >}{\partial \mathrm{r}} + \frac{\partial^2 < \mathrm{P} >}{\partial \mathrm{r}^2} \tag{4.42}$$

To approximate the first and second order derivatives in the equation above, the central-difference discretisation scheme has been adopted as follows (please note that the '< >' notations are omitted from here till the end of this section):

$$\left.\frac{\partial P}{\partial x}\right|_{i,j} \approx \frac{P_{i+1,j} - P_{i-1,j}}{2\Delta x} \tag{4.43}$$

$$\left.\frac{\partial^2 P}{\partial x^2}\right|_{i,j} \approx \frac{P_{i+1,j} - 2P_{i,j} - P_{i-1,j}}{(\Delta x)^2} \tag{4.44}$$

Where $P_{i,j}$ is the static pressure at the point indexed by i and j, and Δx is essentially the length of each PIV interrogation cell ($\Delta x = \Delta x_{PIV}$). Having applied the same central differencing scheme to $\partial < \mathrm{P} > / \partial \mathrm{r}$ and $\partial^2 < \mathrm{P} > / \partial \mathrm{r}^2$, Eq. 4.42 is expanded into a summation of five points, as shown in Fig. 4.17. The coefficients at each one of these five points (e.g. $1/\Delta x^2$ for $P_{i+1,j}$) are denoted by C_p, also detailed in Fig. 4.17.

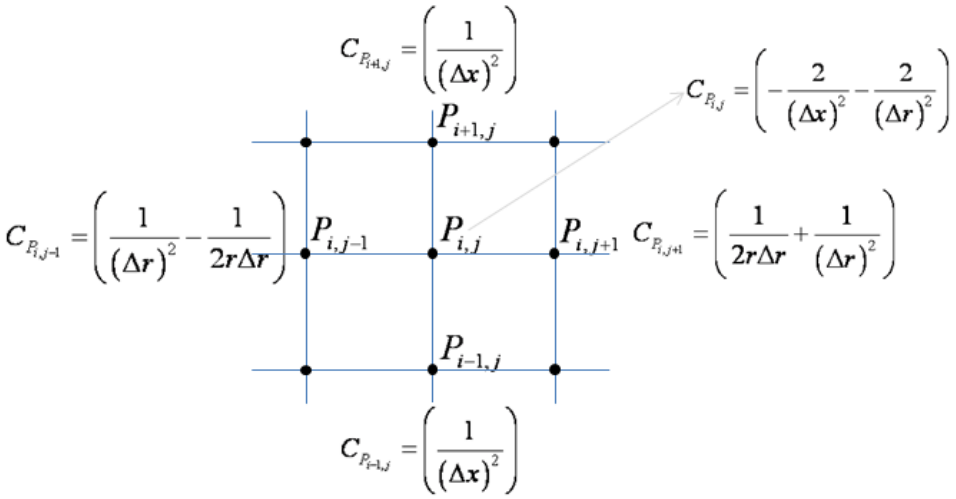

Fig. 4.17 Pressure on a rectangular grid segment

Fig. 4.17 shows the coefficients of 5 points inside the boundary, but on the four boundaries of the computational plane, as illustrated in Fig. 4.18, different boundary conditions have been applied.

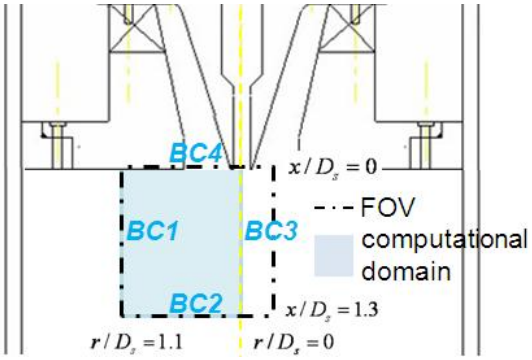

Fig. 4.18 Boundaries of the computational domain

As the measurement FoV did not include the wall and no experimental pressure data is available for the prescription of boundary condition (BC1) along r/D_s=1.1, it was decided to use the LES predictions of Dunham (2010). Along BC1, the LES-predicted time-mean static pressure along BC1 is axially constant of around ~3500(Pa). Along BC2, a second-order upwind discretisation scheme (Neumann boundary condition) has been applied:

$$\left.\frac{\partial P}{\partial x}\right|_{i,j} \approx \frac{3P_{i,j} - 4P_{i-1,j} + p_{i-2,j}}{2\Delta x} \tag{4.45}$$

Thus, for every point ($P_{i,j}$) along BC2, there are two other unknowns, the coefficients of all three points are $C_{Pi,j}$=(3/2Δx), $C_{Pi-1,j}$=(-2/Δx), and $C_{Pi-2,j}$=(1/2Δx).The third boundary (BC3) lies along the centreline, as indicated by the dashed yellow line in Fig. 4.18. Along BC3, it is assumed that the radial pressure gradient is zero, using a second-order upwind scheme:

$$\left.\frac{\partial P}{\partial r}\right|_{i,j} \approx \frac{-P_{i,j+2} + 4P_{i,j+1} - 3p_{i,j}}{2\Delta r} = 0 \tag{4.46}$$

The coefficients that are applied along this boundary are $C_{Pi,j}$=(-3/2Δr), $C_{Pi,j+1}$=(2/Δr), and $C_{Pi,j+2}$=(-1/2Δr). Finally, the fourth boundary (BC4) is at the first available position at fuel injector exit, near x/D_s~0, where a similar (Neumann boundary) second-order upwind scheme was applied.

$$\left.\frac{\partial P}{\partial x}\right|_{i,j} \approx \frac{-P_{i+2,j} + 4P_{i+1,j} - 3p_{i,j}}{2\Delta x} \tag{4.47}$$

So that the coefficients are $C_{Pi,j}=(-3/2\Delta x)$, $C_{Pi+1,j}=(2/\Delta x)$, and $C_{Pi+2,j}=(-1/2\Delta x)$. Having determined the coefficients, the LHS of Eq. 4.41 is now simply $-1/\rho C_P P$. Every term in the RHS can be directly computed from the time-mean SPIV data using the central differencing scheme; the addition of all the terms on the RHS yields a single value B(i,j) at each point. The Matlab script of the addition of all the terms can be found in the Appendix 4.3. Overall, for every point location (i,j) there is a known coefficient C_p and a known B evaluated from SPIV statistics; by rearranging B so that $-1/\rho C_P P=B$, P, the static pressure, can be directly evaluated:-

$$P = -\rho C_p^{-1} B \tag{4.48}$$

Where matrix P has a size of (3604×1), C_p is (53×68), and B has been rearranged to (3604×1) also. The computed P matrix is then converted back to physical locations with the same size as C_p.

4.6.2 Validation on a simple flow case

In order to validate the Matlab code that was developed on the basis of the VVB method, as described in the previous section, a simple test case – fully developed flow in a 2D square duct – was produced in Fluent. After having specified uniform inlet conditions and a surface roughness, the software computes the time-averaged 3C velocities, Reynolds stresses, and the pressure distribution. The mean velocities and the Reynolds stresses outputted by Fluent were input into the pressure computation software, which applied the same boundary conditions at the four edges. The two contours of time-mean static pressure are shown in Fig. 4.19. It can be seen that data along x=0.02 and r=0.05 is lost due to the central differencing method. Other than this, the agreement is perfect.

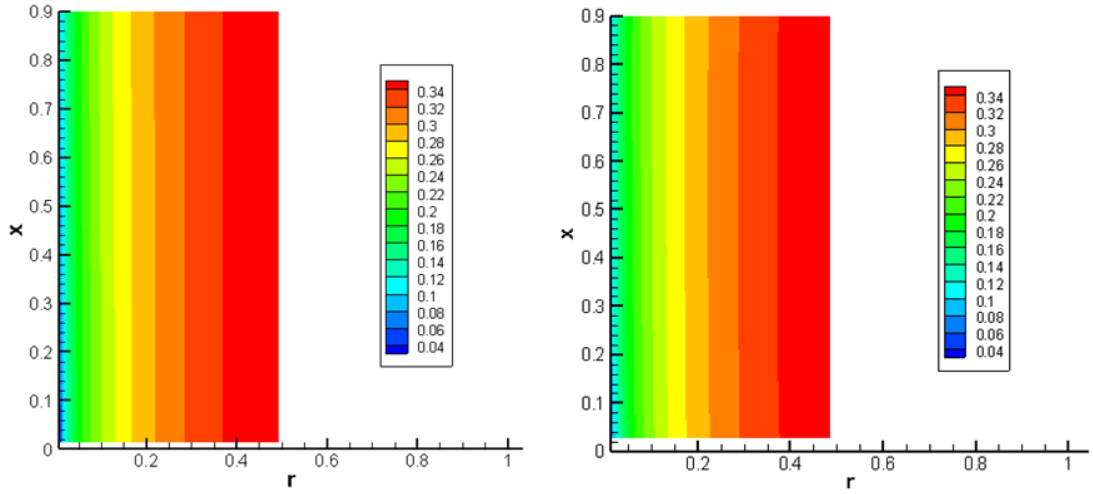

Fig. 4.19 Static pressure (left) Fluent, (right) calculated using the VVB method

4.7 Coherent structure identification

4.7.1 Conditional averaging

Conditional averaging is commonly used to visualize dominant flow structures by carrying out the averaging operation only if the fluctuating component is larger or smaller than the prescribed limits. This idea is illustrated in Fig. 4.20.

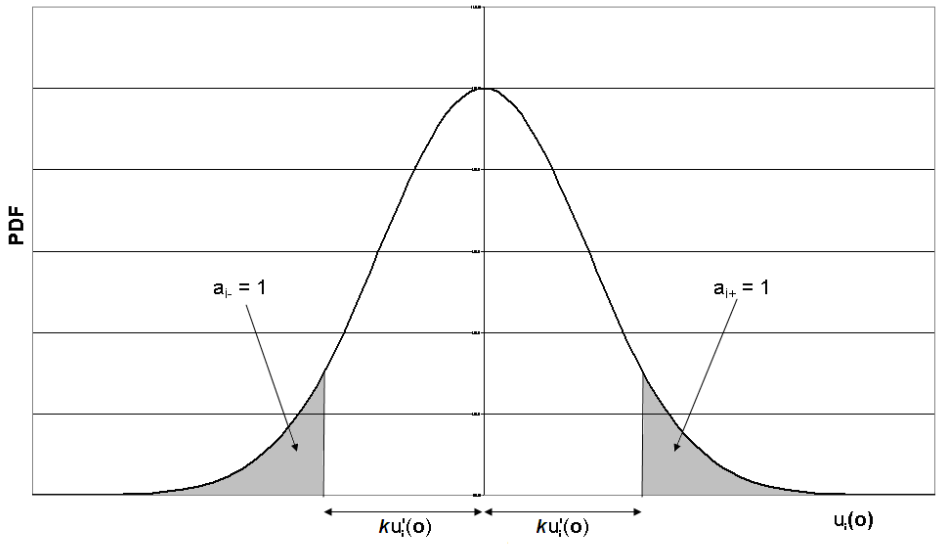

Fig. 4.20 Conditional averaging of a pdf distribution

$$\left\langle u_{i,caj+}(\mathbf{x})\right\rangle = \frac{1}{N_{ca+}}\sum_{k=1}^{N_s} a_{j+}(t_k)u_i(\mathbf{x},t_k) \quad \mathrm{a_{j+}} = \begin{matrix} 0 \\ 1 \end{matrix}\Bigg| \begin{matrix} \mathrm{u_j}(x_o,y_o,\mathrm{t_k}) < k\,\mathrm{u_j}'(x_o,y_o) \\ \mathrm{u_j}(x_o,y_o,\mathrm{t_k}) \geq k\,\mathrm{u_j}'(x_o,y_o) \end{matrix} \quad N_{ca+} = \sum_{k=1}^{N_s} a_{j+}$$

$$\left\langle u_{i,caj-}(\mathbf{x})\right\rangle = \frac{1}{N_{ca-}}\sum_{k=1}^{N_s} a_{j-}(t_k)u_i(\mathbf{x},t_k) \quad \mathrm{a_{j-}} = \begin{matrix} 0 \\ 1 \end{matrix}\Bigg| \begin{matrix} \mathrm{u_j}(x_o,y_o,\mathrm{t_k}) > k\,\mathrm{u_j}'(x_o,y_o) \\ \mathrm{u_j}(x_o,y_o,\mathrm{t_k}) \leq k\,\mathrm{u_j}'(x_o,y_o) \end{matrix} \quad N_{ca-} = \sum_{i=1}^{N_s} a_{j-}$$

(4.49)

where *k* is a coefficient that is specified to ensure that the samples averaged provide a reliable estimate, and a_j represents the samples that are averaged. From Hollis (2004) and Midgley (2005), it was shown that a value of k=±1.5 works well and would be equivalent to the most extreme ±10% of a normal distribution. In the current work, conditional averaging is used alongside SVC or SSC with a user-specified reference point location.

4.7.2 Proper Orthogonal Decomposition

After Lumley (1981) first applied POD to the study of fluid mechanics, the method has become widely used for the identification of dominant unsteady structures, and it has become more popular in the field of combustion fluid dynamics in recent years. For examples, Midgley (2005) used POD to visualise the inner shear vortices in the Turbomeca fuel injector flowfied, Rupp et al (2010) used POD to distinguish the effects of damping by combustor liner apertures with and without acoustic forcing, Storh (2012) combined the method with phase averaging to study the vortex-flame interaction in a complex-geometry dual-swirl fuel injector. Studies that involve applying POD to simultaneous 3C velocity and passive scalar, however, remain rare. POD is based on the Karhunen-Loéve decomposition of probability theory, which states that a random function can be approximated by a series of deterministic functions with random coefficients. The method is able to extract ordered, energetic mode shapes such that when it is applied to current combined PIV-PLIF data, the most energetic turbulent motions and their effect on scalar mixing can be identified. The standard calculation method can be found in Midgley (2005) and Robinson (2009). A fluctuating velocity (single-component, such as u – axial velocity) or scalar field with a sample size, N_s, may be represented by a set of spatial functions, $\varphi_k(\mathbf{x})$, and uncorrelated temporal coefficients, $a_k(t)$, such that the following equation can be written:-

$$u(\mathbf{x},t_i)=\sum_{k=1}^{N_s} a_k(t_i)\varphi_k(\mathbf{x}) \qquad \text{for i = 1,…,N}_s \qquad (4.50)$$

Where k is the mode number, and the maximum number k can be set to equal to N_s. The spatial functions are obtained by firstly constructing the matrix **A**:

$$\mathbf{A}=\begin{bmatrix} u(x_1,t_1) & \cdots & u(x_1,t_{N_s}) \\ \vdots & \ddots & \vdots \\ u(x_m,t_1) & \cdots & u(x_m,t_{N_s}) \end{bmatrix} \qquad (4.51)$$

Where *m* is the number of spatial locations present on the 2D velocity or scalar field, so that the first row in the matrix is essentially the time series at that point, and x_i is the two-dimensional location, for example, $(x,r)_i$. The spatial correlation matrix, **R**, between all points in the field may be obtained from Eq. 4.52.

$$\mathbf{R}=\frac{1}{N_s}\left(\mathbf{A}\mathbf{A}^T\right) \qquad (4.52)$$

Chatterjee (2000) showed that R can be obtained from the Matlab function for Singular Value Decomposition (SVD) such that:-

$$\mathbf{R}=\mathbf{U}\mathbf{\Sigma}\Phi^T \qquad (4.53)$$

Where **U** is a matrix of ($N_s \times N_s$), **Φ** is a ($m \times m$) matrix, and **Σ** is a ($N_s \times m$) matrix, which contains only zero elements except on the leading diagonal, where the elements are the singular values arranged in descending order. The columns of **Φ** are the eigenvectors; hence, by taking the k^{th} column of **Φ** across the field the k^{th} spatial POD mode can be extracted. The SVD method involves computations on very large matrices which can be as large as ~ (4096×4096), which is computationally expensive. An alternative, or a condensed version of the SVD, had been demonstrated by

Sirovich (1987), in which the matrix size can be reduced to ($N_s \times N_s$) without compromising accuracy of the results. Using the condensed version (snapshot method) instead of R, the matrix **C** is generated such that:

$$\mathbf{C} = \frac{1}{N_s}\left(\mathbf{A}^{\mathrm{T}}\mathbf{A}\right) \tag{4.54}$$

Performing an SVD on **C** now produces the coefficients κ as eigenvectors. Linear combination of the k^{th} column of eigenvectors with the fluctuation matrix then yields the k^{th} spatial POD mode:

$$\varphi_k(\mathbf{x}) = \sum_{i=1}^{N_{samp}} \kappa_k(t_i) A(\mathbf{x}, t_i) \tag{4.55}$$

Thus N_s, rather than *m*, POD modes are obtained. In Eq. 4.53, the singular values on the diagonal of the **Σ** matrix are the square roots of the eigenvalues, λ, of the **A** matrix. These eignenvalues can be used to indicate the energy contained within each mode. Thus, the cumulative contribution of energy by each mode, E_k, can be defined as,

$$E_k = \frac{\sum_{i=1}^{k} \lambda_i}{\sum_{i=1}^{N_{buf}} \lambda_i} \tag{4.56}$$

The cumulative distribution of the eigenvalues gives a representation of the turbulent kinetic energy contained across the POD modes. Robinson (2009) observed that the first few lower modes account for almost half of the eigenvalues, which is also the case with the current work (see Section 5.3.4), hence around only 500 samples are needed for a converged solution on the lower modes. This greatly reduced computational time and memory requirements, and it also allows low-speed datasets with lower N_s (N_s~1000) to be used.

4.8 Chapter summary

This chapter starts with a description of the data reduction of single-point statistics. This is followed by a brief review of the scales of turbulence, which is discussed with an emphasis on the measurement's spatial resolution. It was shown that the PIV interrogation cell size was much larger than the Kolmogorov lengthscale; thus the measurement was not able to capture the finest-scale turbulence. In addition, since the Batchelor scale relates to the Kolmogorov scale by the power of -3/4, the PLIF measurements are also unable to resolve the smallest scales of scalar dissipation. But the measurements are generally able to capture large-scale turbulent motions in the energy-containing range, as demonstrated by the spatially distributed errors, which show that the highest errors in both velocity (~20%) and scalar (~2%) are found near the outer radius of the central jet, just downstream of the exit plane. In the rest of the FoV, velocity errors average to around ~7% while scalar errors are about ~0.8%. To control the error associated with the spatial averaging of scalar, an adaptive averaging scheme is developed so that the error associated with additional filtering (of row single-pixel concentrations) is limited to within 0.5% or lower. The method is designed on the basis of a well-established correction technique for spatial averaging of fluctuating velocity, so its application to fluctuating scalar has also been validated on i) synthetic data, ii) current experimental data, and iii) experimental data available in literature. Because the velocity errors are much larger than the scalar ones, it is proposed that the former are used to correct for the scalar flux profiles. A detailed statistical convergence study has been presented, with the experimental data showing errors of 5% to 10% for a typical range of velocity-scalar correlation coefficients in regions that are important to scalar mixing. With all 3 velocity components available, it is possible to reduce the time-mean static pressure field from Reynolds averaged momentum equations with several assumptions, which have been discussed. Finally, the last section introduces two well-established techniques for the identification of coherent structures: conditional averaging and POD.

Chapter 5

5. RESULTS: NON-PREMIXED TEST

The ability to measure 2C or 3C velocity simultaneously with scalar allows for the visualisation of vortex-scalar dynamics. Inspection of the shear stresses and velocity-scalar covariance also provide additional understanding of the flow and mixing fields induced by the Turbomeca fuel injector.

Section 5.1 focuses on the time mean flowfield characteristics, including profiles of all 3 mean and RMS velocities. A combination of x-r and r-θ plane contours of instantaneous through-plane velocities will be presented to show that the coherent structures are three dimensional. Statistics such as Reynolds stresses, TKE, and static pressures are also presented to highlight the regions that are influenced by the coherent structures.

Section 5.2 starts with a discussion of the time-mean and RMS scalar data, including a comparison with the previous data for the purpose of validation. This is followed by more detailed visualisation and analyses of the instantaneous and Reynolds decomposed scalar fields, providing additional insights into vortex-scalar interaction. All three turbulent scalar fluxes are also provided in this section, in which the discussion focuses on explaining how the net direction of turbulent transport of scalar affects the sign of the time-mean data.

Section 5.3 starts by showing pdf's of 3-C velocities and scalar, followed by an extensive study of their power spectral densities in different locations. Contours of their maximum amplitudes have also been plotted to identify the regions which are affected by the coherent structures. Finally, techniques such as conditional averaging and POD have also been applied to demonstrate the most energetic fluctuating velocity and scalar fields.

Section 5.4 discusses how the LES predictions of Dianat (2007) can be used to improve the understanding of turbulent mixing. In addition, validations of scalar

mixing via direct comparisons of velocity, scalar, and scalar flux profiles are also provided in this section.

5.1 Time mean flowfield characteristics

Section 5.1.1 focuses on the time averaged flow field characteristics, with emphasis on describing the mean and rms velocity fields. Results from spatially-resolved 2D-2C data in the x-r plane and those from 2D-3C data are included for illustration and discussion. The validity of the results being presented is discussed in Section 5.1.2 via direct comparison with other data. Section 5.1.3 looks at Reynolds stresses and turbulent kinetic energy, which provides a good illustration of the localised regions of high turbulence. Using the pressure reduction technique described in Section 4.6, the time-averaged static pressure field has been calculated and is discussed in Section 5.1.4.

5.1.1 Time-mean flow field characteristics

Fig. 5.1 shows the time-mean axial velocity contour with the stream traces superimposed. The central jet is directly injected into the cylindrical expansion chamber, where all measurements are made. The axial station of time-mean stagnation between the forward flowing jet and reverse flow is near x/D_s=1. The swirl stream, on the other hand, penetrates further downstream and impinges the wall near x/D_s = 1.2, following which a wall-jet can be seen that extends all the way down to x/D_s = 4. The flow then exits the cylindrical chamber at x/D_s = 4.25 into the annulus before reaching the exhaust manifold. The region that is bounded within the swirl stream is commonly referred to as the ‘swirl cone’ which has a deflection angle of 23°, as indicated in Fig. 6.1. From the contour colours, which can be seen more clearly in Fig 5.2, strong velocity difference exists between the forward flowing swirl jet and the CTRZ. Between the outer swirl cone and the corner of the cylindrical expansion chamber lies a well-defined corner recirculation zone (CRZ), whose axial length is defined by the reattachment location of the outer swirl shear layer on the wall of the expansion chamber (around x/D_s=1.2).

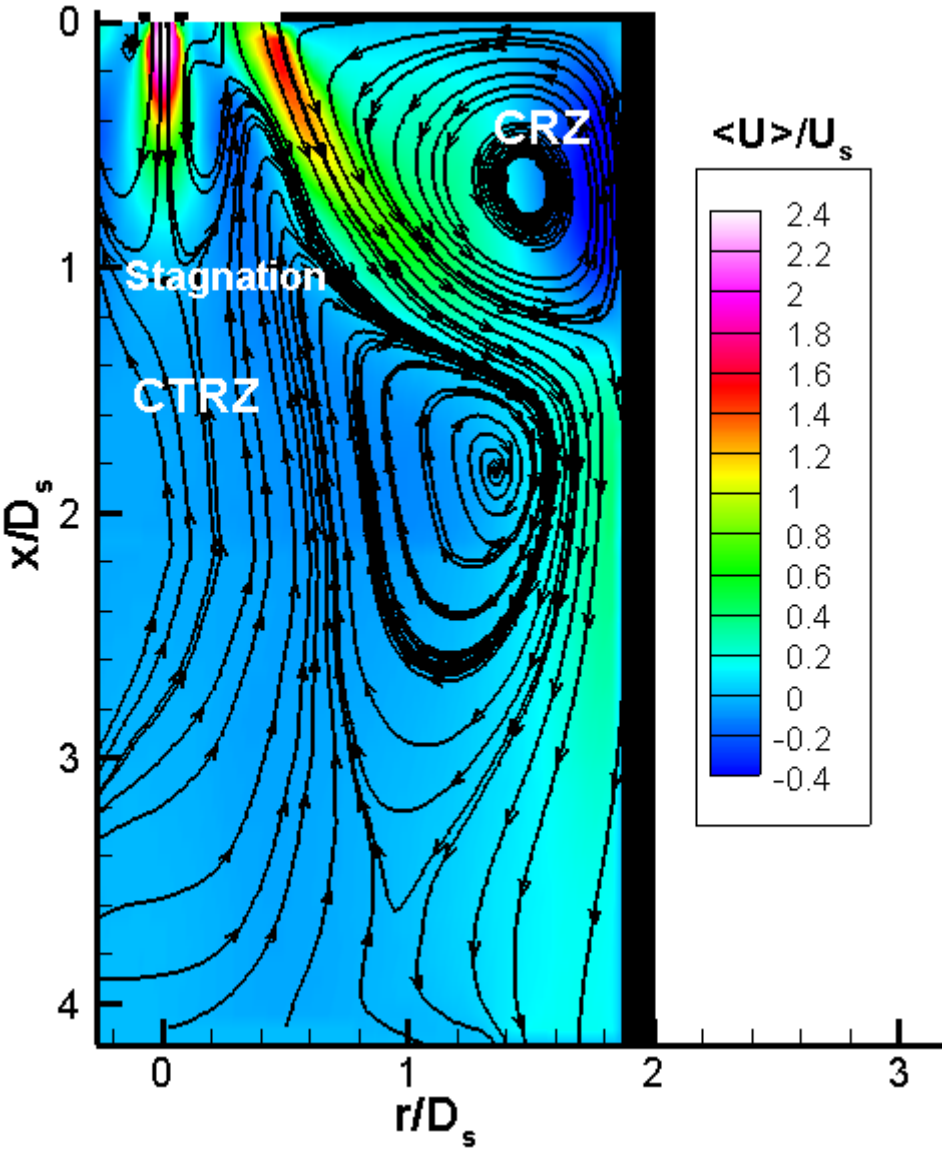

Fig. 5.1 Stream traces on mean axial velocity contour

Fig. 5.2 zooms into the near-field of the swirler exit bounded by r/D_s = 0 to r/D_s=1 and x/Ds=0 to x/D_s=1. The time-mean stream traces plotted near the inner wall of the swirl passage clearly indicate backflow that is confined between the central jet and the swirl stream. Another feature that can be seen is that the central jet's forward penetration quickly diminishes in strength: at x/D_s=0.2, around 90% of the exit axial velocity is maintained, but it quickly reduces to around 50% at x/D_s=0.6. The commonly used references to different flow features and locations are defined in Fig. 5.2. In general, there are three shear layers: jet shear, inner swirl shear, and outer swirl shear; the locations of these shear layers can be time-dependent, the indications of these locations shown in Fig. 5.2 are arbitrarily drawn for the purpose of general reference. The CTRZ is sandwiched by the inner swirl shear and the central jet spread.

Near the inner wall of the swirl passage, a region characterised by time-mean backflow can be seen.

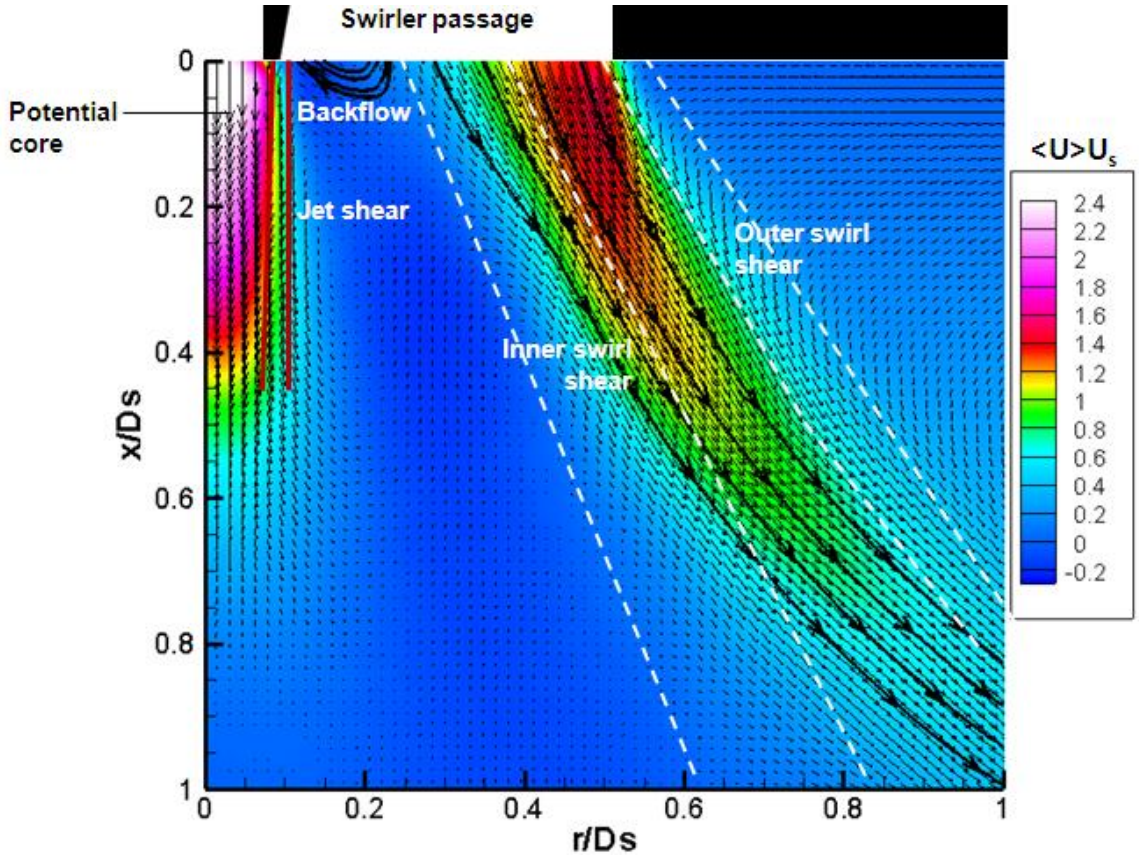

Fig. 5.2 Axial velocity contour near-field of the fuel injector exit

Time-mean rotational symmetry is an important flow feature that cannot be evaluated with one or two slices of x-r plane data alone. Hence, the 3-C data taken using SPIV in the r-θ plane at x/D_s=0.02 has been selected for demonstration in Fig. 5.3, which shows good circumferential uniformity for all three velocity components, with a range of deviation that does not exceed 5% in general. Fig. 5.3(a) shows a 'ring' of negative axial velocity bounded within r/D_s~0.1 and r/D_s~0.15; this is consistent with the location of the stream traces shown in Fig. 5.2 that indicate back flow into the swirl passage. Fig. 5.3(b) also shows a 'ring' of negative radial velocity from r/D_s~0.1 and r/D_s~0.2; this likely indicates that flow separation occurs in the swirl passage. The positive <W> in Fig. 5.3(c) means that the direction of the swirling flow is counter-clockwise. Fig. 5.3(c) also confirms that the core of the swirling flow matches well with the geometric centre.

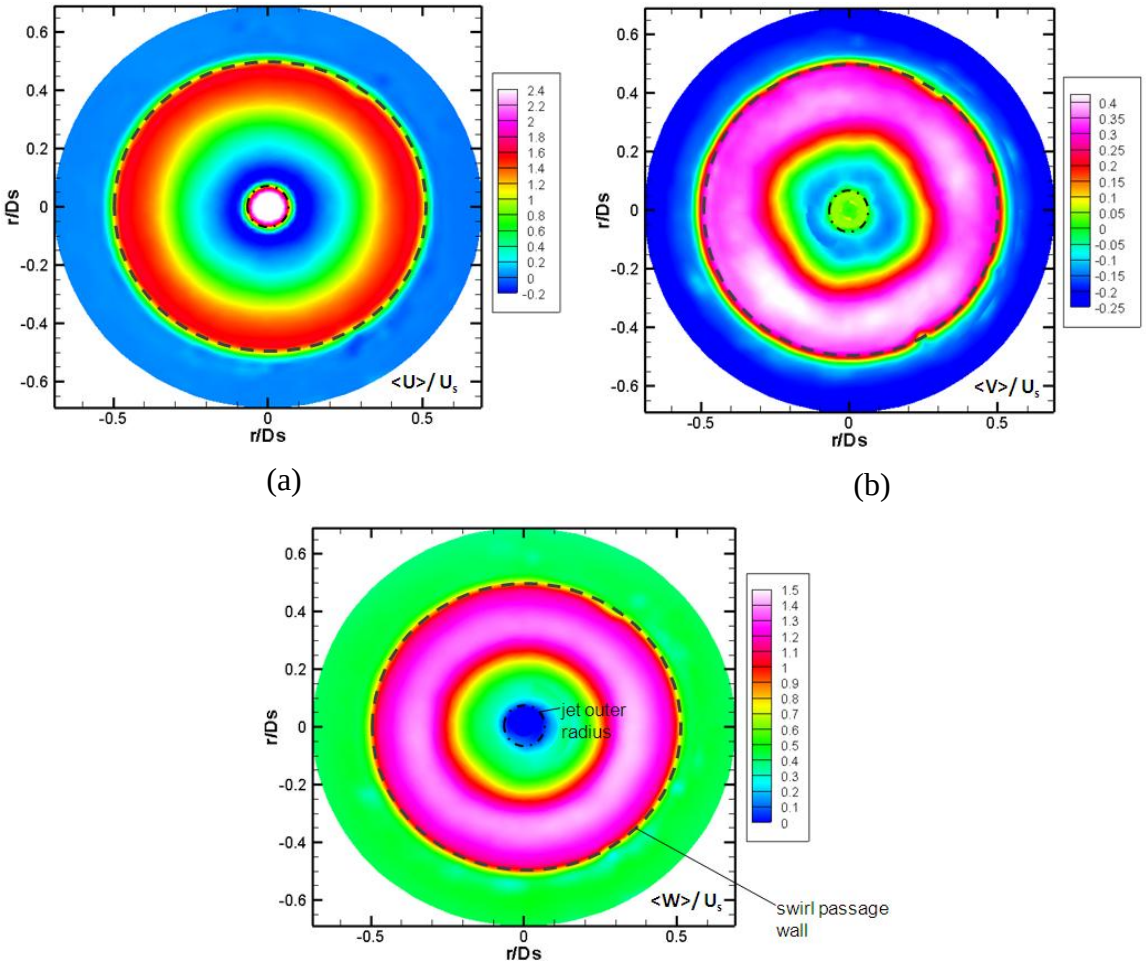

Fig. 5.3 Time-mean velocity contours at x/Ds=0.02: (a) axial velocity, (b) radial velocity, (c) tangential velocity

Because previous studies by Midgley (2005) and Wegner (2007) have shown that turbulence is strongest in the near-field, a zoomed-in FoV ($x/D_s < 1.2$) has been selected to illustrate the regions of high turbulence intensity. Fig. 5.4 shows the RMS contours of all 3-component velocities from an x-r plane SPIV dataset. The RMS axial velocity contour shown in Fig. 5.4(a) shows two peak regions: the first one is in the inner swirl shear layer while the second one is in central jet shear layer. The RMS radial velocity contour has a similar distribution of peak values, although much lower in the jet shear. The RMS tangential velocity contour is again similarly distributed. With the RMS axial and the RMS tangential components being around 20% and 30% higher than the RMS radial component, the jet shear is characterised with stronger fluctuations in the streamwise and circumferential directions. The rise in turbulence intensities in all three velocity components in the inner swirl shear layer is due to the

existence of coherent structures that travel along helical paths. Iso-surfaces based on vorticity that show the helical paths can be found in Wegner et al (2007) and Cheng et al (2012).

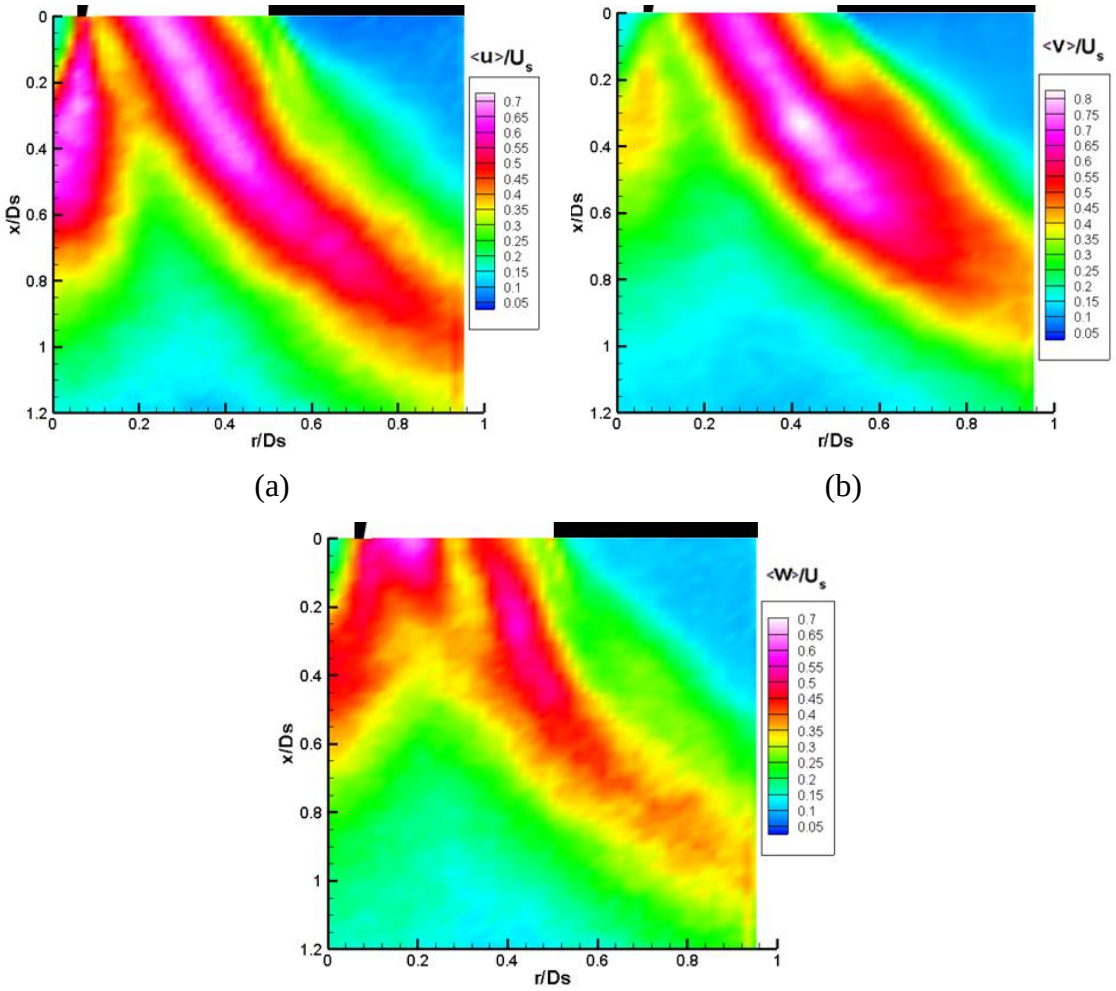

Fig. 5.4 Contours of RMS (a) axial, (b) radial, (c) tangential velocities

5.1.2 Time-mean velocity profiles

Profiles of the three time-mean velocity components at four axial stations (x/D_s = 0.02, 0.27, 0.53, 10.6) are shown in Fig. 5.5. Data collected in the current project using SPIV are represented by coloured solid lines while Midgley's 2C-PIV data (Midgley, 2005) is represented by dotted symbols. Repeatability and accuracy of the measurements can be demonstrated by the excellent agreement between the two datasets.

Fig. 5.5 quantifies the previous observation pointing to the rapid decay of the central jet: the axial velocity along the centreline at x/D_s=0.53 has decayed by 70% of that of the peak value at the exit plane. At x/D_s=1.06, zero axial velocity is seen, indicating this is a region of free stagnation that is characterised with forward flowing central jet and backward flowing CTRZ. The velocity profile of the swirl stream path at the exit plane is not uniform as that of the central jet; a bias towards the peak value of $<U>/U_{x,s}$ = 1.5 exists at r/D_s=0.47, near the outer radius of the swirl passage. Towards the inner radius of the swirl passage (r/D_s~0.09), the axial velocity decreases quite sharply. The fact that the axial velocity at x/D_s=0.02 turns negative in the range $0.09<r/D_s<0.17$ is consistent with the stream traces that show backflow into the fuel injector, as shown in Fig 5.2. Along the streamwise or axial direction (x/D_s=0.02-1.06), flow reversal, indicated by negative axial velocity, expands radially, but the peak magnitude of negative axial velocity decreases from x/D_s=0.53 to x/D_s=1.06. These observations indicate radial expansion of the swirl stream to form a swirl cone, within which reversed flow (CTRZ) dominate the mean bulk flow (also shown in Fig. 5.1). In addition, as the swirl expands radially outward and becomes more spread out, the streamwise momentum is also reduced; this is because as the area of swirl jet expands, velocity must decrease to maintain a constant mass flow rate.

As shown in Fig. 5.6, at x/D_s=0.02, a change in sign of the radial velocity is seen at r/Ds~0.07, which is in the vicinity of the central jet's outer radius. The sign remains negative till r/D_s=0.2, as opposed to the swirl stream's bulk radial outward motion. The radial inward flow in this region is evidence of flow separation inside the swirl passage. The locations of the sign changes are also somewhat consistent with those of the axial velocity, suggesting that they are due to the backflow marked in Fig. 5.2. Unlike the peak axial velocity, the radial velocity in the swirl stream shown in Fig. 5.6 actually increases as the swirl cone expands from x/D_s=0.02 to x/D_s=0.53. The increase in radial velocity stops near x/D_s=1, where the influence of the wall becomes more pronounced.

The tangential velocity profiles of the swirl stream shown in Fig. 5.7 follow a decreasing trend in the mean swirl stream path, similar to the axial velocity profiles. The decay of the tangential velocity in the axial direction is a signature of vortex breakdown in a swirling flow, resulting in an aerodynamic blockage. The swirling

flow generates a natural radial pressure gradient (dp/dr) due to the term W^2/r, where W is the tangential velocity. As W decays in the axial direction, dp/dr is also progressively reduced, meaning a lower radial pressure gradient is required to balance the decaying tangential velocity along the axial direction. This in turn sets up a negative dp/dx; if the axial velocity couples with the decaying tangential velocity downstream, as is the case here, momentum carried by the weakening forward axial flow would not be strong enough to overcome the adverse axial pressure gradient, finally resulting in a vortex breakdown and the formation of a recirculation bubble. In addition, the tangential velocity profile at the exit plane is of a Rankine shape, with a peak at r/D_s~0.35, which features a region of forced (rotational) vortex within the swirl cone and a region of free (irrotational) vortex outside of it. This combination is particularly susceptible to the formation of a precessing vortex core (Syred, 2006), although Midgley (2005) has shown that the PVC is damped by the central jet. A comparison of the with-jet and central jet flow fields is presented in Section 5.1.

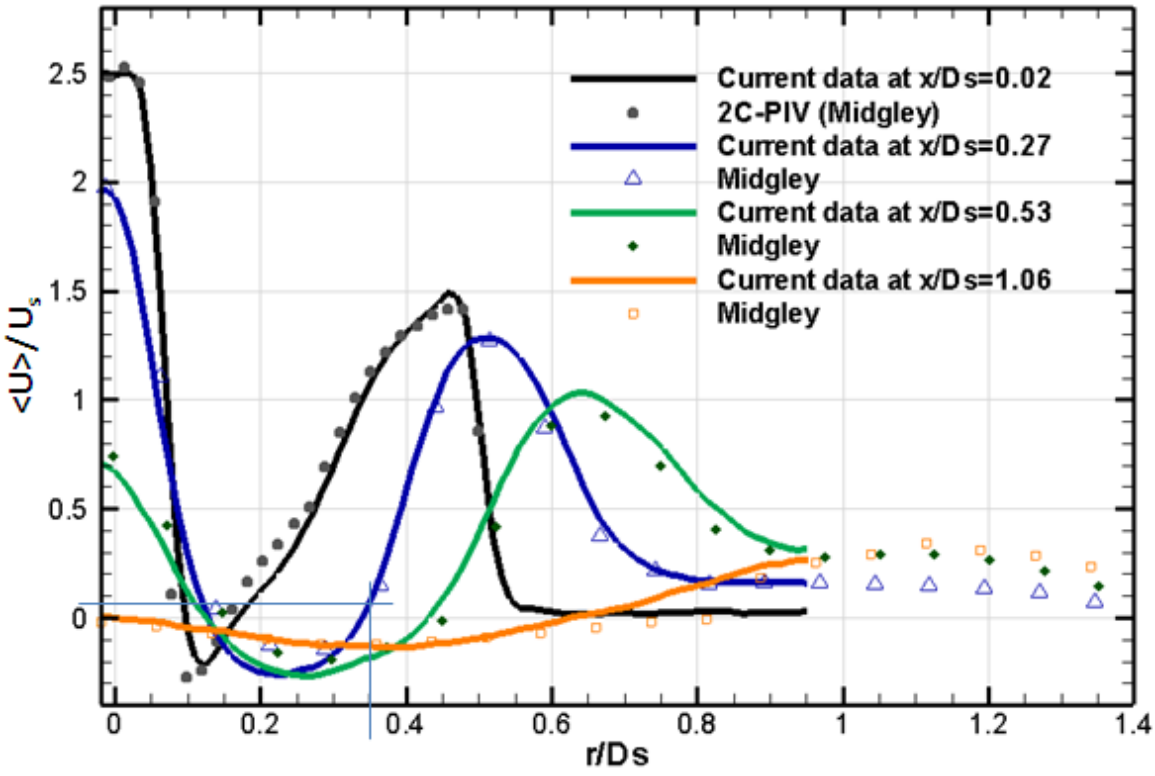

Fig. 5.5 Mean axial velocity profiles at 4 axial stations

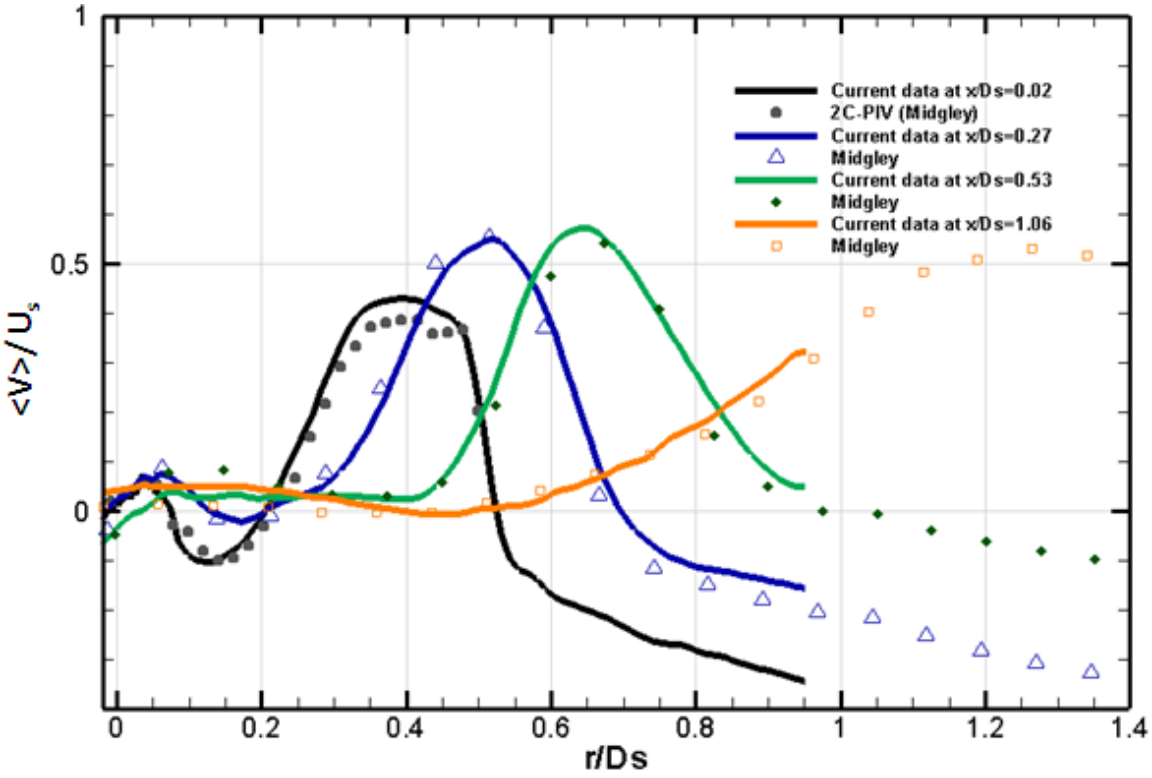

Fig. 5.6 Mean radial velocity profiles at 4 axial stations

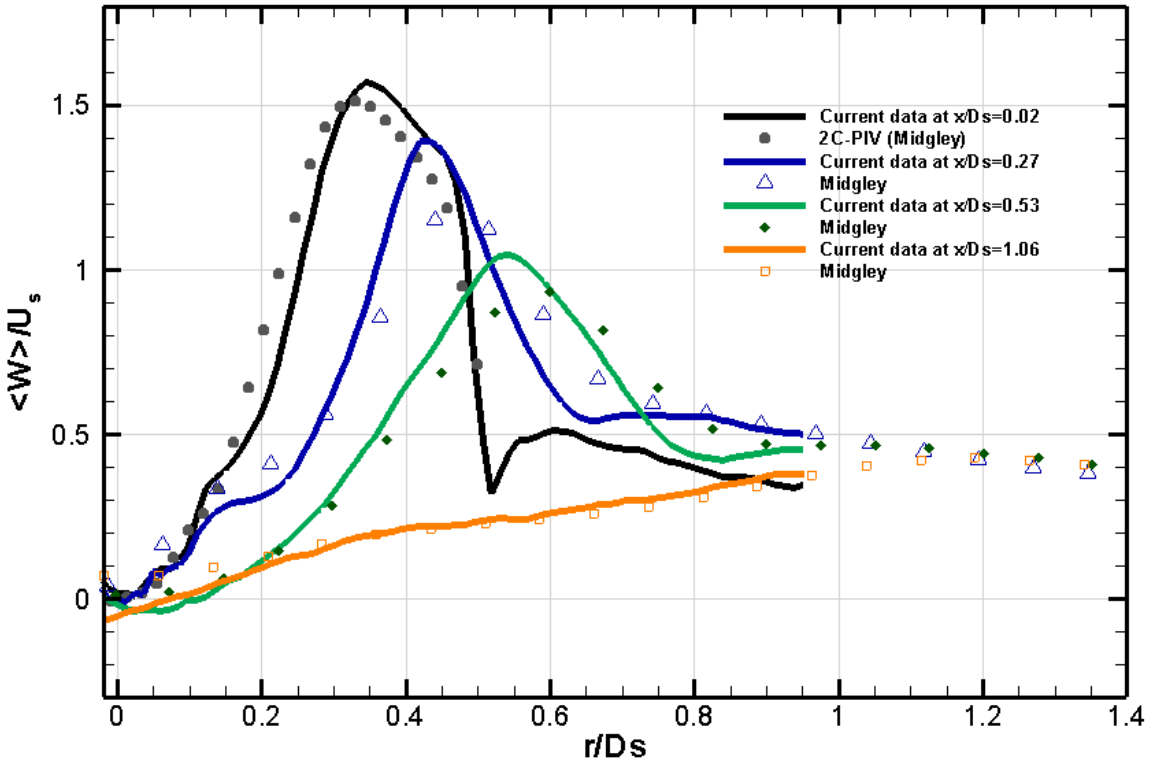

Fig. 5.7 Mean tangential velocity profiles at 4 axial stations

The RMS axial, radial, and tangential velocities are shown in Fig. 5.8, Fig. 5.9, and Fig. 5.10 respectively. Again there is good agreement between the two datasets in terms of the locations of the peaks and shapes of the curves. The profiles of both datasets have been corrected using the Spencer and Hollis method (2005) to account for the effect of sub-grid filtering in PIV. The maximum range of correction is the jet shear of around 10% to 15% (recall that <W> has not been corrected due to difficulties associated with the computation ${}^3L_{33}$, as discussed in Section 4.4.4).

The RMS axial velocity at the exit plane, as shown in Fig. 5.8, exhibits two distinct peaks with similar magnitude: the first one is located at the outer radius of the central jet (x/D_s~0.07) while the second one is located in the inner shear layer of the swirl stream (see dashed line in Fig. 5.2). The first peak is consistently picked up by all experimental datasets and the LES prediction (see Section 5.4). The reason for the undershoot in Midgly's data is unclear even though a higher spatial resolution was employed (Δx_{PIV}=0.64mm in Midgley's data versus dx_{PIV}=1.20 mm in the current data). The radial locations of the second peaks are consistently found within the inner shear of the swirl cone, and its magnitude decreases with downstream distance from the exit plane. The RMS radial velocity at the exit plane also exhibits a first peak near the outer radius of the central jet, though with a magnitude that is just half of the $<u>/U_s$. This is indicative of a localised turbulence structure near the exit. The locations of the second peaks are also quite similar to those of the axial components, pointing to strong coupling of radial and axial components in the inner swirl shear layer. Unlike the RMS radial and axial components at the exit plane, the RMS tangential velocity actually exhibits three peaks. The first peak is located near x/D_s=0.18, where stream traces indicate a backflow. The second peak is located in the inner swirl shear layer while the third peak is located just outside the swirl passage's outer radius. The second and the third peak are not seen in Midgley's data; a possible explanation for this has to do with the optical distance limitation caused by the downstream blockage, resulting in a rather poor spatial resolution (Δx_{PIV}=4.8mm). SPIV in the current project allowed the cameras to be brought closer to the measurement plane, thereby significantly improving the spatial resolution (Δx_{PIV}=1.4mm). Again, the error associated with this grid size, $Err(\Delta x_{PIV}/{}^3L_{33})$ could not be evaluated due to the difficulty in computing ${}^3L_{33}$.

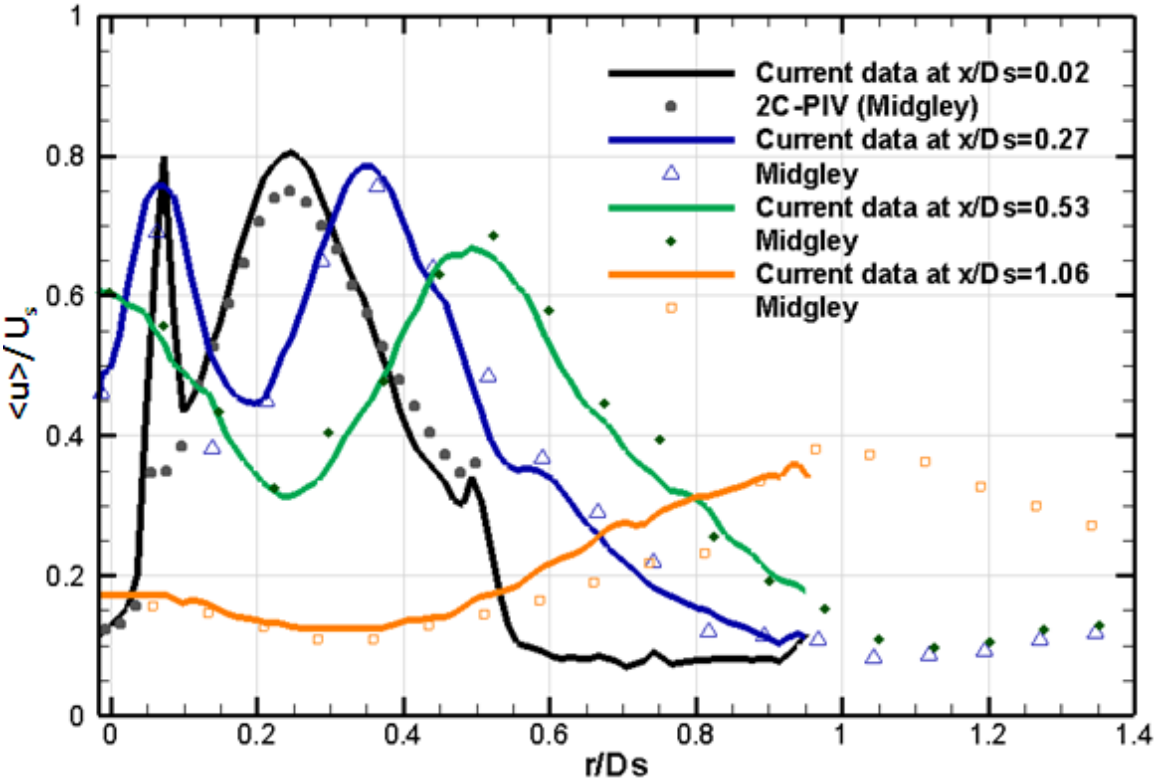

Fig. 5.8 RMS axial velocity profiles at 4 axial stations

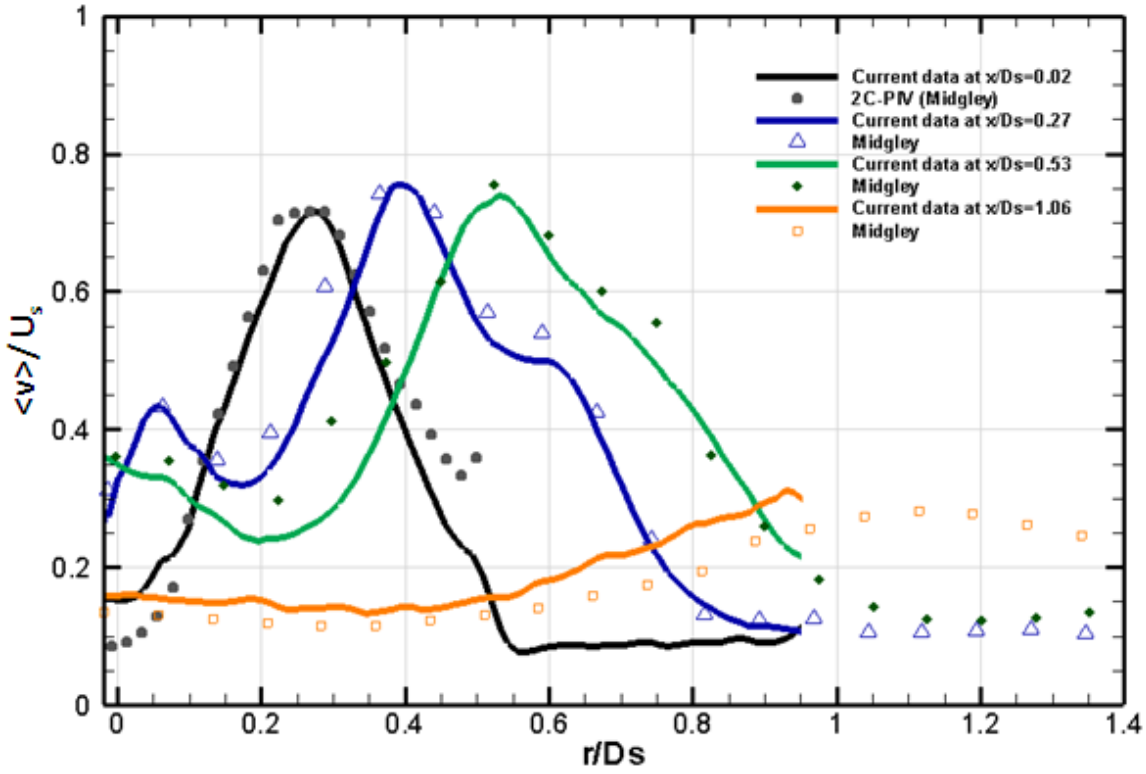

Fig. 5.9 RMS radial velocity profiles at 4 axial stations

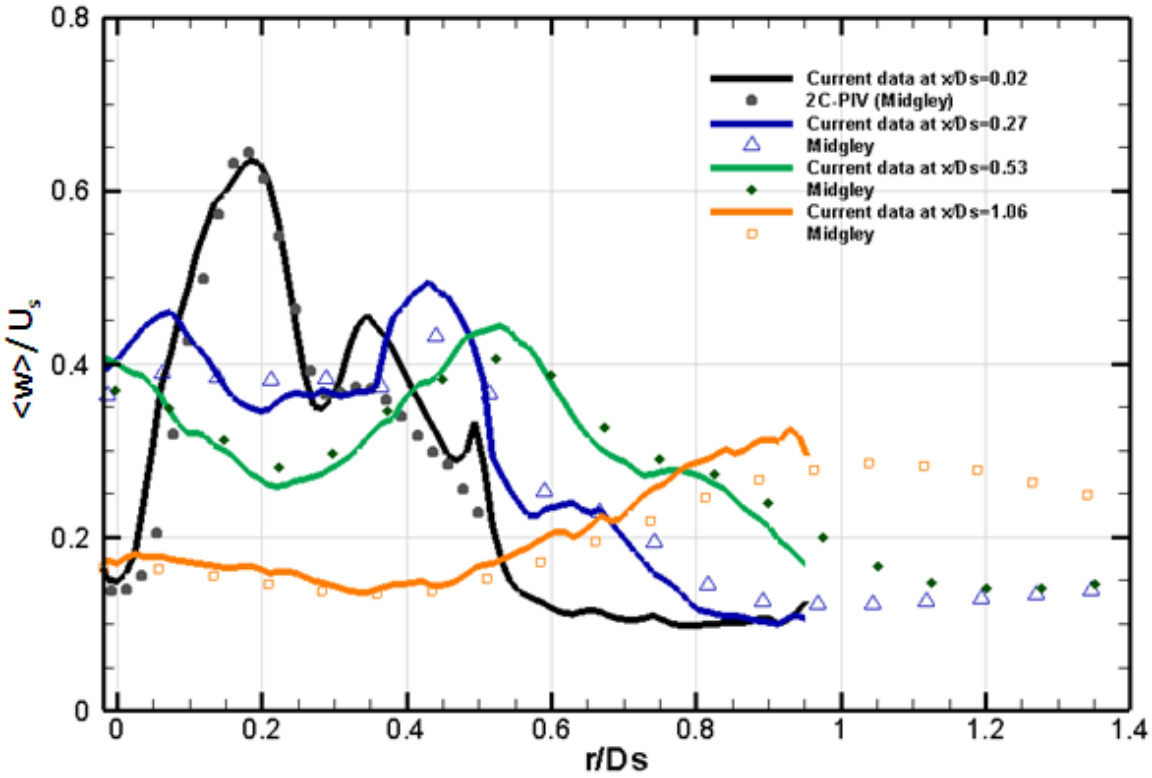

Fig. 5.10 RMS tangential velocity profiles at 4 axial stations

5.1.3 Shear stresses and turbulent kinetic energy

The RMS 3C velocities shown in Figures 5.8 to 5.10 indicate a large degree of anisotropy in the near-field, at $x/D_s<1$. However, from the geometric centreline to r/D_s=06 at x/D_s=1.06, all three components have decayed to roughly similar levels (isotropy is restored). The shear stresses exhibit a similar behaviour, as shown in Fig. 5.11 (with mean vector field superimposed). It should be noted that these shear stresses have not been corrected for sub-grid filtering, hence their accuracy is highly dependent on the grid-size to length scale ratio, $\Delta x_{PIV}/^{i}L_{ii}$, the resulting error of which varies spatially.

Fig. 5.11(a) shows a strip of high negative axial-radial velocity correlation with the peak value at r/D_s~0.35 at the swirler exit, or inlet of the measurement plane; it expands radially outward and diminishes in strength downstream until it reaches zero around x/D_s=0.9. The most energetic coherent structure in the flow field is certainly contained in the inner swirl shear layer because |<uv>| in this region is significantly higher than those found in the jet shear and the outer swirl shear layer. As

demonstrated in Fig. 5.11(a), the minus sign is evidently caused by the vortices, which lead to bursts of flow reversals (-) in the inner swirl shear and their coupling with the radial outward (+) fluctuation. These vortices also result in a coupling between axial and radial velocity components near the outer swirl shear, as will be explained in Section 5.2.3, resulting in the rise of <uv> there. The rise in <uv> in the jet shear is likely due to the varying jet penetration strengths and the jet shear vortices, which draw the central jet away with increased radial (+) and axial (+) momentums, as illustrated by the red arrows shown in Fig. 5.15(a). Whether the much-smaller jet shear vortices are in phase with the inner swirl shear coherent structures is to be discussed in Section 5.3.2. In the remaining parts of the FoV, <uv> is negligible.

Somewhat different than <uv>, rises in <uw> are found in only two regions: namely jet shear and inner swirl shear. Interpretation of <uw> is slightly complicated: following the right-hand cylindrical sign convention, positive tangential velocity in the swirl stream would be defined as going out of the page in Fig. 5.11(b). Hence, the rise in <uw> between the central jet and swirl stream is certainly due to coupling between reversed flows (-) and into-the-page (+) circumferential motion, simultaneous surges (due to the vortices) in these two components in this region is demonstrated in Fig. 5.15(b). A rise in <uw> is also seen in the swirl stream that extends to about x/D_s~0.4, this is also due to the bursts of tangential momentum (+) carried by the vortices, as well as its coupling with the surges in instantaneous axial velocity (+); these are again supported by the example shown in Fig. 5.15. The rise in <uw> in the jet shear indicates that the jet shear vortices are also three-dimensional, as rises in into-page tangential velocity (-) are coupled with rises in forward axial velocity (+).

Again, rise in <vw> in the jet shear is seen in Fig. 5.11(c) with roughly similar magnitudes as those of <uw>. As shown in Fig. 5.3 $<W>/U_s$ in the jet shear is positive but has a very low magnitude, negative <vw> means that coupling exists between in-to-page flow (-W) and radial expansion of the central jet (+V). The +<vw> along the inner swirl shear is likely a result of co-increases in V and W, which is a result of the passage of a clockwise vortex, as shown in Fig. 5.15(b). In other regions, the magnitudes of <vw> are much lower than those of <uw>.

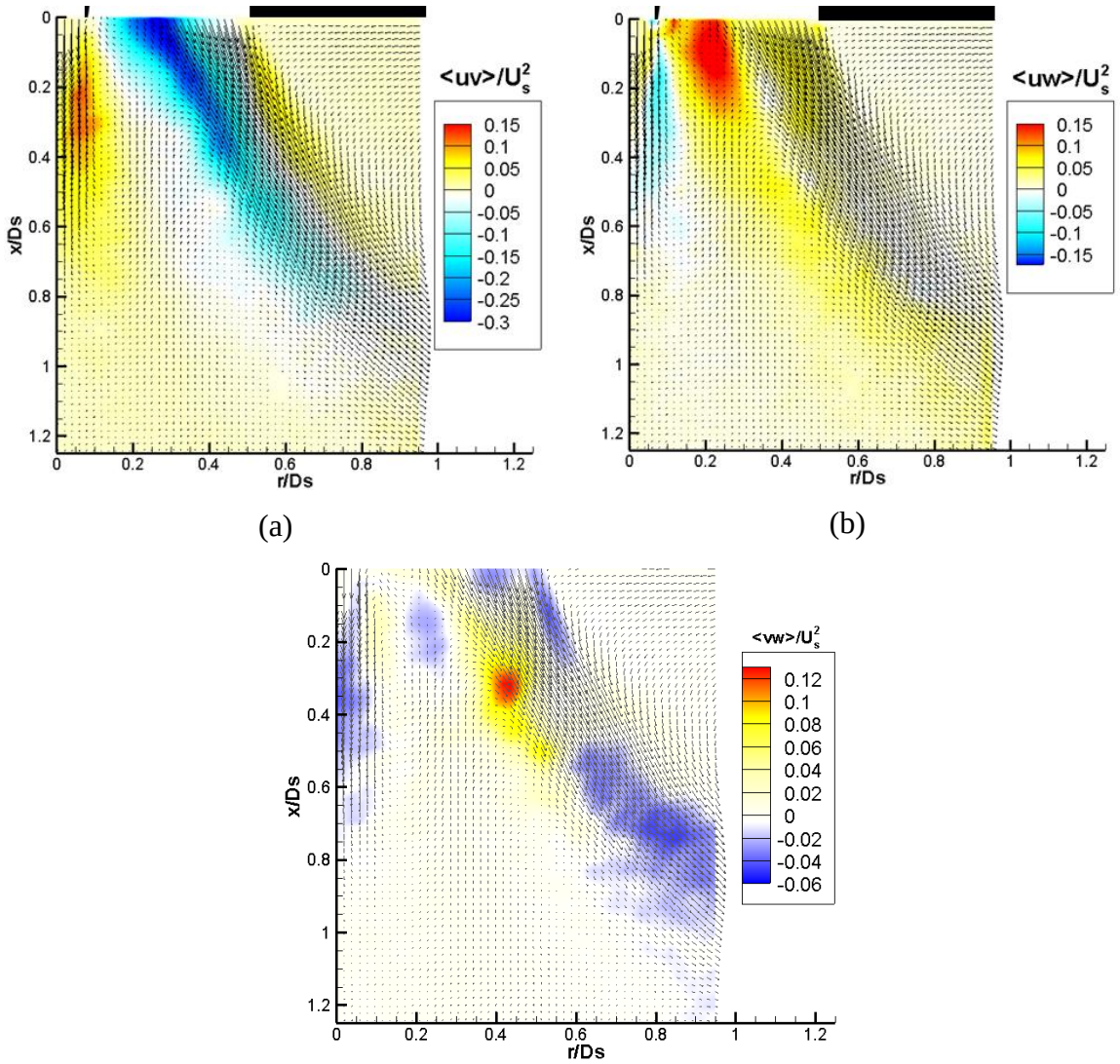

Fig. 5.11 Shear stresses: (a) axial-radial, and (b) axial-tangential

Similar to the shear stresses, regions of high TKE, shown in Fig. 5.12, are limited to the central jet shear and the inner swirl shear layer. Outside these regions, the TKE is close to zero. It is worth noting that turbulence production by the CTRZ, which generates shear flows in the central jet and inner swirl stream interfaces, cannot explain the fact that TKE in the former is only half of that in the latter. Hence, this confirms the presence of a discrete turbulence structure that follows a path along the inner swirl shear layer.

Comparisons of the TKE profiles with Midgley's 2C-PIV data at x/D_s=0.02 and x/D_s=0.27 are shown on the right of Fig. 5.12. While the general shapes agree quite well, the locations and magnitudes of the peaks differ somewhat. The discrepancy can be attributed to the fact that the out-of-plane component was not available in

Midgley's 2C-PIV data; to make up for this, the author used one of the two in-plane components to represent the missing out-of-plane one (e.g. using axial component to represent the missing tangential one in an x-r dataset).

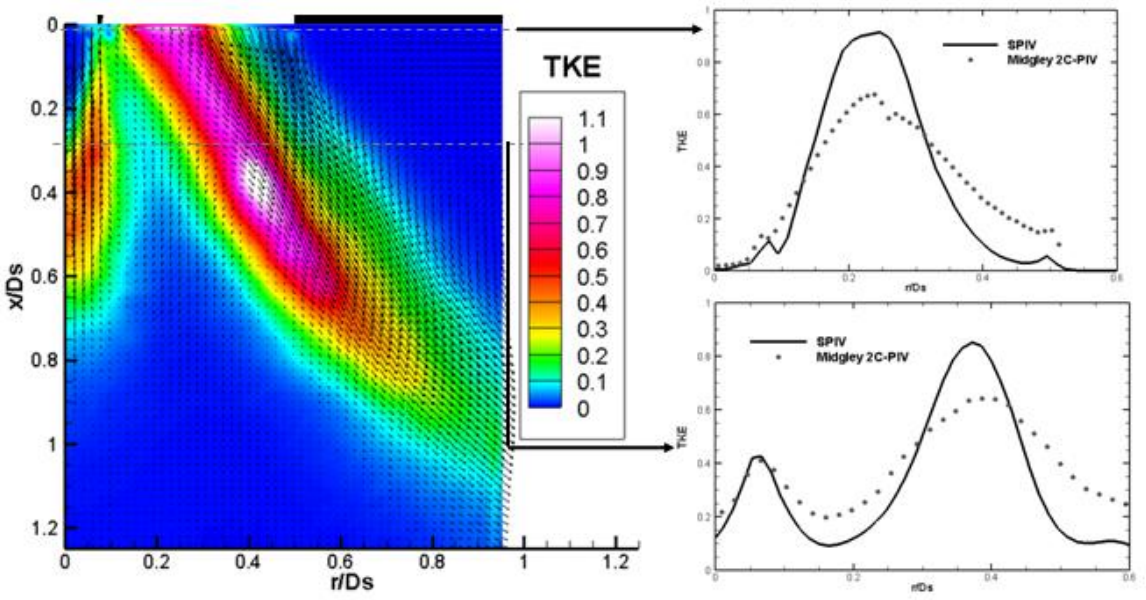

Fig. 5.12 Turbulent kinetic energy

5.1.4 Time mean pressure field

Based on the TKE contour shown in Fig. 5.12, it has been argued that there exists a discrete turbulence event in the vicinity of the inner swirl shear. The pressure reduction method developed by VVB (2008) has been applied to determine if this turbulence event results in a distinct signature in the pressure field. For a simple axially-fed swirling flow field with a swirl number of 0.74[6], the authors showed that when the time-mean static pressure, $<P_{st}>$, is decomposed into a swirl-induced component, $<P_{sw}>$, and a non-swirl component, P_{ns}, the former dominates the latter in terms of the relative contribution to $<P_{st}>$. The same method was applied here and the three pressure fields are shown in Fig. 5.13. It should be noted the computation has been performed in the radial range of $0<r/D_s<1.05$, taken from a measurement FoV bounded within r/D_s=-0.2:1.05 and x/D_s=0:1.25, and the remaining part of the FoV (r/D_s=-0.2:0) was simply curtailed. Then the computed pressure field was simply flipped about the centreline, assuming axis-symmetry, to enhance visualisation by

[6] The swirl number of the current fuel injector flow is identical.

allowing the left side of the FoV to be superimposed with time-mean velocity stream traces.

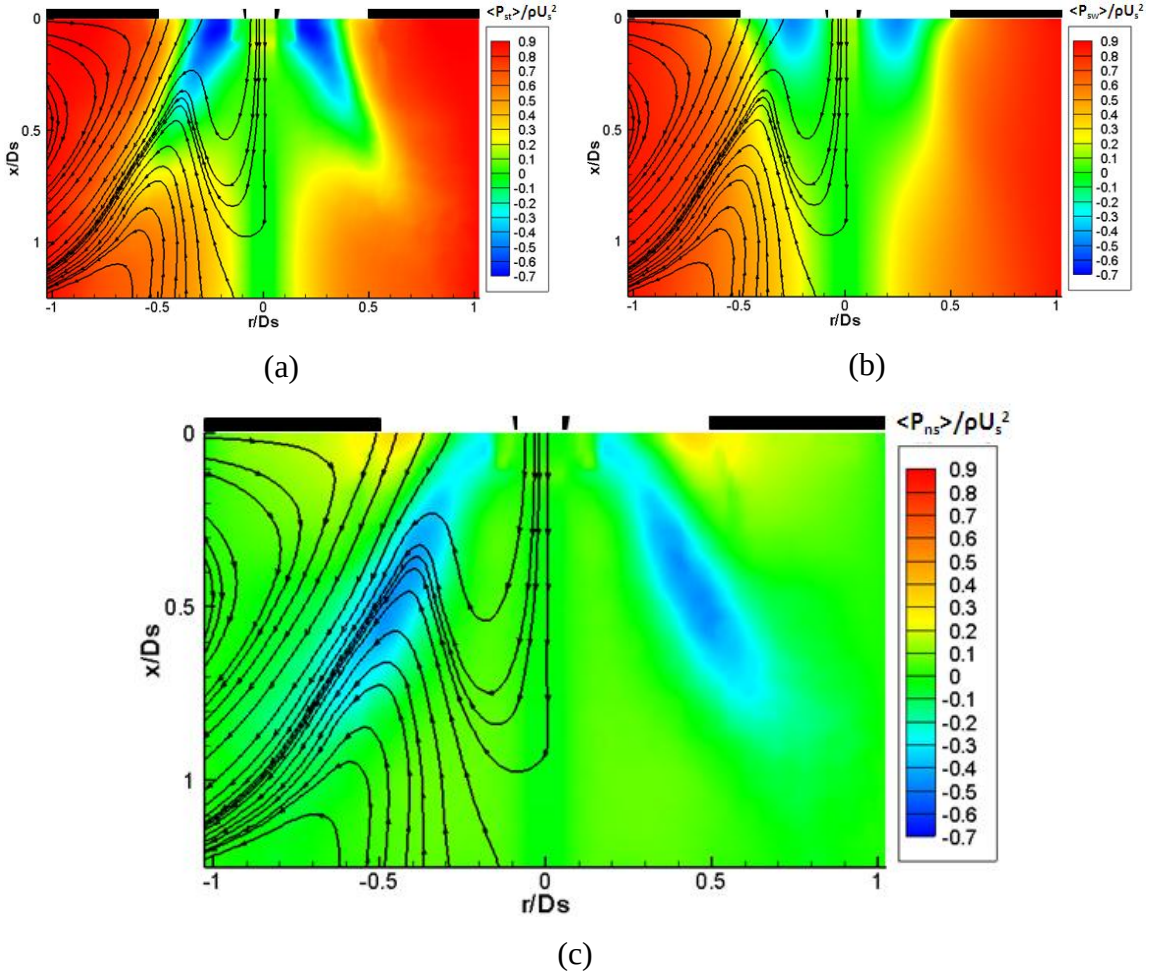

Fig. 5.13 Contours of (a) static pressure, (b) swirl-induced pressure, and (c) non-swirl-induced pressure

As shown in Fig. 5.13(a), the largest static pressure gradient is located in the inner swirl shear layer downstream of the swirler passage. The deflection angle of this region of sub pressure (from dark blue in the exit to green at $x/D_s=0.5$) is similar to that of the swirl stream (~23°). Interestingly, this is not a result of the swirling flow field, as Fig. 5.13(b) shows that the centrifugal force has little contribution to it. Instead, when removing the effect of the swirl-induced pressure from the static pressure ($\langle P_{ns} \rangle = \langle P_{static} \rangle - \langle P_{swirl} \rangle$), an elongated strip of sub pressure along the inner swirl shear layer is revealed. The location of the sub pressure region coincides well with the region of maximum TKE; in other words, sub $\langle P_{ns} \rangle$ in the inner shear swirl shear is evidently a time-mean footprint of the low-pressure centres of the helical vortices.

The dynamic pressure <P_{dm}> has also been calculated and added to <P_{st}> to provide the total pressure (<P_{tot}>=<P_{dm}>+<P_{st}>). As shown in Fig. 5.14, the total pressure is strongest in the very near field in the central jet and the swirl stream. Negative < P_{tot} > are set up in between the inner swirl shear and the jet, as well as at r/D_s<~0.25 about the centreline; which are regions characterised with reverse flows.

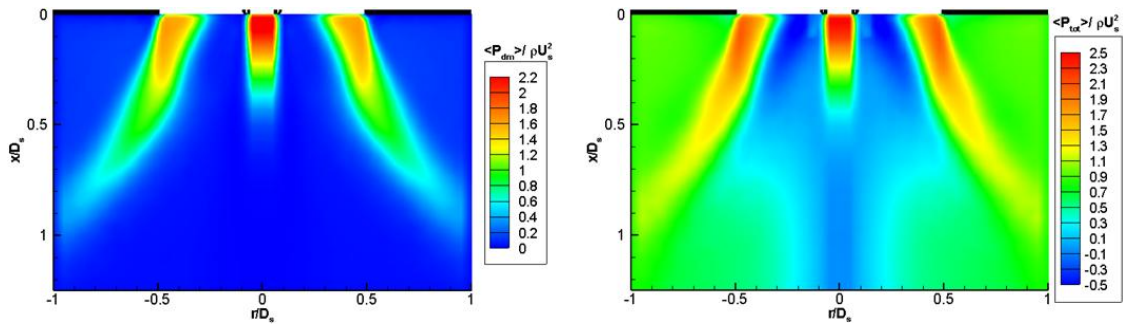

(a) (b)

Fig. 5.14 Contours of (a) dynamic pressure and (b) total pressure

5.1.5 Instantaneous flow field visualisation

Fig. 5.15(a) shows the contour of axial component and Fig. 5.15(b) shows that of the tangential component, the former is superimposed with arbitrarily plotted stream traces that identify the vortices and the latter is superimposed with mean axial-radial velocity vectors. The vortex just downstream of the fuel injector exit not only induces a strong reverse flow that extends into the inner half of the swirler passage, but it also causes surges in axial velocities in the swirl stream (U/Us≥1.8, much higher than <U>/Us~1.5). In addition to this vortex, the second vortex indicated by the stream traces in the inner swirl shear further downstream (with eye at x/D_s~0.65) is also responsible for creating localised bursts of positive axial flow in the swirl stream and reverse flow in the inner swirl shear. The strong momentum carried by these vortices appear to distort the efflux angle of the swirl streams; moreover, the reverse flow induced by the second vortex likely adds to the strength of the CTRZ, resulting in an instantaneously inflated recirculation bubble. The inner swirl shear vortices can also interact with the central jet in two ways: first, the vortex may carry enough radial momentum such that the jet spread is drawn towards the right side of the FoV (see bias of jet axial velocity contour at x/D_s~0.6 in Fig. 5.15(a)); second, the vortex can

interact with shearing actions in the jet shear and resulting in smaller vortices (see red-coloured stream traces in Fig. 5.15(a)).

Fig. 5.15(b) exhibits a similar phenomenon where the vortices also lead to surges in instantaneous tangential velocities in the swirl stream, as well as negative tangential velocities in the region between the jet spread and the swirls stream. As explained in Section 5.1.3, the covariance, as well as the sign changes, in the swirl stream, inner swirl shear, and jet shear are all consistent with the distribution of <uw> shear stresses in Fig. 5.11(b).

Fig. 5.16 shows axial velocity contours in the r-θ planes at x/D_s=0.02 and x/D_s=0.27, both of which exhibit two vortices separated by θ=π. The vortices are indicated by the stream traces of instantaneous radial-tangential components. These stream traces of the vortices follow a counter-clockwise rotation, which is consistent with that of the bulk swirling flow direction. This pair of vortices induces an increase in forward axial velocity over quite a large angular span in the swirl stream (Δθ~π/3 in both Fig. 5.16(a) and Fig. 5.16(b)). They also result in large parcels of flow reversals, which are more pronounced at x/D_s=0.27 than at x/D_s=0.02.

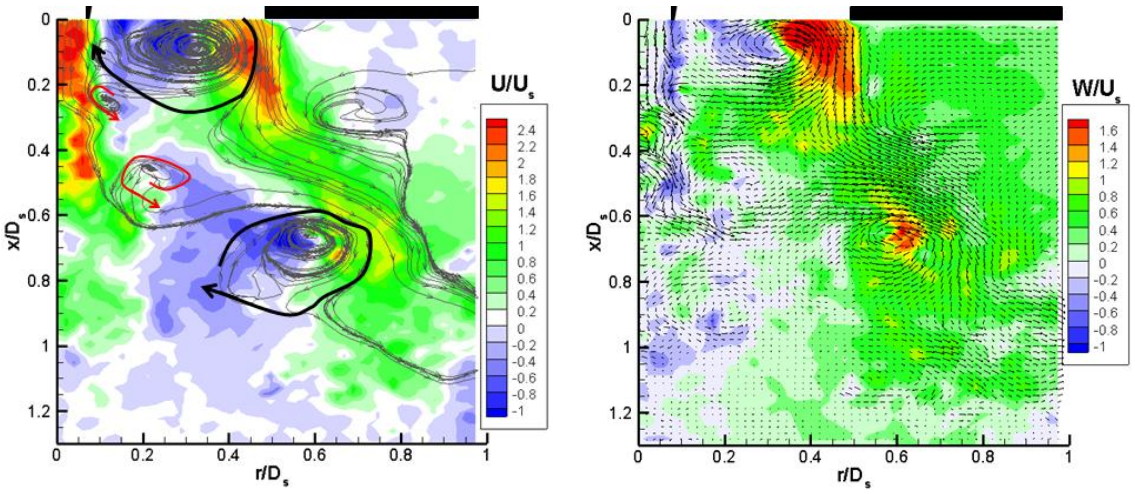

(a) (b)

Fig. 5.15 Contours of (a) axial velocity superimposed with arbitrarily plotted stream traces and (b) tangential velocity with superimposed U and V vectors

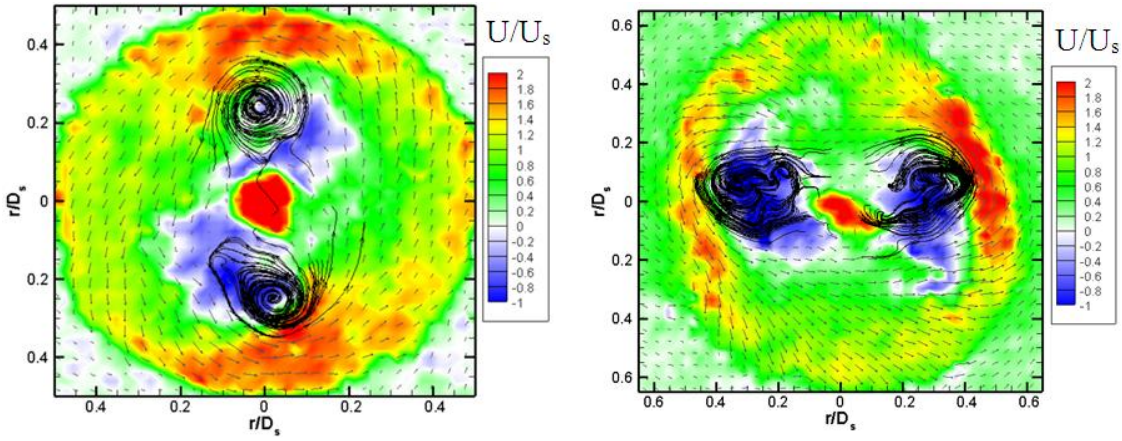

(a) (b)

Fig. 5.16 Contours of axial velocity in the r-θ plane at (a)x/D_s=0.02, and (b) x/D_s=0.27

By defining the inner swirl shear to be located within a radial span (e.g. $0.15<r/D_s\leq0.5$ at x/D_s=0.27), reverse flow in the inner swirl shear can be distinguished from that in the jet shear. Using this crude demarcation, instantaneous reverse mass flow induced by the vortex pair can be roughly estimated by integrating across areas where U(i,j)<0 (see Eq. 2.1), then taking an ensemble average of the data. It was found that reverse flow by swirl shear vortices is about 15% of the total forward flow at x/D_s=0.27.

5.2 Mixing field characteristics

5.2.1 Time mean scalar field

Fig. 5.17 shows the time-mean concentration field with superimposed velocity stream traces on the left half. The concentration is normalised by the central jet intensity, which is the same as the 100% concentration value during calibration. Similar to the decay of the axial velocity along the centreline, the concentration decreases quite rapidly: at x/D_s=0.5, the concentration has already dropped to half. At x/D_s>1.5, the concentration decreases to 5% to 6%, which is expected as the mass flow split between the central jet and the swirl stream is about $5.14*10^{-2}$. Given that this is the fully mixed concentration, it is interesting to see that the central jet's radial spread reaches the fully mixed level at r/D_s=0.5, which is equivalent to the swirler's outer radius. Other than the central jet spread, the swirl stream penetration is the only region with a concentration that is notably different from the fully mixed level. The swirl jet penetration region is characterised by low mean concentration, C~0.02, which follows

the cone angle and reaches the fully mixed value at r/D_s=0.8 and x/Ds=0.6. In the study reported by Janus et al (2007), time-mean OH-PLIF data indicates that the flame is lifted from the exit plane and the probability for stoichiometric condition is highest in the stagnation region, which scales to x/D_s~0.83; also, the most upstream location at which combustion occurs is in the inner swirl shear layer near x/D_s~0.3 even though that particular location is not noted for high probability of stoichiometry.

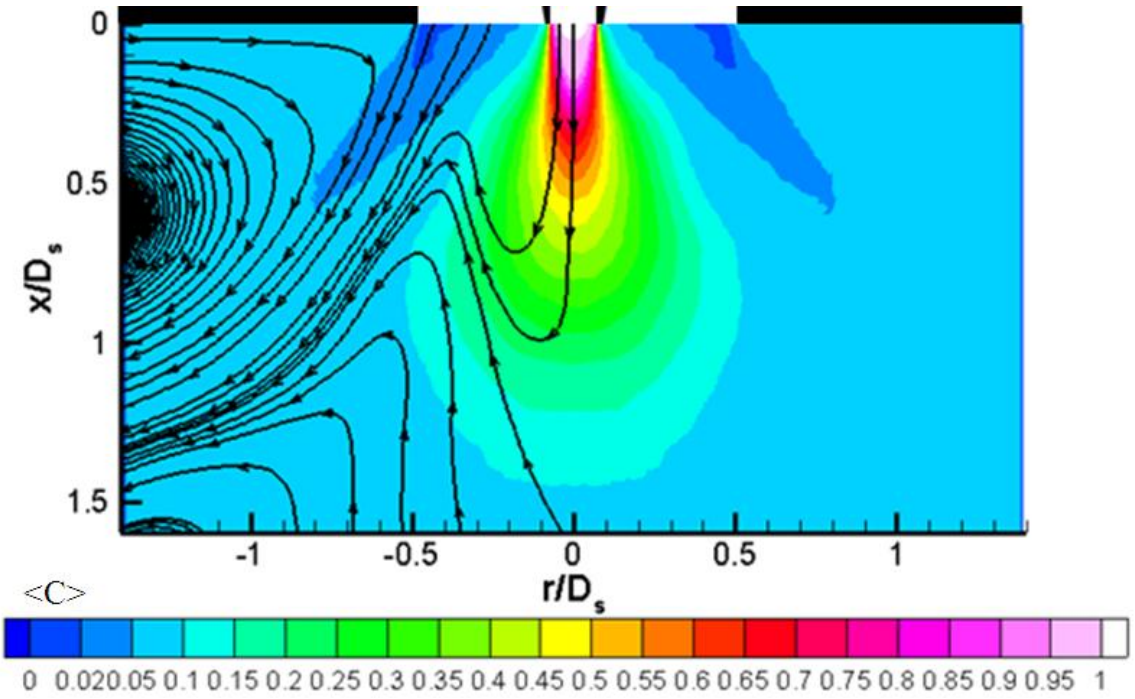

Fig. 5.17 Time-mean concentration field

The mean concentration fields at x/D_s=0.02 and x/D_s=0.27 are shown in Fig. 5.18(a) and (b), respectively. Again, there is good rotational symmetry. It should be noted that the colour band of C=0.03 was added to Fig. 5.18(a), and the contrast between it and C=0.05 marks a clear boundary of the swirler outer radius.

The RMS concentration is shown in Fig. 5.19 with time mean vectors superimposed on the left half. The RMS concentration peaks just downstream of the fuel injector exit at x/D_s~0.1 in the central jet shear layer, which is characterised by strong scalar gradient in the radial direction. It is worthwhile to note that RMS scalar of c>0.07 is contained within r/D_s<0.5 and x/D_s<1.25, suggesting that turbulent mixing takes place rapidly as the central jet exits into the expansion chamber. However, the RMS concentration remains quite low, c~0.02, in the inner swirl shear layer, which is

characterised by strong TKE (see Fig. 5.12). In other words, the localised turbulence structure in this region does not necessarily lead to large time-mean scalar fluctuation.

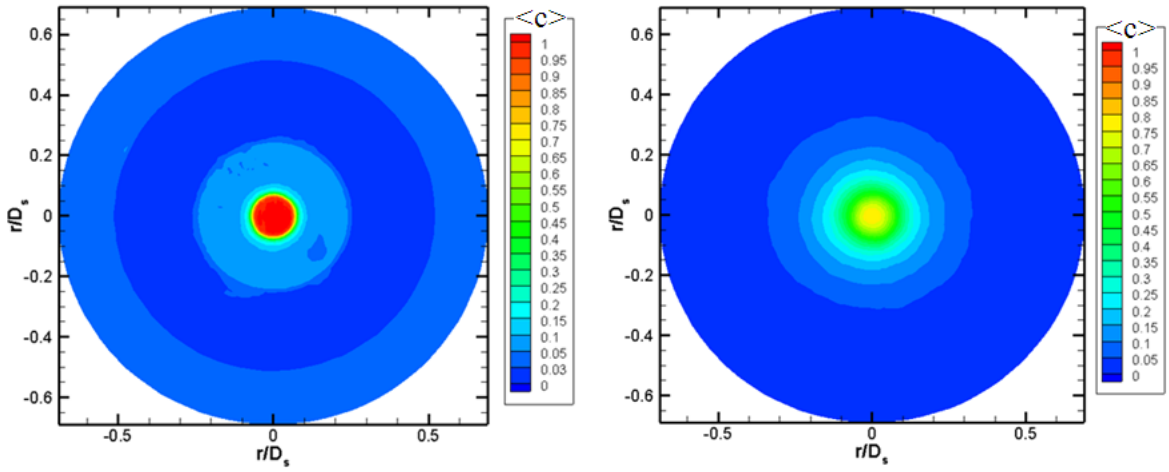

Fig. 5.18 Time-mean concentration field at the exit plane at (a) x/D_s=0.02 and (b) x/D_s=0.27

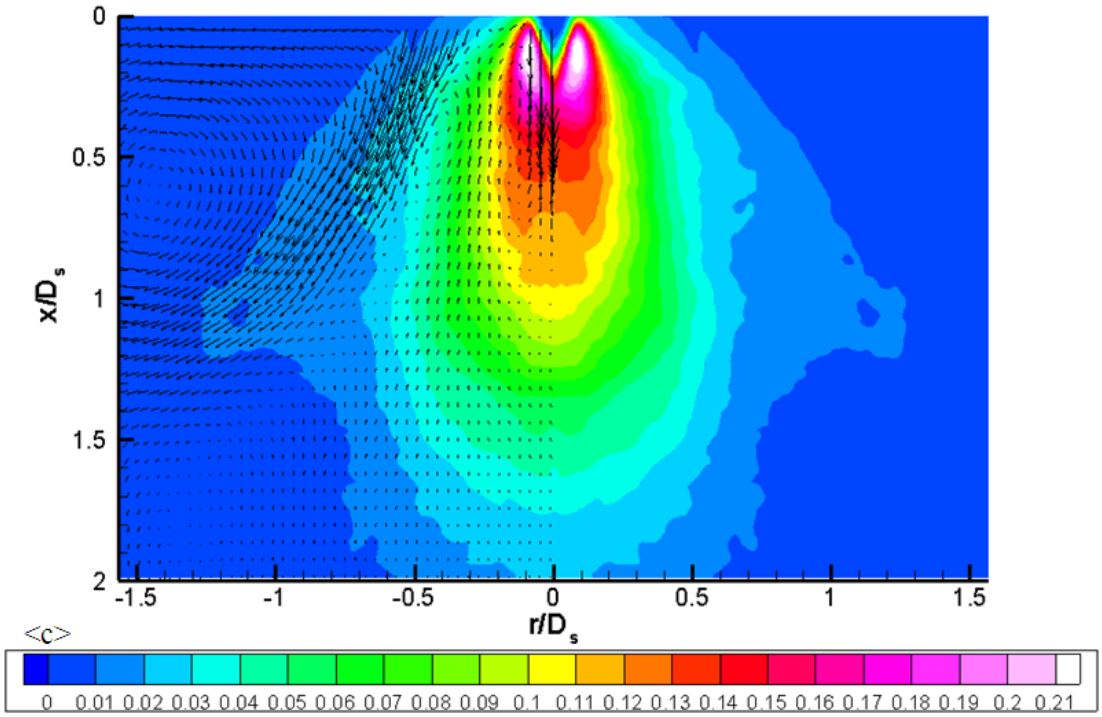

Fig. 5.19 RMS concentration

5.2.2 Data validation

The mean concentration profiles at four axial stations are shown in Fig. 5.20. There is very good agreement between the x-r plane data of the current work with Midgley's

data (Midgley, 2005). Therefore, this demonstrates good repeatability of the experiment. However, the r-θ plane profiles are consistently lower than x-r plane ones from Fig. 5.20(b) to Fig. 5.20(d). This is believed to be caused by streaks in the light sheet in which the intensities are lower (streaky behavior is somewhat visible in Fig. 5.18(a)). Due to the circumferential averaging operation, the effect of these lower-intensity streak lines are more pronounced in the r-θ profiles than the x-r ones.

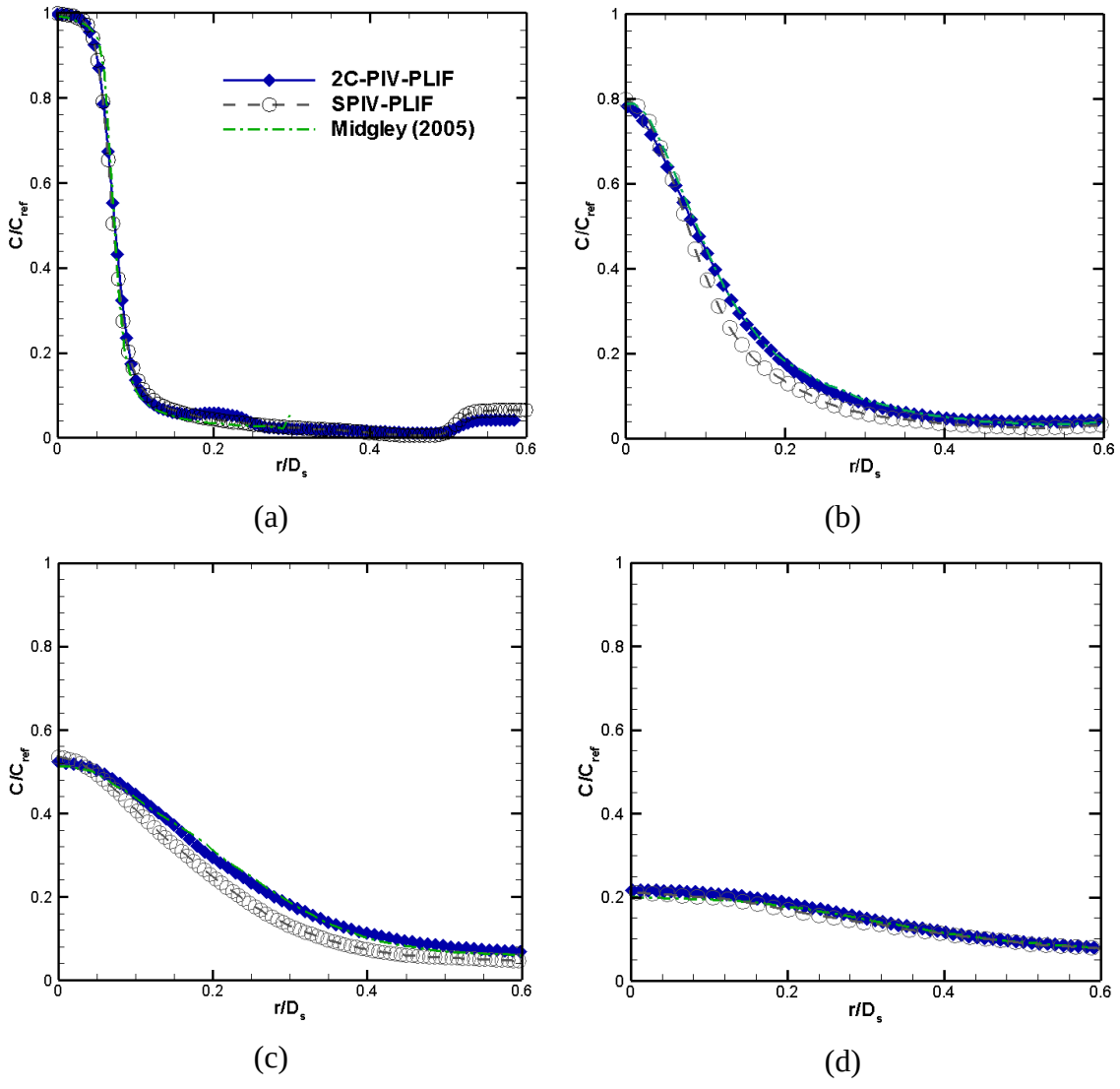

Fig. 5.20 Comparison of time-mean concentration profiles at (a) x/D_s=0.02, (b) x/D_s=0.27, (c) x/D_s=0.53, and (d) x/D_s=1.06

Again, the RMS concentration profile comparisons in Fig. 5.21 show good agreement in terms of the shapes and locations of the peak values. However, the x-r plane profile is consistently higher than the r-θ ones and Midgley's data. This difference is most pronounced near the central jet's outer radius at the exit plane. The scalar spatial

filtering error of ~2% does not explain the discrepancy (c=0.17 for the x-r data vs c=0.13 for the r-θ data).

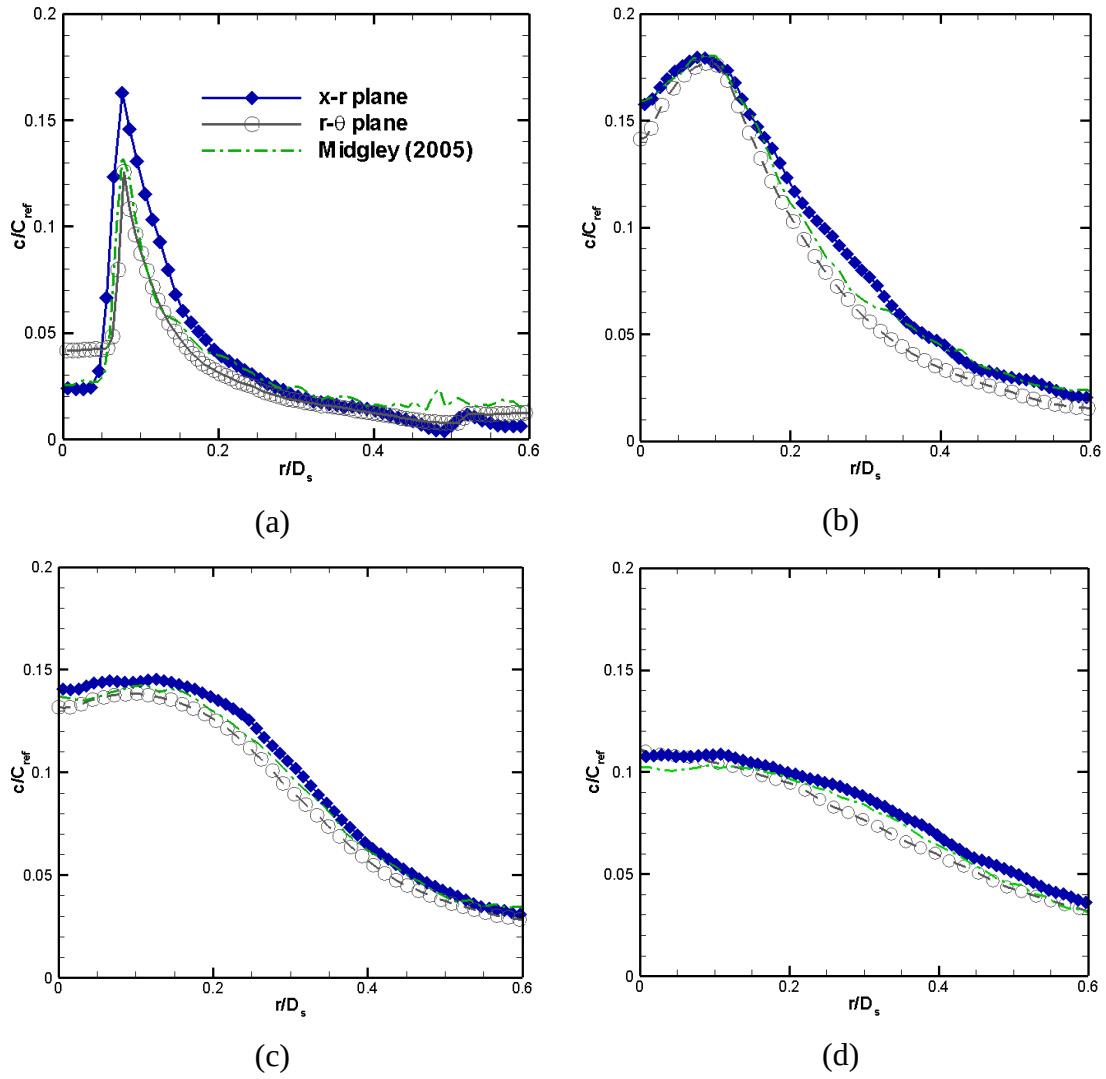

Fig. 5.21 Comparison of RMS concentration profiles at (a) x/D_s=0.02, (b) x/D_s=0.27, (c) x/D_s=0.53, and (d) x/D_s=1.06

5.2.3 Instantaneous scalar fields

Although the time-averaged scalar fields show good levels of rotational symmetry, careful inspection of the instantaneous scalar fields revealed that the central jet may be drawn by either of the two strong vortices and spread towards the left or the right side of the x-r plane FoV; an example of this is illustrated in Fig. 5.22 (taken from HS-xr1 data). It should be noted that the color contour has been cut off at C=0.15 to highlight the entrainment of scalar by the vortices.

Fig. 5.22(a) and (b) show notable asymmetry almost as soon as the jet exits into the dump expansion chamber. Passage of the vortex at x/D_s~0.05 entrains a parcel of jet fluid, as indicated by the 'entrainment' circle in Fig. 5.22(b). At x/D_s~0.2, the jet penetration becomes strongly biased to the left-hand side of the image plane; and further downstream near x/D_s~0.5, the high-concentration jet fluid is drawn onto the vortex on the left side of the FoV. Also, as shown in these two successive images separated by 0.001s in time, it is evident that the region of reverse transport is also biased towards the left half of the image plane, as indicated by the red dashed-line eclipse (x/D_s=0.6 to x/D_s=1.2). This confirms the tendency for the jet to 'flap' about the axis of symmetry and the observation that the flapping may be strongly influenced by the inner swirl shear vortices.

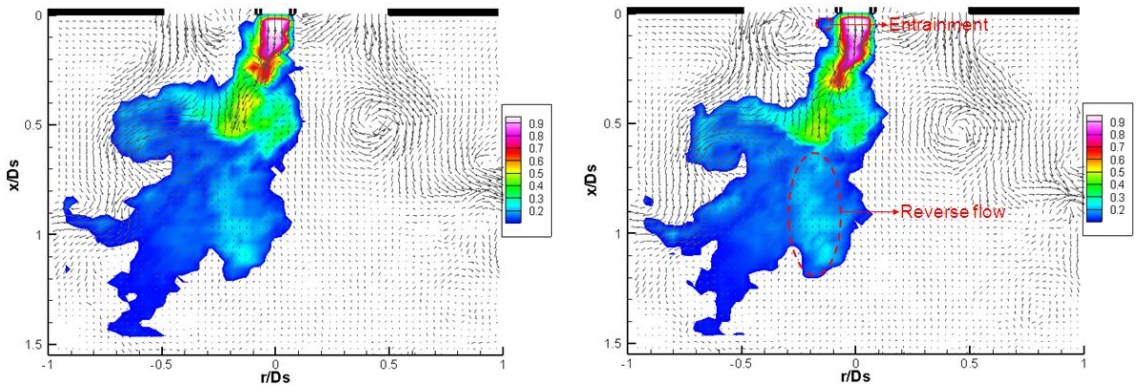

(a) t = 0.796s (b) t = 0.797s

Fig. 5.22 Sequence of snapshots of scalar fields with overlaid velocity vectors

While large-scale entrainment of jet fluid and asymmetry of the jet spread are a result of the helical vortices, the jet shear is dominated by vortices of smaller length scales. These vortices are responsible for diluting the jet by exchanging the swirl stream fluid (of zero or very low concentration) with the high-concentration jet mixture. The dilution of the jet occurs rapidly and may cause up to 50% in concentration reduction in the region where the jet is shown to be broken up, as indicated by the dashed line in Fig. 5.22(b). It is therefore believed that these jet shear vortices also contribute to the rapid mixing. Further downstream (near x/D_s=0.65) in Fig. 5.23(a), there exists an axis-symmetric vortical structure which resembles the profile of a vortex ring (Gharib, 2005). Such flow feature can be observed when axis-symmetry of the jet penetration is restored because there is constant, axis-symmetric supply of shear energy from the

velocity gradient between the reverse-flowing CTRZ and the forward-flowing jet. This vortex-ring-like structure near the free stagnation region (x/D_s~0.9 in this case) also spread the high-concentration mixture radially outward and stabilise the central jet penetration.

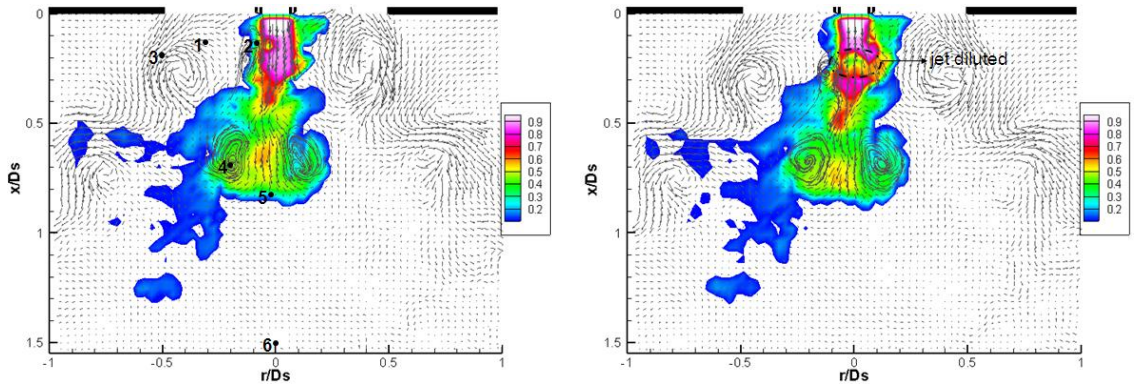

(a) t = 2. 745s (b) t = 2.746s

Fig. 5.23 Examples of shear layer vortices

Large-scale entrainment by vortex pairs

The entrainment of scalar by the helical vortex pairs can be studied in more details by looking at the fluctuating components, two example snapshots of which, selected from combined SPIV/PLIF dataset r-θ3, are shown in Fig. 5.24.

The streamlines are arbitrarily plotted from the fluctuating radial-tangential velocity field, yielding two pairs of distinctive vortex structures that are separate by 90 degrees ($\pi/2$). The first pair can be easily identified from stream traces of an instantaneous shot, while the second pair only becomes visible when the velocity field is Reynolds decomposed. The first pair, which has the same counter-clockwise rotation as the bulk swirling flow, is described as "strong" while the second pair, which has a clockwise rotation, is referred to as the "weak" pair. It has been shown in Midgley (2005) that both vortex pairs follow helical paths as they convect downstream. As shown on the left of Fig. 5.24(a), there are two parcels of strong positive scalar fluctuation separated by $\theta \sim \pi$. Each of these parcels is sandwiched between a strong vortex and a weak vortex. This suggests that the counter-rotating relationship between the strong and the weak vortices, which are adjacent to either other, is conducive to the entrainment of scalar by imposing their co-directional bias on the jet. As the high-concentration jet fluid is entrained by the vortices into the top and the bottom "quadrants" in the inner

swirl shear layer (Fig. 5.24(b)), what was originally a round jet is now stretched, resulting in localised spots of low concentration fluctuations on the left and right 'quadrants'. As it was discussed in Section 5.2.1, Janus et al (2007) reports that the free stagnation region has a high probability of stoichiometry; if the time-mean concentration contour shown in Fig. 5.17 were used as a reference, it can be seen that <C(r/D_s=0, x/D_s=0.85)>~0.35. As shown in Figs. 5.24(a) and (b), the concentrations of the entrained jet fluid into the two quadrants are within c=0.3 to c=0.35 (C=0.35 to C=0.4). Because this range is quite close to C under the stoichiometric condition, localised combustion events could occur in the inner swirl shear. In Section 5.3.2, it will be shown that this large-scale entrainment of scalar into the inner swirl shear is also strongly periodic, with clear implications on heat release oscillations.

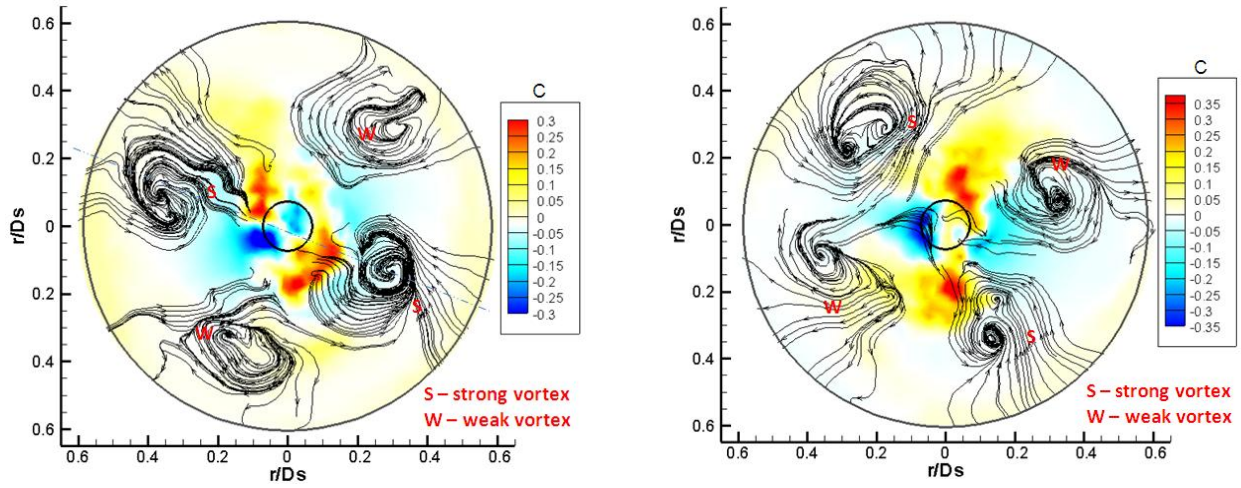

(a) t = I (b) t = II

Fig. 5.24 Snapshots of fluctuating scalar with superimposed streamlines at x/D_s=0.27

Jet shear vortices

In addition to the large-scale entrainment, rapid mixing can also be attributed in part to smaller vortices in the jet shear, as evidenced by roll-up and stretching of the jet fluid in the jet shear. An example of these is illustrated in the instantaneous scalar field with superimposed streamlines in Fig. 5.25, which was selected from the low-speed xr1 dataset due to its high spatial resolution. In this example, the jet shear layer rolls up to form three visually identifiable spiral-shaped stream traces. Just downstream of these vortices, there is notable entrainment of jet fluid and radial outward transport. Whether these jet shear vortices are periodic or are induced by the

helical vortex will be explored in the next section. As a qualitative observation, these vortices and their effect on the jet fluid are a likely manifestation of the Kelvin-Helmholtz instability. External disturbances such as the helical vortices may trigger the formation of Kelvin-Helmholtz waves in the jet shear, and as these waves grow, they may roll up in discrete vortices, as is the case here. The rotation of these jet shear vortices are responsible for the exchange of high-concentration jet fluid with the adjacent, incoming stream of low-concentration fluid, thereby contributing to rapid dilution of the central jet.

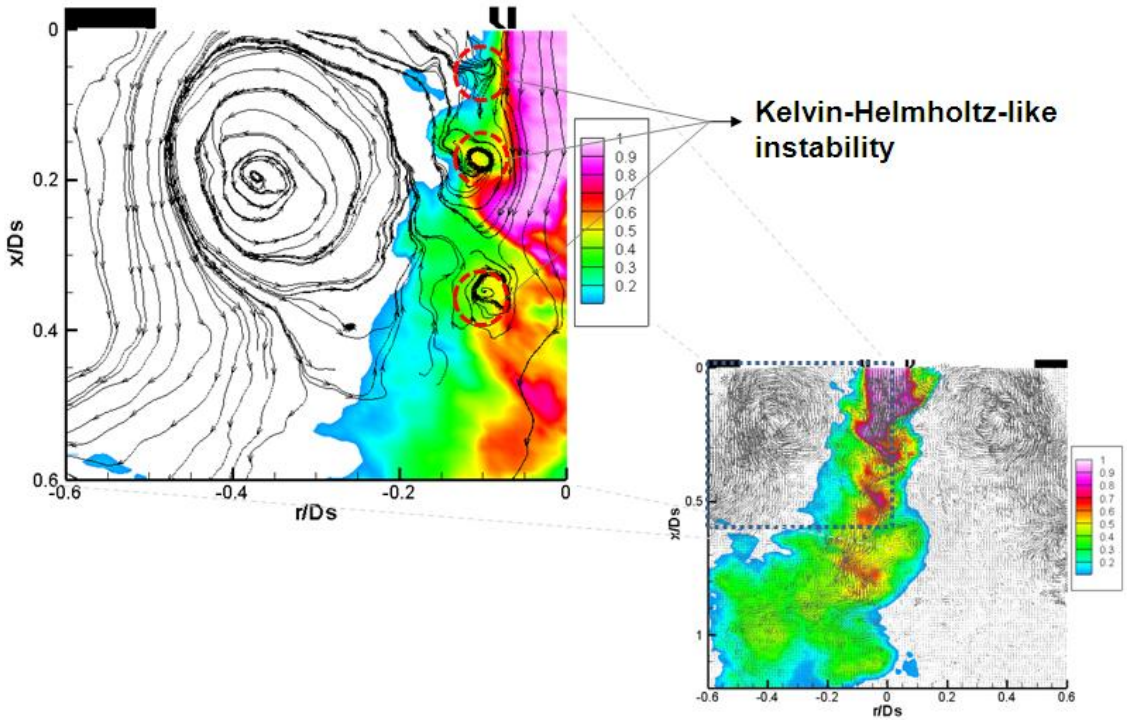

Fig. 5.25 Jet shear vortices and mixing

5.2.4 Scalar fluxes

Fig. 5.26 shows a sequence of three consecutive snapshots captured at a frame rate of ΔT=0.001s. Columns (a1) to (a3) show the fluctuating scalar concentration superimposed with instantaneous vectors, columns (b1) to (b3) show the instantaneous turbulent axial scalar flux superimposed with Reynolds decomposed vectors, and columns (c1) to (c3) show the instantaneous radial scalar flux, also superimposed with decomposed vectors. As indicated by the red arrows in Fig. 5.26(b2), counter-rotating vortices adjacent to one another exist in the swirl stream. The strong vortices can be identified by looking at the instantaneous vectors in

columns (a1) to (a3), but the weak ones are only revealed in the Reynolds decomposed vector fields. At x/D_s~0.2, the radial direction of the two adjacent vortices match, resulting in outward radial bias on the jet shear. The evolution from Fig. 5.26(a2) to (a3) clearly indicates that the strong vortex (with eye located at x/D_s~0.45) not only imposes a radial bias on the jet shear, but it also draws higher concentration fluid from downstream and causes it to rotate in the wake. In other words, scalar concentration (+) is entrained into the inner swirl shear by the outward (+) radial bias of the two adjacent vortices, thereby forming a trail of positive vc in the wake of the strong vortex. But uc is negative in this region as it is dominated by reverse flows of the coherent structures.

Unlike the inner swirl shear vortices, which remain coherent in Fig. 5.26 over the duration of the three snapshots, jet shear vortices at x/D_s<0.5, as indicated by the stream traces in Fig. 5.26(a1) and (b1), tend to be dissipated much more quickly and become unidentifiable within ΔT. These high-frequency jet shear eddies are conducive to the rapid exchange of fluids at smaller length scales, as evidenced by the sudden appearance of a parcel of –c at x/D_s~0.1 in Fig. 5.26(a3) and the corresponding –uc in Fig. 5.26(b3), the high-frequency fluctuations of –uc shown in Fig. 5.28 also supports this observation. In contrast, the vortex identified in the jet shear further downstream (vortex centre at x/D_s~0.85 in Fig. 5.26(a1)), is stagnant throughout the period of the period of the three snapshots. Similar effect is seen in the turbulent scalar fluxes: whereas uc and vc fluctuate quite rapidly in the jet shear, changes in uc occur much more slowly in the free stagnation region.

Fig. 5.27 shows another flow scenario in which patches of positive uc and vc are found in the jet shear, but in this case the combinations of the signs are different. As shown in Fig. 5.27(a), the jet spread is biased to the left half of the image plane, leaving the right side with low Reynolds decomposed scalar values, which in turn multiply with negative u due to reverse flow of the CTRZ and the strong vortex (with eye at x/D_s~0.55) to form a strip of +uc. Also shown in Fig. 5.27(a) and (b) are zoomed-in views that show a parcel of –uc and +vc; such a combination tends to occur near the inner edge of the swirler passage where backflow is found.

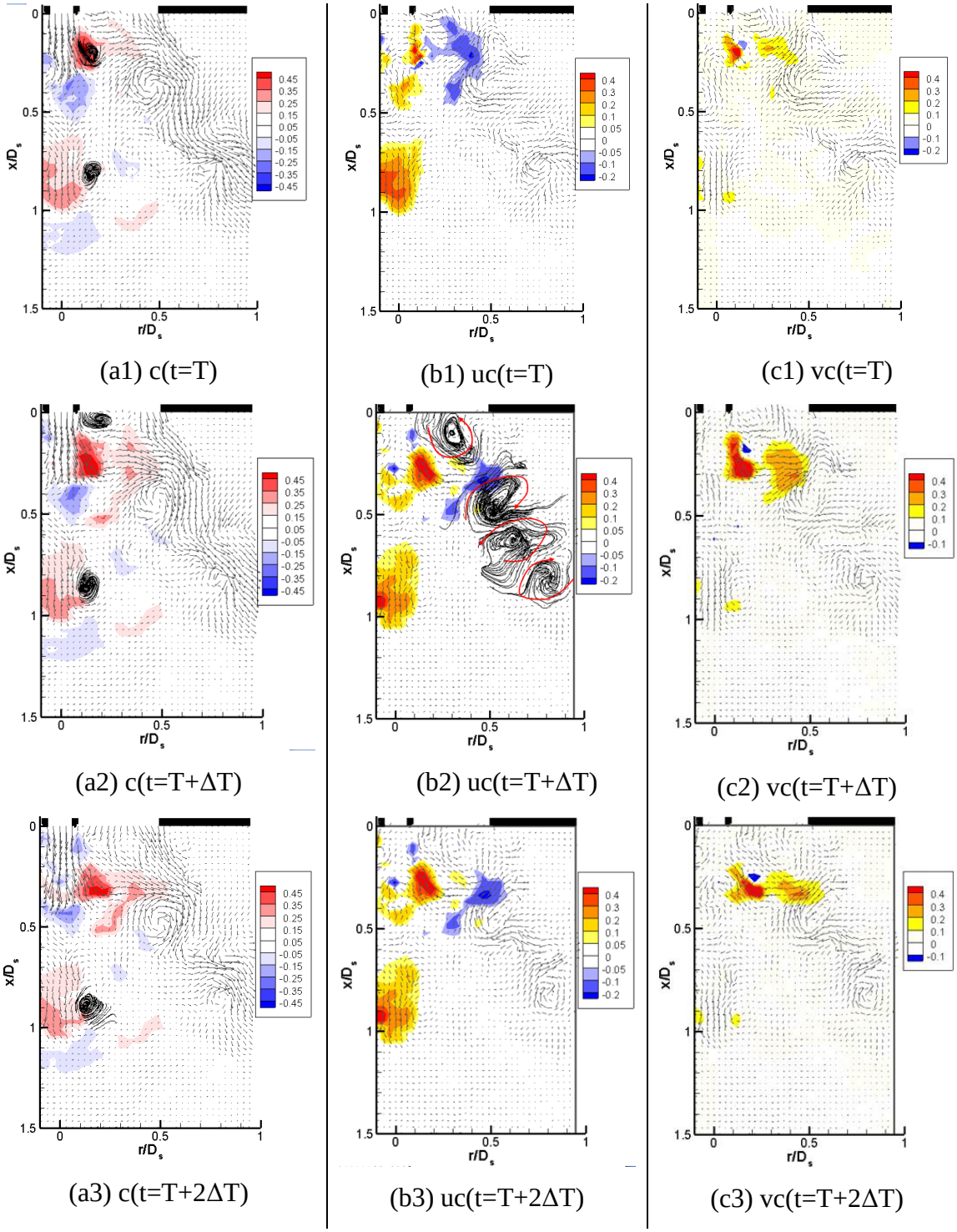

(a1) c(t=T) (b1) uc(t=T) (c1) vc(t=T)

(a2) c(t=T+ΔT) (b2) uc(t=T+ΔT) (c2) vc(t=T+ΔT)

(a3) c(t=T+2ΔT) (b3) uc(t=T+2ΔT) (c3) vc(t=T+2ΔT)

Fig. 5.26 Instantaneous snapshots of (a) fluctuating scalar, (b) axial scalar flux, and (c) radial scalar flux

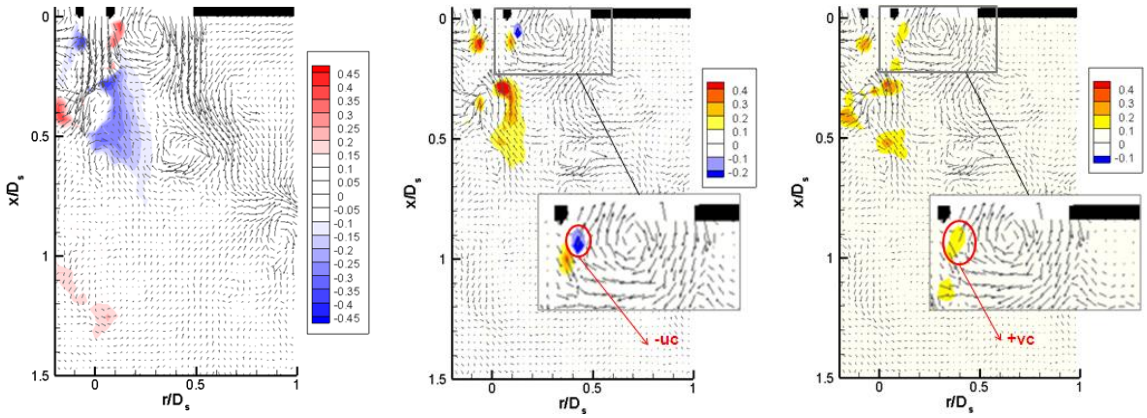

(a) c (b) uc (c) vc

Fig. 5.27 Instantaneous snapshot of (a) fluctuating scalar, (b) axial scalar flux, and (c) radial scalar flux

Fig. 5.28 shows that positive covariances of uc and vc dominate the negative ones in terms of intensity. This is consistent with the rise of +uv in the jet shear shown in Fig. 5.11(a), thanks to the two dominant flow scenarios: (1) increases in forward momentum in the jet shear is likely coupled with radial outward entrainment of scalar, and (2) reverse flows, or reductions in forward momentum, are likely coupled with radial inward flows of undyed fluid from the swirl stream, or asymmetric radial velocity profile in the case of jet flapping. More evidences of these two dominant jet mixing scenarios are to be presented later. Comparison between Fig. 5.28 and Fig. 5.29 indicates that velocity-scalar covariance in the jet shear occurs with much higher intensities and frequencies than those found in the inner swirl shear. While the fluctuations in Fig. 5.29 look somewhat periodic, the time series shown in Fig. 5.28 actually resemble those of white noise or broadband turbulence. This finding suggests that fluid exchange by the smaller eddies in the jet shear may be independent of the large-scale entrainment by the helical vortices in the inner swirl shear. A data reduction method developed by Westerweel et al (2009) could potentially be used to quantify the respective contributions to mixing of the jet, but unfortunately due to the spatial resolution requirements on the jet shear, the application of this method is out of the scope of the current project.

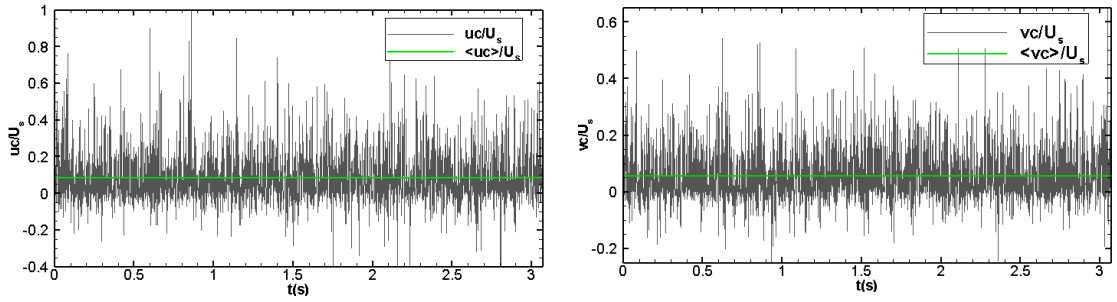

(a) axial scalar flux (b) radial scalar flux

Fig. 5.28 Point histories of turbulent scalar flux at x/D_s=0.15, r/D_s=0.15 in the inner swirl shear

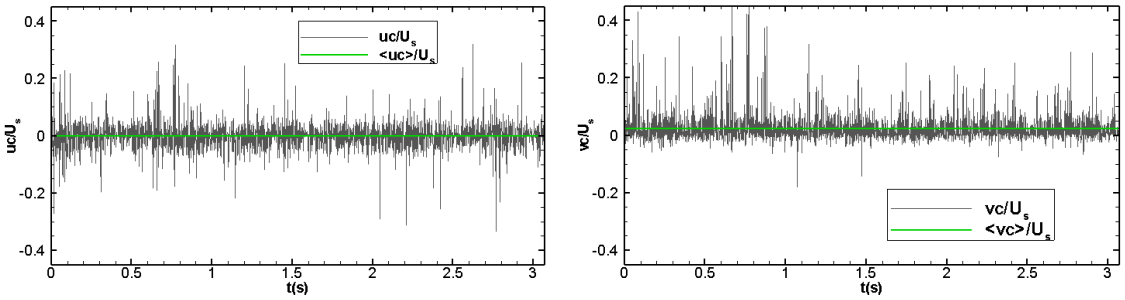

(a) axial scalar flux (b) radial scalar flux

Fig. 5.29 Point histories of turbulent scalar flux at x/D_s=0.27, r/D_s=0.27 in the inner swirl shear

The time-mean turbulent scalar fluxes <uc>, <vc>, and <wc> are shown in Fig. 5.30, Fig. 5.31, and Fig. 5.32, respectively. Figs 5.30 and 5.31 are taken from the 2C-PIV-PLIF measurements while Fig. 5.32 is taken from the SPIV-PLIF measurement; the respective spatial resolutions can be found in Section 3.6.1. The non-swirl induced sub-pressures shown in Fig. 5.13(c) have been overlaid (in dashed lines) onto the scalar flux contours to represent the time-mean path of the coherent structures that dominate in the inner swirl shear. In general, peak values of all 3 turbulent scalar fluxes are found in the jet shear, in which the maxima of <uc> is roughly twice higher than that of <vc> and three times higher than that of <wc>. Again, the rapid decays of all three fluxes are consistent with the previous argument that the jet fluid undergoes rapid mixing due to the turbulence structures that exist in the near field.

As shown in Fig. 5.26 and discussed with reference to Fig. 5.27, increases in scalar concentration in the jet shear are highly correlated with increases in axial forward momentum, while negative fluctuating scalar tends to be coupled with reverse flows or forward flows that are weaker than the time-mean values in the event of the jet's flapping. The resultant time-mean <uc> shown in Fig. 5.30 verifies the observation

that these are the two dominant flow and mixing scenarios in the jet shear. Outside the jet shear, the inner dashed line almost precisely marks the boundary at which the sign of <uc> flips; the fact that the majority of the inner swirl shear is characterized with -<uc> confirms the high probability for scalar drawn into the wakes of the vortices to couple with their reverse flows. Indeed, such a large radial span of -<uc> is not observed in the scalar flux data reported by Feng et al (2007), Loffler et al (2008), and Borg et al (2001), on turbulent jet flows, suggesting that its presence may be less dependent on the jet-induced fluctuations and more dependent on the coherent structures. The -<uc> that prevails in the inner swirl shear clearly indicates net transport of jet fluid in the reverse direction; and the rise of -<uc> that is located in the inner edge of the swirl passage, which is consistent with the location of backflow shown in Fig. 5.2, also indicates a net turbulent transport of jet fluid into the swirl duct.

As shown in the vc time series in Fig. 5.28(b) and Fig. 5.29(b), vc is dominated by positive peaks, which suggest that the turbulent transport of scalar into the inner swirl shear is strongly coupled with increases in radial outward momentum. It is unlikely for the combination of negative scalar fluctuations and radial inward flows to be the dominant mode in the inner swirl shear because the mean scalar concentration in the region is very low ($C \leq 0.05$). Hence, bursts of jet fluid entrained into the inner swirl shear are certainly a result of the coherent structures, as demonstrated by the instantaneous examples shown in Fig. 5.24. The <vc> contour shown in Fig. 5.31 is consistent with this observation. It is interesting to note that <vc> becomes insignificant (<uc><0.005) almost as soon as the outer dashed line is crossed. This implies that the turbulent transport of jet fluid in the radial direction is limited to the inner swirl shear, and that the outer swirl shear and the CRZ are unlikely to exert any influence on the turbulent mixing in the radial direction.

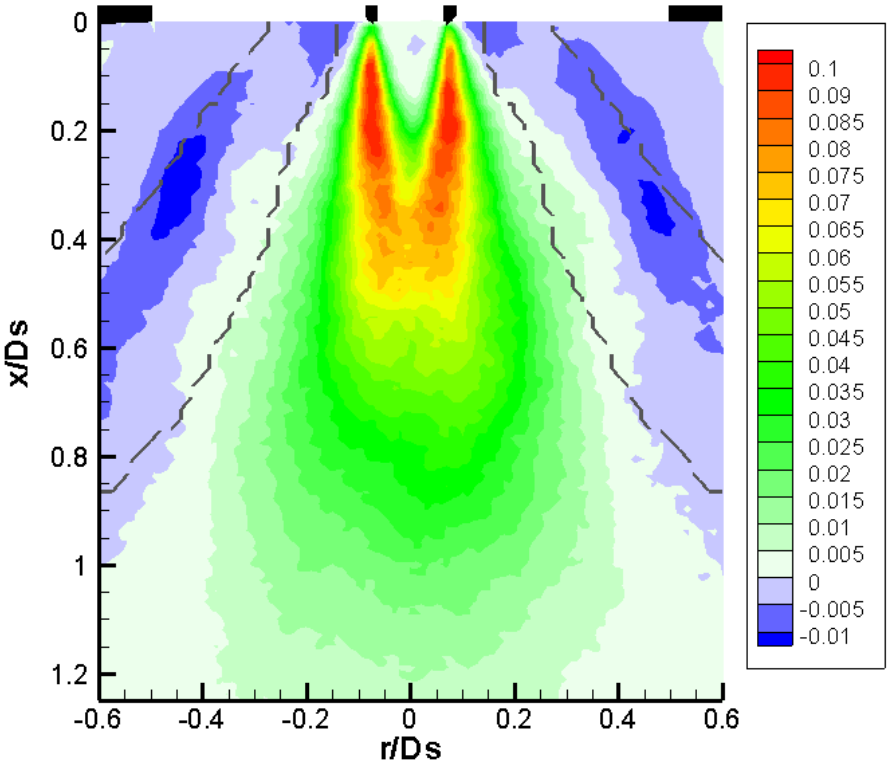

Fig. 5.30 Time-mean axial scalar flux, $\langle uc \rangle / U_s^2$

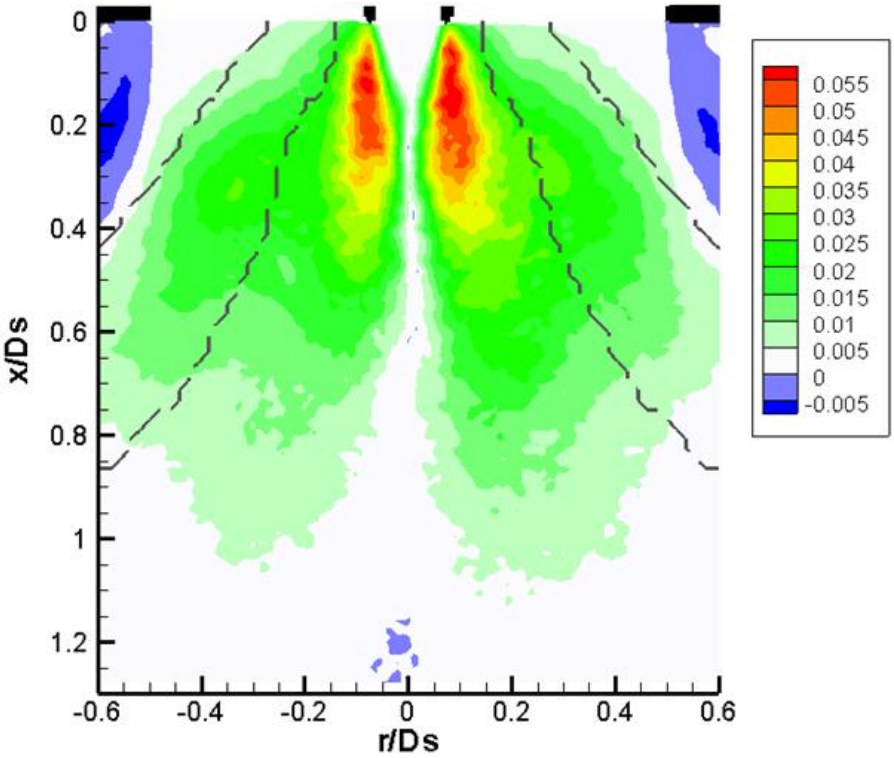

Fig. 5.31 Time-mean radial scalar flux, $\langle vc \rangle / U_s^2$

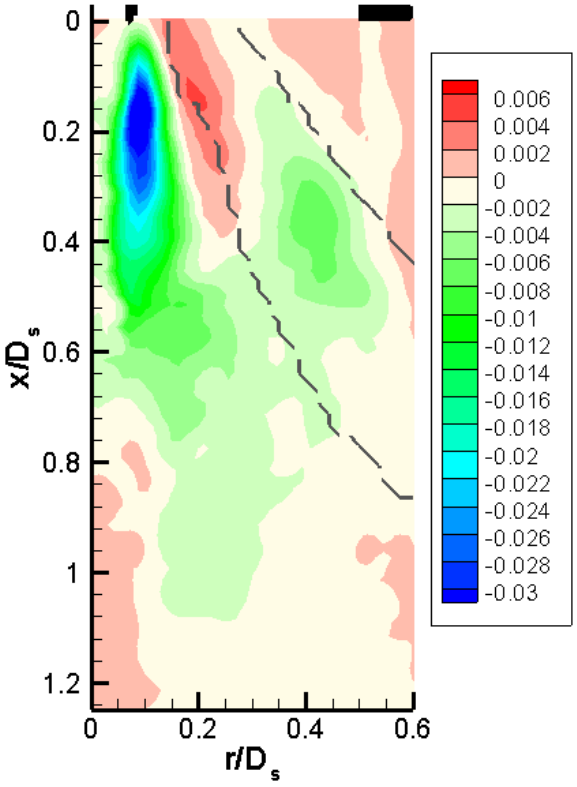

Fig. 5.32 Time-mean tangential scalar flux, $\langle wc \rangle / U_s^2$

Following the right-hand rule, mean bulk flow in the circumferential direction in Fig. 5.32 is out-of-page. Given that the coherent structures draw the jet fluid into the inner swirl shear, $-\langle wc \rangle$ within the dashed lines indicates that the entrained jet fluid then undergoes a net turbulent transport in the into-page direction. This can be demonstrated by taking a cross section through the centres of the strong vortices, as demonstrated by the dashed line in the instantaneous snapshots of Fig. 5.24(a). Also suggested by Fig. 5.32 is the tendency for negative fluctuating tangential velocities to couple with higher levels of concentration in the jet shear as the central jet is distorted by the coherent structures. In addition, the sign change of $\langle wc \rangle$ near the jet shear boundary again indicates a net into-page turbulent transport that is opposite to the bulk out-of-page swirling flow.

As indicated by instantaneous snapshots of Fig. 5.26 and the time-mean scalar fluxes shown in Fig. 5.30 and 5.31, it has been argued that radial transport of jet fluid into the inner swirl shear is coupled with reverse transport. As a means of quantifying the level of coupling, the time series of uc and vc in Figs 5.28 and 5.29 have each been cross correlated, each with a bound of ±64 time steps. The results of the cross

correlations are shown in Fig. 5.33. As shown in Fig. 5.33(b), the time series of uc and vc are quite well correlated with a correlation coefficient ($\rho_{uc,vc}$=-0.6) at t=0, and the negative sign agrees with the description of the coupling. Remarkably, mild levels of correlation occur at t~0.011s and again at t~0.023s – these periodicities match those of the strong vortex-pair system and of the single strong vortex – as will be discussed in Section 5.3.2. Although maximum $\rho_{uc,vc}$ in the jet shear (Fig. 5.33(a)) has a similar magnitude and therefore also indicates strong correlation, the lack of outstanding maxima in $\rho_{uc,vc}$ in other time lags proves that the coherence in time is much less pronounced.

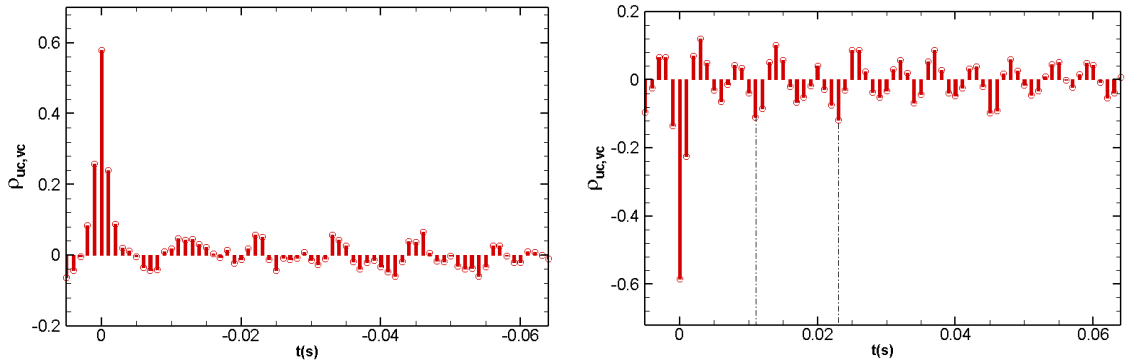

(a) jet shear (b) inner swirl shear

Fig. 5.33 Cross correlation of uc and vc of a point in the (a) jet shear, and (b) inner swirl shear

5.3 Coherent structure and spectral analysis

5.3.1 Single point statistics

As shown in Fig. 5.16, two localised regions of strong axial flow reversals, separated by $\theta=\pi/2$, exist in the inner swirl shear layer. At the other two quadrants, however, such flow reversals are not present. This observation suggests that at any circumferential point within the radii of the inner swirl shear, the flow may exist in two states. The observation can be verified by looking at the probability density function (pdf) of the ensemble data. Fig. 5.34 shows the pdf of instantaneous velocity and scalar at r/D_s=0.18, x/D_s=0.02; the respective time-mean values are indicated by the dashed light-gray lines. The axial velocity at this point location is characterised by strong bimodal behaviour, in which the distribution of negative values indicate reverse flow, which is largely attributed to the vortex passage. Although the radial and

tangential velocities show less pronounced bimodal distributions, they still have long tails towards the negative values. The mean concentration in this location is 0.06, which is biased towards higher values due to the entrainment of high-concentration jet fluid.

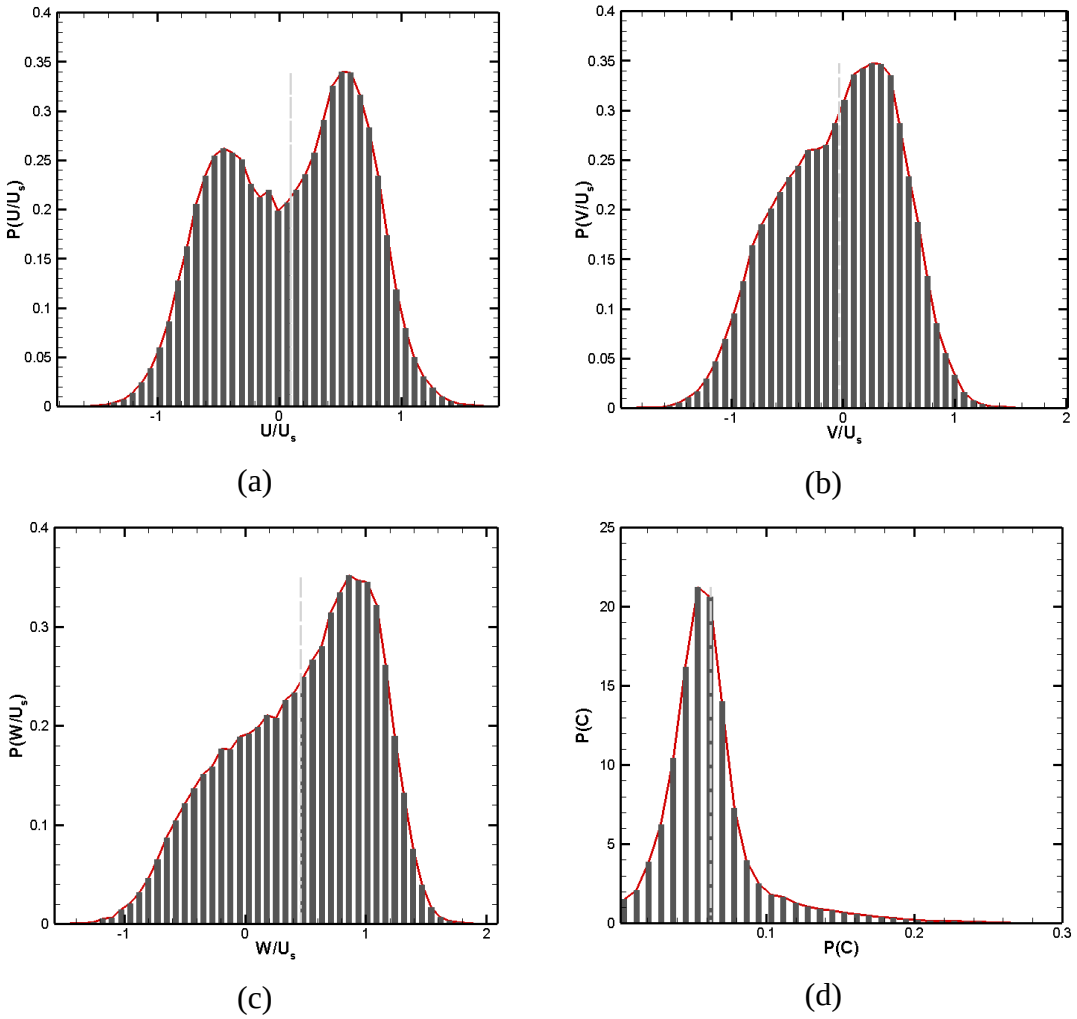

Fig. 5.34 Normalised pdf of (a) axial velocity, (b) radial velocity, (c) tangential velocity, and (d) scalar at $r/D_s=0.18$, $x/D_s=0.02$

Further downstream in the inner swirl shear, as shown in Fig. 5.35, the pdfs of the axial and radial velocities remain bimodal shaped, but the pdf of the tangential velocity approaches that of a normal distribution with a skewness of -0.31. The concentration again exhibits a long tail towards the positive values, indicating considerable probability of rises in scalar concentration in the inner swirl shear.

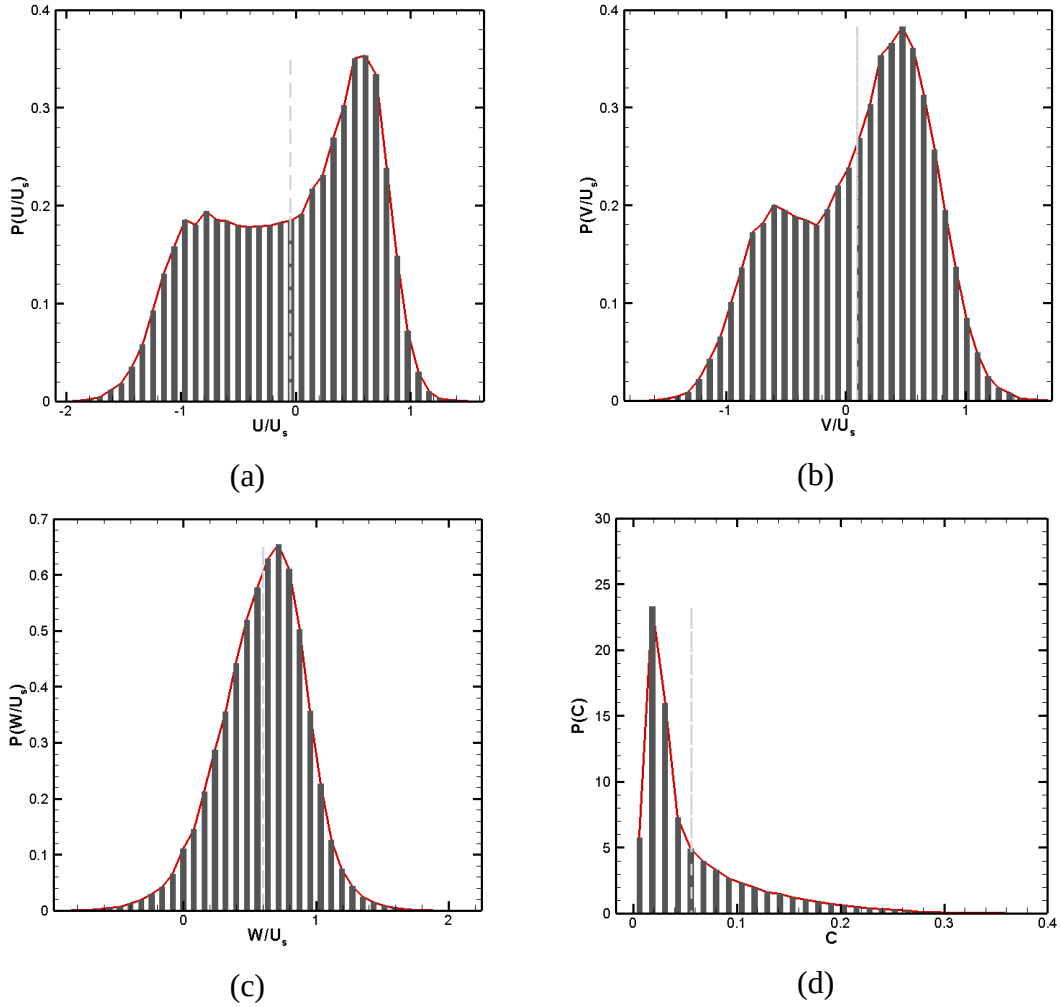

Fig. 5.35 Normalised pdf of (a) axial velocity, (b) radial velocity, (c) tangential velocity, and (d) scalar at r/D_s=0.30, x/D_s=0.27

5.3.2 Temporal characteristics

Discussion in the previous section highlighted flow transitions between bimodal states, particularly for the axial velocity component. The characteristic frequencies of the vortex pairs and their influence on different regions of the flow field can be studied using PSD estimates. Here PSD analyses have been performed on the six representative point locations, as indicated by the black dots in Fig. 5.23(a). The high-speed dataset HS-xr1, recorded at 1000Hz, provides simultaneous axial and radial velocities and scalar, hence PSD was also computed with the turbulent scalar fluxes.

Point 1 is located in the inner swirl shear (x/D_s=0.15, r/D_s=0.27). As shown in Fig. 5.36, PSD performed at this point location yields two notable peaks in the velocity data and three distinct peaks in the scalar data. For reasons that will be elaborated

throughout the remaining parts of this chapter, the first peak (S_t~0.61) is the characteristic frequency of the strong vortex, the exact doubling of frequency of the second peak (S_t~0.1.22) is due to pairing of the two strong vortices shown in Fig. 5.24, and the third harmonic is due to the co-existence of the strong and the weak pairs. While the first peak is seen in the scalar PSD, it is less distinguishable in the velocity PSDs. Despite this, the ACF shown in Fig. 5.37 still indicates a consistent correlation pattern among all three variables. The higher ρ_{cc} maxima may explain why the E_{cc} peak is more distinguishable than E_{uu} and E_{vv} at S_t=0.61. In addition, the strong repeating patterns with a period of 0.11s (S_t~1.21) means lower harmonics which are not representative of a vortex may also be registered by the PSD computation, as evidenced by the weakly appearing E_{vv} and E_{cc} maxima near S_t=0.41 and S_t=0.21.

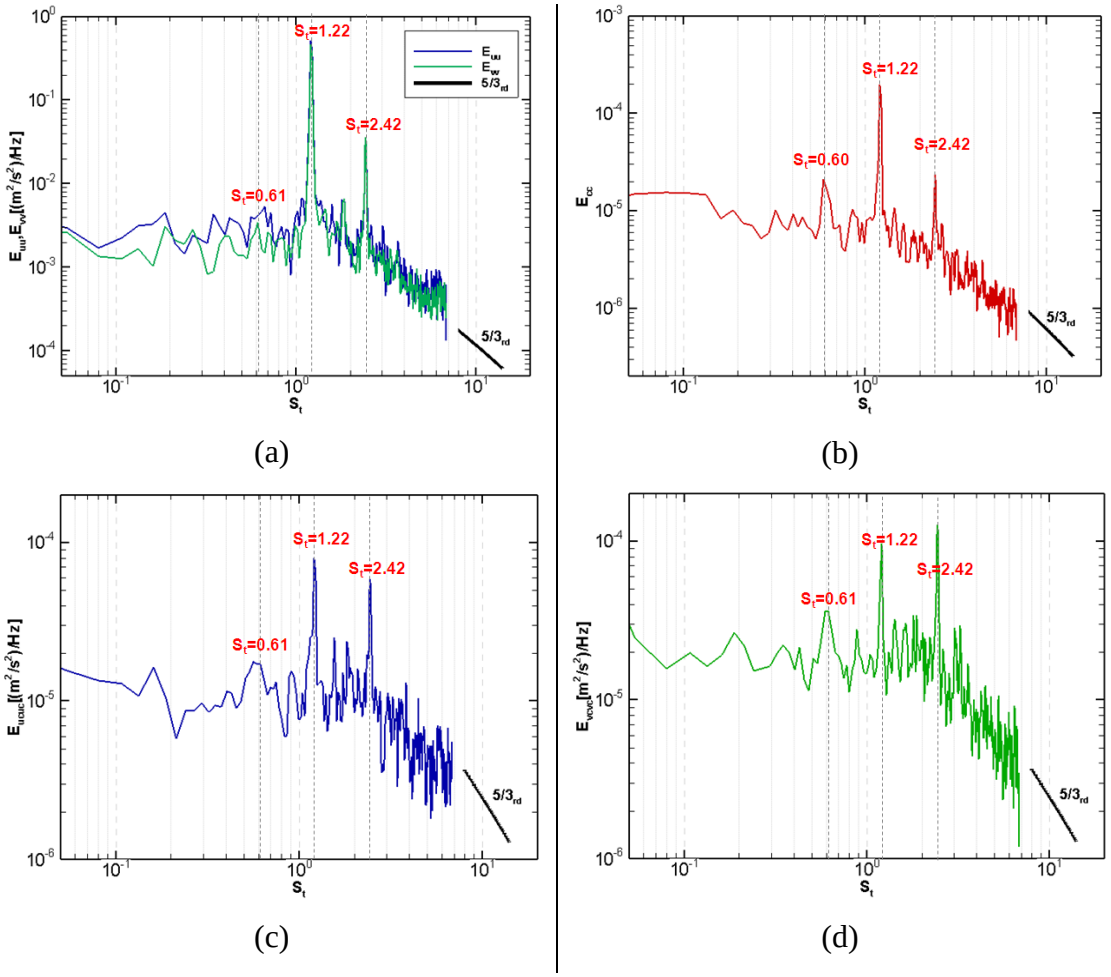

Fig. 5.36 PSDs of (a) u and v, (b) c, (c) uc, and (d) vc of a point in the inner swirl shear

Interestingly, the common correlation pattern shared by u, v, and c is also manifested in the PSDs of uc and vc, where identical S_t's of peaks support the previous argument

that the coherent structures are responsible for large-scale entrainment of jet fluid into the inner swirl shear. The fact that the amplitude of E_{vcvc} is higher than that of E_{ucuc} at S_t=2.42 also supports the previous observation that the counter-rotating relationship between the strong and the weak vortices, which are adjacent to each other, is conducive to the radial outward transport of jet fluid.

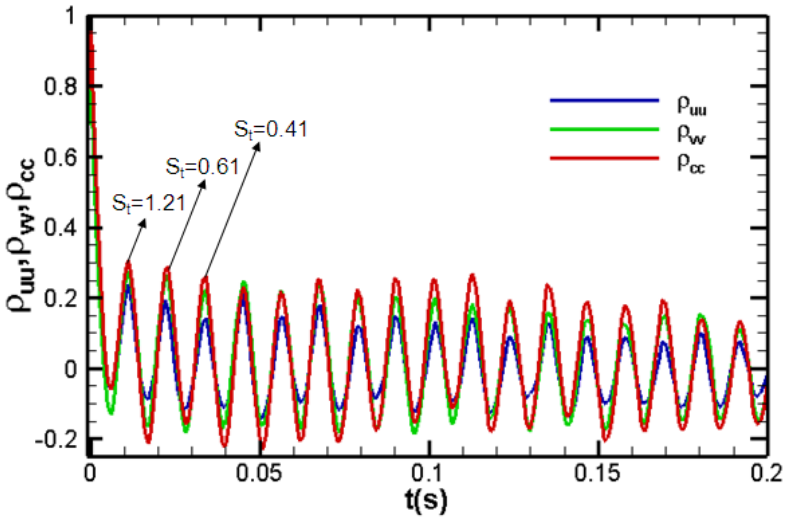

Fig. 5.37 ACF of u, v and c of a point in the inner swirl shear

Unlike the inner swirl shear, PSD in the jet shear at x/D_s=0.12, r/D_s=0.08, as shown in Fig. 5.38, exhibits only one dominant peak at S_t=1.22 for both velocity components and scalar. This implies that the weak vortex pair does not have a significant influence on the jet shear relative to background turbulence at higher frequencies. While maximum amplitudes of E_{uu} and E_{vv} in the jet shear are only slightly higher than those in the inner swirl shear, the maximum amplitude of E_{cc} in Fig. 5.38(b) is about an order of a magnitude higher than that in Fig. 5.36(b). Figs. 5.38(c) and (d) only exhibit weak peaks at S_t=1.22 because the energy levels of the background broadband frequencies are very high: the average amplitudes of E_{ucuc} and E_{vcvc} are about an order of a magnitude higher than those of the inner swirl shear, as shown in Figs. 5.36(c) and (d). When comparing the amplitudes of E_{ucuc} and E_{vcvc}, it is obvious that the former is an order of a magnitude higher than the latter. In other words, turbulent transport of scalar in the axial direction dominates in the jet shear. Moreover, not only do E_{ucuc} and E_{vcvc} observe the $-5/3_{rd}$ Kolmogorov decay, the intensities of energy fluctuations actually increase drastically with higher frequencies. This implies that higher-frequency turbulence in the jet shear more likely represents energy-containing

range rather than inertial subrange, while the latter is the case with the inner swirl shear. It should be noted that the Kolmogorov -5/3 spectrum decay fits well for both E_{ucuc} and E_{vcvc} in other locations, although the 7/3rd decay has been shown to better represent the shear stress co-spectrum (Lumley 1967) and turbulent scalar flux co-spectrum (Mydlarski 2003 and Sakai et al 2008).

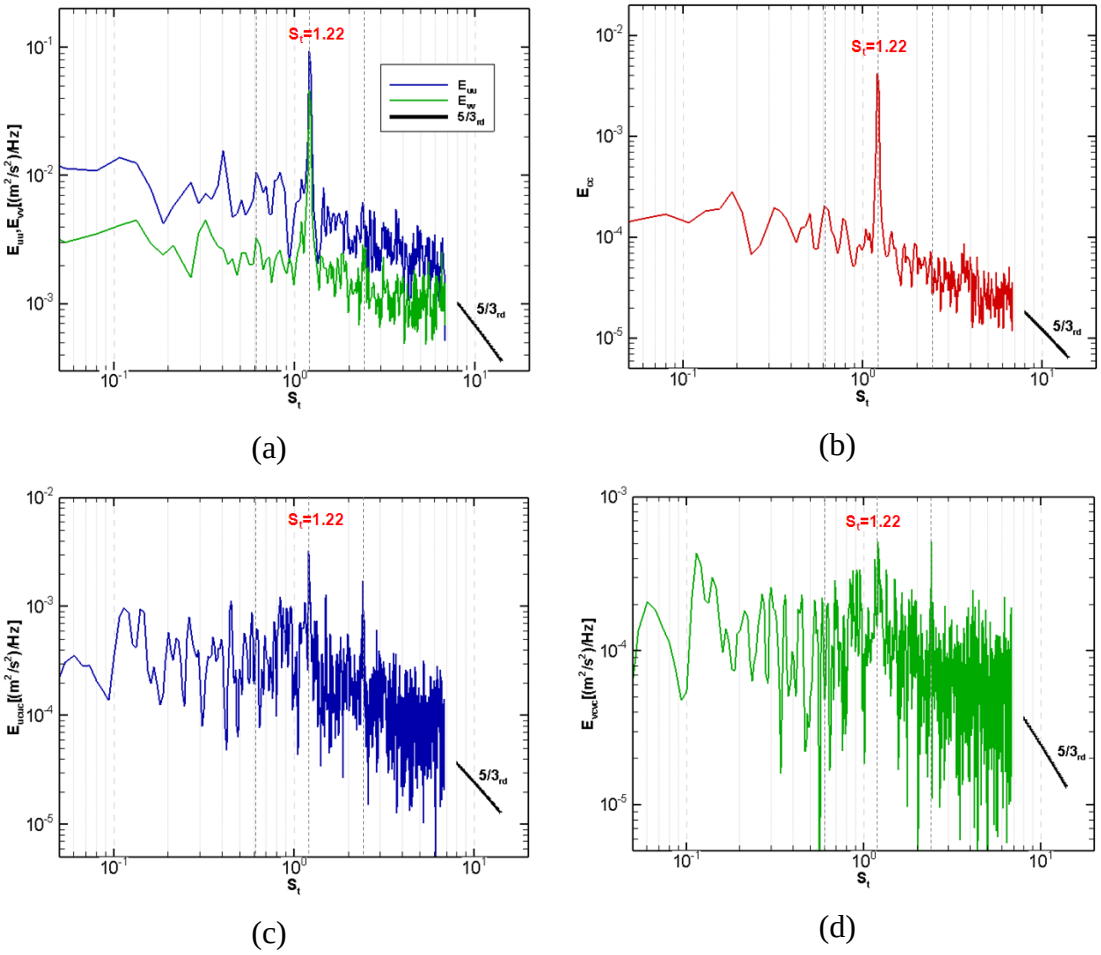

Fig. 5.38 PSDs of (a) u and v, (b) c, (c) uc, and (d) vc of a point in the jet shear

As shown in Fig. 5.39, both E_{uu} and E_{vv} have dominant spikes at S_t=1.22, but unlike the perfect match between $E_{uu}(S_t=1.22)$ and $E_{vv}(S_t=1.22)$ in Fig. 5.36(a), E_{vv} is roughly an order of a magnitude higher than E_{uu}. The much lower E_{uu} implies that perturbations of the axial velocity are damped by the strong forward momentum of the swirl stream. E_{cc} shown in Fig. 5.39(b) also has a dominant spike at S_t=1.22, but its amplitude is about an order of magnitude lower than that in the Fig. 5.36(b), thus a significant amount of scalar fluctuation energy is clearly dissipated in the inner swirl shear. The peaks of E_{uu}, E_{vv}, and E_{cc} at S_t=2.42 are also consistent with those found in

the inner swirl shear, but again the amplitudes are significantly lower. Finally, the peak at S_t=1.22 for E_{ucuc} and E_{vcvc} are not nearly as outstanding as those found in the inner swirl shear, and the amplitudes are also considerably lower. In other words, velocity-scalar coupling reduces significantly in the swirl stream, which also coincides the radial gradient of <uc> and <vc> shown in Fig. 5.30 and Fig. 5.31, respectively.

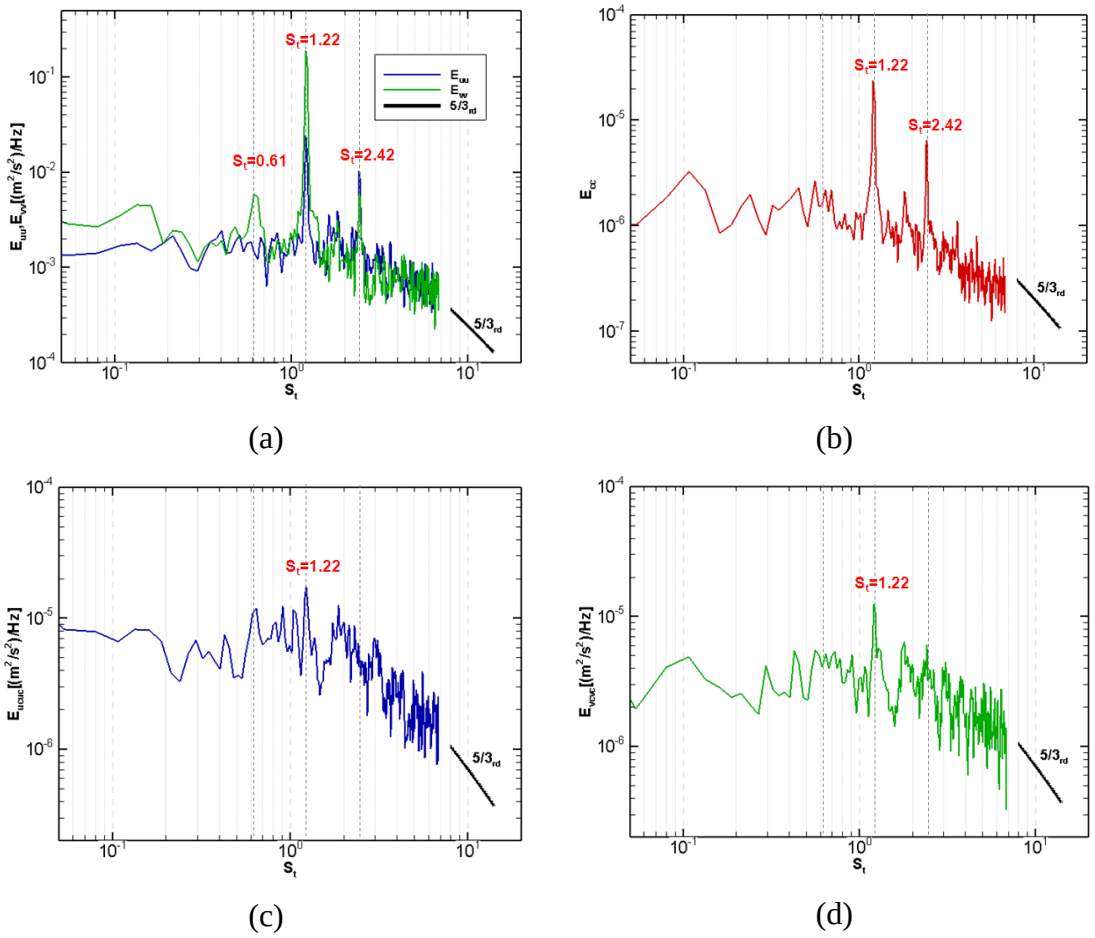

Fig. 5.39 PSDs of (a)u and v, (b) c, (c) uc, and (d) vc of a point in the swirl stream

Instantaneous snapshots shown in Fig. 5.22 highlights the tendency for the jet penetration to flap and that the radial distortion or bias of the jet spread may occur at x/D_s<0.5. Since both the jet shear and the inner swirl shear exhibit PSD peaks at S_t=1.22, it is therefore of interest to understand if directional bias of the jet spread further downstream can also be associated with the strong vortex pair. Thus, PSDs have been evaluated at x/D_s=0.7, r/D_s=0.2. As shown in Fig. 5.40, there is no evidence to suggest that radial variation in the jet spread at this location, in terms of both E_{vv} and E_{cc}, occurs with a dominant frequency. The lack of a distinguishable

spike in E_{uu} also suggests that vortices in the region are either not coherent in time or are occurring at a frequency that is too low to be resolved. Since there are no peaks found in E_{uu}, E_{vv}, and E_{cc}, plots of E_{ucuc} and E_{vcvc} have been omitted.

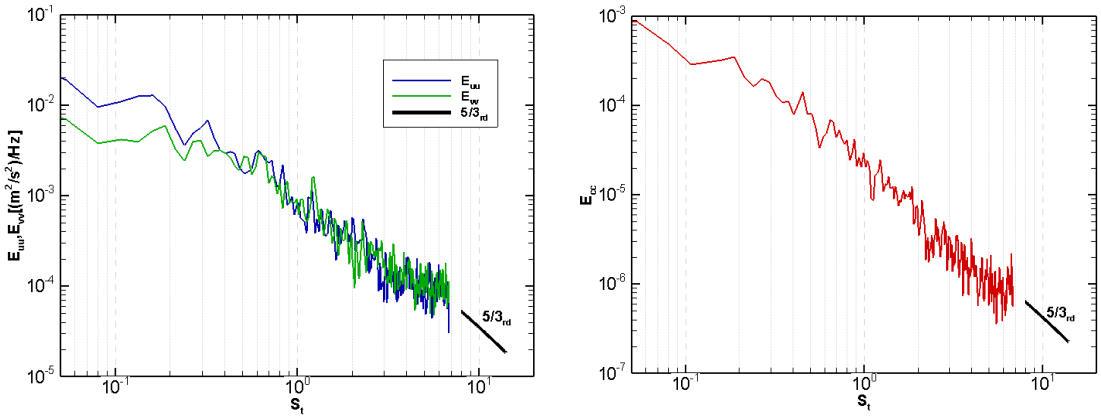

(a) (b)

Fig. 5.40 PSDs of (a) u and v, and (b) c of a point in the downstream jet spread

Besides flapping sideways, inspection of the instantaneous scalar fields (Fig. 5.22 and Fig. 5.23) reveals a variation in the downstream penetration distance as well. In addition, as it has been discussed in Section 5.2.3, a parcel of +c remains almost unchanged in the free stagnation region from Fig. 5.26(a1) to (a3), alluding to a possible low-frequency fluctuation. However, PSD evaluated at $x/D_s=0.8$, $r/D_s=0$, which is at the start of the free stagnation region, shows no dominant periodicity. Finally, the PSD computed at a point further downstream ($x/D_s=1.5$) along the centreline, as shown in Fig. 5.42, also shows no apparent spikes.

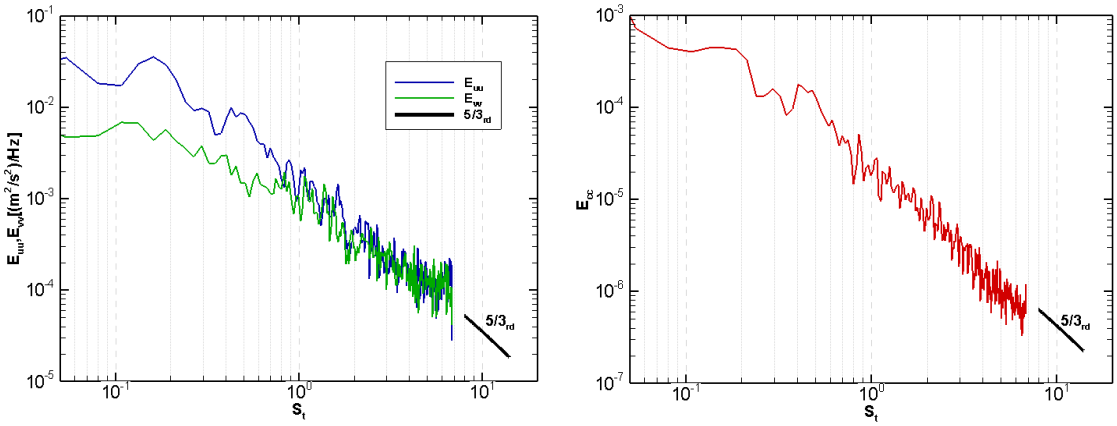

(a) (b)

Fig. 5.41 PSDs of (a)u and v, and (b) c of a point in the free stagnation region

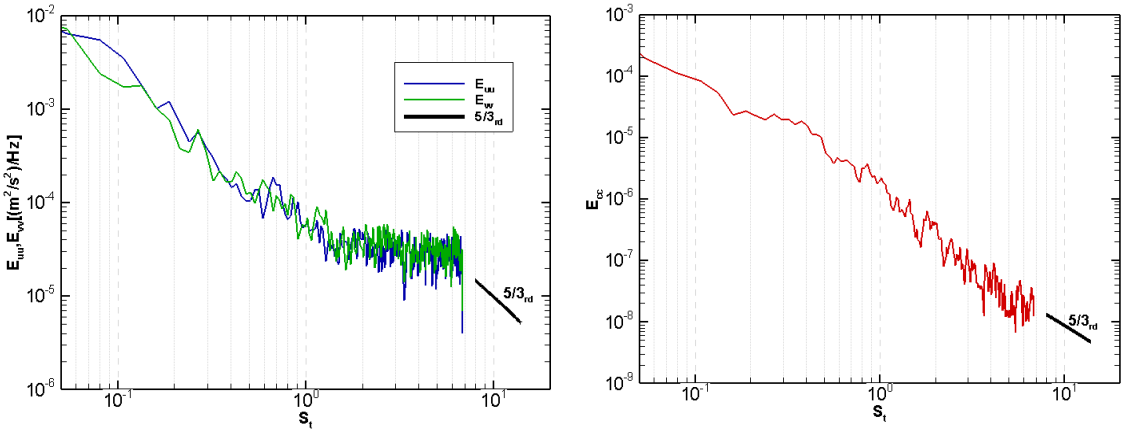

(a) (b)

Fig. 5.42 PSDs of (a)u and v, and (b) c of a point at x/D_s=1.5, r/D_s=0

Although characteristic Strouhal numbers of the coherent structures have been identified, maximum amplitudes of the spikes and how they are distributed in the flow field remain unknown. Here the maxima of E_{uu}, E_{vv}, and E_{cc} within ±3% of S_t=1.22, which represents the strong vortex pair, are plotted across the FoV, as shown in Fig. 5.43. The area characterised with non-swirl induced sub-pressure (Fig. 5.13(c)) has been superimposed to indicate contour positions relative to the inner swirl shear. Distributions of E_{uu} and E_{vv} shown in Fig. 5.43(a) and Fig. 5.43(b) confirm that effect of the strong vortex pair is not just limited to the inner swirl shear, but can also extend to the entire swirl stream to x/D_s=1; the amplitudes generally become weaker in the radial direction past the outer sub-pressure boundary. While $E_{uu}(S_t=1.22)$ decreases downstream along the inner swirl shear, $E_{vv}(S_t=1.22)$ actually increases and reaches a highest value at (x/D_s=0.4, r/D_s=0.5). As shown in Fig. 5.43(c), the radial expansion of E_{cc} from the jet shear into the swirl shear implies that the instantaneous snapshots shown in Fig. 5.24 occur periodically. This confirms periodic entrainment of the jet fluid with a concentration level that is quite to close that under stoichiometric condition, thus alluding to the possibility of heat release oscillations in the inner swirl shear.

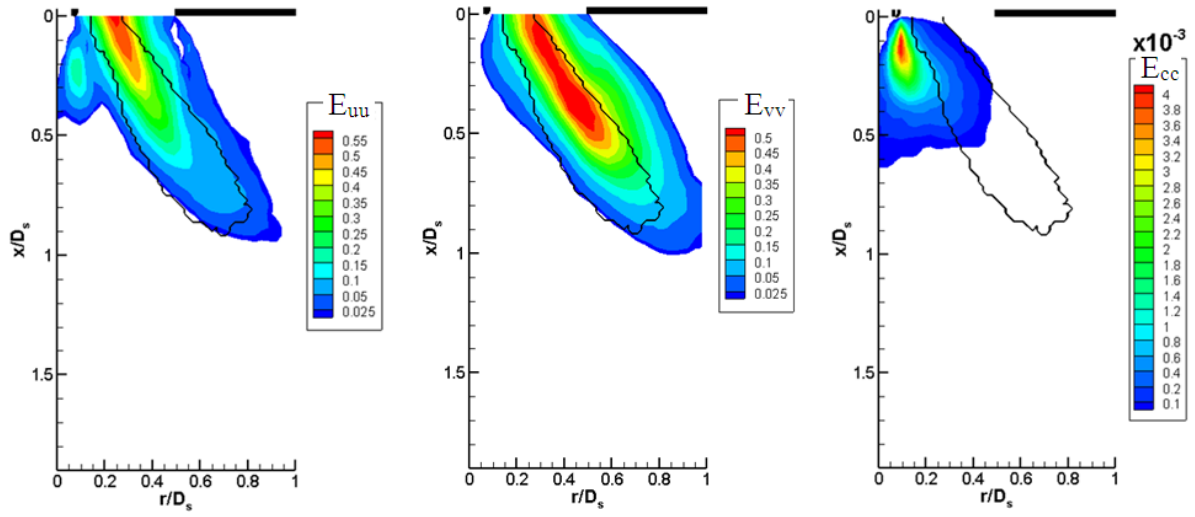

(a) (b) (c)

Fig. 5.43 Amplitude of the primary PSD spike at S_t=1.19: (a) E_{uu}, (b) E_{vv}, and (c) E_{cc}

Contours of the maxima within ±3% of S_t=2.42, which represents the frequency that combines both the strong and weak vortex pairs, are plotted in Fig. 5.44. Here each of E_{uu}, E_{vv}, and E_{cc} is about an order of a magnitude lower than its counterpart at S_t=1.22. The similarity between the contour distributions confirms that the weak vortex pair also follows the same helical paths as the strong pair, but its contribution to scalar entrainment and turbulent mixing is significantly weaker.

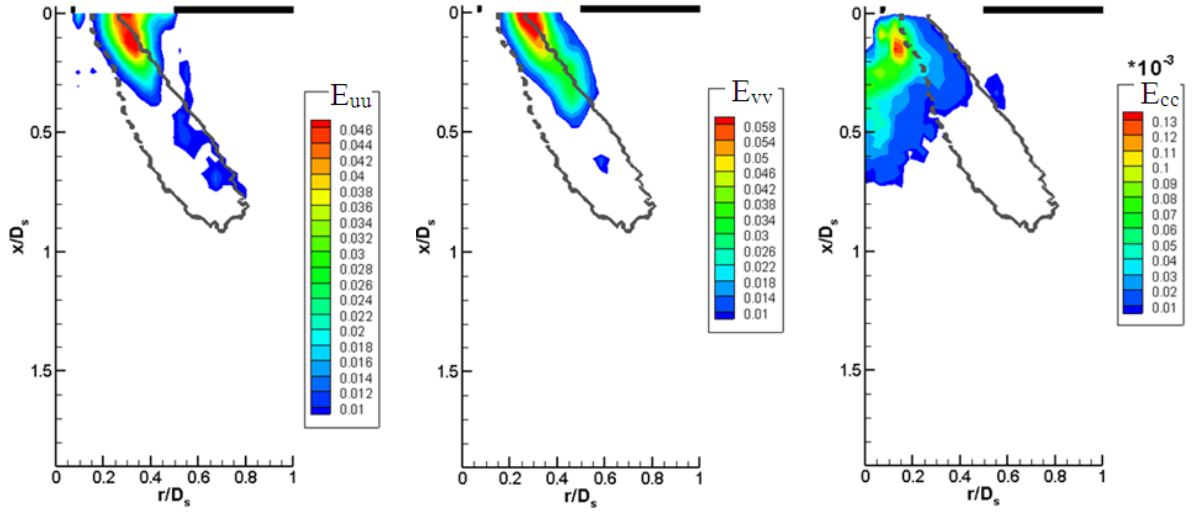

(a) (b) (c)

Fig. 5.44 Amplitude of the secondary PSD spike at S_t=2.38: (a) E_{uu}, (b) E_{vv}, and (c) E_{cc}

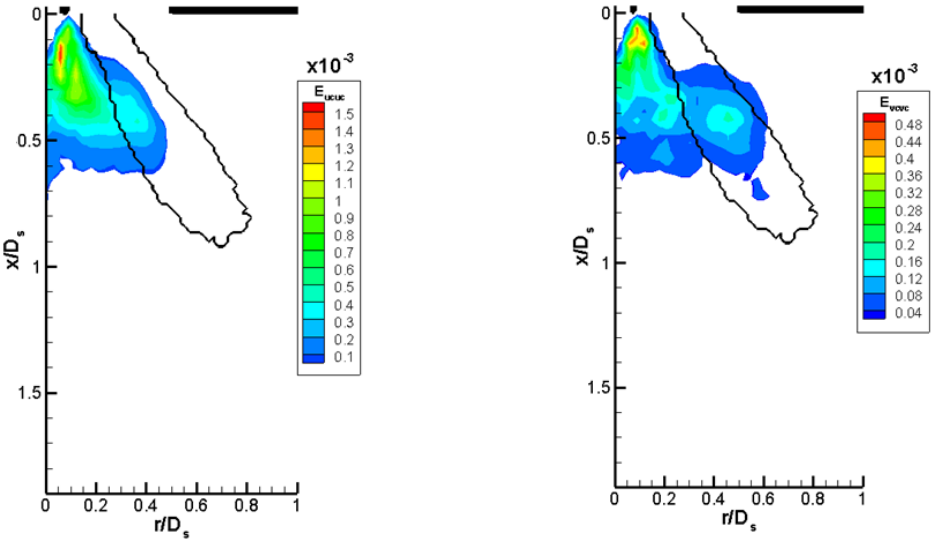

(a) (b)

Fig. 5.45 Amplitude of the secondary PSD spike at S_t=1.22: (a) E_{ucuc} and (b) E_{vcvc}

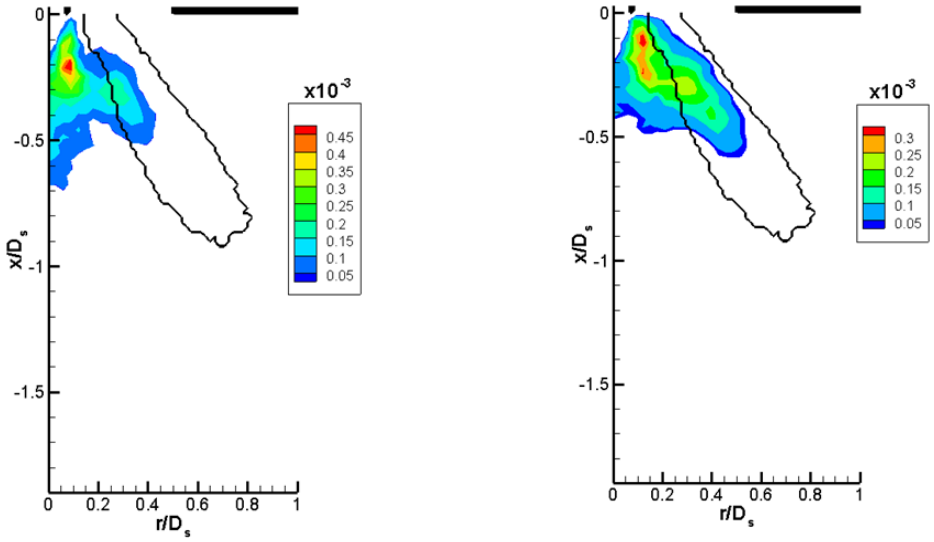

(a) (b)

Fig. 5.46 Amplitude of the secondary PSD spike at S_t=2.42: (a) E_{ucuc} and (b) E_{vcvc}

The same PSD computations have also been made on the turbulent scalar fluxes, the contours of maxima $E_{ucuc}(S_t=1.22)$ and $E_{vcvc}(S_t=1.22)$ are shown in Fig. 5.45. Again, Figs. 5.45 and 5.46 indicate majority of the turbulent transport of jet fluid by the coherent structures is limited to the very near field ($x/D_s<0.6$) and does not extend beyond the inner swirl shear.

5.3.3 Conditional averaging

Previous discussions highlighted that the coherent structures dominate the near field with discrete frequencies, as illustrated by the PSD estimates, but examples of the vortex-scalar interaction have only been illustrated using instantaneous snapshots. In this section, the techniques of conditional averaging (CA) and spatial correlations (SVC for velocity or SSC for scalar) are combined to provide more insight into the spatial behaviour of the coherent structures in the near field. As shown in Fig. 5.47, the points selected for the computation of SVC are both located in the inner swirl shear as indicated by a cross, and the contours shown are the SVC of the axial velocity, SVC(u). The stream traces that are superimposed on the contours are drawn from the conditionally averaged radial and tangential velocities, CA(<U>,<V>|u). The stream traces reveal two vortex pairs at both axial stations; again the strong vortices have the same rotational direction as that of the bulk swirling flow whereas the weak ones rotate in the opposite direction. Like the separation between the strong vortices or the weak vortices, the regions of positive SVC(u) are also separated by $\theta=\pi$. The distribution of SVC(u) is consistent with the bimodal pdf of the axial velocity shown in Fig. 5.34(a). In other words, while two quadrants are seeing strong localised reversals, the other two actually feature forward flows, as demonstrated in Fig. 5.16. The entire pattern of vortices and flow reversals is believed to rotate in the swirl direction with the local tangential velocity. In Fig. 5.47(a), the radial locations of the vortex 'eye' is at $r/D_s=0.29$, where $W/U_s=1.3$, and towards the outer edge of the vortex, $W/U_s(r/D_s=0.4)=1.45$, as shown in Fig. 5.7. Assuming the pattern rotates at the local time-mean tangential velocity, the Strouhal number, which can be computed as follows, should match that of the strong vortex.

$$S_t(r) = \frac{(W/U_s)}{2\pi(r/D_s)}\frac{D_h}{D_s} \tag{5.1}$$

The Strouhal numbers at the two representative radial locations are: $S_t(r/D_s=0.29)=0.58$ and $S_t(r/D_s=0.4)=0.64$, both of which are fairly close to Strouhal number of the strong vortex at $S_t=0.61$. This confirms that the doubling in frequency of the spike at $S_t=1.22$ must be the effect pairing of two strong vortices. The fact that the secondary spike is exactly twice that of the primary one implies that $S_t=2.38$ must

therefore be associated with the passage of the vortex pairs. In other words, the vortex pairs are rotating with the mean tangential velocity at the exit plane.

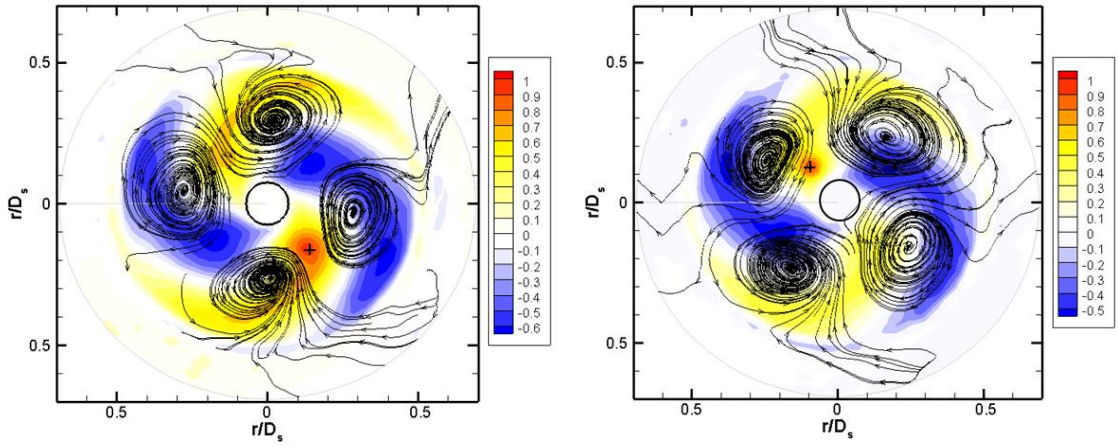

(a) (b)

Fig. 5.47 Contours of SVC(u) with superimposed stream traces of radial-tangential velocity, averaged conditionally upon axial velocity at (a) x/D_s=0.02 and (b) x/D_s=0.27

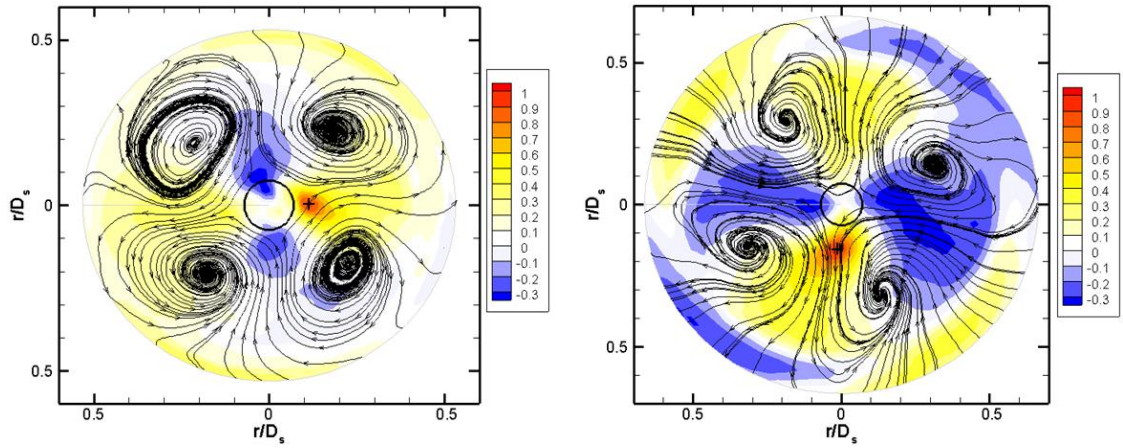

(a) (b)

Fig. 5.48 SSC contours of concentration with superimposed stream traces of radial-tangential velocity, averaged conditionally upon concentration at (a) x/D_s=0.02, and (b) x/D_s=0.27

Fig. 5.48 shows the SSC at x/D_s=0.02 and x/D_s=0.27. The correlation patterns at the two axial stations are similar, although the SSC at x/D_s=0.27 is more dispersed than that at x/D_s=0.02 since the jet has spread downstream. Fig. 5.48 again reinforces the observation that the pattern of counter-rotating vortices is conducive to drawing jet fluid into two quadrants while leaving the other two in fuel-lean condition. Such contrast of rich and lean states also oscillates with the distinct Strouhal numbers identified earlier. Although the reference points are located in the inner swirl shear,

the distributions of positive and negative SSC clearly extends into the jet shear, meaning that scalar perturbations in the inner swirl shear are correlated with those in the jet shear.

Conditional averaging has also been applied to highlight the effect coherent structures have on the scalar flux, as shown in Fig. 5.49. The conditionally averaged dataset was created by selecting instantaneous velocity vector fields greater than 1.5 times the radial RMS at the point located at x/D_s=0.1, r/D_s=0.33, as indicated by the red dot in Fig. 5.49. From the low-speed xr data of 1500 samples, a subset of 230 samples satisfies this criterion. The scalar flux of this subset was then calculated. Again, a sequence of counter-rotating vortices is present in the swirl stream. The axial scalar flux contour of this subset agrees well with that of the complete set (Fig. 5.30 and Fig. 5.31) in terms of the shape but the magnitudes are about 40% higher than the latter in the jet shear. The radial scalar flux of the subset also shows similar radial expansion (between x/Ds=0.15 to x/Ds=0.4), but the magnitudes of the radial scalar flux here is also around 40% higher than that of the complete set.

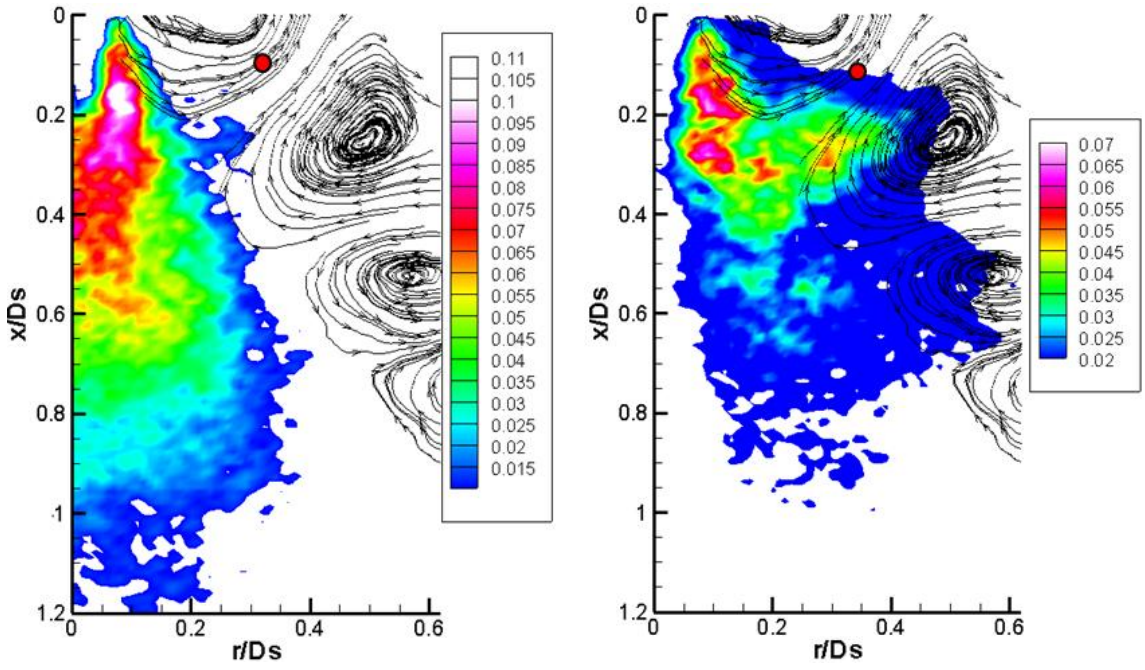

(a) (b)

Fig. 5.49 Stream traces of conditionally averaged fluctuating velocity superimposed on (a) radial scalar flux and (b) axial scalar flux contours

5.3.4 Proper orthogonal decomposition

Although instantaneous and conditionally averaged velocity and scalar fields reveal the shapes and locations of coherent structures, they do not necessarily provide quantitative information regarding their contribution to turbulent energy. For this purpose, POD was used as a means to estimate the percentages of energy contained in the most energetic turbulent motions, as represented by the first two or three POD modes. POD had been applied by Midgley (2005) on an x-r plane and r-θ plane data, these are shown in Fig. 5.50. The first POD mode in the x-r plane shows vortices that decay in strength in the axial direction, with the weakest vortex at x/D_s~1.1 becoming barely visible. This is similar to the TKE shown in Fig. 5.12 and the amplitudes of the PSD shown in Fig. 5.43, both of which show sharp decline near the same location. The first POD mode in the r-θ plane shown in Fig. 5.50(b) reveals two counter-rotating vortex pairs; this mode accounts for 23% of the energy for the flow at this axial station.

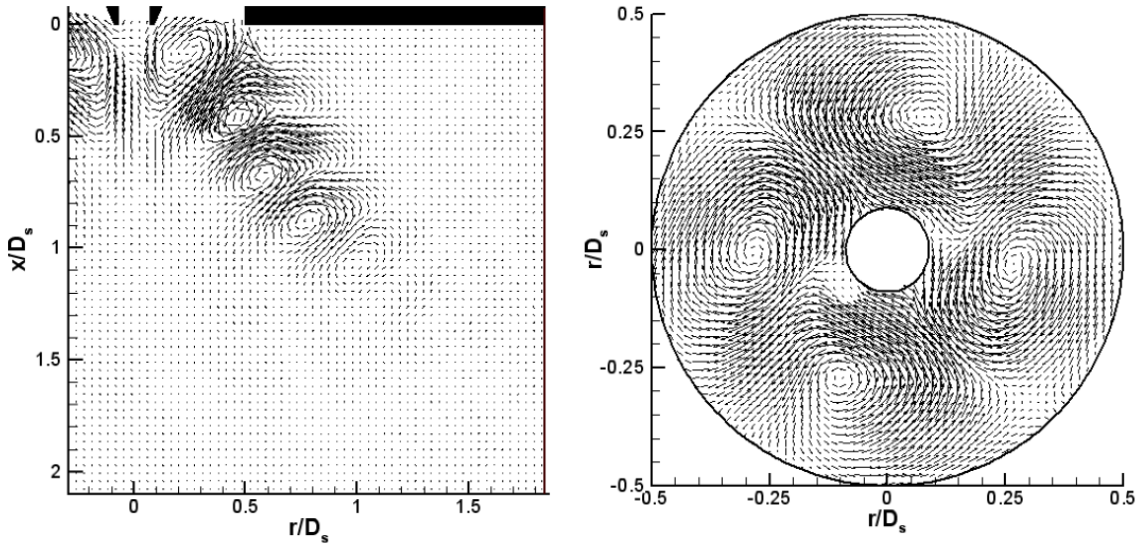

(a) (b)

Fig. 5.50 First POD mode (a) in the x-r plane, and (b) in the r-θ plane at x/D_s=0

Despite having identified the sequence of vortices in the x-r plane in the two vortex pairs in the r-θ plane, POD modes of the axial velocity and the concentration in the r-θ plane, which are two equally important flow attributes, were not provided. For the first time, POD analyses on all three velocity components and scalar have been performed on this fuel injector. Fig. 5.51 shows the first two POD modes of axial

velocity contour with radial-tangential velocity stream traces in the r-θ plane at x/D_s = 0.02. The first and second POD modes of the axial velocity component show two pairs of spiral-shaped regions of forward flow and reverse flows. The same pattern of vortices can also be seen in the contours of SVC(u) in Fig. 5.47. There is also an angular separation of roughly θ~π/4 between the first and the second POD modes. The maxima of flow reversals are located at r/D_s~0.2, as indicated by the dark blue colour bands, these locations of these relative to the vortices are quite similar to those identified in Fig. 5.16(a). Hence, the first and second POD modes indicate that radial outward turbulent motion is associated with flow reversals, the strength of which reaches maximum in the inner swirl shear. The other two quadrants in the inner swirl shear show an entirely opposite condition, where strong positive (forward) flows prevail. The patterns of the negative axial velocity could also imply that it is the strong vortices that are responsible for creating bursts of flow reversals in the inner swirl shear, but they also extend into the swirl stream and couple with the weak vortices that are θ~π/4 away.

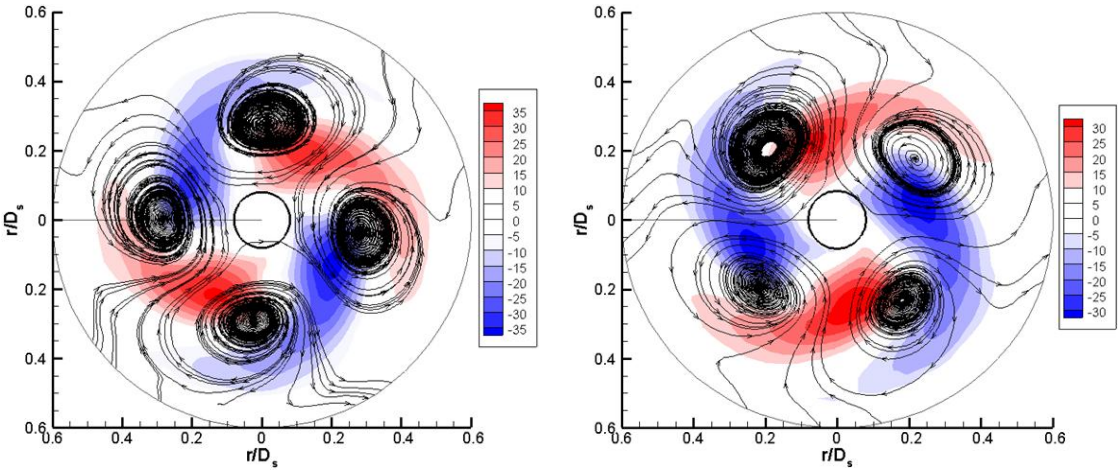

(a) (b)

Fig. 5.51 Contours of (a) First and (b) second POD modes of axial velocity with superimposed radial-tangential stream traces at x/D_s=0.02

The first and second POD modes of concentration shown in Fig. 5.52 indicate that parcels of high concentration are found when the streamlines between two neighbouring vortices point radially outward, while the opposite is true when the streamlines point radially inward. Moreover, the circumferential distributions of positive and negative contours of scalar in the jet shear (Figs. 5.52(a) and (b)) are very

similar to those of axial velocity (Figs. 5.53(a) and (b)) in the inner swirl shear. This suggests that the two minima of axial velocity in the first two POD modes are likely correlated with the low-pressure cores of the vortices, which help to draw the jet fluid outward. The finding here is consistent with Fig. 5.48(a), proving that although the coherent structures dominate only in the inner swirl shear, the low pressure centres it generates are strong enough to cause distort the jet exit profile. This, along with Fig. 5.54(b), again confirms the previous observation that the near-field experiences alternating patterns of fuel-rich and fuel-lean conditions in each quadrant from the jet shear to the inner swirl shear, and the oscillation of this pattern occurs at the specific frequencies identified in Section 5.3.2.

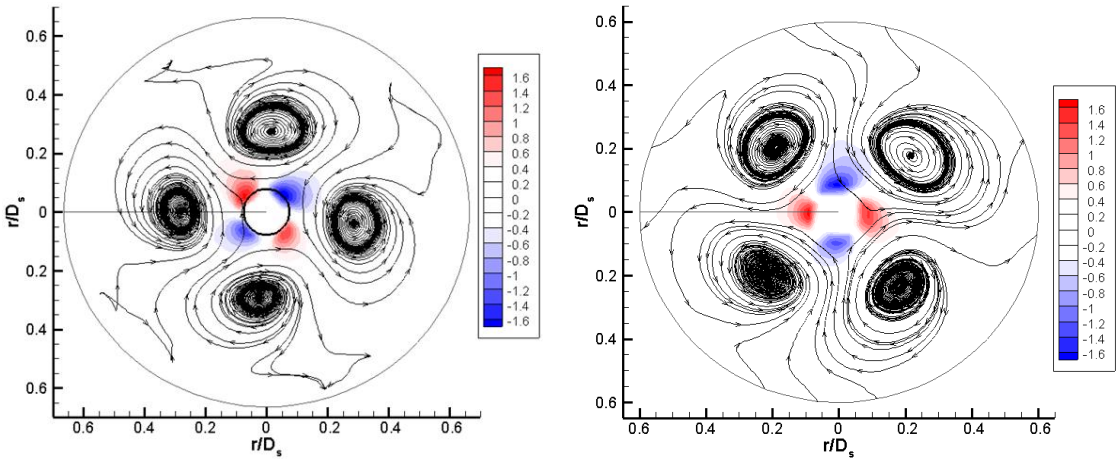

(a) (b)

Fig. 5.52 (a) Contours of (a) First and (b) second POD modes of concentration with superimposed radial-tangential stream traces at x/D_s=0.02

Cumulative energy distribution of the higher modes has been omitted in Fig. 5.53 because the first 50 account for more than 70% of the total turbulent energy and scalar energy. In fact, the first two modes of velocity account for 47% to 50% of the turbulence energy, and the first two modes of scalar accounts for around 50% of the scalar energy. Although not shown here, it may be noted that the 3rd and 4th POD modes reveal a total of 4 pairs of vortices, thus they are not representative of physical flow structures.

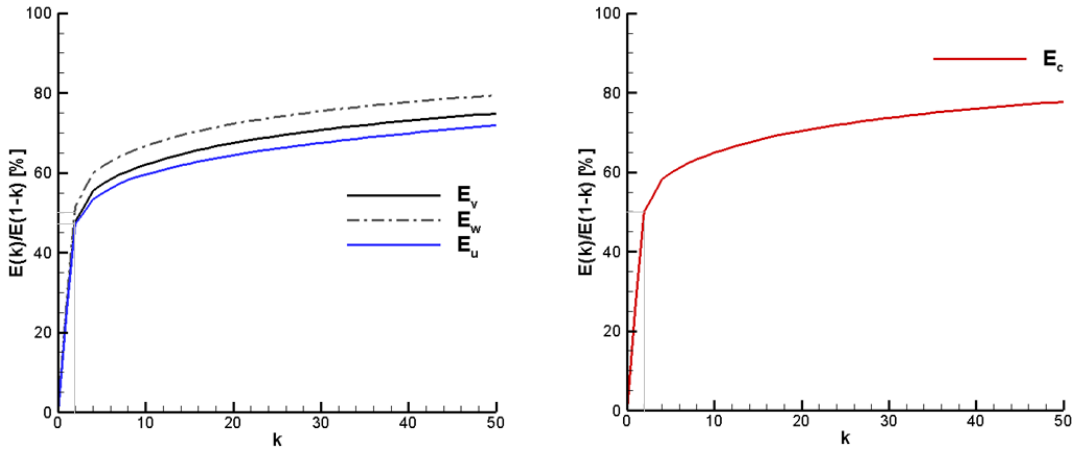

(a) (b)

Fig. 5.53 Cumulative distribution of energies across the first 50 POD modes of (a) 3C velocity and (b) concentration

Fig. 5.54 shows the 1st POD mode of velocity and scalar at x/D_s=0.27. As expected, the alternating patterns of maxima and minima, as well as the 'eyes' of the vortices, have all spread out in accordance with the expansion of the swirl cone. Similar to Figs. 5.51 and 5.52, positive patches of scalar in the jet shear are followed by negative trails of axial velocities in the inner swirl shear. In addition, the fact that both contours of axial velocity and scalar appear to spiral towards the clockwise direction suggests that the paths of vortices are also wound in the clockwise direction, opposed to the bulk flow, as will be discussed in more details in Section 5.4.1.

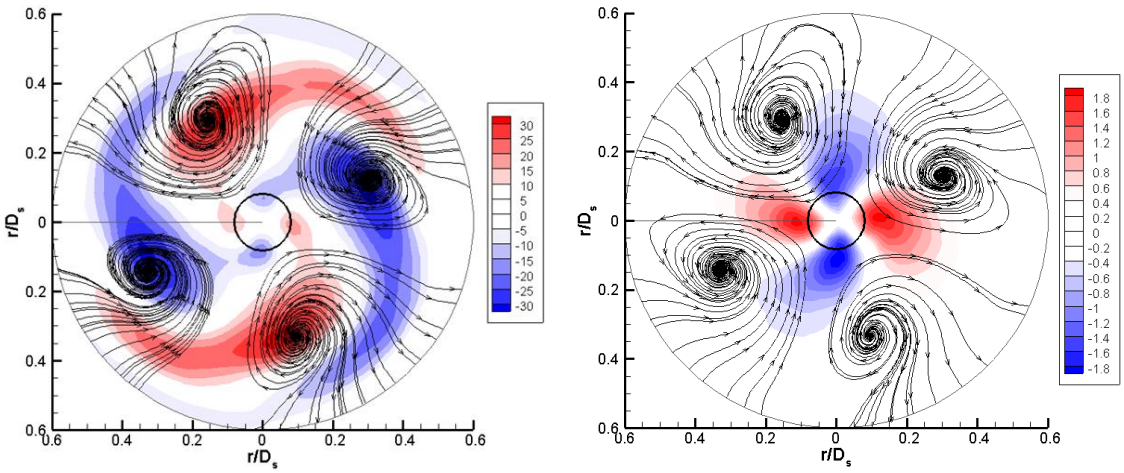

(a) (b)

Fig. 5.54 1st POD mode of (a) axial velocity and (b) concentration with superimposed radial tangential stream traces at x/D_s=0.27

5.4 Reference to LES predictions

Given that the LES predictions reported by Dianat (2007) are carefully validated against the current experimental data, as described in Cheng et al (2012), then LES results can be referenced to provide additional understanding of the flow and mixing characteristics. For example, LES predictions can complement experimental data in terms of its ability to fully characterise 3D flow and mixing fields throughout the dump expansion chamber and, more importantly in the swirl passage, where high-quality near-wall measurements of passive scalar are particularly difficult to acquire due glare and hence a low ratio of fluorescence to background noise. Similarly, LES predictions can serve as a valuable alternative in regions where measured errors associated with spatial averaging are known to be large. A brief description of the simulation method, including the LES mesh geometry, is provided in Appendix 5.1. A comparison of the LES implicit filter width and PIV interrogation window size, relative to the local integral length scale, is provided in Appendix 5.3. This section starts by discussing the LES-predicted flow and mixing features that could not be confidently determined from planar imaging experiments, followed by direct comparisons of first and second-order statistics with a focus in regions/stations of main discrepancies.

5.4.1 LES results

Perhaps the most important new finding from the LES data is that the flow separation that occurs in the inner surface of the swirl passage is time-dependent and can occur with varying tangential locations depending on the location of the vortex, which also draws jet fluid from the cylindrical chamber upstream into the fuel injector. Fig. 5.55 shows that the flow separation near x/D_s=-0.25 is associated with a vortex that has strong flow reversal near the inner wall of the swirl passage, and a parcel of jet fluid is clearly entrained by the vortex's low pressure centre from under the jet lip into the swirl passage. This is consistent with the -<uc> in the inner swirl shear just downstream of the exit plane, as shown in Fig. 5.30. Fig. 5.56, taken at an arbitrary time period after Fig. 5.55, shows that the vortex has moved outside the swirl passage and the flow in it is now fully attached. This transition from separation to attachment is consistent with the bi-modal nature of pdf(U) shown in Fig. 5.34(a).

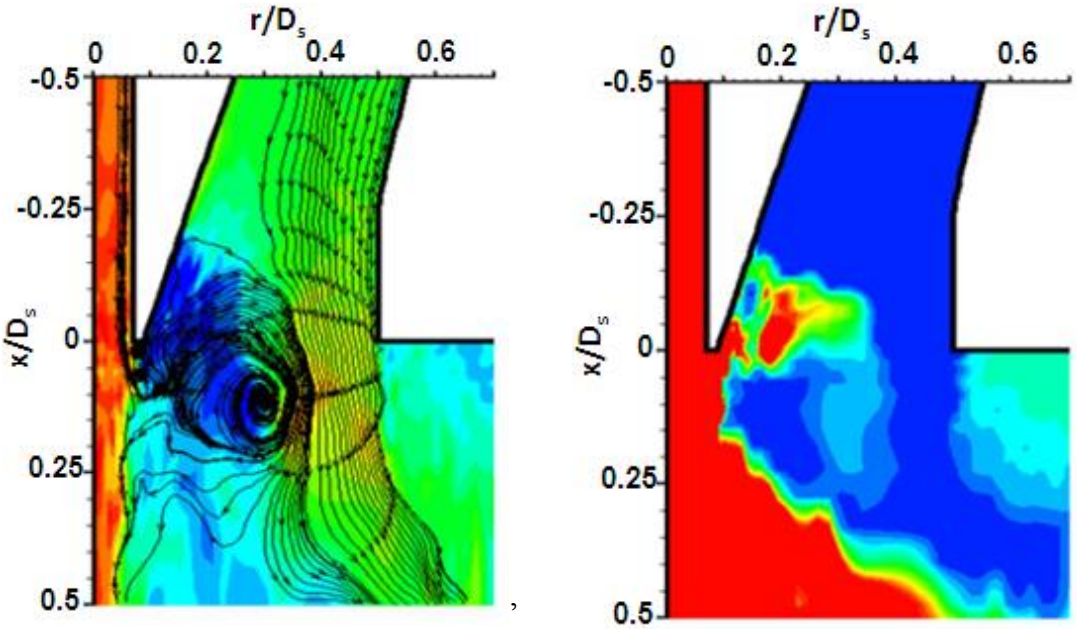

(a) (b)

Fig. 5. 55 Instantaneous (a) velocity and (b) concentration at t=I

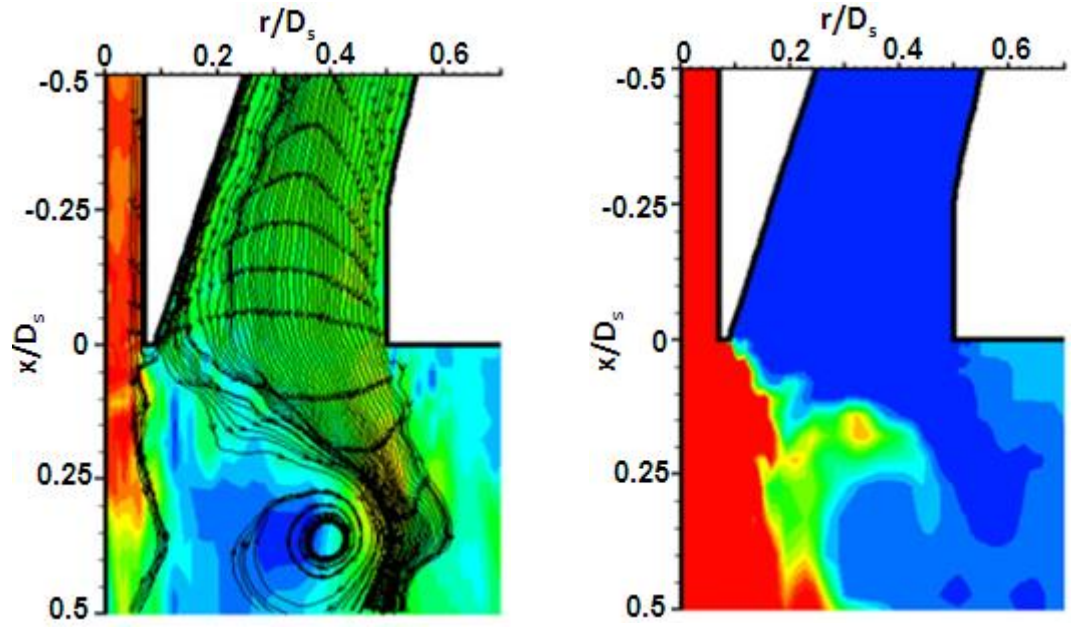

(a) (b)

Fig. 5.56 Instantaneous (a) velocity and (b) concentration at t=II

Another important flow feature that could not be confidently determined from planar PIV data is the helical path each of the two-strong and two-weak vortices takes. Fig.

5.57 is taken from Dunham (2010), which shows the iso-surface of R_{ww} with the reference point at x/D_s=-0.2, r/D_s=0.1, θ=0.

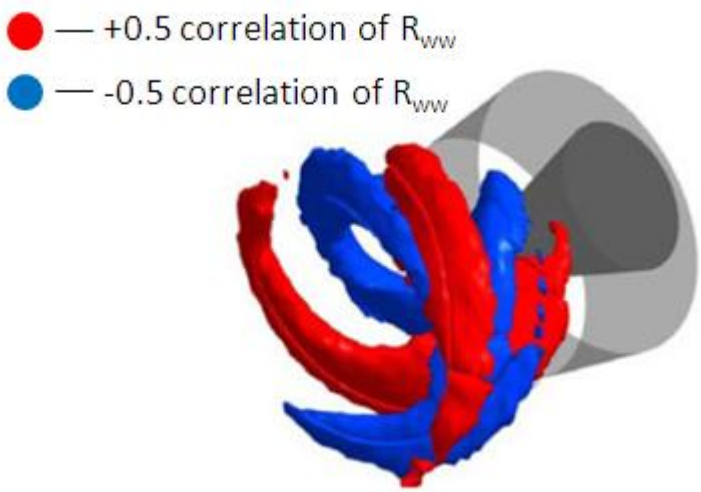

Fig. 5.57 Iso-surface of correlation of axial velocity

Two pairs of helices have been identified and they spiral downstream in the clockwise direction, which happens to be opposite to the counter-clockwise direction of the bulk swirling flow. Although not explicitly marked in Fig. 5.57, these helices are bounded within the swirl cone and the level of correlation becomes negligible near x/D_s=1.0. Moreover, the characteristic frequencies (Strouhal numbers) of these pairs of vortices are predicted quite well by LES, as detailed in Cheng et al (2012).

5.4.2 Validation of LES predictions

In general, there is good agreement between LES predictions and experimental data in terms of the shapes, sign, locations of maxima and minima, and rates of decay. Direct comparisons of time-mean and RMS velocities and concentrations at different axial stations are presented in Appendix 5.2; discussion here is mainly focused on regions and/or stations where notable discrepancies are found. Although the profiles at the exit plane are in excellent agreement (see Appendix 5.2), Fig. 5.58(a) shows that the mean centreline axial velocity is overpredicted by about 20% at x/D_s=0.27. The discrepancy here cannot be explained by the experimental error, as indicated by the red error bar, which was estimated by summing the sample size error (Eq. 4.31) and uncertainty in the mass flow split (Section 2.1.6). Fig. 5.58(b) also shows that LES

overpredicts the axial velocity again at x/D_s=1.06, where the time-mean measured data indicates stagnation. Here the error bars are not plotted because the absolute values are near zero. Also, the values at larger radii ($r/Ds \geq 0.5$) are underpredicted. A small adjustment (reduction) in the value chosen for the SGS Schmidt number may help in improving the predicted profile, but no attempt has been made to explore this.

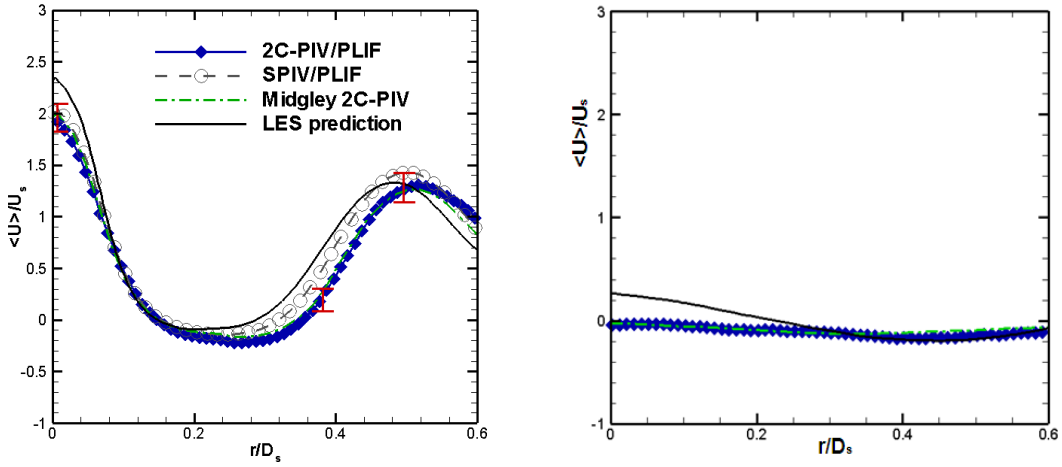

(a) x/D_s=0.27 (b) x/D_s=1.06

Fig. 5.58 Profiles of $<U>U_s$ at (a) x/D_s=0.27 and (b) x/D_s=1.06

Similar to the differences in $<U>/U_s$, the mean concentrations predicted by LES also overshoots those of experimental data, as shown in Fig. 5.59. Interestingly, the same discrepancies were found in the work reported by Wegner et al (2007), in which the LES predictions also consistently overshoot the acetone PLIF data of Janus et al (2004) even though the exit-station profiles agree well. The error bars plotted in Fig. 5.59(a) are estimated by the summing the PLIF error (Section 3.3.6) and sample size error.

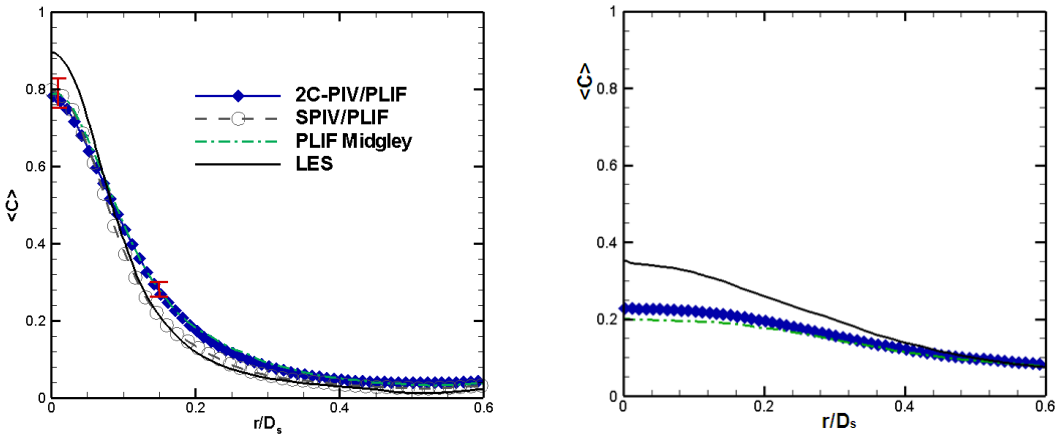

(a) x/D_s=0.27 (b) x/D_s=1.06

Fig. 5.59 Profiles of <C> at (a) x/D_s=0.27 and (b) x/D_s=1.06

Predictions and experimental data for velocity rms and scalar fluctuations at injector exit are shown in Fig. 5.60. The rms experimental data has been corrected using the method of Spencer and Hollis (2005) with the exception of $<w>/U_s$ due to the limitation with calculating tangential integral length scales. The measured <u> is reproduced quite well, the two peaks on the inner and outer swirl shear layer edges are in good agreement with measured data; in between these peaks the shape is reproduced but the level is underpredicted. Similar remarks can be made for the radial and tangential rms velocities although the outer edge peak is overpredicted. Overall the agreement is encouraging, the main region where large discrepancies also happen to be where the measured errors are largest.

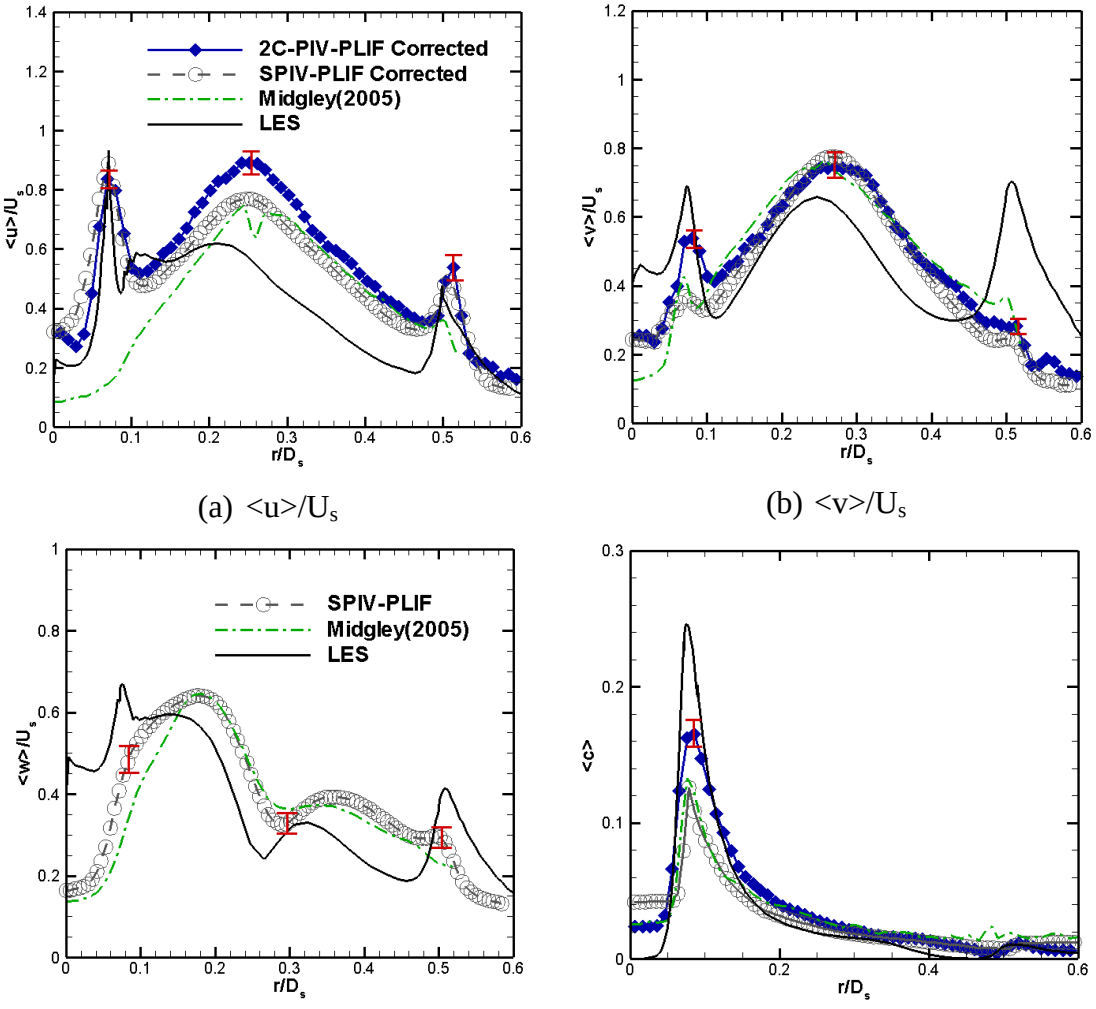

(a) $<u>/U_s$ (b) $<v>/U_s$

(c) $<w>/U_s$ (d) <c>

Fig. 5.60 RMS velocity and scalar profiles at x/D_s=0.02

Finally, the most direct measure of accuracy of modeling of scalar mixing is to compare the predicted turbulent scalar fluxes against the current combined PIV-PLIF data. An overview of this for the whole near field is shown in Fig. 5.61, which shows that the main regions of peak turbulenet scalar fluxes are well predicted by LES and the locations of sign changes are also remarkably similar. The overlaid gray lines in Fig. 5.61(a) and (b) indicate the regions where errors in velocity due to spatial averaging are in excess of 10%: $Err(\Delta x_{PIV}/{}^{1}L_{11})>10\%$ in Fig. 5.61(a) and $Err(\Delta x_{PIV}/{}^{2}L_{22})>10\%$ in Fig. 5.61(b). Their counterparts in scalar, namely $Err(\Delta x_{PLIF}/{}^{1}L_{44})$ and $Err(\Delta x_{PLIF}/{}^{2}L_{44})$, are not shown because they are relatively insignificant, as discussed in Section 4.3. It is clear that the main regions where errors in velocity can impact the turbulent scalar fluxes are in the jet shear at $r/D_s<0.1$. Since the accuracy of the measured fluctuating velocity in the region is poor and LES employs much higher spatial resolutions in this region (see Appendix 5.3), it cannot be stated with certainty that the LES predictions are in error.

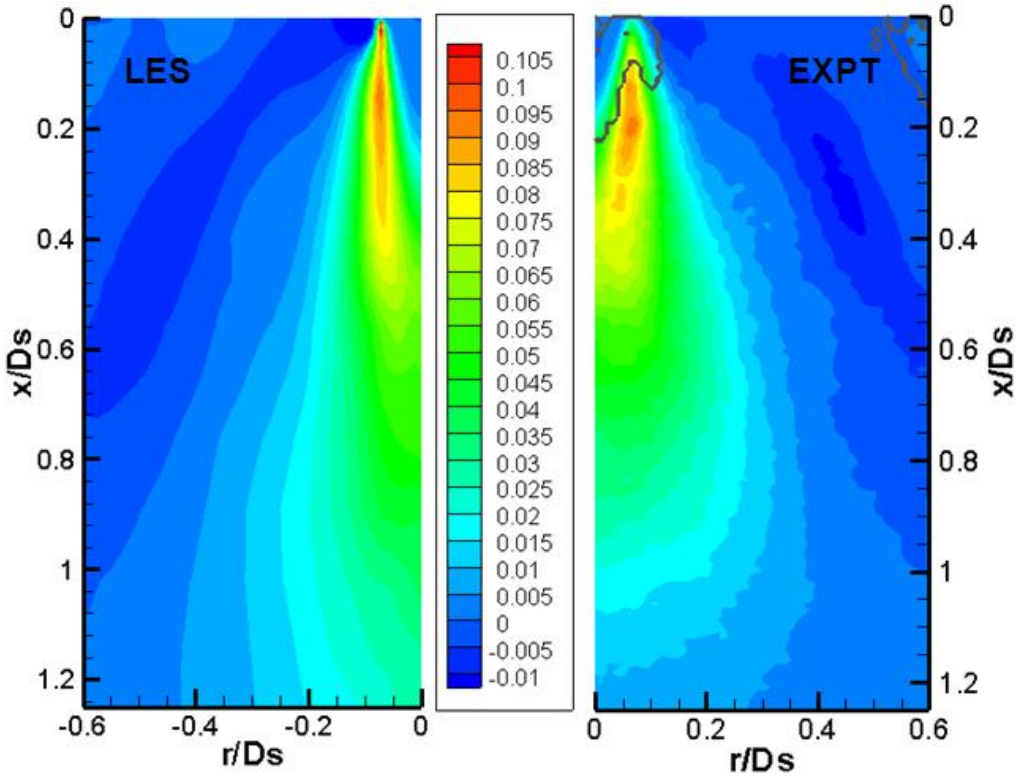

(a)

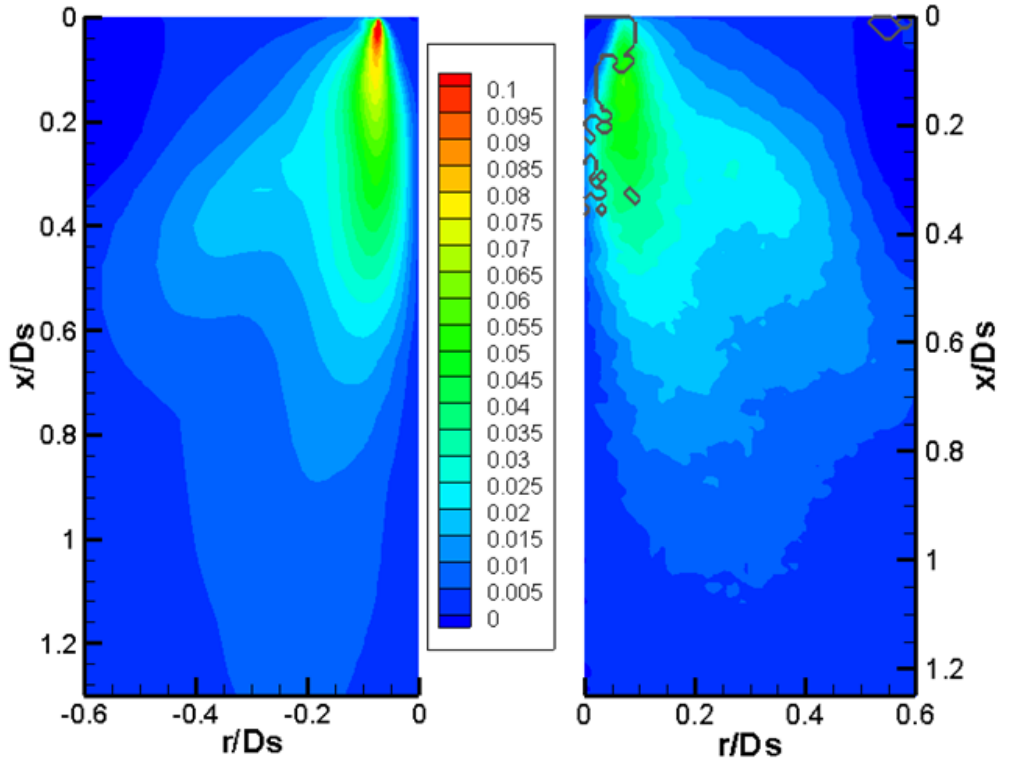

(b)

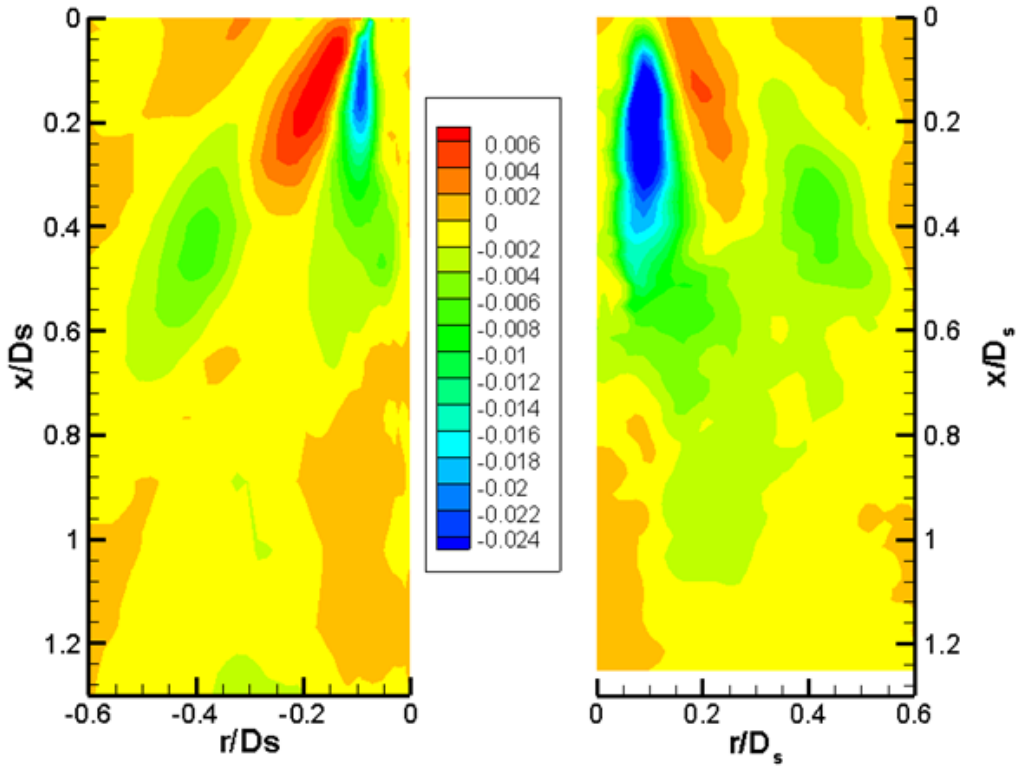

(c)

Fig. 5.61 Scalar flux contours, LES versus experiment: (a) <uc>/U_s, (b) <vc>/U_s, and (c) <wc>/U_s

A more precise and quantitative validation test is to compare radial profiles directly; this is done in Fig 5.62 in axial stations: x/Ds=0.13 and x/Ds=0.53 (comparisons at other axial stations can be found in Appendix 5.2).

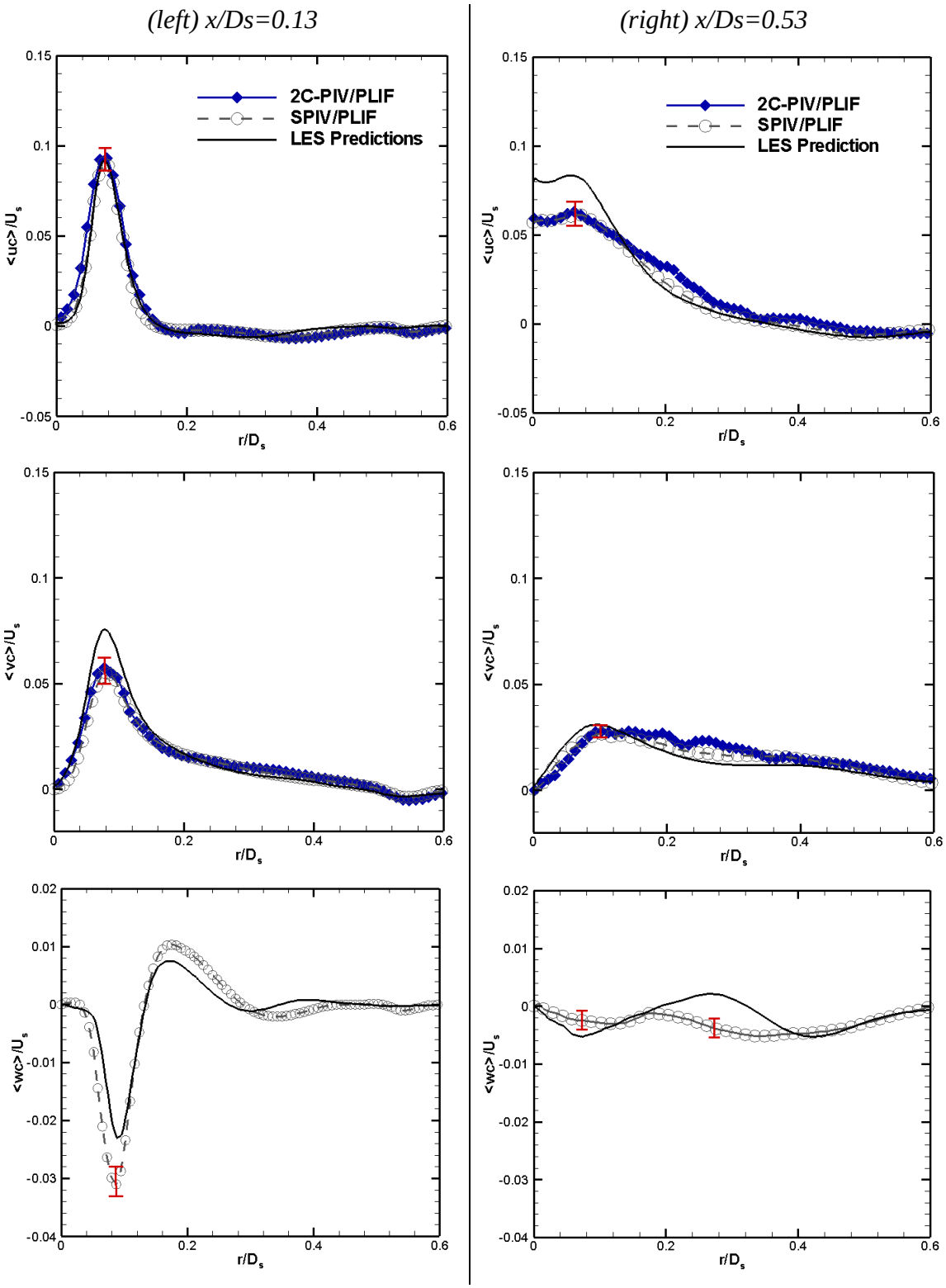

Fig. 5.62 Turbulent scalar flux profiles at two locations, x/DS = 0.13 (*left*) and x/DS = 0.53 (*right*) axial (*top*), radial (*middle*), tangential (*bottom*)

The error bars indicate the combined error estimate of sample size error (Eq. 4.34) and PLIF error (Section 3.3.6). While discrepancies can be seen, again in particular for some peak values, the agreement with measured data on sign, profile shape, rate of decay, and the relative magnitude of axial, radial, and tangential turbulent scalar fluxes is considered excellent. It is a considerable achievement to have this level of agreement for all three turbulent scalar fluxes in a flow as complicated as the present case with a scalar SGS model as simple as that selected for use in the present LES. This is new and significant validation of the ability of LES, incorporating what is the simplest SGS model for scalar mixing (constant Schmidt No.), to predict the important properties controlling scalar mixing in this practically relevant flow test case.

Finally, comparisons of the pdf's are presented in Fig. 5.63. The measured and predicted data at a point close to the injector exit plane and located in the propagation path of the helical vortices emanating from the injector internal separation (x/D_s=0.02, r/D_s=0.23, θ=0) have been analysed. As shown in Fig. 5.63, the velocities exhibit bimodal pdfs in both LES predictions and measurements, although to different extents, but the second maximum in the predicted scalar pdf at C~0.02 is not seen in the measured pdf. Although scalar-related quantities of interest were not adversely affected by errors associated with spatial filtering, they can indeed be affected by an overall error of 3.7%, as discussed in Section 3.3. In particular, the small pulse-to-pulse variation of laser sheet intensity (~2.9%) introduces a 'noise floor' for scalar concentration data close to zero, so that the LES-predicted scalar pdf shape shown in Fig. 5.63(d) cannot be resolved accurately by the current experimental method. Therefore, for the scalar concentration here, it has only been possible to analyse the LES data, and similar bimodal pdf's of scalar have also been observed and attributed to the passage of large-scale structures by Froehlich et al (2008). Unfortunately, its experimental confirmation has to await an improved experimental technique, perhaps based on monitoring and correction for variation in laser source energy pulsations.

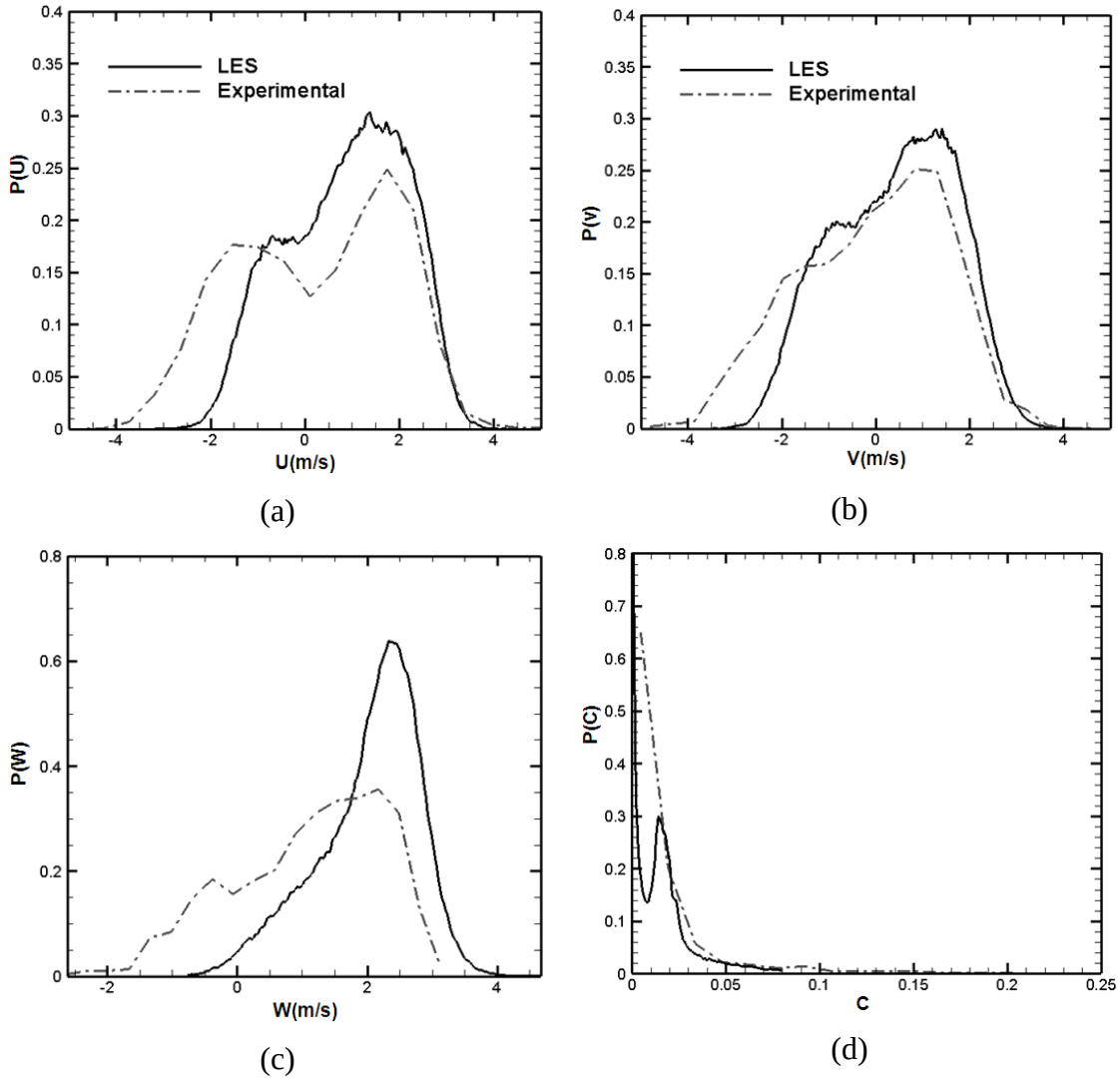

Fig. 5.63 pdf's of (a) axial, (b) radial, (c) tangential velocities, and (d) scalar concentration

5.5 Chapter summary

This chapter starts with an overview of the flow field, in which the main flow features such as jet penetration, free stagnation region, outer wall attachment location, CTRZ, CRZ, and backflow into the swirl passage have been identified. Discussions on the time-mean 3-component velocity profiles focused on the sign changes of radial and axial velocities at the exit plane, alluding to the probability of flow separation well inside the swirl passage. Profiles of the tangential velocity decay in the axial direction, resulting in progressively reducing dp/dr downstream; this causes a lower radial pressure gradient and sets up a negative dp/dx. Coupling between the axial and tangential components means momentum carried by the weakening forward axial flow would not be strong enough to overcome the adverse axial pressure gradient,

finally resulting in a vortex breakdown and the formation of a recirculation bubble. Profiles of rms velocities and contours of turbulent shear stresses reveal high turbulence intensities in the jet shear and the inner swirl shear layers, and the latter's rise in turbulence intensities is linked to the presence of coherent structures. The time-mean static pressure field reduced from the Reynolds averaged momentum equation was further divided into a swirl-induced component and a non-swirl-induced one. The latter shows that the inner swirl shear is dominated by high sub-pressures, which indicate the time-mean path taken by the coherent structures. This is consistent with examples of instantaneous 3C flow fields, which show that two strong vortices, separated by $\theta=\pi$, exist in the swirl stream and they induce strong flow reversals in the inner swirl shear.

The time-mean scalar field shows that the concentration decays rapidly and becomes fully mixed at about 1.5 swirl diameters. RMS concentrations peak in the jet shear and also decay rapidly in the axial and radial directions. Examples of instantaneous scalar fields indicate large-scale entrainment of jet fluid and asymmetry of the jet spread, both of which can be attributed to the presence of the vortices. Streamlines of the fluctuating components in the r-θ planes reveal another pair of vortices, which are referred to as 'weak' ones. The combined radial outward motion of the two adjacent (strong and weak) vortices draws the jet fluid into the inner swirl shear. Instantaneous snapshot also indicate that the strong vortices not only imposes a radial bias on the jet shear, but they also draw higher concentration fluid from uptream and causes it to rotate in the wake. From the time-mean turbulent scalar fluxes, two major mixing scenarios have been identified: increases in scalar concentration in the jet shear are highly correlated with increases in axial forward momentum, while negative fluctuating scalar tends to be coupled with reverse flows or forward flows that are weaker than the time-mean values in the event of the jet's flapping.

The pdf's of all three velocity components in the inner swirl shear exhibit bimodal distributions, implying that the flow exists in two states – one with the passage of the vortex and the other without it. Power spectral density estimates in the same region reveal three distinct peaks, with $S_t=0.61$ indicating the strong vortex, $S_t=1.22$ indicating pairing of the two strong vortices and $S_t=2.42$ indicating the strong and the weak vortex pairs. Spatial distributions of maximum amplitudes of velocity PSD at

S_t=1.22 confirm that the strong vortex pair has strong significant influence on the jet shear, inner swirl shear, as well as the swirl stream. The radial expansion of E_{cc} from the jet shear into the swirl shear implies that scalar entrainment also occurs on a periodic basis, which translates to the periodic bursts of heat release with stiochiometric fuel mixtures in two quadrants (separated by $\theta=\pi$) whereas the other two are lean. The same time-dependent spatial distributions of scalar mixing have also been identified using conditional averaging and POD. The latter technique shows that as much as 50% of the scalar fluctuation energy is contained in the first 2 spatial eigen-modes.

The LES predictions reported by Dianat (2007), Dunham (2010), and Cheng et al (2012) have also been used to complement experimental data. Flow separation is shown to occur in the inner surface of the swirl passage with temporally varying tangential locations. Scalar concentration is also clearly drawn by the strong vortices inside the swirl passage. Iso-surfaces of spatial tangential velocity correlations reveal that each of the 2-strong and 2-weak vortices follows a clockwise spiral path, which is bounded within the swirl cone and diminishes near x/D_s~1. Direct comparisons of 1st and 2nd order velocity and scalar statistics, as well as all three turbulent scalar fluxes, have been provided. The overall agreement in terms of sign, profile shapes, rate of decay and locations of peak magnitudes is considered very encouraging. It is a considerable achievement to have this level of agreement for all three turbulent scalar fluxes in a flow as complicated as the present case with a scalar SGS model using a constant Schmidt number. The jet shear at the immediate fuel injector exit is the region with the largest discrepancies in peak values, but this is also the same region that has been identified to be prone to considerable spatial averaging errors. Also, because of the noise ground associated with pulse-to-pulse energy variation, the experimental technique could not resolve LES's bimodal scalar pdf in the inner swirl shear where the second maximum is at C~0.02.

Chapter 6

6. RESULTS: PREMIXED TEST

The results reported in the previous chapter and those referenced to Midgley (2005) are with the fuel injector operating in the diffusion-flame mode, in which dye fluid is directly injected into the dump expansion chamber. This chapter reports experimental results with the fuel injector operating in the *premixed configuration*, in which the dye fluid is premixed with fresh water within the swirl passage. Two test cases are reported – with and without jet.

Section 6.1 provides a concise overview, built mainly upon literature review, of the velocity field characteristics. Notable differences in the flow physics between the two test cases – with jet and no jet – will be pointed out.

Section 6.2 discusses both instantaneous and time-averaged velocity and scalar data acquired in the present experimental study. The turbulent scalar fluxes are presented. Analysis of the coherent structure's effect on scalar fluctuation is reported.

Section 6.3 presents the global convection, half-life, and total residence time distributions of both test cases. Example time histories are demonstrated, followed by a detailed comparison of the characteristic times between the two test cases. This section ends with a repeatability study of the technique. It should be noted that residence time measurements have not been performed with the fuel injector operating in non-premixed mode.

Finally, Section 6.4 looks at combusting test results in the literature, from which a qualitative discussion is built. Similarities in the mixing characteristics are pointed out, and a brief reference to NO_x production is provided.

This chapter is concluded by Section 6.5, which is the chapter summary.

6.1 Flow field characteristics of premixed configuration

Schematics of the fuel injector running in the premixed configurations for both test cases can be found in Section 2.3.2, which also includes a table of the dye-to-water mass flow ratio; and for the with-jet case, the swirl-to-jet mass flow split remains the same as the main condition reported throughout the thesis. Turbulence in the swirl slots induced by the injection of dye through the premixing ports is believed to be negligible and is not expected vary between cases as the central jet is physically isolated from the swirl slots in the fuel injector (see Fig. 2.15). Therefore, previous experimental data – without the fuel injector running in the premixed mode – can be referenced here for a qualitative comparison.

6.1.1 Time averaged flow field

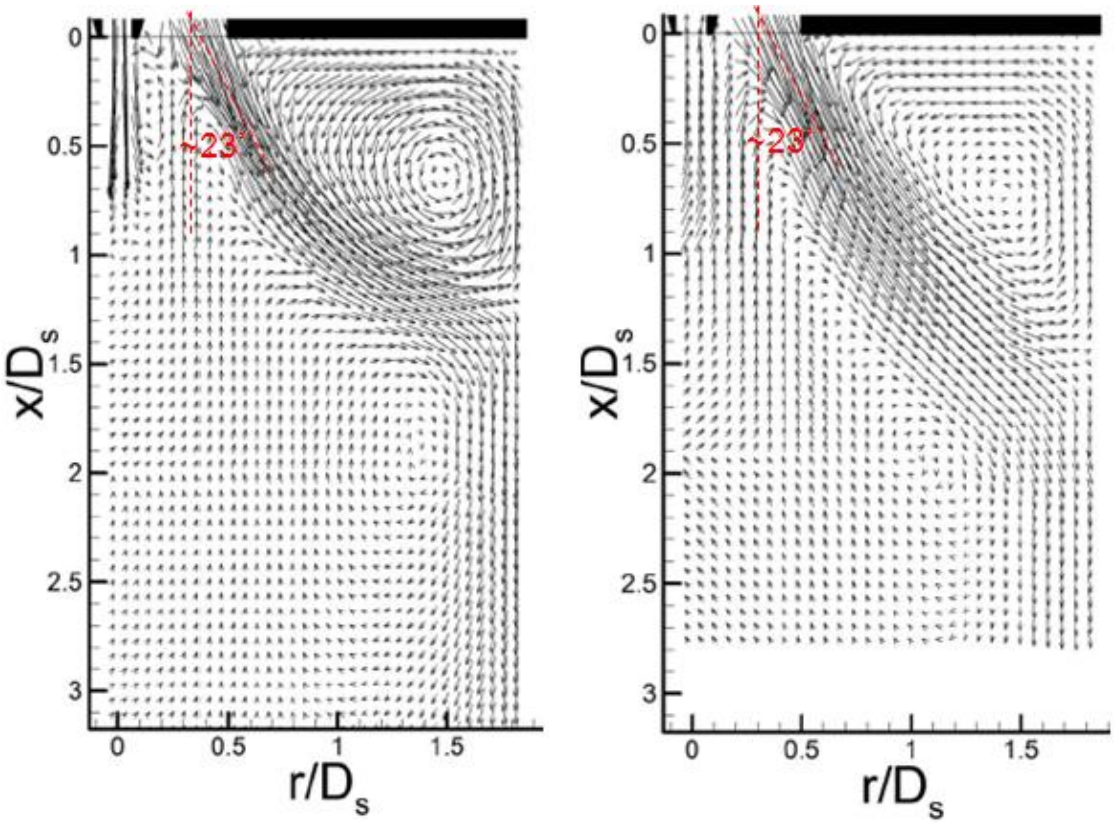

(a) (b)

Fig. 6.1 Mean velocity vectors with cone angles in the x-r plane: (a) with-jet, and (b) no-jet (Midgley, 2005)

As shown in Fig. 6.1, without the central jet, the reverse flow extends all the way to the fuel injector exit plane about the geometric centreline. Despite having the same

cone angle, the structures of the swirl streams are quite dissimilar in three aspects: first, the no-jet case has a more spread-out swirl stream; second, swirl stream of the no-jet case has a further penetration distance downstream; third, their attachment points on the outer wall are also quite different: x/D_s~1.2 for with-jet and x/D_s~1.5 for no-jet. With-jet case's more upstream outer wall attachment location is also associated with a stronger radial velocity component, which probably contributes to the stronger, more well-defined CRZ. Mean tangential velocity contours shown in Fig. 6.2, which were previously unavailable prior to SPIV measurements, provide additional comparison that supports the afore-mentioned observations.

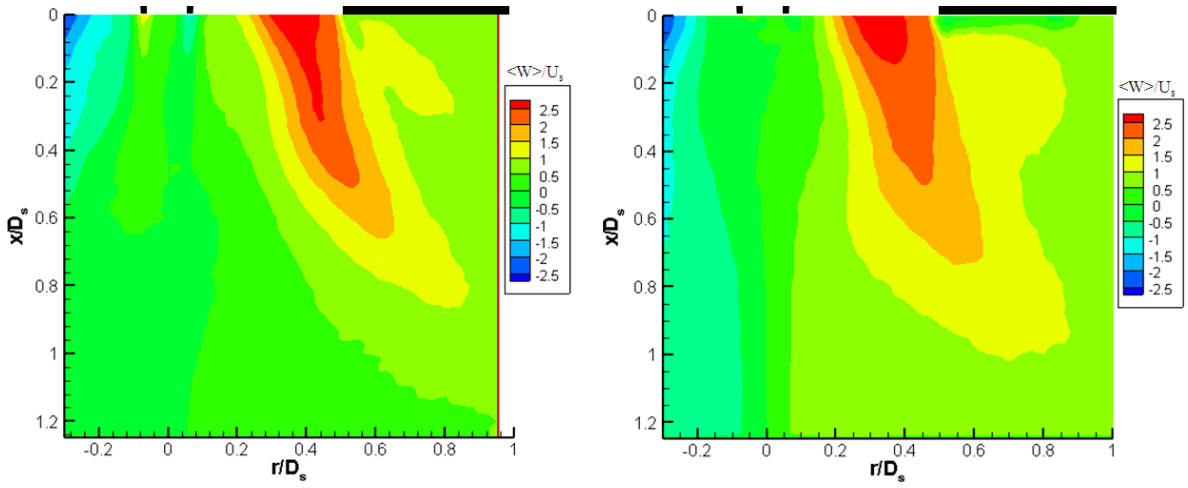

(a) (b)

Fig. 6.2 Mean tangential velocity contours in the x-r plane: (a) with-jet, and (b) no-jet

Following the right-hand convention, positive <W> contours indicate out-of-page motion. Hence, it is obvious that both test cases have the same swirl direction – counter-clockwise. As shown in Fig. 6.2, the exit plane tangential velocity is biased towards the outer radius (r/D_s>0.25) in both test cases. Fig. 6.2(b) has a more spread-out contour in the swirl stream; this is consistent with the previous observation. Fig. 6.2(b) also shows that in the region where the CRZ attach the swirl stream, higher tangential velocities than those of the with-jet case are found. As it will be discussed in the following sections, the more compact swirl stream of the with-jet case results in a more stable swirl cone.

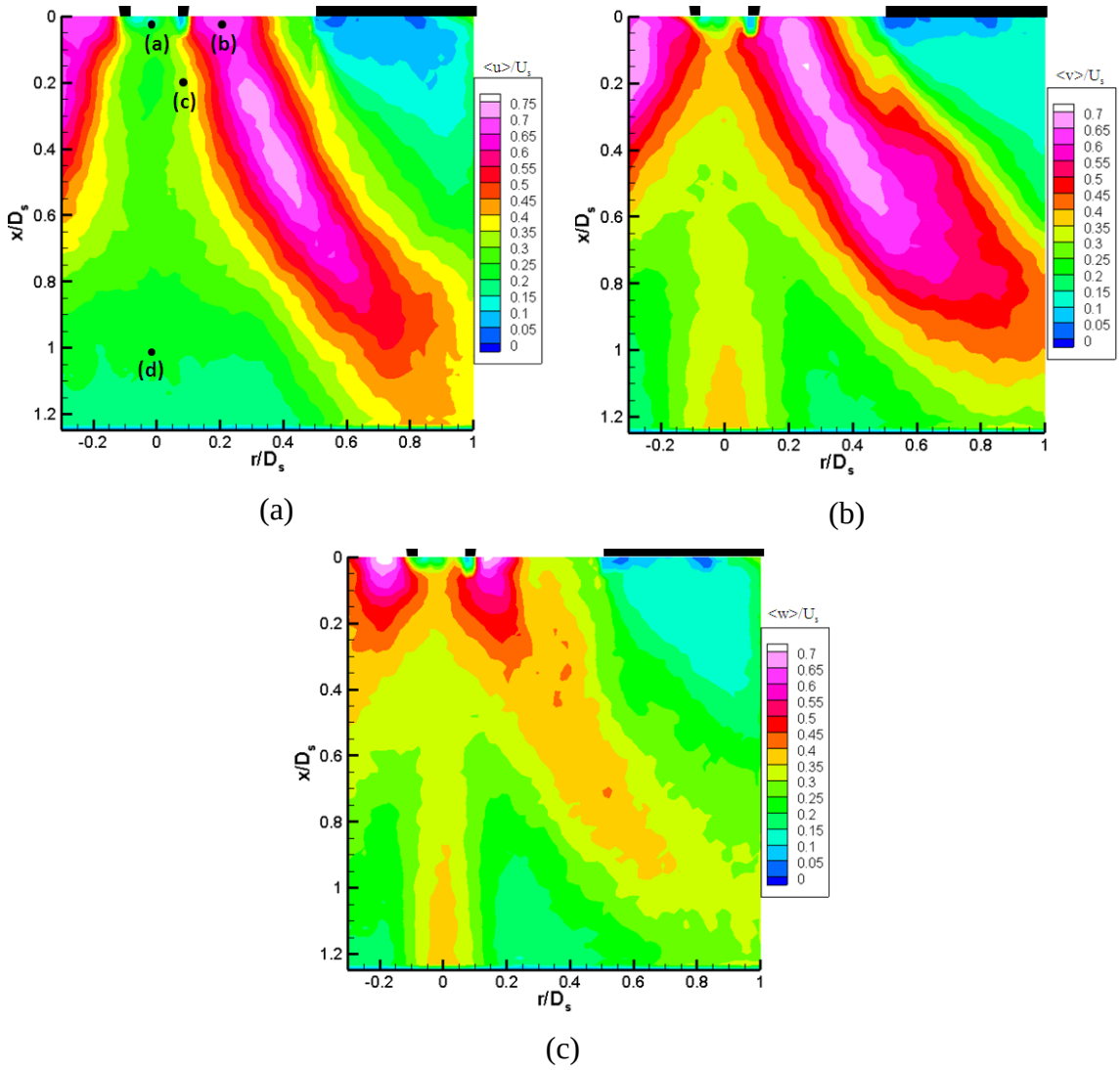

Fig. 6.3 RMS velocity contours of no-jet test case: (a) axial, (b) radial, and (c) tangential velocity

Fig. 6.3 shows the no-jet turbulence intensities. Upon comparison with Fig. 5.4 in Section 5.1.1, several major differences can be seen. The central jet obviously introduces an additional region of high turbulence intensity – in the jet shear – and this is true for all three velocity components. Without the central jet, the strips of high turbulence intensity in the inner swirl shear layer move radially inward. As it has been discussed in Chapter 5, high turbulence intensity in the inner swirl shear is associated with the existence of helical vortices. This is also seen in no-jet fuel injector flows, as reported in Spencer et al (2008) and Dunham et al (2009). Another crucial difference is that the no-jet case features a PVC, which is manifested in the high radial and tangential turbulence intensities along the geometric centreline. About the geometric centreline and downstream of x/D_s~0.8, RMS radial and tangential velocities are remarkably similar in terms of both magnitudes and shapes of the contours; and these

turbulence levels are higher than the RMS axial velocity component by a factor of 2. This suggests that the flow reversal via CTRZ along the geometric centreline is influenced by the PVC. Syred (2006) has shown that the PVC is linked to the wobbling of the swirl cone, i.e. the recirculation bubble becomes unstable. This could also be the case here, where de-stabilisation of the swirl cone results in temporal variations in swirl stream characteristics, hence more spread-out time-mean velocity contours. In summary, the helical vortices are responsible for the high turbulence intensity in the inner swirl shear for both test cases, while the PVC contributes to high turbulence intensity along the centreline downstream of x/D_s~0.8 in the no-jet case.

6.1.2 Temporal characteristics

Four point locations, as indicated in Fig. 6.3(a), have been selected to illustrate the power spectra of the no-jet case; these are shown in Fig. 6.4. As shown in Fig. 6.4 (a), a spike of E_{vv} is found at S_t=0.60; E_{uu} is also seen reaching a maximum at this S_t although with an amplitude that is an order of a magnitude lower than E_{vv} and also distributed over a wider range of frequencies. The spike of E_{vv} at this location (x/D_s=0.05, r/D_s=0) is not seen in the with-jet case; therefore, without the central jet, disturbances in the inner swirl shear is able to spread into the geometric centreline just downstream of the fuel injector. The change in flow radial direction as a result of this disturbance is illustrated in Fig. 6.11. Fig 6.4(b), taken from a point in the inner swirl shear, shows two distinct peaks – S_t=0.60 and S_t=1.20. As stated in Spencer et al (2008), the appearance of multiple peaks confirms that a vortex pair system must still be present in the no-jet case. However, unlike the with-jet case, in which the strong vortex pair results in the highest peak at S_t=1.21, temporal coherence between the pair of vortices in the no-jet case appears to be weaker. As shown in Fig. 6.4(c), the amplitude of the second peak at S_t=1.20 decreases by about an order of a magnitude compared to that of Fig. 6.4(b). With the sampling rate of 500Hz and 1000Hz, no clearly identifiable peak can be identified in Fig. 6.4(d) despite the rise in turbulence intensity at this location. Although no distinct frequency is seen in Fig. 6.4(d), energy content over a broad low-frequency range points to either inappropriate frequency resolution (to capture low-frequency motions) or the existence of a quasi-periodic structure. Midgley (2005), Spencer et al (2008), and Dunham (2010) have identified latter to be the case, and it is associated with a PVC (S_t=0.01), which is captured at

further downstream locations ($x/D_s>2$). As demonstrated in Dunham (2010), the effect of the PVC is found along the geometric centreline between $x/D_s\sim1$ and the downstream boundary of the cylindrical chamber, and the precession is limited to within $r/D_s\leq0.1$.

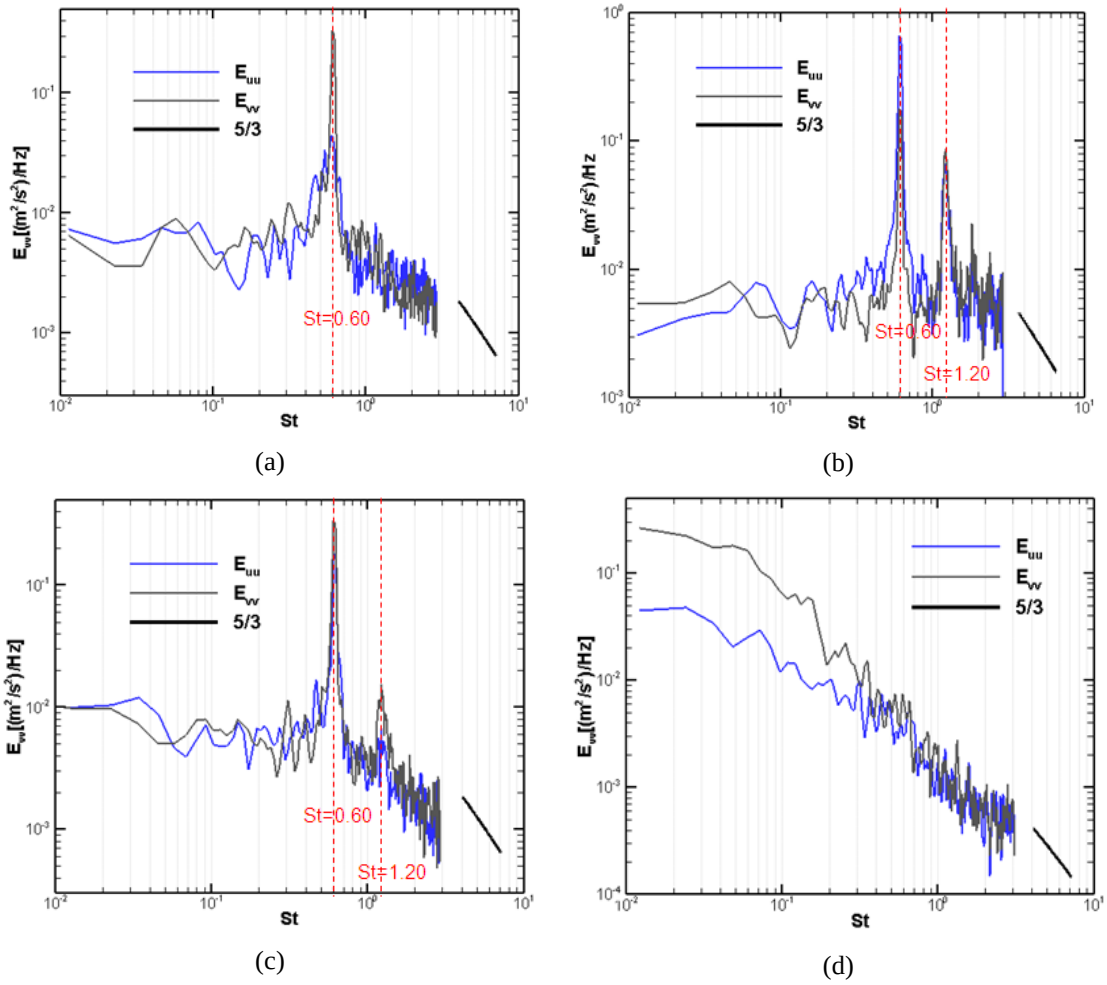

Fig. 6.4 PSD estimates at four point locations

Having identified the characteristics frequencies of the inner shear vortices, spatial distributions of the periodic events can be visualised. This follows the same method as that used in the with-jet case, as described in Section 5.3.2. Spatial distributions of PSD amplitudes of the two velocity components are clearly different: the inner swirl shear is dominated by high amplitudes of E_{uu}, while strong E_{vv} dominates in the outer swirl shear, particularly at $0.2 < x/D_s < 1$. Its close proximity to the CRZ probably influences its convection path as well, hence making the CRZ less well-defined than in the with-jet case. Moreover, the concentrated region of high E_{vv} along the centreline, just downstream of the blocked central jet, confirms the previous

observation from single-point PSD. This suggests that the CTRZ can become radially biased at $x/D_s<0.7$. The fact that the distributions of the PSD amplitudes of the two velocity components are substantially different confirms weaker spatial coherence between the two velocity components at $S_t=0.60$. Comparison of the with-jet (Section 5.3.2) and no-jet PSD amplitude contours suggests that the central jet prevents inner swirl shear disturbances from propagating into the CTRZ (the radial velocity component, in particular); and by doing so, it probably serves to stabilise the swirl cone as well.

Unlike the PSD amplitudes of the primary peak, those of the secondary peak both are found in the inner swirl shear layer only, and they are significantly lower than those of the with-jet case. It should be noted that the secondary peak here is actually referred to as the primary peak at $S_t=1.22$ in the with-jet case, as shown in Fig. 5.43. Hence, Figs 6.5 and 6.6 suggest that while it is possible for the single vortex to exert its influence on the CTRZ, disturbances associated with the vortex pair are limited to the inner swirl shear. This has to do with the rotational directions of the vortices in the no-jet case, as will be elaborated in Sections 6.2.4.

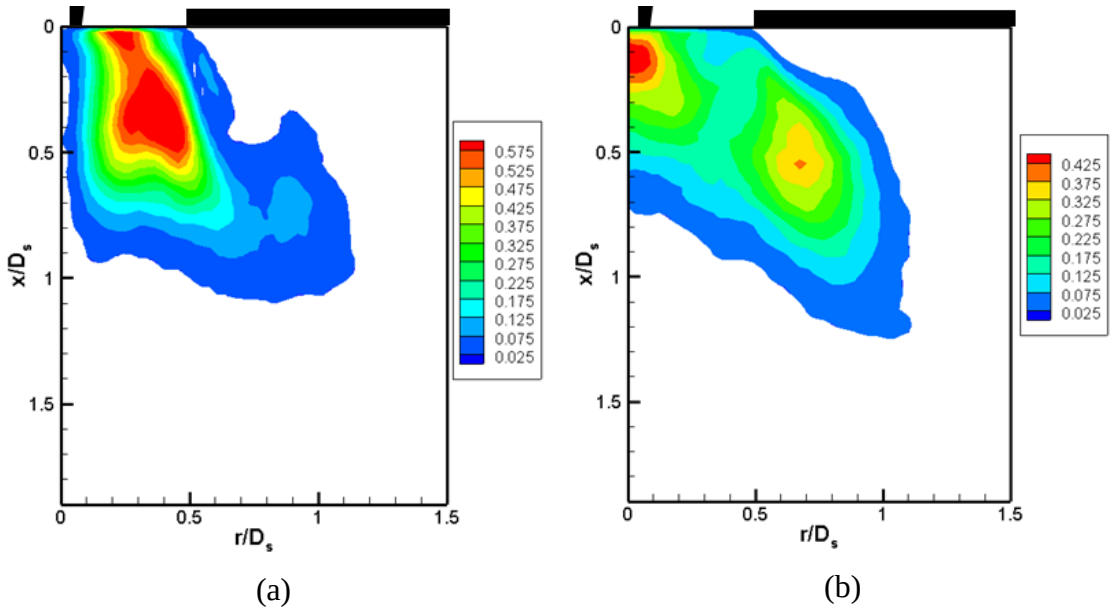

(a) (b)

Fig. 6.5 PSD amplitude of primary peak (no-jet), $S_t=0.60$, of (a) axial, and (b) radial velocity

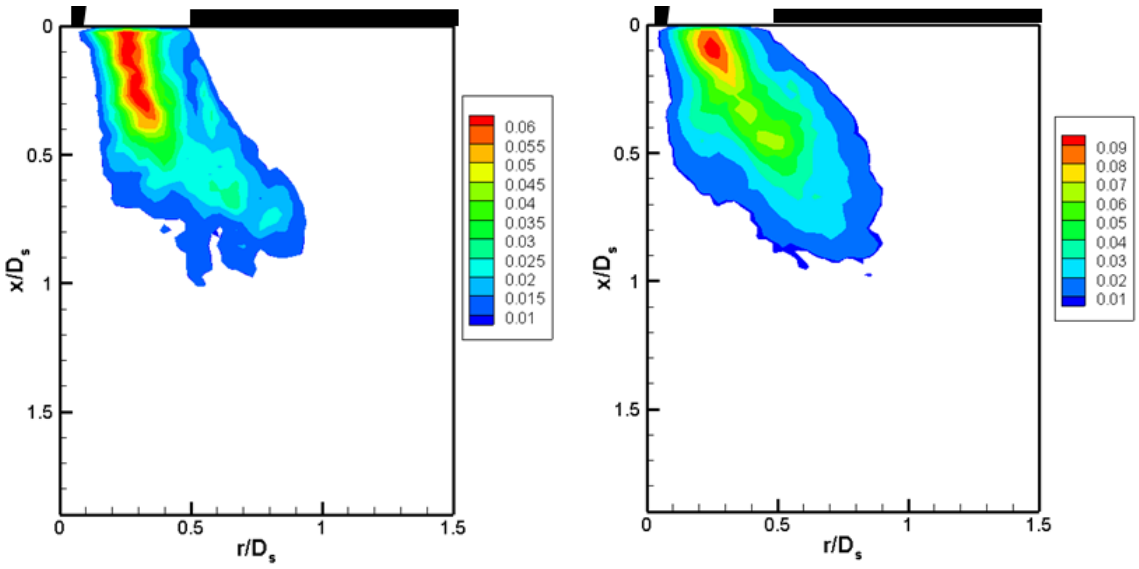

Fig. 6.6 PSD amplitude of secondary peak (no-jet), S_t=1.20, of (a) axial, and (b) radial velocity

The previous discussion has highlighted no-jet's swirl cone being less stable. This is consistent with the findings of Midgley (2005), who shows that the pdfs of the outer wall attachment location are notably different between the two test cases. As shown in Fig. 6.7, attachment locations of the no-jet case are distributed over a much wider range than that of the with-jet. This implies that the swirl cone of the no-jet case tends to be less stable as they flap around.

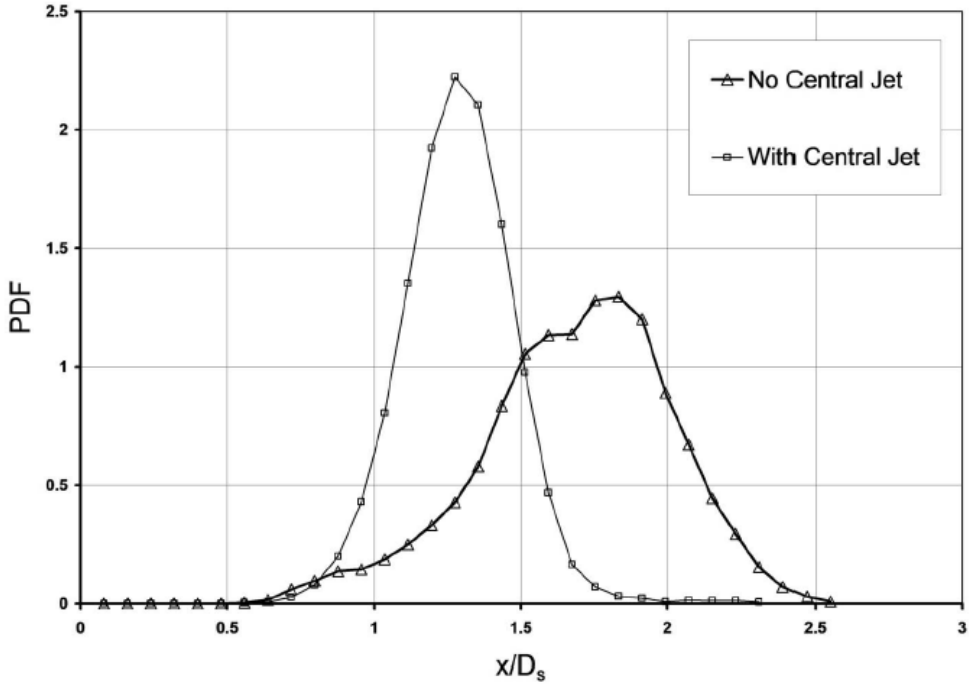

Fig. 6.7 pdf of spatial attachment point of swirl cone (Midgley, 2005)

The afore-mentioned comparative study can be summarised as follows:

1. The no-jet case features a more rapidly diffusing swirl stream and inner swirl shear layer.
2. The no-jet case has a less well-defined CRZ.
3. High radial and tangential turbulence intensities along the centreline in the no-jet case is evidently due to the presence of a PVC, which is damped in the with-jet case.
4. There is also a vortex pair system in the no-jet case, but the 'pairing' in the no-jet case is significantly weaker than the with-jet case, in terms of both PSD amplitudes and spatial coherence.

These briefly reported findings, which highlight aerodynamic differences between the with-jet and no-jet cases, support the previous work of Midgley (2005), Spencer et al (2008), and Dunham et al (2010). The findings and the reviews of the two test cases discussed thus far in this chapter will help the readers understand mixing and residence time characteristics, which are described in the following sections. Readers interested in further details of the flowfields of the two test cases are encouraged to refer to the three publications mentioned above.

6.2 Mixing field characteristics of premixed configuration

Unlike the velocity fields, the study of which could be aided by a literature review on the with-jet and no-jet cases, passive mixing fields of the premixed configuration are presented here for the first time on the Turbomeca fuel injector. The time-mean scalar fields, temporal characteristics, and the scalar flux of the two test cases are presented in this section.

Fig. 6.8 shows the time-mean scalar fields that are normalised by the respective maxima. For both test cases, regions of highest concentration are found just downstream of the fuel injector exit, bound within the inner swirl shear layer of the swirl stream ($r/D_s<0.35$). The main difference is obviously due to the presence of the central jet: the fresh water washes out the high concentration fluid along the centreline, forcing it radially outward, though it remains confined within the inner swirl shear layer of the swirl stream.

6.2.1 Time mean mixing field

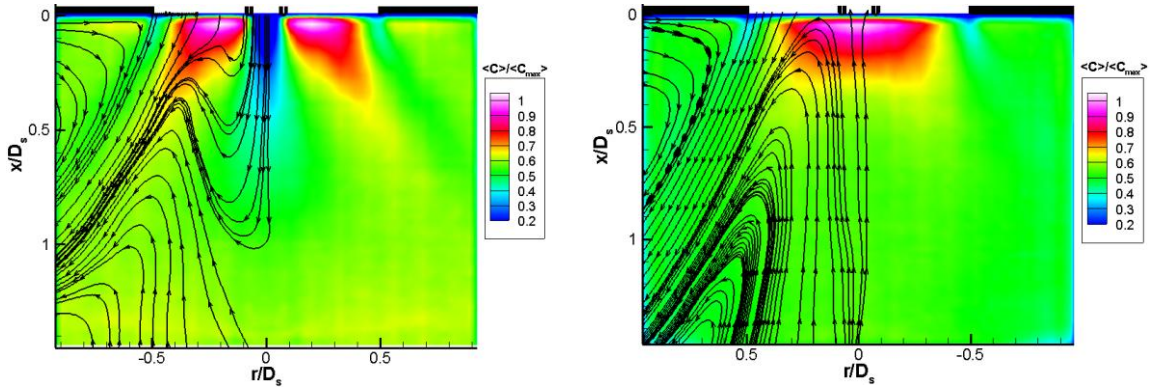

(a) (b)

Fig. 6.8 Time-mean scalar field normalised by maxima of (a) with-jet and (b) no jet

For the no-jet case, the fact that the highest concentration is found along the centreline, just downstream of the blocked central jet, suggests that dye fluid exiting the swirl duct is quickly transported radially inward, rather than following the time-mean stream traces and completing one recirculation through flow, as shown in Fig. 6.1(b). It is likely that the tendency for the CTRZ at $x/D_s<0.7$ to take on a radial direction bias, as identified in Section 6.1.2 (see the E_{vv} contour in Fig. 6.5(b)), is responsible for this radial inward transport. In addition, significant variation in time-mean scalar across the fuel injector exit indicates incomplete mixing in the swirler passage. In other words, the injected dye fluid is not fully mixed out by the exit plane, resulting in a mean concentration that is biased towards the inner wall. This is probably due to a short mixing distance from the premixing port to the swirler exit, along with insufficiently penetrating fuel jets in the swirl slots. Due to the difficulty associated with acquiring good optical access inside the angled swirl slots and swirler passage, this has not been investigated further. The with-jet case exhibits a much more well-defined and stronger-penetrating outer swirl shear layer, which is characterised by concentration that is roughly 20% lower than the fully-mixed level. This has to do with the previous finding that the with-jet case features a more a stable swirl stream, while the no-jet case's less stable, more rapidly diffusing swirl stream is more conducive to mixing out the outer swirl shear layer.

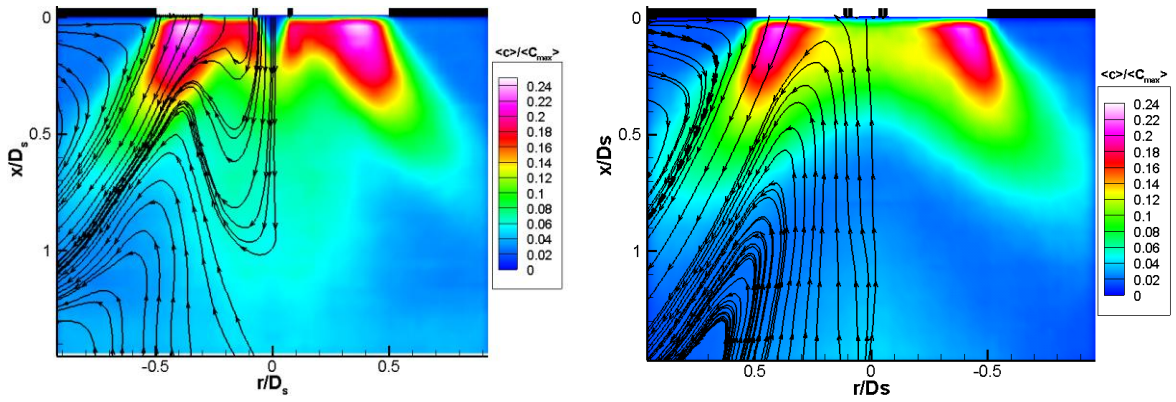

Fig. 6.9 RMS scalar field normalised by maxima of (a) with-jet and (b) no jet

High scalar fluctuations are found in the swirl stream shear layer for both cases as shown in Fig. 6.9(a) and (b). These localised regions of high scalar fluctuation (larger than 20% of the mean) at the immediate swirler exit indicate the region where the helical vortex structure rapidly mix out the radial bias in the concentration such that the dye is more or less fully mixed at between 1 and 1.5 injector diameters downstream, where the concentrations approach 0.5. The higher scalar fluctuation in the with-jet case can be expected due to central jet's continuous supply of scalar gradient as low-concentration central jet expands and mixes with high-concentration swirl stream via both shearing motion and the helical vortex pairs. Another notable difference can be observed along the centreline, as shown in Fig. 6.10: while the with-jet case's scalar fluctuation decreases with distance downstream, that of the no-jet decreases from the exit to about x/D_s=0.7, from which it increases again up till the edge of the FOV at x/D_s=1.45. This increase in scalar fluctuation is arguably due to the low-frequency PVC; its contribution to the increase in scalar fluctuation may be due to the entrainment of higher concentration fluid into the low-pressure region in the PVC centre, and radial and tangential displacement of the higher-concentration PVC centre in time translates to the increase in the ensemble-averaged scalar fluctuation. It should be noted that although the presence of the PVC in the no-jet Turbomeca fuel injector flow field has been known for some time, its effect on the mixing field is actually presented for the first time here.

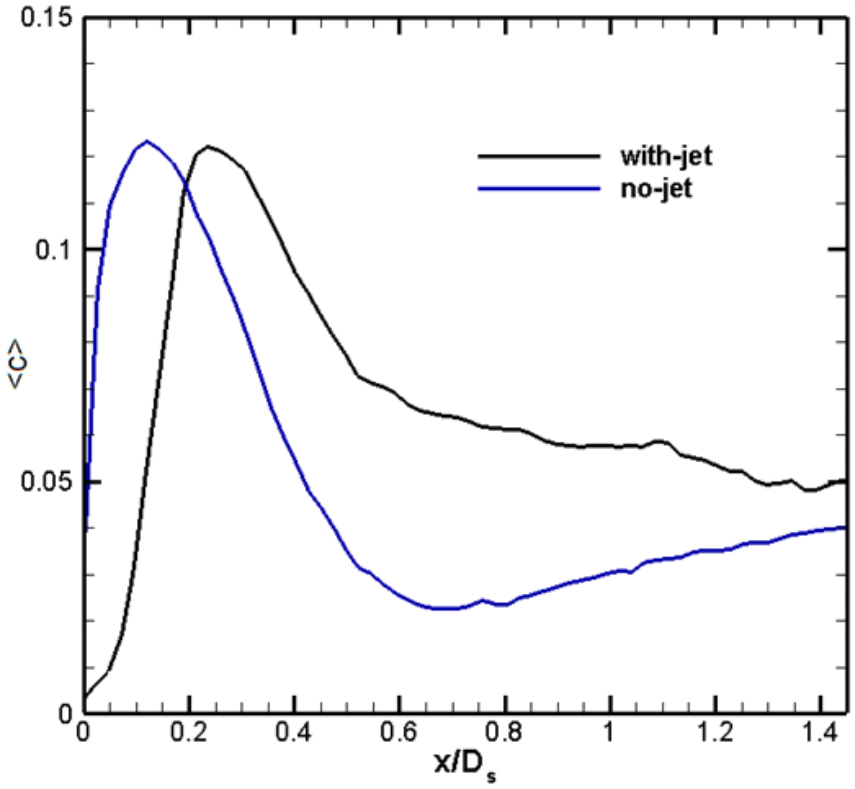

Fig. 6.10 RMS scalar profiles along the centreline

6.2.2 Instantaneous scalar fields

Prior to analysing the coherent scalar structures and characteristic periodicities in scalar mixing, it is helpful to visualise the localised regions or patterns of scalar fluctuations. Fig. 6.11 and Fig. 6.12 show a consecutive series of 6 instantaneous fluctuating scalar snapshots, which are superimposed with stream traces of Reynolds decomposed velocity field, of the with-jet and no-jet test cases respectively. The 6 snapshots are randomly selected but are all sequential instances separated by the actual capture rate of 1kHz, or T_s=0.001s.

As shown in Fig. 6.11(a) and (b), there is a pair of vortices just downstream of the swirler exit with vortex 'eyes' located near x/D_s=0.1. The axial and radial directions of the two vortices match; both vortices' stream traces indicate positive radial and negative axial flow along x/D_s=0.05. High-concentration fluid that is located near the outer wall of the swirler can be seen being entrained into vortex centres. The low-concentration fluid located on the boundary of this vortex pair and just downstream of the jet lips is a result of the entrainment of jet fluid (fresh water) by the low-pressure

centres of the clockwise vortex pair. The arrow heads clearly indicate that the jet fluid is being transported upstream, into the swirl passage. The reader may recall that Fig. 5.55(b) shows an example of LES-predicted reverse transport of jet fluid, with the fuel injector operating in the diffusion-flame mode.

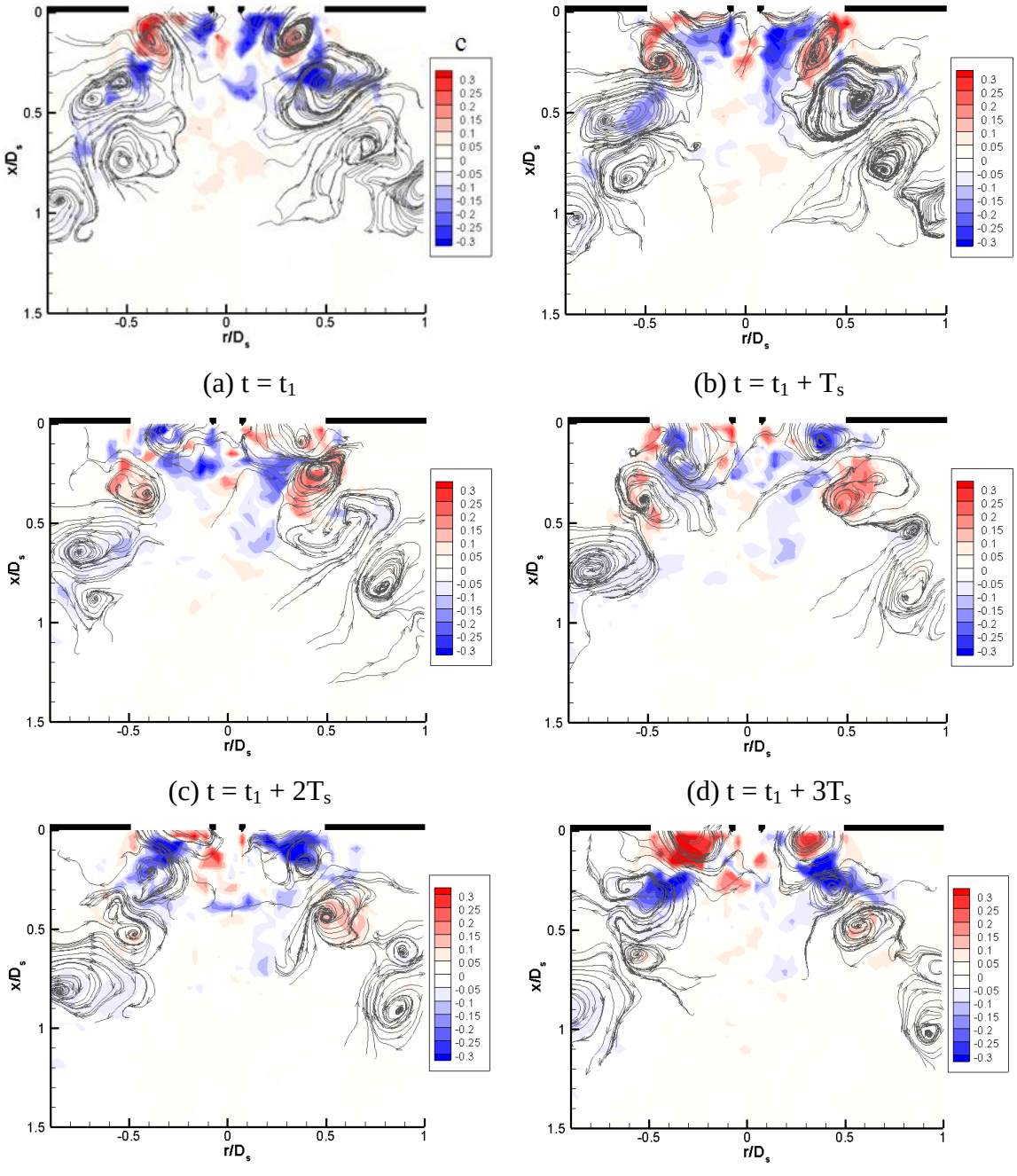

(a) $t = t_1$ (b) $t = t_1 + T_s$

(c) $t = t_1 + 2T_s$ (d) $t = t_1 + 3T_s$

(e) $t = t_1 + 4T_s$ (f) $t = t_1 + 5T_s$

Fig. 6.11 Reynolds decomposed instantaneous scalar fields with superimposed stream traces of Reynolds decomposed axial-radial velocity vectors, with-jet test case

The same effect is seen here, except with the central jet fluid being of low concentration. Such reverse transport of jet fluid into the swirl passage can contribute to the dilution of premixed mixture in the swirl passage, resulting in negative scalar fluctuation exiting the swirler (Fig. 6.11(d) and (e)). However, whether such fluctuation is entirely due to reverse transport of jet fluid or also partially due to a short mixing length within the swirl passage cannot be answered with the current data. As shown in Fig. 6.11(e) and (f), the scalar fluctuations are characterised with lengthscales up to the entire length of the swirler exit. The fact that the parcels of scalar fluctuations remain strongly correlated with the vortices implies that the alternating patterns of c in the inner swirl shear occur with the characteristic frequency of the vortex pair (S_t=1.20), as confirmed by the E_{cc} contours shown in Fig. 6.15.

Unlike the with-jet case, stream traces of the vortices shown in Fig. 6.12 are less circular and less well-defined. They also take up a larger radial span and can in certain instances expand into the CRZ. Spatial and temporal unmixedness across the swirler exit is still present. Stream traces just downstream of the blocked central jet indicate radial transport of fluid between two quadrants of the swirler exit. The evolution between Fig. 6.12(a) and (b), for example, shows an increase in the positive fluctuation and reduction in the negative one, suggesting transport of increased higher concentration fluid from the "right side" of the swirler exit to the "left side". Such direction of transport can change, as evidenced in Fig 6.12(e) and (f), which now show transport from the "left side" to the "right side". This supports the observation made with regard to Fig. 6.5(b) in Section 6.1.2, which underscores the tendency for the flow reversal to take on a radial direction bias with a characteristic frequency of S_t=0.60. In contrast to the with-jet case, in which the flow directions of the pair of vortices match, the inner shear layer vortices (separated by $\theta=\pi$) in the no-jet case exhibit opposite flow directions. In Fig. 6.12(a), for example, the vortex (centre at x/D_s~0.2) on the right exhibits <u>negative</u> radial component while its counterpart on the left exhibits <u>positive</u> radial component. This difference in flow directions thus results in a net flow direction – to the left – between the two vortices. And this is believed to be the cause of radial bias in the reverse flow about the geometric centreline.

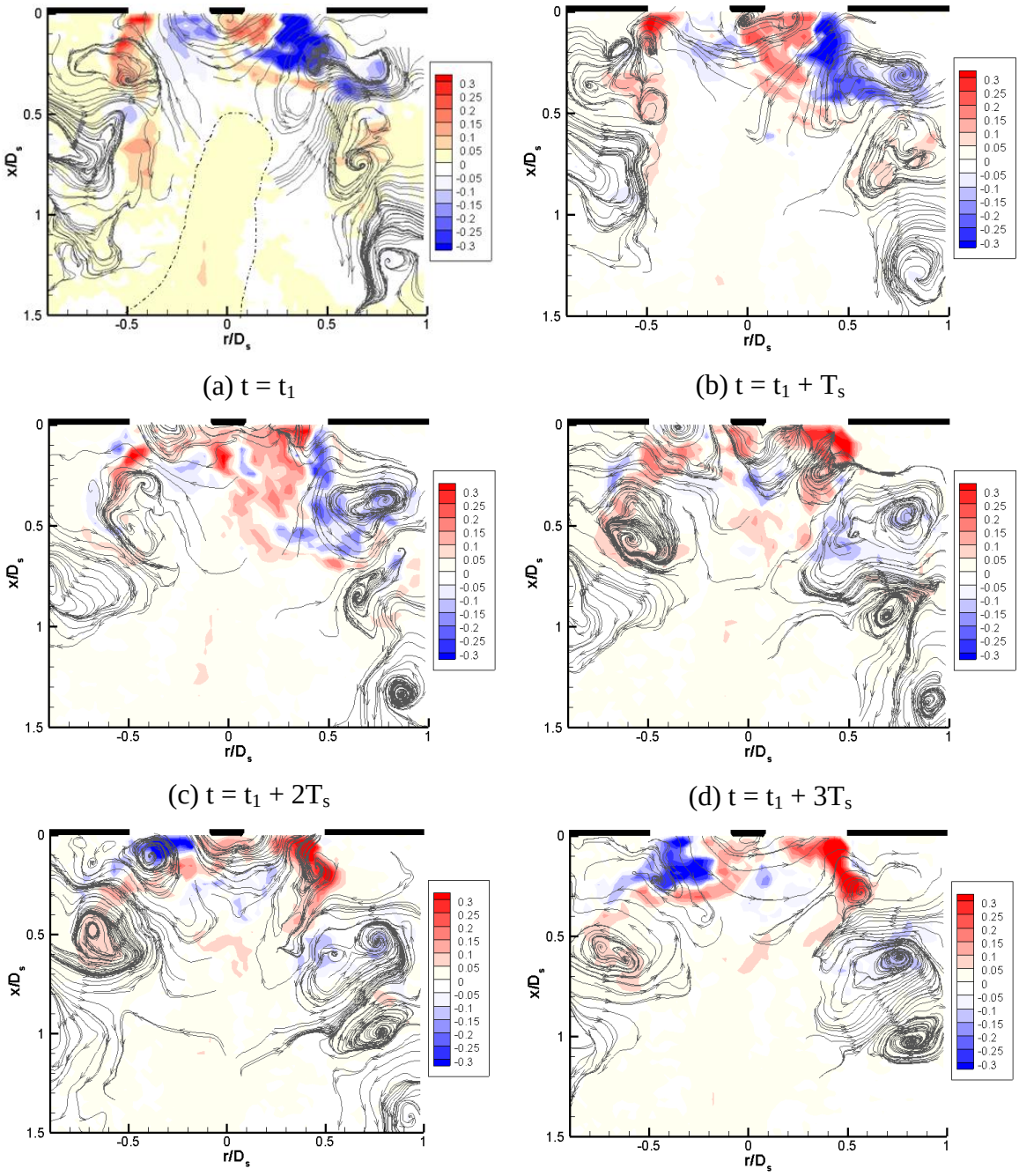

(a) $t = t_1$ (b) $t = t_1 + T_s$

(c) $t = t_1 + 2T_s$ (d) $t = t_1 + 3T_s$

(e) $t = t_1 + 4T_s$ (f) $t = t_1 + 5T_s$

Fig. 6.12 Reynolds decomposed instantaneous scalar fields with superimposed stream traces of Reynolds decomposed axial-radial velocity vectors, no-jet test case

Another important instantaneous scalar structure that has been highlighted in Fig. 6.12(a) via adjusting the colour band (C=0 to C=0.05) is the presence of a positive scalar fluctuation region that is slightly off the geometric centreline; this region is indicated by the dashed line. This particular region of positive scalar fluctuation almost appears to stagnate from Fig. 6.12(a) to (f) – a stark contrast to the rapidly changing fluctuating scalar contours in the swirl stream. The scalar fluctuation in this

region is associated with the less turbulent CTRZ, but the fact that it is off the geometric centreline (while <c> is symmetric) in these instantaneous snapshots implies that it may be associated with a slow off-axis precession. Indeed, it is likely influenced by the low-frequency PVC identified earlier; as it takes roughly 1.33 seconds (f=0.75Hz) to complete one precession about the centreline (Midgley, 2005), the instantaneous scalar contours would undoubtedly appear static within 0.006 seconds of measurement duration.

6.2.3 Turbulent scalar fluxes

Axial scalar fluxes of the two test cases are shown in Fig. 6.13. The jet shear of the with-jet case is dominated by -<uc>, the sign of which is the opposite of that shown in Fig. 5.30, but the flow and mixing mechanisms that result in this are similar (refer to discussion in Section 5.2.4). The patch of +<uc> near the inner wall of the swirl passage implies that the region is dominated by reverse transport (-u) of jet fluid (-c) into the swirl passage; examples of this can be found in Figs. 6.11(a), (b), and (e). For the no-jet case, -<vc> located near the inner wall of the swirl passage is characterised by reverse flow (-) of swirl stream's high concentration fluid (+), examples of which can be seen in Figs. 6.12(d), (e), and (f). In the inner swirl shear and the swirl stream, magnitude <uc> of the no-jet case is significantly lower than that of the with-jet because the former's larger vortex and scalar fluctuation lengthscales mean velocity-scalar correlations are more spread out. The -<uc> along the inner swirl shear in the with-jet case can be explained by the bi-modal behaviour of axial velocity and scalar: with the passage of a vortex, high-concentration swirl-stream fluid (+c) is being drawn in the reverse direction (-u); and in the event without the vortex, jet-spread fluid (-c) is being transported downstream by the swirl stream (+u). Also, because the swirl stream in the with-jet case is more stable, rise in <uc> is limited to the inner swirl shear. Rise in <uc> in the no-jet case, on the other hand, can be seen occupying a larger radial span and towards the outer part of the swirl stream, where <c> reaches a maximum (Fig. 6.9(b)) but <C> is at a minimum (Fig. 6.8(b)). Hence, +<uc> is likely associated with the bursts of forward momentum (+u) with partially unmixed dye fluid; examples can be seen in Figs. 6.12(a), (d), (e), and (f). Despite these differences, both test cases exhibit rapid mixing as <uc> decays to zero near x/D_s~0.6.

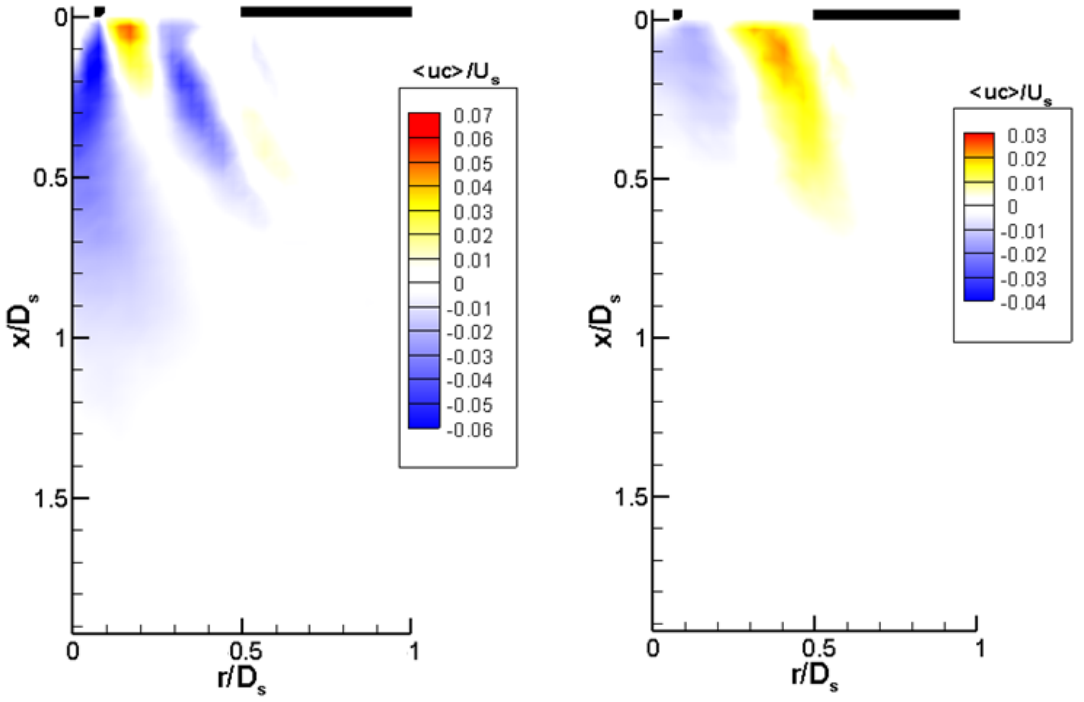

(a) (b)

Fig. 6.13 Axial scalar flux of (a) with-jet and (b) no-jet

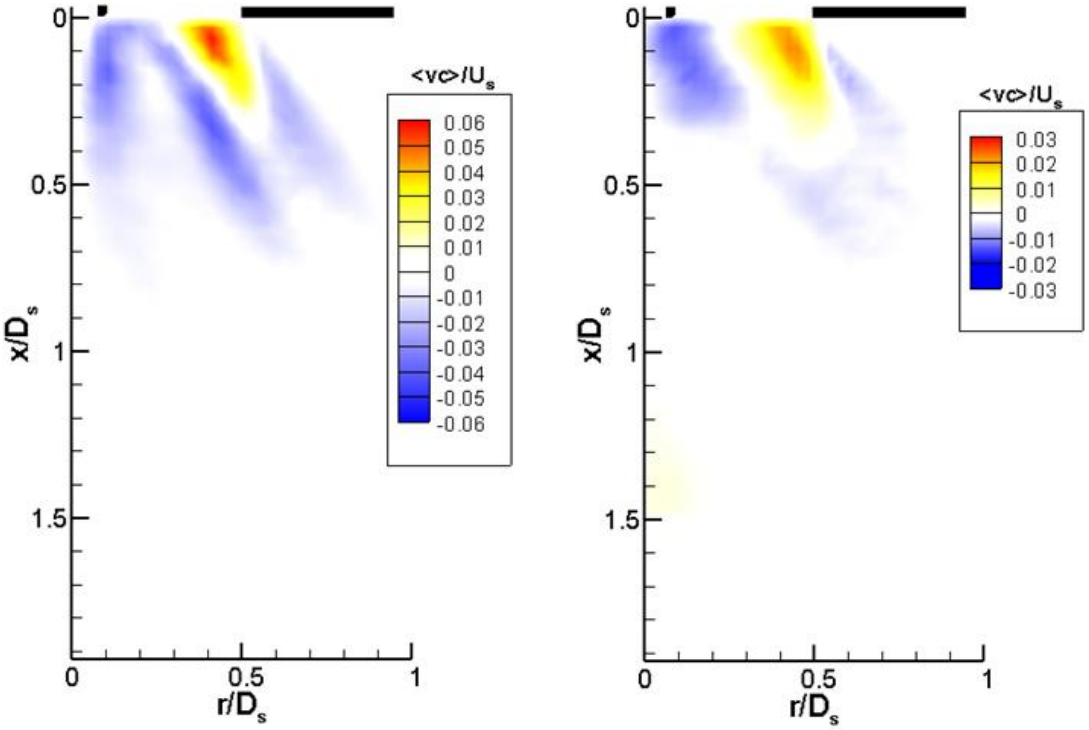

(a) (b)

Fig. 6.14 Radial scalar flux of (a) with-jet and (b) no-jet

The distributions of <vc> shown in Fig. 6.14 are grossly similar, but again the no-jet case is characterised with considerably lower <vc> due to its more spread-out swirl stream. The -<vc> along the inner swirl shear is likely a result of the radial inward transport (-v) of swirl stream's high-concentration fluid (+c); examples of this transport are abundant in Figs. 6.11 and 6.12. Also, the rise in <vc> towards the outer wall of the swirl passage is consistent with the RMS scalar contours shown in Fig. 6.9, suggesting that radial velocity component fluctuation in the region may be responsible for scalar fluctuation as well.

6.2.4 Coherent scalar structure

Figs. 6.15 and 6.16 show how scalar fluctuation in the near field is correlated with that at the reference point (x/D_s=0.09, r/D_s=0.34) in the with with-jet and no-jet cases, respectively; the superimposed stream traces in the swirl stream are plotted from the conditionally averaged axial-radial velocity. In terms of the conditionally averaged flow features, several differences between the two test cases are notable. First, as shown in Fig. 6.16, stream traces just downstream of the blocked central jet confirm fluid transport across two quadrants of the swirler exit separated by π, while those of the with-jet case shown in Fig. 6.15 are discontinued about the centreline and instead two counter-rotating vortices form in the vicinity of the jet lip. Second, vortices in the no-jet case are more spread out in both radial and axial directions; in other words, they are characterised with larger lengthscales. Finally, as indicated by the red arrows in the two figures, the 'paired' vortices in the with-jet case are counter-rotating, while those of the no-jet case are co-rotating. Across any given axial station, the counter-rotating relationship of the with-jet vortices results in identical flow directions in the vortex pair, while the co-rotating relationship of the no-jet vortices results in opposite flow directions. Given the lengthscales of the vortices and the radial bias in the CTRZ, it is believed that the co-rotating vortices can impose a directional bias on the swirl cone as well, causing it to wobble as the vortices travel helically downstream. No-jet's much more spread-out tangential velocity contour in the swirl stream (Fig 6.2(b)) and large radial span of E_{uu} and E_{vv} (Fig. 6.5(b)) both support this argument. It may also be noted that the strong vortex symmetry in the with-jet case and the lack of it in the no-jet case is consistent with the doubling of Strouhal numbers of the axial and radial components in the with-jet case.

The swirl stream vortices also play a major role in shaping the spatial distributions of R_{cc} for both test cases. R_{cc} in the swirl stream shows remarkable axis-symmetry in the with-jet case (Fig. 6.15), but axis-asymmetry in the no-jet case (Fig. 6.16). For example, the R_{cc} contours in the vicinity of the counter-rotating vortices with their 'eyes' at x/D_s=0.25, as indicated by the red arrows in Fig. 6.15, are axis-symmetric across the swirl streams. The co-rotating relationship between the vortex pair in the no-jet case shown in Fig. 6.16, in contrast, leads to asymmetry in R_{cc}. This may be explained by considering a scalar transport scenario: whereas the vortex on the right entrains high-concentration fluid from the inner swirl shear, the one on the left entrains lower-concentration fluid from the CRZ, thereby resulting in the negative scalar correlation. This also supports the argument that the co-rotating relationship in the no-jet case leads to wobbling of the swirl cone. Finally, it is important to point out that R_{cc} flips sign from the outer swirler exit to the inner wall in both cases. Such alternating patterns of R_{cc} across the across the swirler exit is a further evidence of unmixedness associated wtih the coherent structures. This is evidently related to the flow separation that occurs inside the swirler passage, Midgley (2005), Dunham (2010), and Cheng et al (2012). Unfortunately, without concentration data within the swirl passage, the question still remains as to what extent the poor mixing is due to insufficient mixing length and/or due to flow separation as well as reverse transport of fluid.

As mentioned earlier, the sequence of snapshots of Reynolds decomposed scalar shown in Fig. 6.12 reveals a large parcel of slow-mixing fluid, which is not present in the with-jet case (Fig. 6.11). The spatial scalar correlation contours shown in Fig. 6.17 confirm this important difference. The wedge-shaped region where R_{cc} is in excess of 0.8 in Fig. 6.17(b) can be interpreted as a footprint of the CTRZ, which has been shown to be influenced by the PVC. The fact that the CRZ is also correlated (R_{cc}~0.6) with the reference point further affirms the low-frequency, thus long-duration, nature of the PVC.

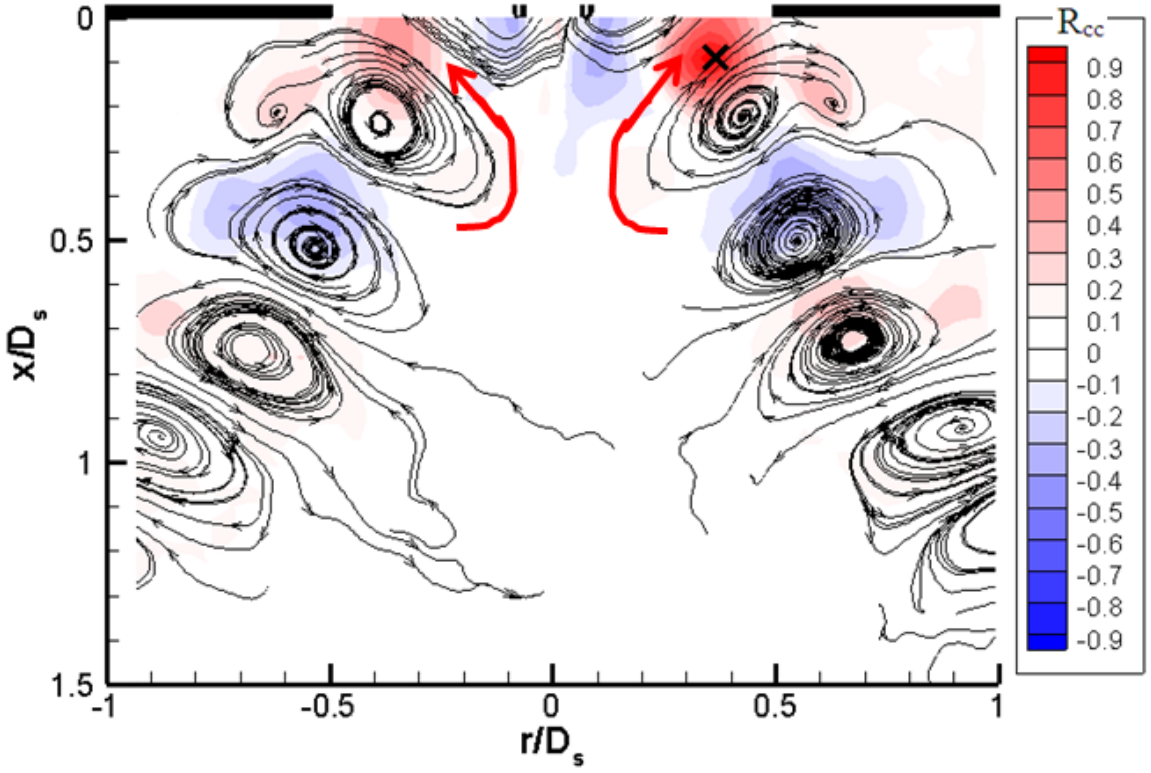

Fig. 6.15 Spatial scalar correlation (R_{cc}) contours of the with-jet case with reference point at (x/D_s=0.09, r/D_s=0.34) with superimposed stream traces of conditionally averaged axial-radial velocity

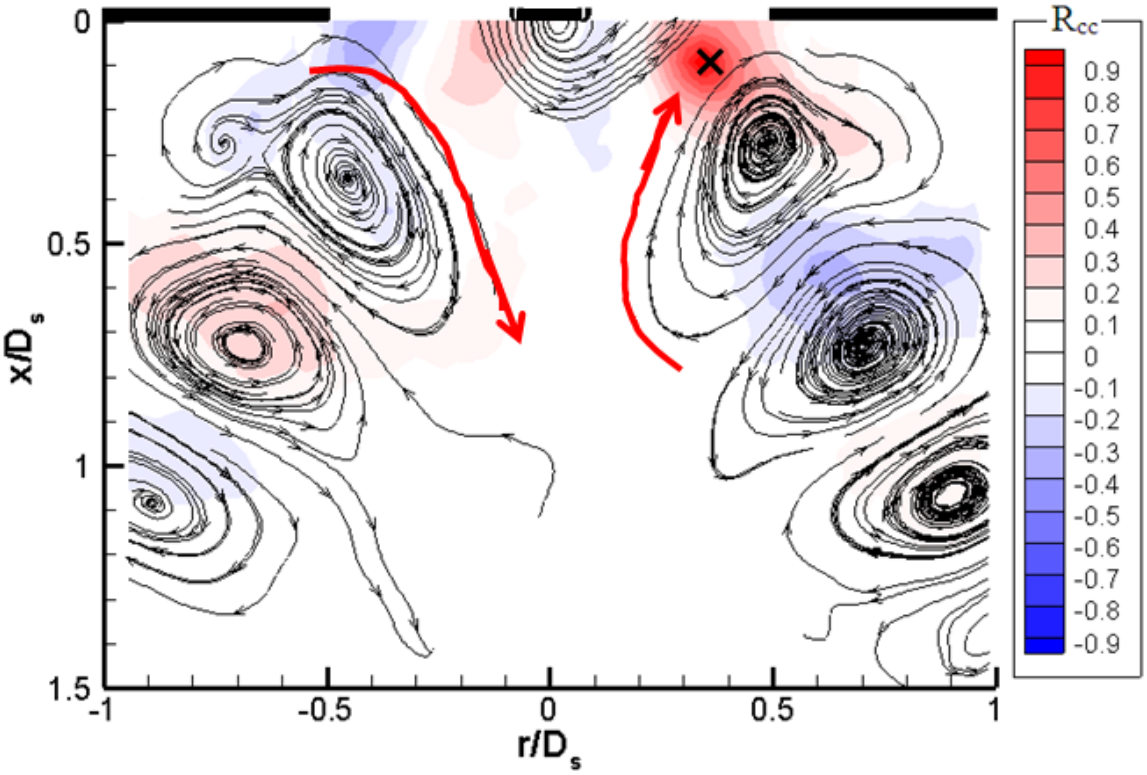

Fig. 6.16 Spatial scalar correlation (R_{cc}) contours of the no-jet case with reference point at (x/D_s=0.09, r/D_s=0.34) with superimposed stream traces of conditionally averaged axial-radial velocity

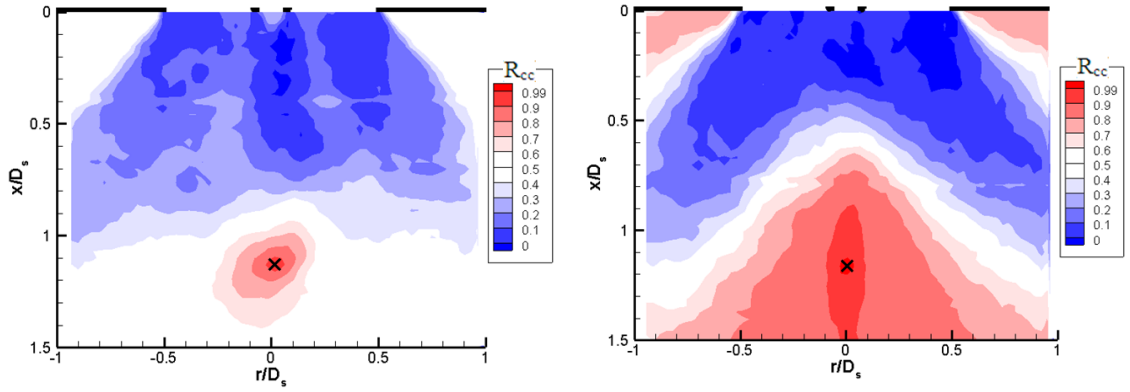

(a) With-jet (b) No-jet

Fig. 6.17 Spatial scalar correlation (R_{cc}) contours with reference point at (x/D_s=1.12, r/D_s=0)

The characteristic frequencies of the scalar fluctuations associated with the helical vortices are identical to those of the velocities for both test cases. Fig. 6.18 and Fig. 6.19 show the amplitudes of the primary and secondary PSD peaks of the with-jet and no-jet cases, respectively. As mentioned earlier, strong symmetry between vortices in the with-jet case result in doubling of the Strouhal number at S_t=1.2, while S_t=2.4 represents the pairs of strong and weak vortices, as discussed in Chapter 5.

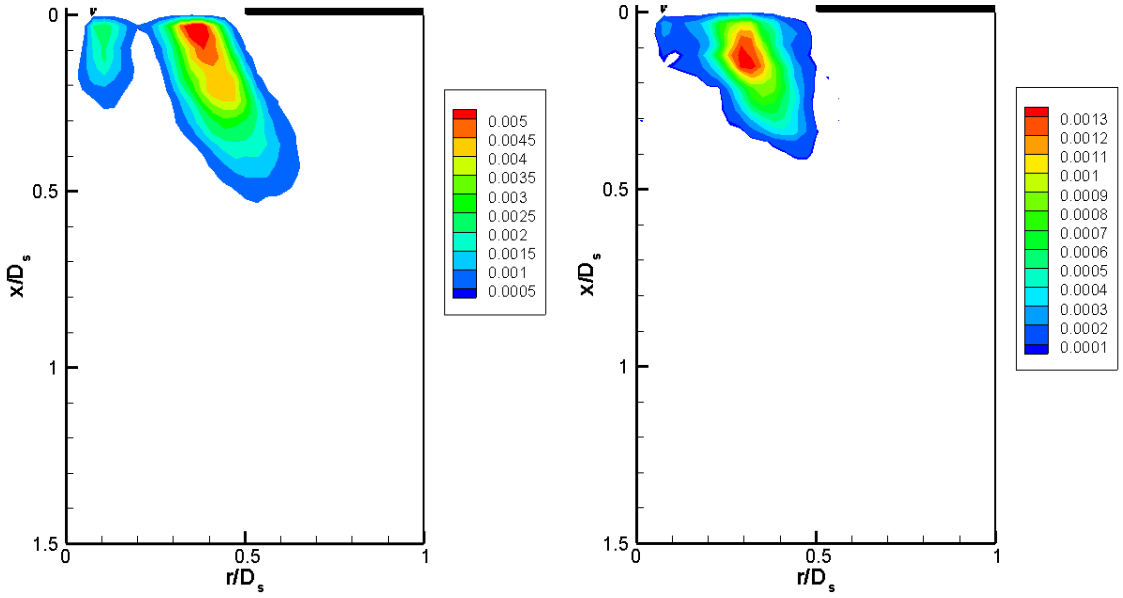

(a) Primary, $E_{cc}(S_t$=1.2) (b) Secondary, $E_{cc}(S_t$=2.4)

Fig. 6.18 PSD amplitudes of a) primary and b) secondary peaks of the with-jet test case, at S_t=1.2 and S_t=2.4, respectively

Spatial distributions of the PSD amplitudes are quite similar; higher amplitudes in the with-jet case are expected as strong symmetry of the vortices contributes to stronger periodic entrainment of fluid in the inner swirl shear layer. Unlike the PSD amplitudes of axial and radial velocities shown in Figs. 6.5, in which amplitudes larger than 0.02 are found at x/D_s=0.8, E_{cc} decays sharply and becomes negligible at x/D_s>0.5. This suggests that coherent scalar structures associated with the vortices are limited to the very nearfield of the fuel injector exit.

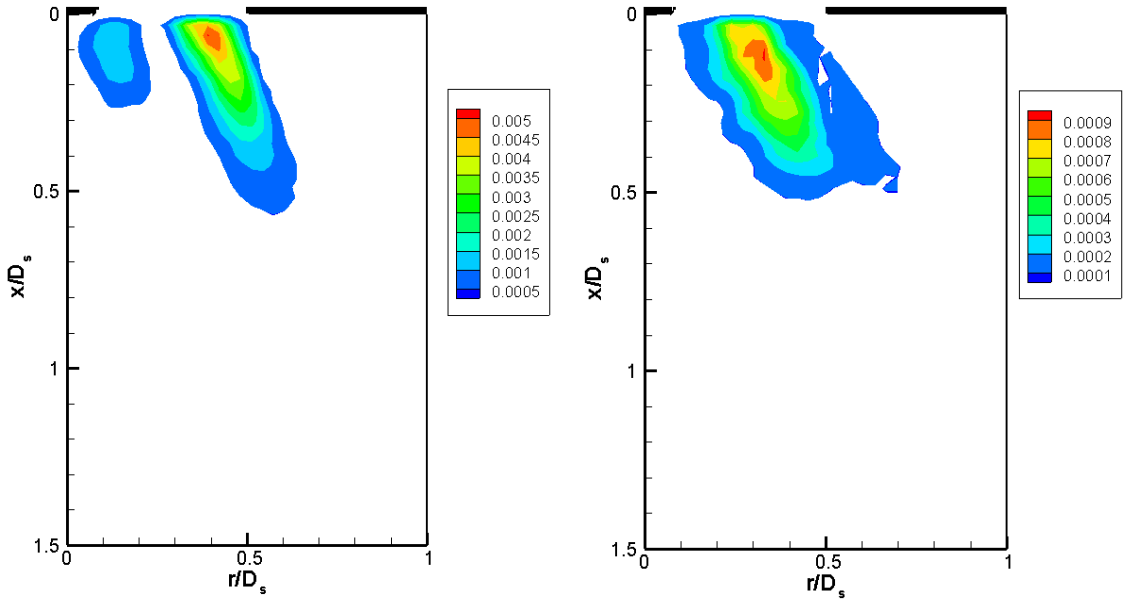

(c) Primary, E_{cc}(S_t=0.6) (d) Secondary, E_{cc}(S_t=1.2)

Fig. 6.19 PSD amplitudes of a) primary and b) secondary peaks of the no-jet test case, at S_t=0.6 and S_t=1.2, respectively

6.3 Residence times

The residence times of both test cases have been characterised using the dye shut-off technique described in Section 3.5. The technique employed to extract convection time and half-life time data from the scalar time histories is demonstrated in 6.3.1, followed by discussions and results of convection time, half-life time, and total residence time in Sections 6.3.2, 6.3.3, and 6.3.4.

6.3.1 Point histories

The technique developed in this work involves the extraction of two characteristic residence times from point histories of scalar after the dye injection is shut: convection time is interpreted as the time difference between the starting temporal 'instant' of decay of the reference point in 2D space and that of any other given point, while half-life time is interpreted as the time it takes for the concentration to decay to half of its original value at the starting 'instant' of decay, where the original value may vary between the time-mean and the time-mean minus one standard deviation (due to a limitation of the algorithm). These two characteristic residence times for a 2D-FoV in an x-r plane are reiterated here for easier referencing.

$$t_{conv}(x,r) = t_d(x,r) - t_{d,ref}(x_{ref},r_{ref}) \quad (6.1)$$

$$t_{1/2}(x,r) = \ln(2)/b(x,r) \quad (6.2)$$

Where t_{conv} is the convection time, t_d is the starting point of decay, $t_{d,ref}$ is the reference point for which t_d at all other points in (x,r) is subtracted, $t_{1/2}$ is the halflife time and b is the best-fit exponential coefficient. The extractions of the two characteristic residence times are demonstrated on a total of 8 points in the x-r plane for both test cases, as shown in Fig 6.20 and Fig. 6.21. It should be noted these particular 8 points are selected because they constitute a good representation of the entire FoV.

Fig. 6.20(a1) and (b1) show the scalar point histories at the reference point, which is located in the inner swirler exit. Despite the with-jet case's higher RMS scalar than the no-jet case in this region (see Fig. 6.8), the starting instant of decay here occurs earlier than any other point along the swirler exit for both test cases. Although the declines of scalar immediately after $t_{d,ref}$ appear very steep and decay fits appear perfect, fluctuations exist because the time durations for the scalar to decay to zero are much higher than the characteristic periodicities of the helical vortices. Take Fig. 6.20(a1) for a roughly estimated example, the time it takes (0.132 seconds) to decay from mean concentration to zero would have allowed more than 10 vortices to pass through this point at a frequency of S_t=1.2. In fact, when zooming into the decay fit, fluctuations of concentrations associated with vortex turnovers are revealed, as shown

in Fig. 6.20(a1). Each of Fig 6.20 (a1), (b1), (a2), and (b2) shows a spike in concentration after the decay fit has reached zero. These post-decay spikes in scalar profiles are likely a footprint of the reverse transport of dyed fluid from the swirl stream into the swirler passage, which have been identified in Figs. 6.11 and 6.12. The spikes are more temporally spread out in the no-jet case (Fig 6.20(b1) and (b2)) than in the with-jet case (Fig 6.20(a1) and (a2)). This is likely due to the no-jet case's larger vortex length scales, implying that the turnover time may be slightly longer. The fact that the with-jet case has a steady supply of low-concentration jet fluid may also result in more rapid mixing of these spikes. Fig 6.20(a3) and (b3) show the time histories at a point located just outside the swirl cone; decays at this point occur at much slower rates for both test cases than in the inner swirl cone because they are associated with slower turnover timescales of the CRZ. Also, although the overall decay trend is captured well, the fit is rather poor due to the high-frequency fluctuation during the decay. As it has been shown in Figs. 6.11 and 6.12, the outer half the swirl stream is characterised with temporally alternating patterns of high and low scalar concentration. In this particularly region, the detection of t_d can also be contaminated by the high-intensity fluctuation as the scalar value can come back up to ~1 after having dropped to 0.2 or lower, which is beyond the range of fluctuation before the decay. Fig. 6.20(a3) demonstrates the halflife time, $t_{1/2}$, as indicated by the spacing of 0.3s at half of the time-mean scalar value. As shown in Fig. 6.20(b3), the time separation between $t_{d,ref}$ and $t_{1/2}$ is then defined as the total residence time, t_{res}. Fig 6.20(a4) and (b4) show the time histories of a point further downstream in the swirl stream, where the initial drop of concentration to about 0.1 occurs at similar rates as those seen across the swirler exit, but this is followed by rises in concentration and ensuing fluctuations, which can again be explained by the post-decay spikes seen in Figs 6.20(a1) and (b1) being transported downstream. Indeed, the rise in concentration after the decay occurs at t~3.8s, which is very short after the concentration in Fig. 6.20(a1) dropped to a minimum, followed by the ensuing spike. This is consistent with the short convection delay (t_{conv}=3.630–3.606) that is detected by the algorithm.

a. with-jet

b. no-jet

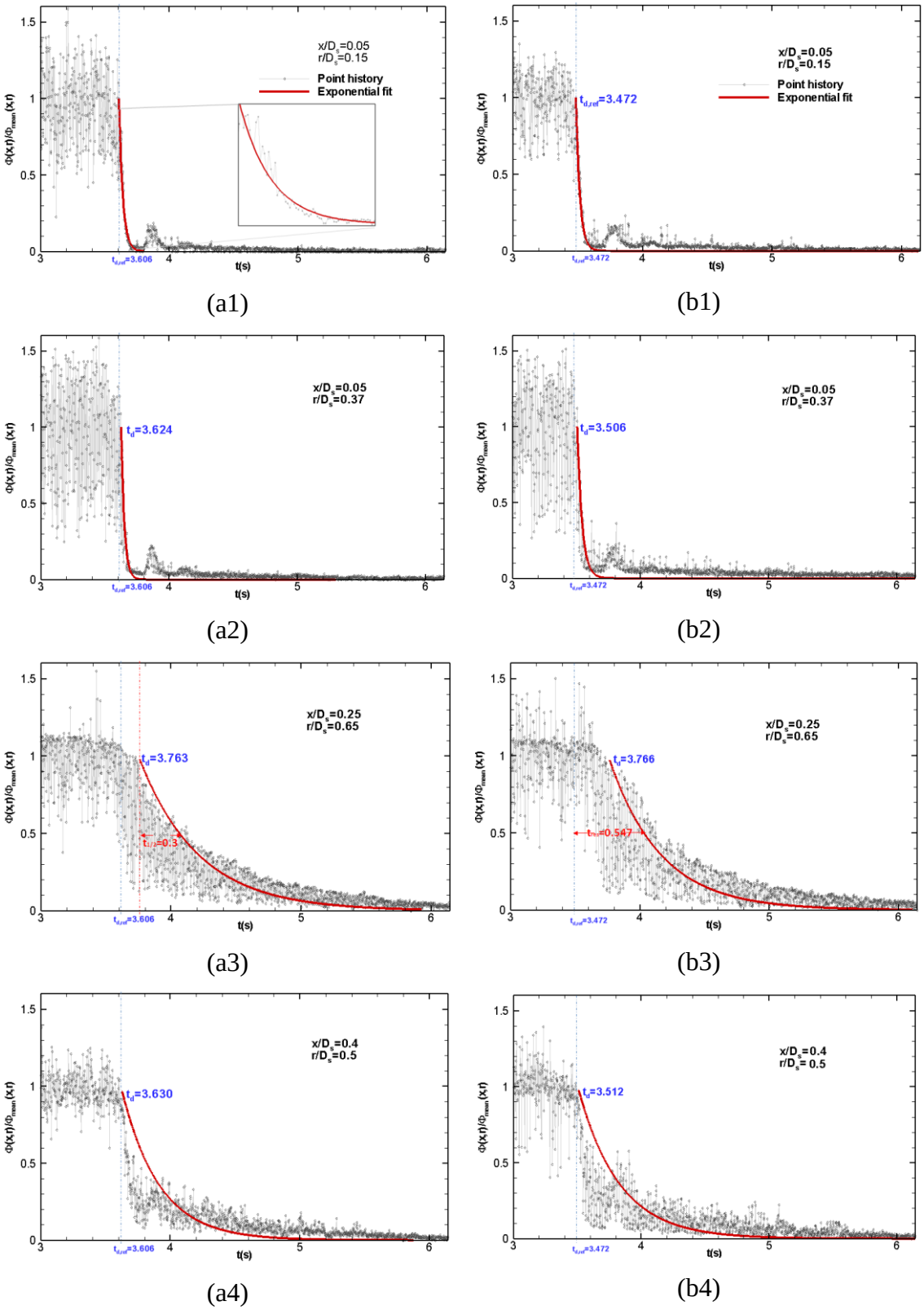

Fig. 6.20 Examples of point histories and decay fits (x/D_s<=0.4)

Figs 6.21(a1) and (b1) are taken from a point located downstream in the swirl stream. The convection times indicate that disturbances in the swirl exit are more quickly transported to this location for the with-jet case (t_{conv}=0.020s for with-jet and t_{conv}=0.048 for no-jet); this is likely a result of the former's more stably anchored swirl cone, as pointed out in Section 6.1.1. Again there is also evidence of the post-decay spikes noted in Fig. 6.20(a1) and (b1) being transported to this location, but post-decay fluctuations in the no-jet case are less pronounced because its longer convection time along the same convection path allowed for more vortex turnovers, which are conducive to mixing out the spike. Figs 6.21 (a2) and (b2) show the time histories of a point at one swirler diameter downstream along the centreline. Fig. 6.21(a2) is located in the free stagnation region, where the low-concentration jet fluid can occasionally penetrate beyond one swirl diameter, possibly resulting in the first dip to below 0.5. The detection of t_d may also be in error here as it is designed to search for the last time instant at which the concentration falls below one standard deviation. In other words, the technique picks up only the last decay trend and ignores all dynamic responses prior to t_d, as is the case throughout Figs 6.21(a3), (b3), (a4) and (b4). There are two major differences in the profiles of scalar decay between the profiles in columns (a) and (b) in Fig. 6.21: first, the with-jet profiles, particularly Figs 6.21(a2), (a3), and (a4)), are poorly fitted due to the sharp decline immediately after t_d, while the no-jet case profiles (Figs 6.21(b2), (b3), and (b4)) feature a more exponential-like decay trend; second, after the initial sharp decay after t_d, the with-jet's fluctuations persist at higher frequencies but with lower amplitudes than the no-jet case. For the with-jet case, the initial sharp decay and the ensuing spike are likely associated with the reverse transport of fluid along the CTRZ as very similar profiles exist along the swirler exit, and the ensuing high-frequency fluctuations associated with broadband turbulence are responsible for the rapid final decay. The decay profiles for the no-jet case, on the other hand, are marked with slower-changing crests and troughs; these are clearly a signature of the precession of dye fluid trapped in the vortex core – as the quasi-periodic PVC moves tangentially into and out-of the measurement plane, the concentration rises and falls slowly with it. These results are echoed by the spatial scalar correlation R_{cc} contours shown in Fig. 6.17.

a. with jet

b. no jet

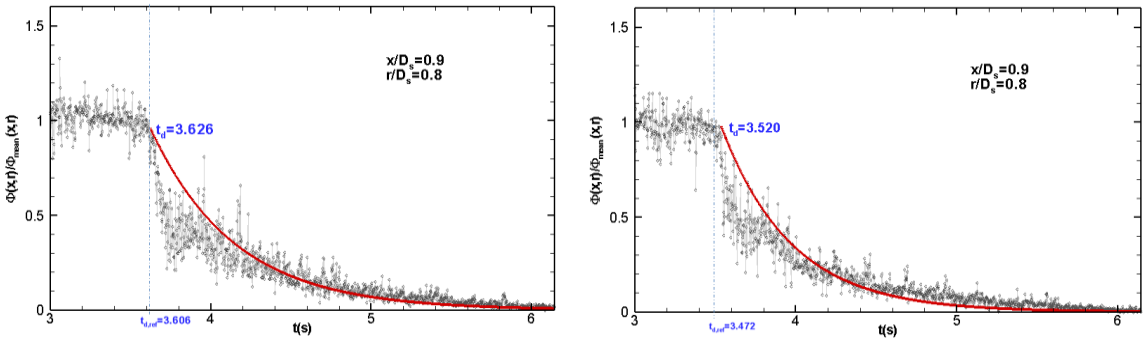

(a1) (b1)

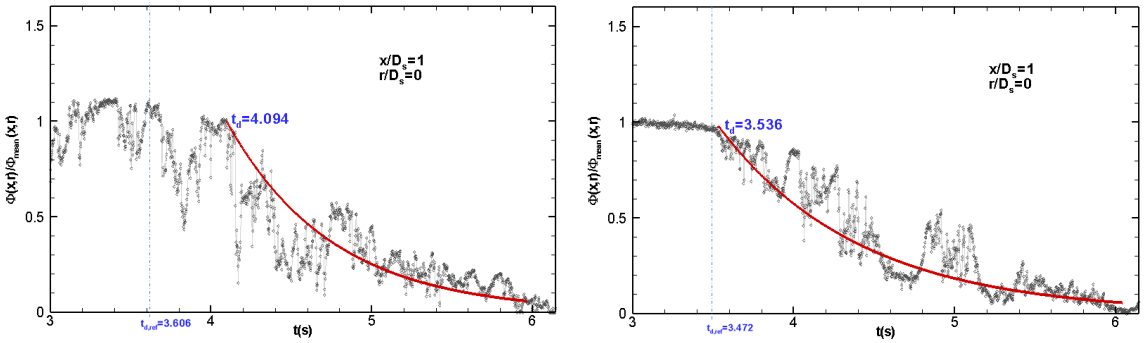

(a2) (b2)

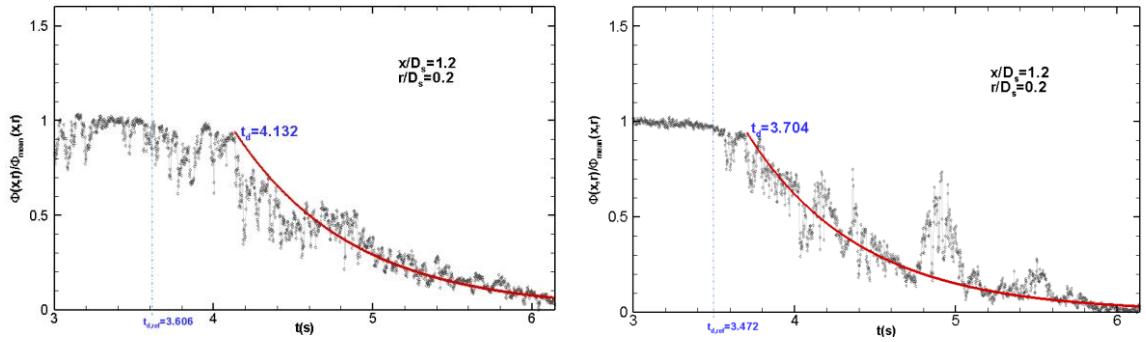

(a3) (b3)

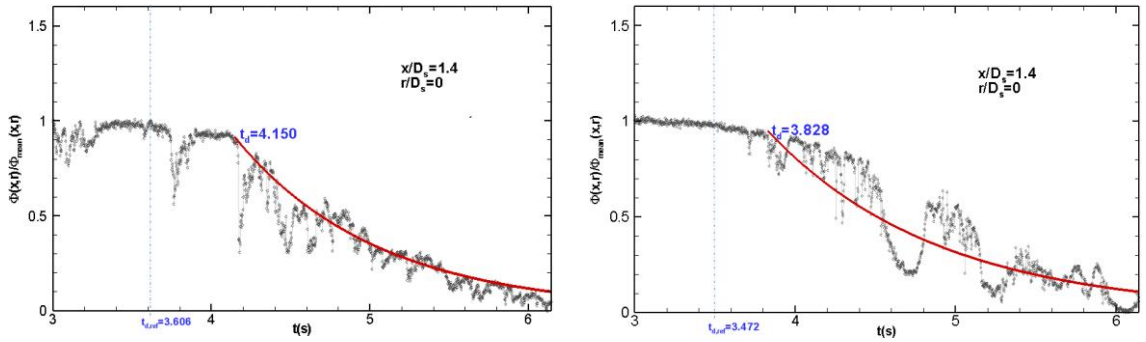

(a4) (b4)

Fig. 6.21 Examples of point histories and decay fits (x/D_s>=0.9)

6.3.2 Convection time

The point histories shown in Fig 6.20 and Fig 6.21 have an x-axis with unit of time in seconds because that allows for a more intuitive understanding of the timescales under discussion. From this section onwards, all characteristics times are to be converted into Strouhal-equivalent dimensionless timescales, denoted by τ_{conv}, $\tau_{1/2}$, and τ_{total}.

The convection times, τ_{conv}, for with-jet and no-jet cases are shown in Figs 6.22(a) and (b), respectively. For the with-jet case, the region along the centerline where the highest gradient of convection time is found (x/D_s ~ 0.7) is midway within the free stagnation region (x/D_s ~ 0.5 to 1.0) between forward flowing central jet and backward central recirculation zone (CTRZ). The convection time of the with-jet case is markedly longer than that of the no-jet case because the central jet stabilizes the CTRZ, resulting in a steadier convective path, which involves the swirl stream recirculating back into the FoV from downstream locations (x/D_s>1.5). The convection path for the no-jet case, on the other hand, is subject to significant variation over time because its CTRZ has been identified to assume a radial bias, and disturbances in one quadrant of the swirl stream can be quickly transported into the geometric centre region. The fact that the vortices are co-rotating in the near field, as shown in Fig. 6.16, can also contribute to this cross-quadrant transport as the swirl cone is drawn towards one quadrant, as evidenced by $+R_{cc}$ in outer swirl stream in one quadrant and $-R_{cc}$ in the other. In other words, the no-jet case's shorter convection time implies that disturbances originating from inside the fuel injector are likely to be transported into the CTRZ through large-scale turbulent features in a more rapidly mixing swirl stream, whereas scalar transport in the with-jet case follows the steadier recirculation path. The much higher τ_{conv} in the free stagnation region (x/D_s=0.7 to x/D_s=1.2) in the with-jet case may be due to possible t_d detection error in the free stagnation region and the definition for τ_{conv}, which requires the scalar to fall by one standard deviation below the steady mean. The outer shear layer of the swirl stream (between it and the corner recirculation) also shows some differences between the two test cases, with the no-jet case having a longer convection time. This demonstrates that the corner recirculation regions have a different dynamic. This is explained because it is found that the reverse flow on the outer wall of the test section extends to x/D_s of 1.5 for the no-jet case (Fig. 6.1(b)), whereas the with-jet case corner

recirculation is smaller, extending to x/D_s of 1.25 and is more stable in this location (Fig. 6.1(a)).

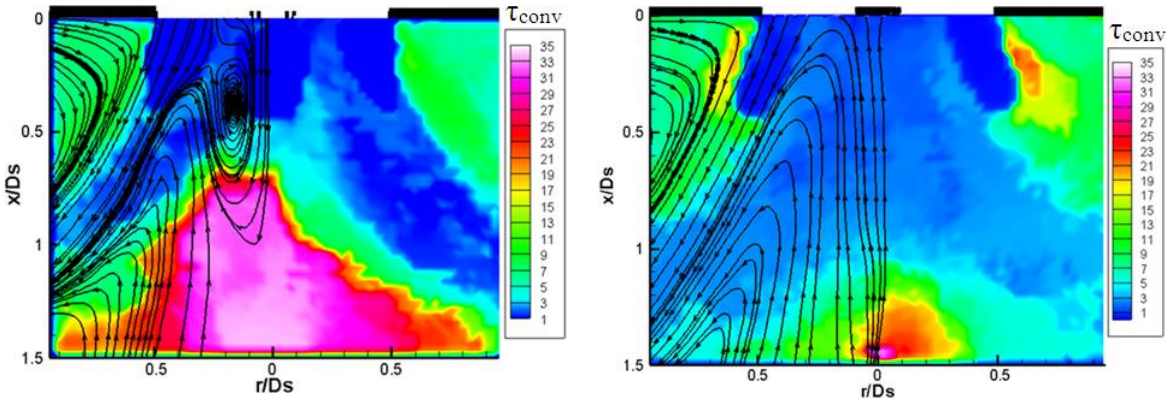

(a) with-jet (b) no-jet

Fig. 6.22 Normalised convection times

It has been shown in Fig. 6.9 that the with-jet case has higher scalar RMS values along the centerline than the no-jet case; thus, it will take longer at a given decay rate to exceed this condition. Supplementary videos are available of the scalar decay (Cheng and Spencer, 2012), which also demonstrates this behavior.

6.3.3 Half-life time

Provided that the disturbance is the sudden cut-off of the dye feed, the halflife time, $\tau_{1/2}$, describes how long it takes for fluid at a given point to reach zero concentration. Although the arrival time of the disturbance can also affect the concentration decay, the main determining factor for the rate of decay is likely associated with the local turbulent mixing rates, or the time rates of mass transport. In other words, in regions where turbulent mixing is relatively slower than in others, the decay of C after the disturbance has arrived will also take longer.

The half-life times shown in Figs. 6.23(a) and (b) reveal two major differences, which are highlighted in the regions bounded by the dashed lines. First, the with-jet halflife time in region (A) is up to 40% higher than the no-jet one. In order to explain this difference, it is important to study the amplitude contours of the primary PSD spikes for both the with-jet case (Fig. 5.43 (a) and (b)) and the no-jet case (Fig. 6.5). The

swirl stream that is dominated by high E_{uu} and E_{vv} are known to be characterized with time-dependent mass transport by the coherent structures, and these have been identified to lead to increased mixing. Here, the PSD amplitude contours are overlaid onto the $\tau_{1/2}$ contours, as indicated by the gray dotted lines in Fig. 6.23(a) and (b) respectively. The gray dotted lines mark the boundaries within which the PSD amplitudes are at least 5% of the maximum. The no-jet case has a significantly larger overlap between the gray dotted lines and region A, which implies that the coherent structure has a large contribution to mixing in the region, in addition to the mixing by the bulk motion of the CTRZ. The with-jet case, in contrast, has no overlap between the area bounded by the gray dotted line and region (A); therefore, inner-shear turbulence has significantly less impact on halflife times. In other words, because the vortex pair in the with-jet case follows a more stable helical path about a more stably anchored swirl cone, the strength of the coherent structure, along with its effect of rapid mixing, is limited to a more confined region in the swirl stream than that of the no-jet case. In summary, as region (A) falls completely outside of the area characterised with significant PSD amplitude, mixing in the region for the with-jet case is instead dominated by the bulk fluid motion associated with the slower-moving CTRZ, resulting in longer decay times. Supplementary videos showing the concentration decay can be found in Cheng and Spencer (2012).

The second most striking difference is located in the region marked by (B), where the half-life times of the no-jet case are about 20–30% higher than the with-jet case. This is believed to be due to the presence of a strong PVC: as dyed fluid is transported along the geometric centerline by the CTRZ, it appears to be trapped in the PVC's low-pressure and low-velocity center, which precesses about the geometric centerline at a low-frequency, as discussed in Section 6.1.2. The high half-life times in region (B) are also consistent with the R_{cc} contours shown in Fig. 6.17(b) and the dashed region of stagnant scalar throughout the six instantaneous snapshots shown in Fig. 6.12. The highest contour level on the centerline of Fig. 6.23(b) highlights the region over which the helical swirl center associated with a PVC is seen to exist through flow visualization. The central jet in the with-jet case has a time-varying penetration distance, which helps to quickly dilute the scalar trapped in the top of the CTRZ, or in the free stagnation region. The dilution by the central jet explains with-jet's significantly lower half-life times from x/D_s=0.6 to x/D_s=1.2. But downstream of

x/D_s=1.2, the rest of the CTRZ appears relatively stagnant and this region is also unaffected by the inner swirl shear turbulence, thus, the decay rates are relatively long for both test cases.

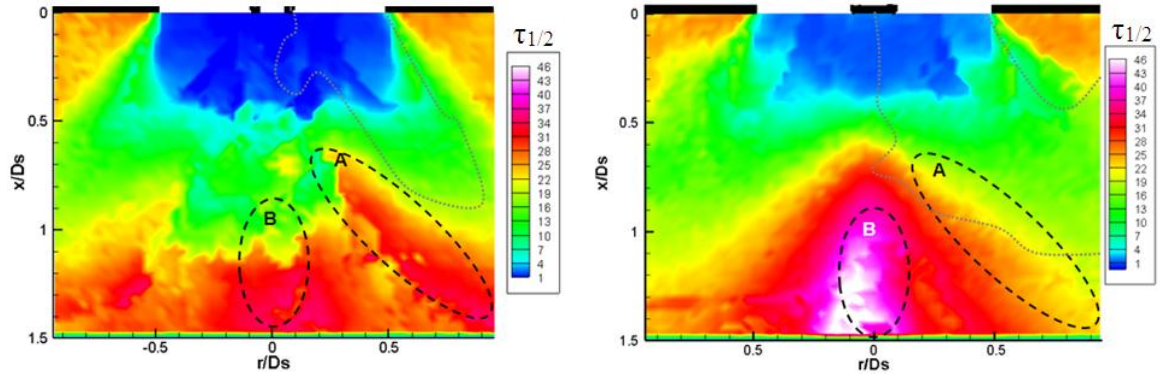

(a) with-jet (b) no-jet

Fig. 6.23 Normalised halflife times

6.3.4 Total residence time

Given the above differences in convective and half-life times, the residence times shown in Fig. 6.24(a) and (b) are found to be not too dissimilar. In general, the CTRZ of the with-jet case is dominated by long convection times and short half-life times, while the no-jet case exhibits an opposite phenomenon. Both test cases feature very low residence times in the immediate swirler exit (x/D_s<0.5), where coherent structures dominate and scalar fluctuations are highest. The residence time results are therefore consistent with the observation that the coherent flow structures are conducive to rapidly mixing out the radial bias in concentration in the swirler exit, as explained in Section 6.2.1 and also evidenced in the Reynolds decomposed scalar contours shown in Fig. 6.11 and Fig. 6.12. Downstream of this point (x/D_s=0.5), the difference between the two test cases' total residence times are mainly explained by with-jet case's longer convection times due to its stable swirl cone and no-jet case's longer half-life time due to its PVC. In other words, the combustion chamber sees inlet disturbances relatively quickly in the case of the no-jet case compared to the with-jet case, but then, the effect of the disturbance takes longer to decay from the chamber. Nevertheless, both test cases have essentially the same global timescale ($\tau_{global}=D_s/U_{ref}$) as the bulk swirl velocity (U_{ref}=U) is consistent for both test cases. An experimentally determined residence time distribution derived from global timescale,

τ_{res}, would therefore be expected to be similar.

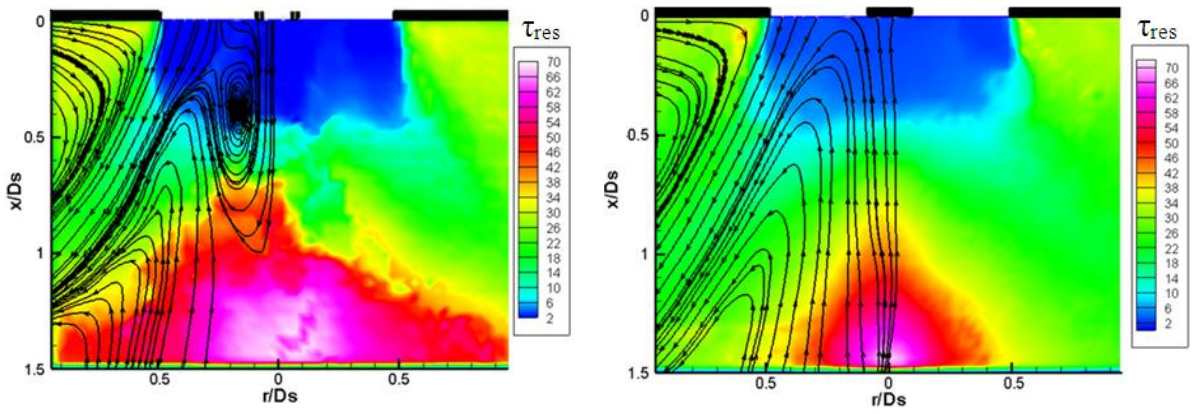

(a) with-jet (b) no-jet

Fig. 6.24 Normalised total residence times

Figs. 6.22 and 6.23, and hence Fig. 6.24, all show that the characteristics times are not well-resolved in the swirl cone in the very near field ($x/D_s<0.5$). Because the measurement duration has to be long enough to capture the longer decay curves at $x/D_s>1$, the relatively shorter convection and halflife times in the region are smeared. Despite this, difference in $\tau_{1/2}$ in the region can still be observed, where $\tau_{1/2}$ in the with-jet case is roughly half of that in the no-jet case; and this difference has also resulted in the difference in τ_{res}. It is argued here that the shorter $\tau_{1/2}$ in the with-jet case (in the swirl cone at $x/D_s<0.5$) is associated with the higher scalar fluxes, as shown in Figs. 6.13 and 6.14. This is because the magnitudes of the turbulent scalar fluxes are likely correlated with the rate of scalar transport in this fuel injector flow; hence the regions of shorter halflife times are likely to be correlated with turbulent scalar fluxes. A more in-depth analysis is required to confirm the relationship between residence times and turbulent scalar fluxes, but with the temporal resolution being the main constraint, this has not been explored further.

6.3.5 Repeatability

Two separate measurements with different FoVs, have been carried out in the xr plane to assess the repeatability of the technique and the data reduction method. Total residence time results of the no-jet case have been selected for illustration, as shown in Fig. 6.25.

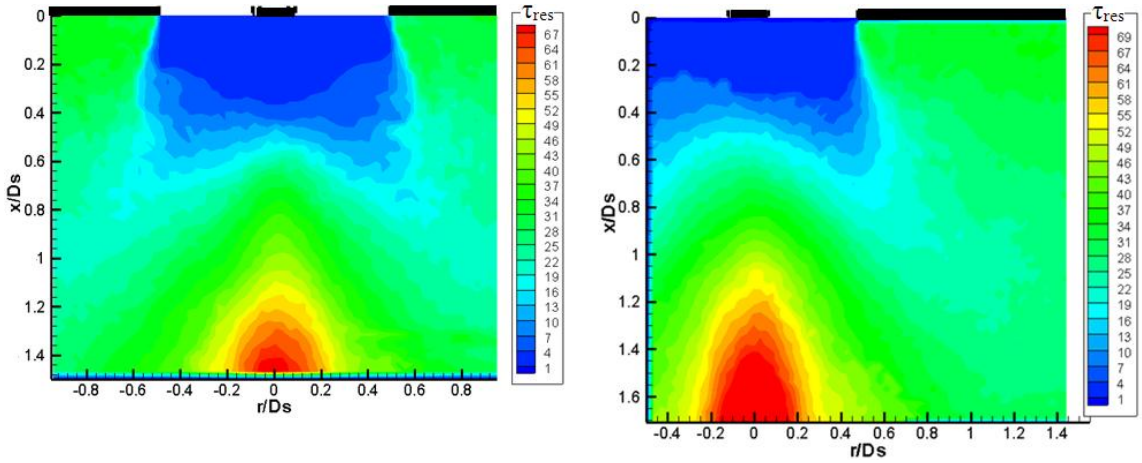

Fig. 6.25 Total residence time, τ_{res}, taken at two different FOVs (a) main test, (b) repeat test

It should be noted that the repeat test has been subject to two changes: first, the mass flow split has been altered (m_{dye} increased by 10%) to assess the sensitivity of the results to a different dye-feed to swirl stream mass flow ratio; second, the fuel injector has been rotated by 60 degrees to assess the level of circumferential uniformity. As shown in Fig. 6.25, there is good agreement between the two measurements in terms of both the distributions of the contours and their magnitudes. The level of agreement can be further scrutinized by comparing the profiles along the centreline, as shown in Fig. 6.26. As shown in Fig. 6.26, there is fairly good agreement between the two centreline profiles. This direction has been chosen since it contains both the near field, dominated by high exit velocities (and therefore short timescales), and also the central recirculation zone, with low-velocity reverse flow (and associated long timescales). A good level of repeatability is seen, despite very high turbulence levels, particularly in the combined residence time. Discrepancy does occur in convection time and half-life. This appears to be due to a difference in the shape of the initial decay curve for the two measurements within the central recirculation zone. The low PVC precession frequency (S_t~0.01) corresponds to a non-dimensional period of around 70 on these figures, so the phase angle of the precession is probably becoming important to the measurement and affecting where the algorithm determines the intercept point that defines the start of the decay. This region is where the largest discrepancies have occurred in all measurements reported here and demonstrates that with a low number of parameters describing the decay (τ_{conv}, $\tau_{1/2}$) single measurements are probably acceptable providing the model decay curve is representative and that the derived

parameters are longer or at least the same order of magnitude when compared to the flow timescales being investigated.

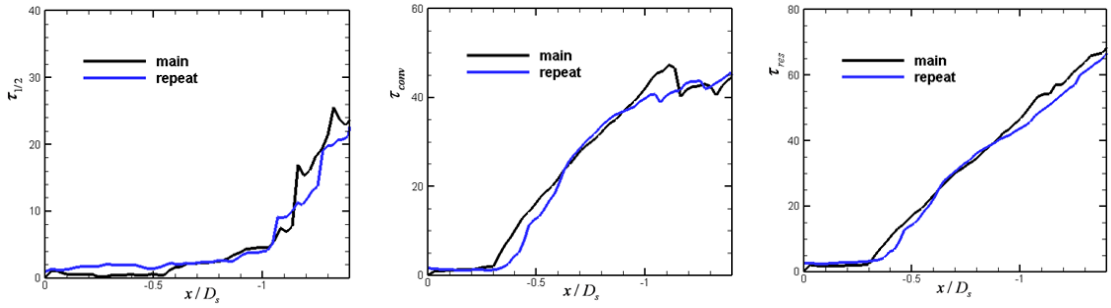

(a) (b) (c)

Fig. 6.26 Centreline profiles of (a) convection time, (b) half life time, and (c) total residence time

Measurements taken in the r-θ plane at 3 axial stations also served as valuable datasets for the purpose of repeatability testing and assessment of circumferential variation. Residence times in the r-θ planes were calculated on specified polar mesh. Since the swirler exit reference point, $t_{d,ref}$, is not available for downstream axial stations, the convection times have been calculated with reference to $t_{ref}=t_{shut}+t_{response}$. The data taken at $x/D_s=0.13$ has been selected for illustration in Fig. 6.27. The level of circumferential variation is also a good test of repeatability in the sense that over a long time average, the velocity and scalar fields are found to be axis symmetric; thus, it would also be expected of the scalar timescales. In general, it can be seen from Fig. 6.27 that the circumferential variation in timescales does not exceed ±5% in the swirl stream exit ($r/D_s<0.5$). In the corner recirculation region for $r/D_s>0.5$, the variation is typically less than 10%, but here, the flow timescales are an order of magnitude larger than for the swirl stream exit. The data in Fig. 6.27 have been circumferentially averaged to produce the radial profile of characteristic times in Fig. 6.28. This process allows for the best estimate of the average of multiple measurements in order to remove variations due to the flow structure rotational phase angle.

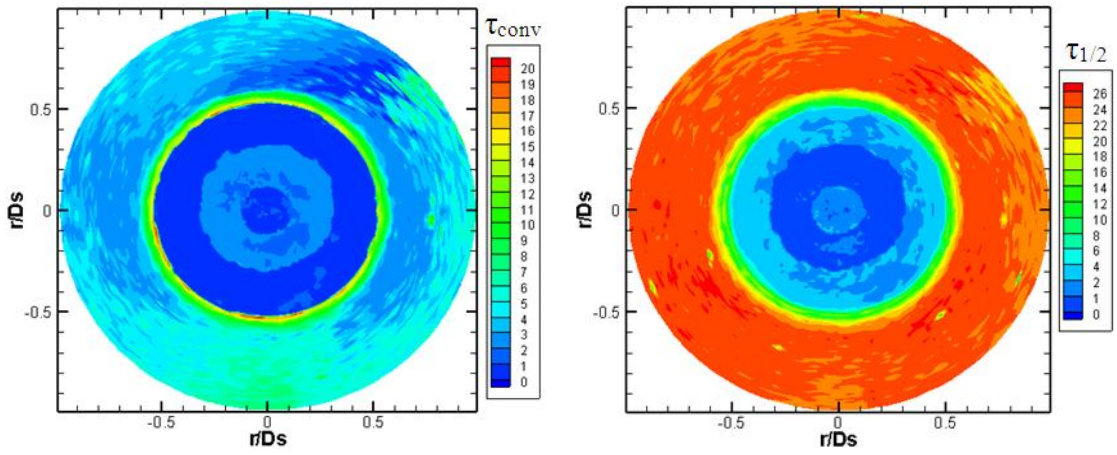

(a) Convection time (b) Halflife time

Fig. 6.27 Measurements of residence times in the r-θ plane at x/Ds=0.13 (with-jet case)

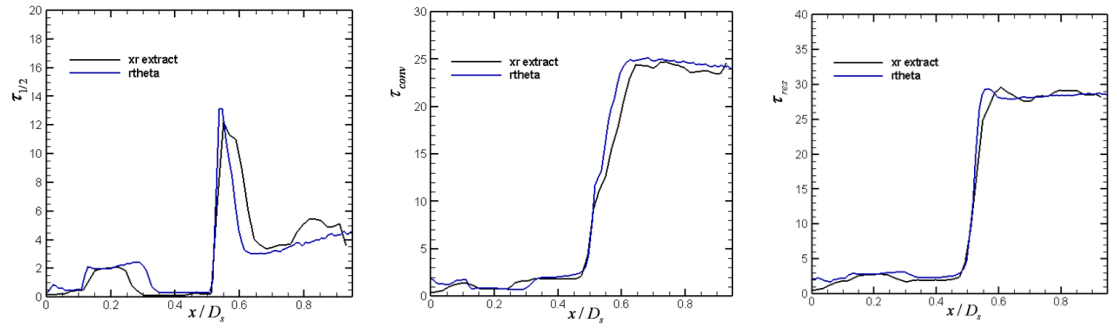

(a) (b) (c)

Fig. 6.28 With-jet residence times in the r-θ plane at x/Ds=0.13: (a) convection time, (b) half-life time, and (c) residence time

The near-zero convection times in Figs. 6.28 (a) and (c) indicate the region around the time reference point at the swirl stream exit has uniform values and is a reliable base time for the time at which the dye shutoff enters the combustion chamber. The circumferentially averaged profiles are compared to an equivalent profile extracted from the x–r plane measurement at x/Ds=0.13 (which can contain no circumferential averaging). There is good agreement between the two with-jet tests on perpendicular planes, demonstrating good repeatability of the technique. The agreement in the no-jet case is also reasonable, but the very long timescale PVC that exists in this condition has reduced the level of agreement that is seen in the with-jet case. This could of course be improved by performing multiple realizations if the additional accuracy is required.

6.4 Reference to combustion data

In actual combustor operations, time-dependent variables such as fuel concentration, chemical reaction, flame location, heat transfer, and thermal expansion can all contribute to and interact with the aerodynamic residence times including both convection and half-life times. Indeed, in addition to the aerodynamic residence time, identification of thermal NO_x production regions and mechanisms also requires the characterisation of several other factors (General Electric, 2001): a) fuel-to-air ratio or firing temperature, b) combustor inlet air temperature and pressure and c) flame zone residence time. Hence, spatially resolved data pertaining to these variables in a combusting, reactive test case is required to quantify their complex interactions in the context of local NO_x production. Although this is outside the scope of the current work, the reacting experiment conducted by Meier et al (2007, 2010) on the Turbomeca fuel injector, operated in the premixed mode without the central jet, provides some of the data, around which a qualitative discussion can be built. In addition to NO_x production, the importance of residence time measurements in the studies of combustion instabilities is also highlighted.

6.4.1 Main flame zone

In the reactive tests performed by Meier et al (2007, 2010) on a very similar Turbomeca fuel injector (different only in size), the global mixture fraction is ζ_{global}=0.0463, which is calculated by dividing the mass flow rate of methane (CH_4) by that of the inlet air. It should be noted that the dye-feed to swirl stream mass flow rate ratio in the current work is 0.0495, which is quite close to ζ_{global}. Along the inner swirl shear at x/D_s~0.21, the mixture fraction varies from ζ=0.03 to ζ=0.075. The authors state that the variation in mixture fraction is due to short mixing length in the swirl duct where methane and air premix. A similar observation, based on the high RMS concentration at swirler exit, has also been noted in Section 6.2.1. OH-LIF test shows that the flame is anchored in the inner swirl shear (for example: r/D_s=0.29-0.43 at x/D_s=0.21), where the flames experiences large variations in mixture fraction and temperature. This is consistent with the radial span of peak RMS concentration at x/D_s=0.21 shown in Fig. 6.9(b). Conditionally averaged velocities and R_{cc} shown in Fig. 6.16 indicates asymmetry of the swirl cone; this has also been observed in the

phase-averaged OH chemiluminescence contours in Meier et al (2007), thought not explicitly stated by the authors. In addition to this, the alternating patterns of high and low scalar fluctuations identified in Fig. 6.16 have also been noted in Meier et al (2007). The convection time of such disturbance in the fuel mixture from the fuel injector port in the swirler to the base of the main flame zone plays a crucial role in completing the instability feedback loop, as discussed in Section 1.2.3. Meier et al (2007, 2010) calculates t_{conv} based on the mean axial velocity and distance to a point in the main flame zone, and the period (plus the convection time from the fuel feed port to the combustor inlet) is found to be quite close to that of the pressure oscillation. However, such method is rather crude and does not help determine if the entire flame zone is characterised with the same convection time. With careful consideration, the technique developed in the current work could be applied to combusting conditions to help identify the regions which are subject to combustion instabilities.

Unfortunately, because there has been no data with the fuel injector operated under with-jet and premixed conditions thus far, it remains questionable as to whether with-jet's much longer convection time, along with the effect of central jet dilution, could damp the pressure oscillations to prevent fuel mixture perturbation, and subsequently eliminate the feedback mechanism.

Boxx et al (2010) also experimented with two types of flame: 'noisy' flame which is thermal-acoustically excited and 'quiet' flame which is without pulsation. In the quiet flame, mixture fraction approaches ζ_{global}, or fully mixed, further downstream (x/D_s~ 1.06 to 2.15), which is similar to that shown in Fig. 6.8(b). With quite flame, the main region of heat release is within (x/D_s~1.1-1.9) along the geometric centreline, which falls within the region of long half-life times (see Fig. 6.23(b)). Despite the flame being more stable (no pulsation), the authors still highlight noticeable scatter in mixture fraction in the main region of heat release but mention neither the cause nor the temporal characteristic of it. It is argued here that the variation of mixture fraction in this particular region is partly due to the PVC as methane-rich combustion products, which result from the poor mixing in the swirl duct, could be entrained into the low-pressure precession centre of the PVC in a region that is dominated by long half-life times. Syred et al (2006), for example, shows that in a swirling flow with a similar swirl number, natural gas is completely entrained into the PVC and burnt on the

boundary. The authors also present the resulting 'rotating' temperature fields, in which maximum temperature was found within the PVC centre. Therefore, the precession with methane-rich gases could have resulted in the variation in mixture fraction, though this was not explicitly stated. Therefore, the main region of heat release can be influenced by variations in fuel concentrations upstream, but once this disturbance is entrained into the PVC, its combination of long half-life times and high flame temperatures can also prove to be favourable to NO_x production.

6.4.2. Effect of helical vortex structure

Thus far, cold flow tests (Dunham, 2010) and reacting tests (Meier, 2007) have not shown clear interaction between the inner shear coherent structure and the PVC; in other words, there has been no evidence to suggest coupling between the two hydrodynamic instabilities. Unlike the low-frequency PVC, the pair of vortices that persists in the inner swirl shear travels along the helical paths at a much higher frequency. Stohr's (2012) investigation on a dual-swirler fuel injector showed that the inner swirl shear vortices periodically enlarges the flame surface and is conducive to mixing of burnt and unburnt gasses. Given that these occur at the characteristic frequencies of the vortices, it is of interest to study if the convection time from the fuel feed to the inner swirl shear is favourable for the coupling between heat release and pressure oscillations. Again, with careful considerations, the method developed in the current project could be used to quantify this convection time. Another possibility is to study the relationship between half-life time and chemical reaction time in the inner swirl shear and other turbulent regions. This could perhaps provide some idea of the flame residence time once a perturbation (e.g. increase in equivalence ratio) is transported to that point.

6.5 Chapter summary

This chapter looks at fuel injector operated in the premixed mode and the fluid mechanics of two test cases has been studied: with a central jet feed of fresh undyed fluid (with-jet) and no central jet (no-jet). The results of a new residence time measurement technique using spatially resolved PLIF have also been provided for the first time.

Section 6.1 discusses the time-mean and time-dependent flow field features. While the central jet penetration and reverse flow via the CTRZ result in a free stagnation region about (x/Ds~0.75), the CTRZ in the no-jet case is seen to extend all the way to the swirler exit plane and possibly impinges on the blocked central jet. The swirl streams are markedly different between the two test cases too: the no-jet case has a much more spread-out swirl stream in which the PSD peaks of the axial and radial velocity components also dominate over a larger area; and the swirl stream's outer wall attachment locations also differ between the two (with jet: x/D_s=1.25, no-jet: x/D_s=1.5). Examination of 3C RMS velocities in the no-jet case reveals strong correlation between the radial and tangential components at x/D_s>0.8, which is due to the presence of a PVC.

The time-mean flow field implies that with-jet case features a more stable and well-defined swirl cone; this is clearly seen in the time-mean scalar data too. For visualisation purpose only, the mean concentration contours shown in Fig. 6.8 are rotated about the x-r plane and cut-off below the fully-mixed concentrations ($\langle C\rangle/\langle C_{max}\rangle$ < 0.55) to show the iso-surfaces of the swirl cones. The highest RMS concentrations found in the swirl stream just downstream of the swirler exit (r/D_s~3-4.5) indicate poor mixing within the swirl duct where dyed fluid mix with fresh water. Scalar fluctuation at x/D_s>0.7 along the centreline also vary between the two cases: while the with-jet case shows a decreasing trend along axially downstream, the no-jet case features a gradual rise due to dyed concentration trapped in the PVC.

The coherent structures that dominate in the inner swirl cone follow helical paths downstream. The characteristic frequency of the with-jet case is double that of the no-jet case due to the pairing of the rotational directions in the former and the lack of it the latter. Entrainment of neighbouring fluid by these helical vortices result in alternating patterns of high and low concentrations in the nearfield (x/D_s<1) in the vicinity of the swirl cone, and the characteristic Strouhal numbers of scalar fluctuation are identical to those of the velocity components.

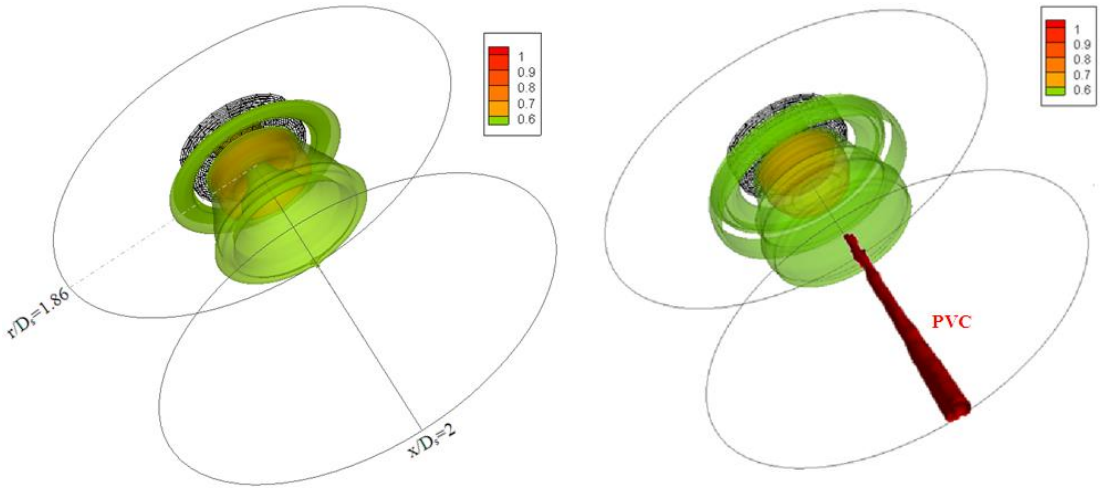

With-jet No-jet

Fig. 6.29 Iso-surfaces of mean concentration ($<C>/C_{max}>0.55$) and an arbitrarily drawn PVC[7]

The residence time characterisation technique developed in this project involves the extraction of convection and half-life time data from scalar point history following a cut-off of the dye feed. A total of 16 examples of scalar point histories have been provided, showing that the single exponential function makes a good decay fit to describe the half-life times in most point locations. The convection and half-life times of the two test cases both suffer poor resolution in the very near field ($x/D_s<0.5$) within the swirl cone due to coarse temporal resolution. Other than this region, it was shown that disturbances are more quickly transported from the swirler exit to the volume enclosed within the swirl cone in the no-jet case due to its less stable, more outspread swirl stream, which is also dominated by coherent structures of larger length scales. The with-jet case's central jet anchors the swirl cone and stabilises the swirl stream such that disturbances follow a more well-defined CTRZ. Also, for the no-jet case, once disturbances are transported to the centreline at $x/D_s>0.6$, it takes much longer to mix out due to the long half-life times there, which are associated with the PVC. With careful considerations, the technique developed could not only be applied to reactive tests to identify the main regions of NO_x productions, but also to study the effect of convection times on the coupling between heat release and pressure oscillation.

[7] The PVC iso-surface is not drawn with basis on any physical quantity. It is arbitrarily drawn for indication of its presence only.

Chapter 7

7. CONCLUSIONS AND RECOMMENDATIONS

7.1 Conclusions

Non-premixed tests

The primary objectives of this thesis were to improve the understanding of turbulent mixing of passive scalar and to provide the much-needed benchmark experimental data for the validation of LES predictions. Although LES and experimental studies on a similar fuel injector geometry had been reported previously by a number of authors, there still lacked combined PIV-PLIF measurements for the validation of all three turbulent scalar fluxes. The fuel injector had been operated in the non-premixed mode where the central fuel jet was directly injected into the cylindrical chamber, in which all measurements were made. In order to ensure similar jet penetration and mixing properties as those found in combusting tests, the test condition was specified such that the momentum flux ratio between the central jet and swirl stream were matched.

Simultaneous measurements of velocity and passive scalar require multi-camera setup, which is now a well-established technique. A series of guidelines had been observed in order to minimise errors in PIV-measured velocity; a step-by-step PLIF image calibration and processing procedure had been followed and the bias error associated with temporal variation of light sheet energy and absorption effect was estimated to be 3.7%.

2C-PIV/PLIF data were collected in an x-r plane, as well as 3C-SPIV/PLIF in both x-r and r-θ planes. Varying filter widths of scalar was shown to have an effect on the computed scalar flux. The subgrid filtering error correction technique developed by Spencer and Hollis (2005) had been applied to scalar data for the first time, after successful validations using the current experimental data, synthetic data, as well as other scalar data available in literature. An adaptive scalar filtering technique had been employed such that additional filtering of the raw pixel data did not give rise to more than 0.5% of error. For both velocity and scalar data, the error associated with spatial resolution (relative to local integral lengthscales) was assessed for x-r plane

data using the highest resolution 2C-PIV measurements. Largest errors in (up to 20% for velocity and up to 2% for scalar) were found near injector exit on the edge of the jet potential core. Only a small distance downstream ($x/D_s > 0.2$) errors had reduced to less than 10%. Sample size effects were also evaluated and suggested the selected sample size of 1500 had a statistical convergence error of ~5% in regions that are important to scalar mixing.

The results showed that the inner swirl shear layer features two strong vortices which are separated by $\theta=\pi$; instantaneous snapshots of 3C-velocity field in the r-θ plane indicate that they are characterized with strong reverse flows. Two weak vortices had also been revealed in Reynolds decomposed velocity fields. These vortices dominate in the inner swirl shear of the swirl cone, as evidence by the existence sub non-swirl pressure in the region. The counter-rotating relationship between the adjacent strong and weak vortices is conducive to drawing jet fluid radially outward, resulting in two fuel-rich quadrants and two lean ones. Coherent structure analyses using conditional averaging and proper orthogonal decomposition both confirm the presence of these coherent structures and their effect on scalar transport. Power spectral analysis showed that the vortices and the scalar entrainment both occurred at two discrete frequencies; these dominated in the inner swirl shear within one swirler diameter downstream of the fuel injector. Because the level of the periodically entrained scalar concentration is quite close to the stoichiometric condition (reference to combusting data, assuming similar mixing properties), there is clear implication on heat release oscillations, as well as NO_x production.

The contours of turbulent scalar fluxes indicated that positive axial velocity fluctuation in the jet shear is likely coupled with radial outward entrainment of jet fluid, while reverse flows are likely coupled with radial inward transport of undyed fluid from the swirl stream. The net tangential transport of jet fluid in the jet shear was in the clockwise direction, as opposed to the counter-clockwise direction of the swirling flow. The fact that the jet shear exhibits high frequency fluctuations of scalar fluxes suggests that fluid exchange by the smaller eddies was independent of the large-scale entrainment by the helical vortices in the inner swirl shear.

Finally, validation of LES predictions by direct comparisons of statistics had been

performed. Comparison of mean velocity and scalar profiles at injector exit showed very good agreement with LES. Comparison of rms velocity and scalar fluctuation profiles at this axial location showed some discrepancies between measurements and LES predictions, although this was mainly in the region of highest measurement uncertainty. All 3 scalar flux profiles compared very well between LES and experimental data throughout the primary mixing region. This work has two main conclusions. Firstly, it is very important to pay special attention to estimate and control (via spatial resolution) errors due to spatial filtering in combined PIV-PLIF measurements of turbulent scalar fluxes if high quality validation data are required. Secondly, the level of agreement between LES (incorporating a very simple constant-Schmidt number SGS model) and measured scalar fluxes shown had provided important validation confirmation of the ability of LES to predict scalar mixing in this fuel injector mixing field.

Premixed tests

In premixed tests, the dye feed and the swirl stream were premixed in the swirler passage prior to exiting into the cylindrical expansion chamber. Two test cases have been studied with the fuel injector operating in the premixed configuration: with central jet (with-jet) and without central jet (no-jet). The primary objectives were to compare and contrast the aerodynamics and mixing characteristics between the two test cases and also to apply a newly developed residence measurement technique. The technique relies on looking at the temporal response to the cessation of the injection of a conserved scalar at the inlet to a particular region of interest. This has been described in literature previously for point-based measurements, but in this work, planar measurements are performed to provide good spatial resolution of timescales within a region of interest.

Combined PIV-PLIF results showed that the no-jet case has a more spread-out swirl stream and also has a less stable swirl cone. Spatial scalar correlation with the reference point in the inner swirl shear, superimposed with conditionally averaged velocity field, reveals the asymmetric nature of the no-jet case with regard to the spatial distribution of scalar correlation and the rotating direction of the vortex pair. The co-rotating relationship between the vortex pair in the no-jet case is believed to

exert a net radial direction bias on the entire swirl cone, while the central jet serves to restore symmetry and to stabilise the swirl cone.

For the residence time measurements, the measured decay curves are characterized using a model decay function consisting of a convection time and half-life time: the former describes the shortest time span by which a disturbance at the fuel injector exit can be transported to the point of interest, and the latter describes the rate of exponential decay after the reduction in concentration due to fuel shut is transported to the point of interest. The residence time (time to reach half of the initial value) can be considered to be the sum of these two quantities. It was found that for the no-jet case, fluid is likely to be transported to the central recirculation zone much more quickly than the with-jet case due to the former's relatively unstable nature. The with-jet case contains two pairs of very coherent helical vortices along with a more stable central recirculation zone, and the rate of mixing between these two regions is seen to be reduced. Thus, in the with-jet case, the central recirculation zone is filled more from the downstream direction rather than direct turbulent transport through the shear layer between it and the swirl cone that surrounds it. In the same region, it was also found that the half-life times of the no-jet case are significantly higher, associated with the presence of the precessing vortex core that appears to trap fluid in the swirl center. Comparisons with repeated data in different field of views and measurement planes show satisfactory agreement, confirming acceptable repeatability of the technique despite its single-realization nature.

7.2 Recommendations for future work

Measurement techniques

- Because planar nature of SPIV makes it impossible to characterize the helical paths of the vortex pairs, such information has been extracted from LES predictions. Also, the calculation of time-mean static pressure using Reynolds averaged momentum equations assumed negligible contribution by derivatives in the circumferential direction; such assumptions will need to be verified by analysis of similar-resolution volumetric PIV data. Tomo-PIV may be able to provide answers to these questions.

- With the fuel injector operating in diffusion flame mode, LES predictions indicate reverse transport of scalar into the swirl passage, but the upstream distance of the reverse transport has not been characterised with experimental data. Similarly, with the fuel injector operating in the premixed mode, the cause of poor mixing in the swirl passage has not been clearly identified. To address these two issues, innovative techniques to measure concentration inside the swirl slots and swirl passage are required.
- The current residence time measurement technique characterises the convection delay from a reference point in the swirler exit to all other points of interest. But in combustion diagnostics such as predicting auto-ignition, for example, there is a need to measure the convection time from the fuel feed port to the swirler exit as well. Therefore, future work may consider modification to the test rig where the dye shut-off is designed in the fuel feed port instead.
- The residence time measurement developed in the current work is of a single realization, meaning that the transient response to upstream disturbance was characterised only once. Future experimental designs may incorporate inputting a sinusoidal disturbance in the fuel concentration upstream, for example, and studying the dynamic changes at different locations downstream.
- The first DNS study of the Turbomeca fuel injector in combusting condition (Moureau et al, 2011) has recently become available. The main focus of the paper was to assess the prediction capabilities of the LES flamelet models, but with more data analyses and subsequent publications to follow, a comprehensive validation of LES predictions against both experimental and DNS data can be expected in the near future.
- Finally, all computational and experimental studies reported thus far were all performed in single-sector expansion chambers. This does not provide insight into the interaction between two or more fuel injector flows in an annular combustor. Hence, future experimental designs in isothermal condition may incorporate multi-sector rigs.

REFERENCES

Adrian R. (1991) – "Particle-imaging techniques for experimental fluid mechanics", *Ann Rev Fluid Mech,* Vol 23: 261-304

Adrian R. (2005) – "Twenty years of particle image velocimetry", *Exp. in Fluids,* Vol: 39 pp 159-169

Agui J., Jiminez J. (1987) – "On the performance of fluid tracking", J. Fluid Mech., Vol 185:447-468

Antonia R., Mi J. (1993) – "Temperature dissipation in a turbulent round jet", *J. Fluid Mech.,* Vol 250:531-551

Arai M, Nomura T, Hiroyasu H (1998) – "Residence time measurement in a swirl type combustor with Helium tracer", *The Japan Soc. Of Mech. Eng,* 86-1302A 2619-2625

Arroyo M. and Greated C. (1991) – "Stereoscopic particle image velocimetry", *Meas. Sci. Technol.* Vol 2 1181–6

Astarita T. (2009) – "Adaptive space resolution for PIV", *Exp. in Fluids,* Vol 46: 1115-1123

Barlow R., Karpetis, A. (2004) – "Scalar length scales and spatial averaging effects in turbulent piloted methane/air jet flames", *Proceedings of the Combustion Institute,* Vol 30:673-683.

Batchelor G. (1959) – "Small-scale variation of convected quantities like temperature in turbulent fluid. 1. General discussion and the case of small conductivity", *J. of Fluid Mechanics,* Vol 5:113–133

Bendat J.S. and Piersol A.G. (1986) – "Random data (analysis and measurement procedures)", *John Wiley*

Bilger R. (2004) – "Some aspects of scalar dissipation", *Flow Turbulence Combust,* Vol 72:93-114

Borg A., Bolinder J., Fuchs L. (2001) – "Simultaneous velocity and concentration measurements in the near field of a turbulent low-pressure jet by digital particle image velocimetry-planar laser-induced fluorescence", *Exp in Fluids,* Vol 31:140-152

Boxx I., Arndt C., Carter C., Meier M. (2010) – "Highspeed LASER diagnostics for the study of flame dynamics in a lean premixed gas turbine model combustor"

15th Int Symp on Applications of Laser Techniques to Fluid Mechanics, Lisbon, Portugal

Boyce M. (2006) –"Gas turbine engineering handbook", *Elsevier*, 3rd edition

Bridges J., Wernet M. (2002) – "Turbulence measurements of separate flow nozzles with mixing enhancement features", *8th AIAA/CEAS Aeroacoustics Conference*, AIAA-2002-2484

Brun C., Balarac, G., da Silva C., Metais O. (2008) – "Effects of molecular diffusion on the subgrid-scale modeling of passive scalars", *Physics of Fluids*, 20, 025102

Canepa E., Di Martino P., Formosa P., Ubaldi M., and Zunino P. (2006) – "Unsteady aerodynamics of an aeroengine double swiler lean premixing prevaporizing burnter", *Journal of Engineering for Gas Turbines and Power***,** DOI: 10.1115/1.1924720

Chatterjee, A – "An introduction to proper orthogonal decomposition", *Current Science*, Vol.78, No.7

Cheng L. and Spencer A. (2012) – "Residence time measurement of an isothermal combustor flow field", *Exp Fluids* Vol 52:647-661

Cheng L., Dianat M., Spencer A., McGuirk J.J. (2010) – "SPIV/PLIF validation of LES predictions of scalar mixing in high-swirl fuel injector flows". *In: ETMM8: 8th Int. ERCOFTAC Symp*. Marseille, France.

Cheng L., Dianat M., Spencer A., McGuirk J.J. (2012) – "Validation of LES predictions of scalar mixing in high-swirl fuel injector flows", *Flow Turbul. Combust.* 88,143-168

Chigier, N.A. and Beer, J.M. (1972) – "Combustion Aerodynamics", *Applied Science Publishers*, England

Coppeta J., Rogers C. (1998) – " Dual emission laser induced fluorescence for direct planar scalar behavior measurements", *Exp in Fluids*, Vol 25: 1-15

Coupland, J., Priddin, C. (1986) – "Modelling the flow and combustion in a production gas turbine combutor", *Turbulent Shear Flows, Vol 5.*

Crimaldi J. (2008) – "Planar laser induced fluorescence in aqueous flows", *Exp. in Fluids*, Vol 44:851-863

Crimaldi J. (2008) – "Planar laser induced fluorescence in aqueous flows", *Exp. in Fluids*, Vol 44:851-863

Crimaldi J., Koseff J. (2001) – "High-resolution measurements of the spatial and temporal scalar structure of a turbulent plume", *Experiments in Fluids,* Vol 31:90-102

Dabiri J. and Gharib M. (2005) – "Starting flow through nozzles with temporally variable exit diameter", *J. Fluid Mech*, Vol 538 111-136

Dahm W. and Dimotakis P. (1990) – "Mixing at large Schmidt number in the self-similar far field of turbulent jets", *J Fluid Mech*, Vol 217 299–330

Davis 7.2 (2009) – "Flowmaster Mannual", *LaVision*

Dewey C. (1976) – "Qualitative and quantitative flow field visualization utilizing laser-induced fluorescence", *In: Proc AGARD Conf Applications of Non-Intrusive Instrumentation in Fluid Flow Research*, AGARD-CP-193, Vol 17 1–7

Dianat (2007) – "LES of flow and mixing through LPP-type combustor", *Rolls-Royce UTC Internal Report,* Loughborough University

Dianat,M., Yang, Z., Jiang, D.,McGuirk J.(2006) – "LES of scalar mixing in a coaxial confined jet", *Flow Turbul. Combust.* 77, 205–227

Driscoll J., Chen R., Yoon Y. (1992) – "Nitric xxide levels of turbulent jet diffusion flames: effects of residence time and Damköhler number", *Combustion and Flame* Vol.88:37-49

Du H., Fuh A., Li J., Corkan A., Lindsey J. (1998) – "PhotochemCAD: A computer-aided design and research tool in photochemistry", *Photochemistry and Photobiology,* Vol 68:141-142

Dunham D. (2010) – "Unsteady Fluid Mechanics of Annular Swirling Shear Layers", *PhD Thesis, Department of Aeronautical and Automotive Engineering, Loughborough University, UK*

Dunham D., Spencer A., Dianat M., McGuirk J. (2009) – "Comparison of URANS and LES CFD Methodologies for Air Swirl Fuel Injectors", *ASME J. of Eng. for GT and Power*, Vol 131: 011502 1-8.

EPA (2012) – "Standards of performance for stationary gas turbines; standards of performance for stationary combustion turbines; proposed rule", *Environmental Protection Agency*, USA

Escudier, M.P. (1988) – "Vortex Breakdown: Observations and Explanations", *Prog. Aerospace Science,* Vol.25 189-229

Feng H., Olsen M., Fox R., Hill J. (2007) – "Conditional statistics for passive-scalar mixing in a confined rectangular turbulent jet", *Physics of Fluids,* Vol 19: 055104

Fukushima C., Aanen L., Westerweel J. (2000) – "Investigation of the mixing process in an axisymmetric turbulent jet using PIV and LIF", *Applications of Laser Techniques to Fluid Mechanics, Lisbon,* Portugal, paper 11-1

Gabriele A., Nienow W., Simmons M. (2009) – "Use of angle resolved PIV to estimate locals pecific energy dissipation rates for up- and down-pumping pitched blade agitators in a stirred tank", *Chemical Engineering Science,* Vol 64: 126-143

Garcia-Villalba, M. Frohlich, J. and Rodi, W. (2007) – "Numerical simulations of isothermal flow in a swirl burner," *Journal of Engineering for Gas Turbines and Power***,** DOI: 10.1115/1.2364198

General Electric GT: Davis L. and Black S. (2001) – "Dry Low NOx Combustion Systems for GE Heavy-Duty Gas Turbines", *General Electric Power systems,* Schenectady, NY

Giordano D, Giammartini S, Manfredi F, Guj G (2001) – "Non dimensional numbers dependency on a Dry Low NOx Annular Burner Analysed with PIV Technique", *9th National Conference AIVELA,* Ancona

Gnirß M., Tropea C. (2008) – "Simultaneous PIV and concentration measurements in a gas-turbine combustor model", *Exp in Fluids,* Vol 45: 643-656

NewWave Solo XT120 Laser Manual (2005)

Grosjean, N., Grafieaux, L., Michard, M., Hubner, W., Tropea, C. and Volkert, J. (1997) – "Combining LDA and PIV for Turbulence Measurements in Un-Steady Swirling Flows", *Measurement Science and Technology,* Vol.8 1523-1532

Gupta A., Lewis M., Daurer M. (2001) – "Swirl effects on combustion characteristics of premixed flames", *Journal of Engineering for Gas Turbines and Power,* DOI: 10.1115/1.1339987

Gupta, A.K. (1984) – "Swirl Flows" *Abacus press, Kent, England*

Hassan E., Aono H., Boles J., Davis D., Shyy W. (2011) – "Adaptive Turbulent Schmidt Number Approach for Multi-Scale Simulation of Supersonic Crossflow", *20th AIAA Computational Fluid Dynamics Conference*, 27 - 30 June 2011, Honolulu, Hawaii

Heywood J., Fay J., Lindern L. (1970) – "Jet aircraft air pollutant production and dispersion" *AIAA,* 70-115

Hinze J.(1959) – "Turbulence: an introduction to its mechanism and theory", *McGraw-Hill Book Company, Inc.*

Hollis D. (2004) – "Particle Image Velocimetry in Gas Turbine Combustor Flow Fields", PhD Thesis, *Loughborough University, UK*

Hollis D. *Email communication in 2008*

Høst-Madsen A., Nielsen A. (1995) – "Accuracy of PIV measurements in turbulent flows", *ASME Laser Anemom.*, Vol 229: 481–488

Hu H., Saga T., Kobayashi T., Taniguchi N. (2001) – "Simultaneous velocity and concentration measurements of a turbulent jet mixing flow" *Ann. N.Y. Acad. Sci.*, Vol 972: 254–259

Huang, Y. and Yang, V.(2005), "Effect of swirl on combustion dynamics in a lean-premixed swirlstabilized combustor," *Proceedings of the Combustion Institiute*, Vol. 30, pp. 1775–1782.

Huchet F., Line A., Morchain J. (2009) – "Evaluation of local kinetic energy dissipation rate in the impeller stream of a Rushton turbine by time-resolved PIV", *Chemical Engineering Research and Design*, Vol 87:369-276

ICAO (2010) – "ICAO environmental report", *ICAO*, 2010.

IPCC (1999) – "Aviation and the Global Atmosphere**",** *IPCC Special Reports on Climate Change*, Cambridge University Press

James S., Zhu J., and Anand M. (2006) – "Large-eddy simulations as a design tool for gas turbine combustion systems", *AIAA Journal*, Vol 44, No. 4

Janus B., Dreizler A., Janicka J. (2004) – "Experimental study on stabilization of lifted swirl flames in a model GT combustor", *Flow Turbul. Combust*, Vol 75 293–315

Janus, B., Dreizler, A., Janicka, J. (2007) – "Experiments on swirl stabilized non-premixed natural gas flames in a model gas turbine combustor", *Proceedings of the Combustion Institute, Vol 31 2091-3098*

Jong J., Cao L., Woodward H., Salazar J., Collis R., Meng H. (2009) – "Dissipation rate estimation from PIV in zero-mean isotropic turbulence", *Experiments in Fluids*, Vol46:499-515

Karasso P., Mungal M. (1997) – "PLIF measurements in aqueous flow using the Nd:YAG laser", *Exp in Fluids*, Vol 23:382-387

Keane R., Adrian R. (1990) – "Optimization of particle image velocimeters. Part I: Double pulsed systems", *Meas. Sci. Technol.*, Vol: 2 963-974

Kemnitz, K., Tamai N., Yamazaki I., Nakashima N., Yoshihara K. (1986) – "Fluorescence decays and spectral properties of Rhodamine B in submono-, mono-, and multilayer systems", *J. Phys. Chem.,* Vol 90: 5094-5101

Kempf A. (2008) – "LES validation from experiments", *Flow Turbulence Combust,* 80:351–373

Kempf A., Klein M., Janicka J. (2005) – "Efficient generation of initial and inflow conditions for transient turbulent flows in arbitrary geometries", *Flow Turbulence Combust,* Vol 74:67-84

Kerr, N.M. and Frasier, D. (1965) – "Swirl Effects of Axi-Symmetrical Turbulent Jets" *J. Inst. Fuel,* Vol 38 19-526

Khezzar, L. (1998) – "Velocity Measurements in Near Field of a Radial Flow Swirler" *Experiments in Thermal and Fluid Science,* Vol.16:230-236

Klein M., Sadiki A., Janicka J. (2003) – "Digital filter based generation of inflow data for spatially devel-oping DNS and LES", *J. of Comp. Phys.,* Vol 186: 625-665

Kline, S., McClintock, F. (1953) – "Describing Uncertainties in Single-Sample Experiments", *Mech. Eng.*

Konle M., Kiesewetter F., Sattelmayer T. (2008) – "Simultaneous high repetition rate PIV-LIF measurements of CIVB driven flashback", *Exp. Fluids,* Vol 44, 29–538

Koutmous, P., McGuirk, J. (1989) – "Isothermal modelling of gas turbine combustors: computational study", *J. Propulsion, 7, No. 6 pp. 1064-1071*

Lartigue, G., Meier, U., and Berat, C. (2004) – "Experimental and numerical investigation of self excited combustion oscillations in a scaled gas turbine combustor," *Applied Thermal Engineering*, Vol. 25, pp. 1583–1592.

Lawson N, Wu J. (1997) – "3D PIV: Experimental error analysis of a digital angular stereoscopic system", *Meas. Sci. & Technol*., Vol 8: 1455–1464

Lee S., Lele S., Moin, P. (1992) – "Simulation of spatially evolving compressible turbulence and the application of Taylors Hypothesis", *Physics of Fluids,*Vol A4:1521-1530

Lefebvre A. (1998) – "Gas turbine combustion", *Taylor and Francis,* 2nd ed

Lehwald A., Thevenin D., Zahringer K. (2010) – "Quantifying macro-mixing and micro-mixing in a static mixer using two-tracer laser-induced fluorescence", *Exp. in Fluids,* Vol 48:823-836

Leibovich, S. and Stewartson, K. (1983) – "A sufficient condition for the instability of columnar vortices" *Journal of Fluid Mechanics,* Vol.126 335-356

Lemonine, F., Antoine, Y., Wolff, M. and Lebouche, M. (1999) – "Simultaneous temperature and 2D velocity measurements in a turbulent heated jet using combined laser-induced fluorescent and LDA" *Experiments in Fluids,* Vol.26:315-323

Libby P (1996) – "Introduction to turbulence", *Taylor & Francis*

Lieuwen T. (2006) – "The gas turbine handbook", *Department of Energy,* USA

Lieuwen T., McDonell V., Petersen E., Santavicca D. (2008) – "Fuel flexibility influences on premixed combustor blowout, flashback, autoignition, and stability", *ASME J. of Eng. for GT and Power,* Vol. 130, 011506-1:10

Lieuwen T., Torres H., Johnson C., Zinn B. (2001) – "A mechanism of combustion instability in lean premixed gas turbine combustors", *ASME J. of Eng. for GT and Power,* Vol 123, p182-189

LIF in liquid fluids (2008), *LaVision Manual*

Loffler M., Pfadler S., Beyrau F., Leipertz A., Dinkelacker F., Huai Y., and Sadiki A. (2008) – "Experimental determination of the sub-grid scale scalar flux in a non-reacting jet flow", *Flow Turbulence Combust,* Vol 81:215-219

Lucca-Negro O. and Doherty T. (2001) – "Vortex breakdown: a review", *Progress in Energy and Combustion Science,* Vol 27 431-481

Lumley J. (1967) – "The structure of inhomogeneous turbulence", In *Atmospheric Turbulence and Propagation,* Yaglom, V. I. Tatarski, pp. 166-78.

Lumley J. (1981) – "Coherent structures in turbulence", *In Transition and Turbulence,* Meyer, pp. 215-42. New York: Academy

Lund T., Wu X., Squires D. (1998) – "Generation of turbulent inflow data for spatially developing boundary layer simulations", *J. Comp. Phys.,* Vol 140:233-258

Frohlich M., Rodi J., Garcia-Villalba W. (2008) – "Scalar Mixing and Large-Scale Coherent Structures in a Turbulent Swirling Jet", *Flow Turbulence Combust,* Vol 80 47–59

Matlab (2010) – "Pearson random number generation, *Matlab,* Help file

Matlab (2010) – "Power spectral density estimate", *Matlab,* Help file

Meier W., Boxx I., Stohr M., Carter C. (2010) –" Laser-based investigations in gas turbine model combustors", *Experiments in fluids,* DOI 10.1007/s00348-010-0889-x

Meier W., Weigand P., Duan X., Giezendanner-Thoben R. (2007) – "Detailed characterization of the dynamics of thermoacoustic pulsations in a lean premixed swirl flame", *Combustion and Flame,* Vol 150 2–26

Melton L., Lipp C. (2003) – "Criteria for quantitative PLIF experiments using high-power lasers", *Exp in Fluids,* Vol 35(4): 310:306

Merkle K., Hassler H., Buchner H., Zarzalis N. (2003) – "Effect of co- and counter-swirl on the isothermal flow and mixture field of an airblast atomizer nozzle", *International Journal of Heat and Fluid Flow,* Vol 24: 529-537

Meyer K., Ozcan O., Larsen O., Gjelstrup P., Westergaard C. (2000) – "Point and planar PLIF for velocity-concentration correlation in a jet in cross flow", *Proceedings of the 10th International Symposium on Applications of Laser Techniques to Fluids Mechanics, Lisbon, Portugal,* 18.5

Moureau V., Domingo P., Vervisch L., Veynante D. (2012) – "From Large-Eddy Simulation to Direct Numerical Simulation of a lean premixed swirl flame: Filtered laminar flame-PDF modelling", *Combustion and Flame,* Vol.158:1340-1357

Mi J. and Nathan, G. (2003) –"The influence of probe resolution on the measurement of passive scalar and its derivatives", *Experiments in fluids,* Vol. 34: 687-696

Midgley K. (2005) – "An isothermal experimental study of the unsteady fluid mechanics of gas turbine fuel injector flowfields", *PhD Thesis*, Loughborough University.

Midgley K., Spencer A., McGuirk J. (2005) – "Unsteady flow structures in radial swirl fed fuel injectors", *ASME J. of Eng. for GT and Power,* Vol 127: 755-764.

Midgley, K. (2005) – "An isothermal experimental study of the unsteady fluid mechanics of gas turbine fuel injector flowfields", *PhD Thesis, Department of Aeronautical and Automotive Engineering, Loughborough University, UK*

Midgley, K., Spencer, A., Mcguirk, J. (2005) – "Unsteady flow structures in radial swirler fed fuel injector", *ASME Journal,* Vol.127:755-764

Mirskii G. (1981) – "Statistical errors of measurement of cross-correlation functions", *Izmeritel'naya Teknika translated by Plenum Publishing Corporation*

MOLECULES Report (2004) – "Modelling of low emissions combustors using large eddy simulations," *Tech. rep.*, Report number: WP3-LOUGH-15M, Deliverable 3.3

Munson B., Rothmayer Al, Okiishi T., and Huebsch W. (2012) –"Fundamentals of Fluid Mechanics", Wiley, 7th Edition

Mydlarski (2003) – "Mixed velocity--passive scalar statistics in high Reynolds number turbulence", *J. Fluid Mech.*, Vol 475 173-203

Nicol D., Steele R., Marinov N., and Malte P. (1995) – "The importance of the nitrous oxide pathway to NOx in lean premixed combustion", *ASME Journal of Engineering for Gas Turbines and Power*, Vol 117 100:111

Noble D, Zhang Q, Shareef A, Tootle J, Meyers A, Lieuwen T (2006) – "Syngas mixture composition effects upon flashback and blowout", *ASME* 2006-90470

Novara M. and Scarano F. (2012) –"Performances of motion tracking enhanced Tomo-PIV on turbulent shear flows", *Experiments in Fluids,* Vol. 52, 4: 1027-1041

Owen E. (1976) – "Simultaneous laser measurements of instantaneous velocity and concentration in turbulent mixing flows", *AGARD-CP193*, Paper No. 27

Ozdemir IB, Peters N (2001) – "Characteristics of the reaction zone in a combustor operating at mild combustion", *Exp Fluids* 30:683–695

Pantano C., Sarkar S., Williams F.A. (2003) – "Mixing of a conserved scalar in a turbulent reacting shear layer", *J. Fluid Mech*, 481:291–328

Pfadler S., Kerl J., Beyrau F., Leipertz A., Sadiki A., Scheuerlein J., Dinkelacker F. (2009) – "Direct evaluation of the subgrid scale scalar flux in turbulent premixed flames with conditioned dual-plane stereo PIV", *Proceedings of the Combustoin Institute*, Vol 32 1723-1730

Pfadler S., Kerl J., Beyrau F., Leiperz A., Sadiki A., Scheuerlein J., Dinkelacker F. (2009) – "Direct evaluation of the subgrid scale scalar flux in turbulent premixed flames with conditioned dual-plane stereo PIV", *Proceedings of the Combustion Institute*, Vol32:1723-1730

Piirto M., Ihalainen H., Eloranta H., Saarenrinne P. (2001) – "2D Spectral turbulence Length Scale Estimation with PIV", *J. of Visualization,* Vol.4:39-49

Pope S. (2000) – "Turbulent Flow", *Cambridge University Press*

Prasad A. and Jensen K. (1995) – "Scheimpflug stereocamera for particle image velocimetry in liquid flows", *Appl. Opt*. Vol 34 7092–9

Putnam A. (1971) – "*Combustion-driven oscillations in industry*", Elsiver

Raffel M., Willert C., Wereley S., Kompenhans J., (2007) – "Particle image velocimetry", *Springer*

Rajan P. and Munukutla S. (1992) – "A comparative study of three techniques for estimation of turbulence energy spectrum", Exp. Fluids, Vol.12:422-424

Rani S., Pitts A., Stewart P. (2005) – "Rapid diffusion of fluorescent tracers into Staphylococcus epidermidis biofilms visualized by time lapse microscopy", *Antimicrob. Agents Chemother.*, Vol 49(2): 728-732

Read R., Hochgreb S. (2010) – "Isothermal flow measurements in a gas turbine combustor using a fast flame ionization detector", *Meas Sci Technol* 21:1–10

Richardson L. (1922) – "Weather Prediction by Numerical Process", C*ambridge University Press*

Ritchie B. (2008) – "Quantitative acetone PLIF measurements of jet mixing with synthetic jet actuators", *PhD Dissertation, Department of Aerospace Engineering, Georgia Institute of Technology*

Robinson M. (2009) – "Unsteady inlet condition generation for Large Eddy Simulation CFD using Particle Image Velocimetry", PhD Thesis, *Loughborough University*

Roffe G., Venkataramani K. (1978) – "Emissions measurements for lean premixed propane/air systems at pressures up to 30 atmospheres", *NASA,* CR-159421

Rolls Royce (1995) – "The Jet Engine" *4th Edition, Rolls Royce Plc*

Ruffles (2003) – "Aero engines of the future", *The aeronautical journal*, June 2003 pp.307-321

Rupp J., Carrotte J., and Spencer A. (2010) – "Interaction between the acoustic pressure fluctuations and the unsteady flow field through circular holes", *ASME J. of Eng. for GT and Power*, Vol 132, 061051-1:9

Rutar T. and Malte P. (2001) – "NOx formation in high-pressure jet stirred reactors with significance to lean-premixed combustion turbines", *Proceedings of ASME: TURBO EXPO 2001,* June 4–7, 2001, New Orleans, Louisiana, USA

Sadanandan R., Stöhr M., Meier W. (2008) –"Simultaneous OH-PLIF/PIV measurements in a gas turbine model combustor", *App. Phys. B*, Vol 90, 609–618

Sakai, Y., Uchida K., Kubo T., and Nagata K. (2008) – "Statistical Features of Scalar Flux in a High-Schmidt-Number Turbulent Jet", *IUTAM Symposium on Computational Physics and New Perspectives in Turbulence*, 2008 209–214.

Sarpkaya, T. (1972) – "Vortex Breakdown in Swirling Conical Flows", *AIAA,* Vol.9 1792-1799

Schlichting, K., Gersten, K. (1975) – "Boundary Layer Theory", *McGraw Hill Co., New York*

Scott, D. (1979) – "On optimal and data-based histograms". *Biometrika* **66** (3): 605–610

Sharp K., Adrian, R (2001) – "PIV Study of small-scale flow structure around a Rushton turbine", *Fluid Mechanics and Transport Phenomena* Vol 47:766–778

Sheng J., Meng H., Fox R. (2000) – "A large eddy PIV method for turbulence dissipation rate estimation", *Chemical Engineering Science,* Vol 55:4423–4434.

Sirovich, L – "Turbulence and Dynamics of Coherent Structures. Part I: Coherent Structures", *Quarterly of Applied Mathematics*, Vol.45,No.3, pp.561-571

Spencer A, Cheng L (2010) – "Combustor residence time measurement using planar laser induced fluorescence", *In: Proc ASME Turbo Expo*, GT2010-22573

Spencer A., Hollis D. (2005) – "Correcting for sub-grid filtering effects in particle image velocimetry data", *Meas. Sci. Technol.*, Vol 16: 2323-2335

Spencer A., Midgley K. K., and McGuirk J. J. (2008) – "Vortex breakdown in swirling fuel injector flows," *ASME J. Eng. Gas Turbine Power*, Vol. 130 021503:1-8

Spencer, A., (1998) – 'Gas Turbine Combustor Port Flows', *PhD Thesis, Loughborough University*

Stanilslas M., Okamoto K., Kahler J., Westerweel J., Scarano F. (2008) – "Main results of the third international PIV challenge", *Exp in Fluids,* Vol: 45 pp27-71

Stohr M., Boxx I., Carter C., and Meier W. (2012) – "Experimental study of vortex-flame interaction in a gas turbine model combustor", Combustion and Flame 159: 2636-2649

Su L., Clemens N. (2003) – "The structure of find-scale scalar mixing in gas-phase planar turbulent jets", *J. Fluid Mech.*, Vol 488:1-29

Sutton J., Driscoll J. (2007) – "Imaging of local flame extinction due to the interaction of scalar dissipation layers and the stoichiometric contour in turbulent non-premixed flames", *Proceedings of the Combustion Institute,* Vol 31:487-495.

Syred, N. (2006) – "A review of oscillation mechanisms and the role of the precessing vortex core (PVC) in swirl combustion systems", *Progress in Energy and Combustion Science,* Vol 32 93–161

Tanaka T., Eaton J. (2007) – "A correction method for measuring turbulent kinetic energy dissipation rate by PIV", *Exp. in Fluids,* Vol 42:893-902

Tennekes H., Lumley J. (1972) – "A first course in turbulence", *MIT Press*

Uzol O., Camci C. (2001) – "The effect of sample size, turbulence intensity and the velocity field on the experimental accuracy of ensemble averaged PIV measurements", *4th International Symposium on PIV*, #1096

van der Lans R., Glarborg P., Dam-Johansen K., Larsen P. (1997) – "Residence time distributions in a cold, confined swirl flow : Implications for chemical engineering combustion modelling", *Chemical Engineering Science*, Vol 52 2743-2756

Vanierschot M., Van den Bulck E. (2008) – "Planar pressure field determination in the initial merging zone of an annular swirling jet based on stereo-PIV measurements", *Sensors*, Vol 8:7596-7608

Veloudis I., Yang Z., McGuirk J., Page G., Spencer A. (2007) – "Novel implementation and assessment of a digital filter based approach for the generation of LES inlet conditions", *Flow Turbulence Combust*, Vol 79:1-24

Wang G., Barlow R. (2008) – "Spatial resolution effects on the measurement of scalar variance and scalar gradient in turbulent nonpremixed jet flames", *Exp. in Fluids*, Vol 44:633-645

Wang, S. and Rusak, Z. (1997) – "The Dynamics of a Swirling Flow in a Pipe and Transition to Axi-symmetric Vortex Breakdown" *Journal of Fluid Mechanics.*, Vol.350 177-223

Wegner, B., Staufer, M., Sadiki, A., and Janicka, J. (2007) "Study of flow and mixing in a generic gt combustor using les," *Flow Turbulence Combust*, pp. 911–923.

Welch P. (1967) – "The use of Fast Fourier Transform for the estimation of power spectra: a method based on time averaging over short, modified periodograms", *IEEE transactions on audio electroacoustics*, Vol 15:70-73

Westerweel J., Fukshima C., Pedersen J., Hunt, J. (2009) – "Momentum and scalar transport at the turbulent/non-turbulent interface of a jet", *J. Fluid Mech.*, Vol 631 199-230

Wieneke B. (2005) – "Stereo-PIV using self-calibration on particle images", *Exp. in Fluids*, Vol 39:267-280

Willert C. (2006) – "Assessment of camera models for use in planar velocimetry calibration", *Exp. in Fluids.*, Vol 41: 135:143

World Health Organization (2008) – "Outdoor air pollution", *WHO Training Package for the Health Sector*

Wygnanski I., Fiedler H. (1969) – "Some measurements in the self-preserving jet", *J. Fluid Mech,* Vol 38:577-612

Yeh Y. and Cummins H. (1964) – "Localized Fluid Flow measurements with an He-Ne Laser Spectrometer", *Applied Physics Letters*

Zarruk G. and Cowen E. (2008) – "Simultaneous velocity and passive scalar concentration measurements in low Reynolds number neutrally buoyant turbulent round jets", *Exp Fluids*, Vol 44:865–872

Appendix

Appendix 1.1 – Vortex breakdown with increasing swirl numbers

Appendix 2.1 – Calibration of orifice plates and manometers based on BS1042

Appendix 2.2 – Mass flow calibrations

Appendix 2.3 Uncertainty analysis of BS1042 manometer readouts

Appendix 4.1 – Confidence weighted integration of SVC

Appendix 4.2 – Assumptions and derivations of Reynolds average momentum equation for the computation of time-mean static pressure

Appendix 4.3 – Matlab script of RHS of Reynolds averaged momentum equation

Appendix 5.1 – LES formulation

Appendix 5.2 – Comparisons between experimental data LES predictions of non-premixed test case

Appendix 5.3 – Comparisons of LES filter width with PIV interrogation cell size

Appendix 1.1 – Vortex breakdown with increasing swirl numbers[8]

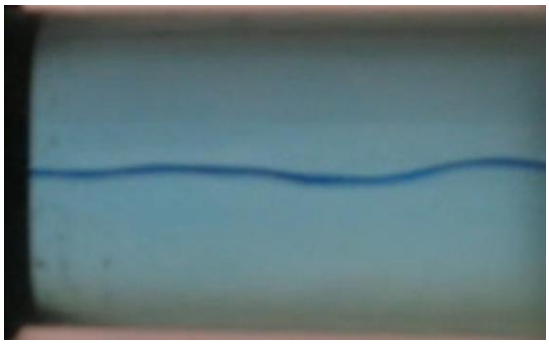

t=13s

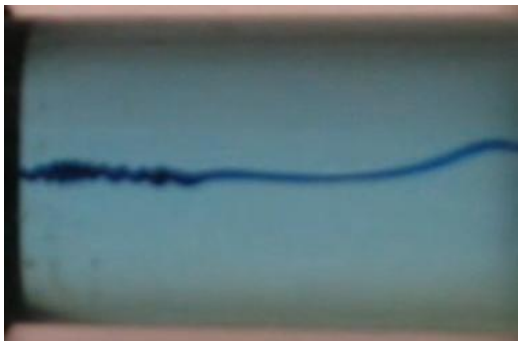

t=33s

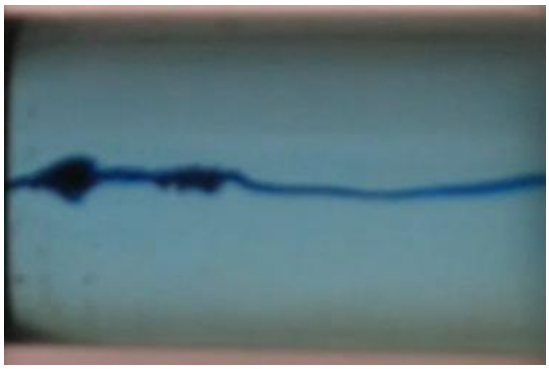

t=38s

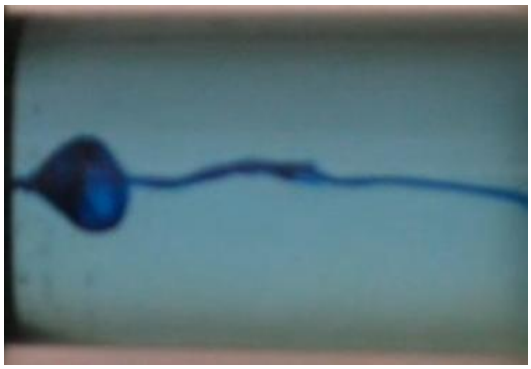

t=48s

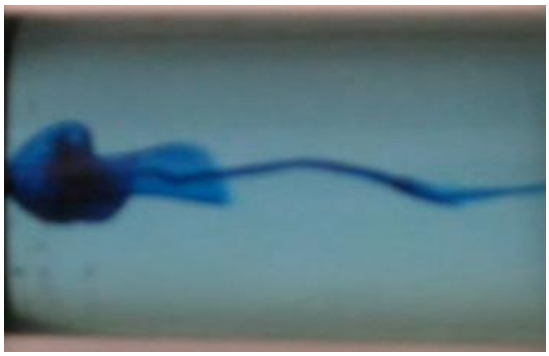

t=56s

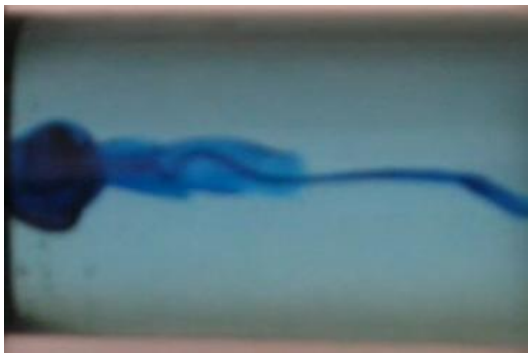

t=62s

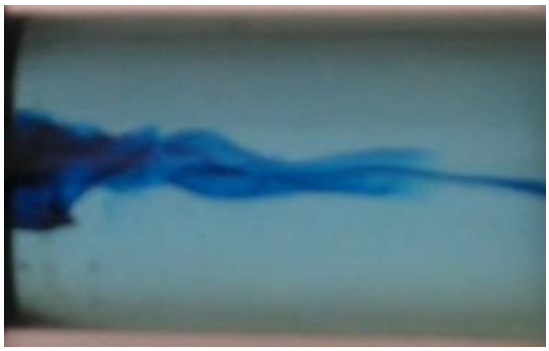

t=70s

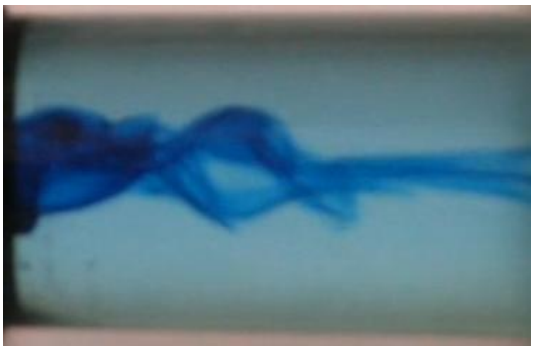

t=90s

[8] Vortex breakdown in a pipe at 2Hz (http://www.youtube.com/watch?v=J66bnOXEu14)

Appendix 2.1 – Calibration of orifice plates and manometers based on BS1042

A large-bore-diameter orifice plate was installed in the top pipe while the other orifice plate with a smaller bore diameter was installed in the bottom pipe. These orifice plates are illustrated in Fig. A2.1. The bottom orifice plate was used for fine tuning the mass flow rate as the pressure differential read by the manometer is more sensitive to changes in the valve opening and can only measure up to about 3kg/s before sub-atmospheric pressure occurs at the corners of the downstream tapping. The top orifice plate, on the other hand, was designed for coarse measurements of larger flow rates, for which the pressure differential read on the manometer is not as sensitive to fine changes in the valve opening.

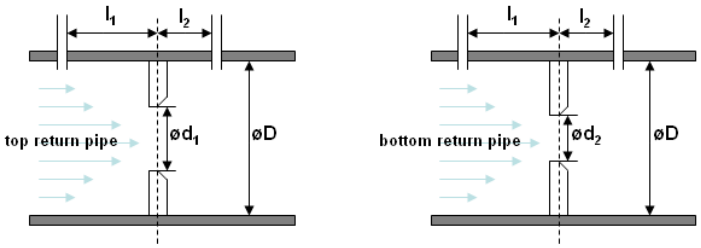

Figure A2.1 Orifice plate schematic: top return pipe (left), bottom return pipe (right)

As stated in the Table A2.1, the calculated mass flow rate is a function of β and the BS1042 standard applies only if β that is within a specified range. The orifice plate installed in the top return pipe, however, has a β that is larger than the specified upper limit. Moreover, both the upstream and downstream pressure tapping distances, l_1 and l_2, are also outside the allowable range specified by BS1042.

	Top Pipe	**Bottom Pipe**
Bore diameter (ød)	45mm	33mm
Pipe diameter (øD)	52mm	52mm
Diameter ratio (β)	0.87	0.63
Range of β specified by BS1042	*$0.1 \leq \beta \leq 0.75$*	
Upstream tapping distance (l_1)	60mm	60mm
l_1 specified by BS1042	*45 ± 0.45 mm*	*33 ± 0.33 mm*
Downstream tapping distance (l_2)	33mm	33mm
l_2 specified by BS1042	*23 ± 0.45 mm*	*17 ± 0.33 mm*

Table A2.1 Orifice plate dimensions and BS1042 specifications

Appendix 2.2 – Mass flow calibrations

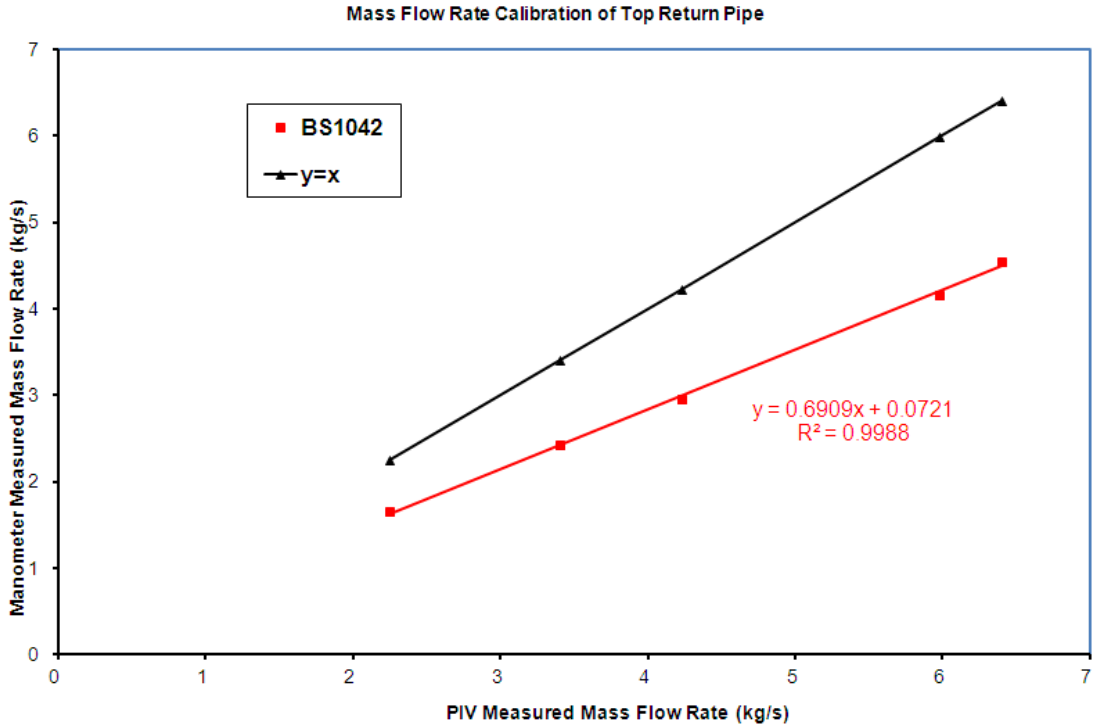

Fig. A2.2 Mass flow calibration of top return pipe flow

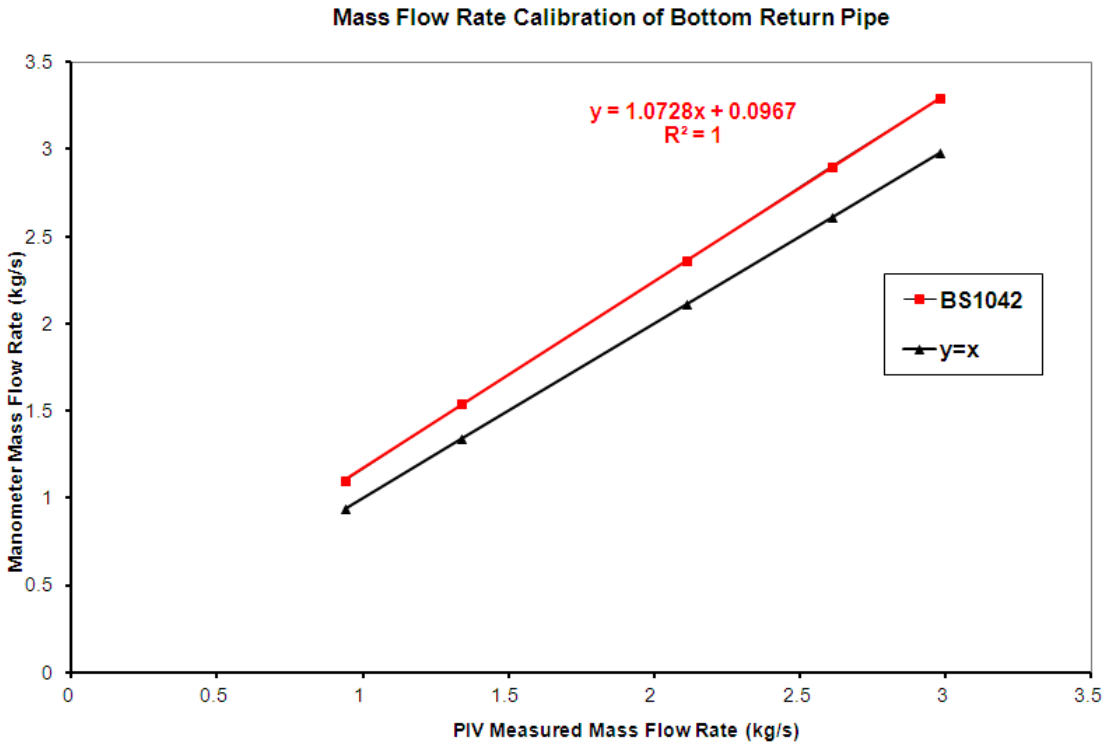

Fig. A2.3 Mass flow calibration of bottom return pipe flow

Shown in Figs. A2.2 and A2.3 are comparisons of the two measured mass flow rates at incremental magnitudes with the perfect model (M_{PIV}=$M_{manometer}$). The linear

relationship makes it possible to correct for the BS1042-manometer mass flow rate by simply adding the offset between the two functions:-

$$M_{top} = 1.309*M_{BS1042} - 0.072$$
$$M_{bottom} = 0.927*M_{BS1042} - 0.097$$

Where M_{top} and M_{bottom} are the corrected mass flow rate of the top pipe and bottom pipe respectively and M_{BS1042} is the mass flow rate calculated from the manometer pressure reading using the BS1042 equations. The least-square fit has an rms of 2.5%, which is accounted to be the uncertainty of this correction method.

Appendix 2.3 Uncertainty analysis of BS1042 manometer readouts

The uncertainty of a dependent variable, ω_R, can be calculated using the following equation:

$$\omega_R = \left\{ \Sigma \left[\left(\frac{\partial R}{\partial x_i} \right)^2 \omega_{x_i}{}^2 \right] \right\}^{1/2} ;$$

Where ω_n is the uncertainty in the result of the uncertainties in the independent variables, x_1, x_2, x_3 ….., x_n, and R is a given function of these independent variables.

In the BS1042 orifice plate uncertainty calculation, the mass flow rate is calculated using the following estimation function:

$$mdot = \alpha\varepsilon \frac{\pi}{4} d^2 \left(2\Delta P \rho_1\right)^{1/2};$$

Where α is the flow coefficient, ε is the expansion factor, d is the orifice diameter, ΔP is the pressure drop across the orifice plate, and ρ_1 is the density of water at 20˚C.

For the calculation of ω_α:

$$\alpha = CE ;$$

Where C is the coefficient of discharge and E is the velocity approach factor, both C and E are functions of β, given by BS1042:

$$C = 0.5959 + 0.0312\beta^{2.1} - 0.184\beta^{8} + 0.0029\beta^{2.5};$$

$$E = \frac{1}{\left(1-\beta^{4}\right)^{1/2}};$$

Then:

$$\frac{\partial C}{\partial \beta} = 0.06552\beta^{1.1} - 1.472\beta^{7} + 0.00725\beta^{1.5};$$

$$\frac{\partial E}{\partial \beta} = \frac{-2\beta^{3}}{\left(1-\beta^{4}\right)^{-3/2}};$$

The uncertainty in β is dependent on the orifice diameter, and is estimated to be ± 0.005. Thus:

$$\omega_c = \left[\left(\frac{\partial C}{\partial \beta}\right)^{2} \omega_B{}^{2}\right]^{1/2} = 0.0098;$$

$$\omega_E = \left[\left(\frac{\partial E}{\partial \beta}\right)^{2} \omega_E{}^{2}\right]^{1/2} = 0.0059;$$

Having calculated the uncertainties of C and E based on β, the uncertainty of α can now be evaluated:

$$\frac{\partial \alpha}{\partial C} = E;$$

$$\frac{\partial \alpha}{\partial E} = C;$$

$$\omega_P = \left[E^{2}\omega_c{}^{2} + C^{2}\omega_E{}^{2}\right]^{1/2} = 0.035$$

For the calculation of ω_P:

$$\Delta P = \rho g \Delta h;$$

Where Δh is the uncertainty on the manometer reading,

$$\omega_h = \pm 0.2in = 0.00508m;$$

And

$$\frac{\partial \Delta P}{\partial h} = \rho g;$$

Thus:

$$\omega_{\Delta P} = \left[\left(\frac{\partial \Delta P}{\partial h} \right)^2 \omega_h{}^2 \right]^{1/2} = 49.835;$$

Now the uncertainties of the independent variables have been calculated. The next step is to differentiate the mass flow rate equation with each variable:

$$\frac{\partial mdot}{\partial \alpha} = \varepsilon \frac{\pi}{4} d^2 \left(2\Delta P \rho_1\right)^{1/2};$$

$$\frac{\partial mdot}{\partial \varepsilon} = \alpha \frac{\pi}{4} d^2 \left(2\Delta P \rho_1\right)^{1/2};$$

$$\frac{\partial mdot}{\partial d} = 2\alpha\varepsilon \frac{\pi}{4} d \left(2\Delta P \rho_1\right)^{1/2};$$

$$\frac{\partial mdot}{\partial \Delta P} = \alpha\varepsilon \frac{\pi}{4} d^2 \left(2\Delta P \rho_1\right)^{-1/2};$$

The uncertainty in the mass flow rate is:

$$\omega_{mdot} = \left[\left(\frac{\partial mdot}{\partial \alpha} \right)^2 \omega_\alpha{}^2 + \left(\frac{\partial mdot}{\partial \varepsilon} \right)^2 \omega\varepsilon^2 + \left(\frac{\partial mdot}{\partial d} \right)^2 \omega_d{}^2 + \left(\frac{\partial mdot}{\partial \Delta P} \right)^2 \omega_{\Delta P}{}^2 \right]^{1/2};$$

This equation is calculated over a range of ΔP in Excel.

Appendix 4.1 – Confidence weighted integration of SVC

When evaluating the integral lenthscale at the edge of a domain, strong asymmetry in the SVC(U_i) often exists, as shown in Fig. A4.1. For treatment of such SVC functions, Hollis (2004) developed a confidence-weighted algorithm.

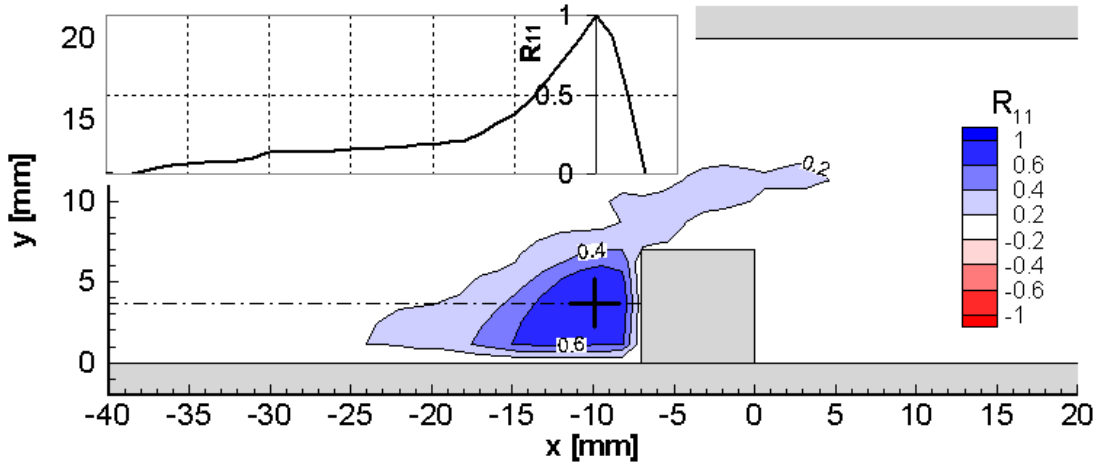

Fig. A4.1 Mass flow calibration of bottom return pipe flow (Hollis, 2004)

C = 0 $\qquad\qquad$ $SVC_{curtailed} > 0.9$

$C = 1.125-(1.25*ACF_{curtailed})$ $\quad 0.1 \leq SVC_{curtailed} \leq 0.9$

$C = 1$ $\quad SVC_{curtailed} < 0.1$

(where C=confidence coefficent)

The above means that if the function is curtailed at anything greater than a value of SVC=0.9, no confidence can be attributed to the integral for that part of the axis because it relies too heavily on an estimated curve. If the function is curtailed at less than 0.1, entire confidence can be placed on the integral, because the estimated portion is so small. Between the two values, a linear relationship between confidence and the curtailed value exists. The actual lengthscale is then calculated from the weighted average, dependant upon confidence levels.

$$^{k}L_{ij} = (C_{-ve}\,{}^{k}L_{ij\,-ve} + C_{+ve}\,{}^{k}L_{ij\,+ve})/(C_{-ve} + C_{+ve})$$

(Where +ve and –ve subscripts refer to parts of the separation distance axis)

The weighted average calculation does mean that near domain edges, the lengthscale is essentially calculated using only the upstream or downstream part of the axis, which contravenes the earlier statement with respect to it having to be an average. However, this method provides more reliable and fluid dynamically consistent values at the domain edges than simple averages. The user must simply be aware of this in interpreting the data near domain inflow and outflows.

Appendix 4.2 – Assumptions and derivations of Reynolds average momentum equation for the computation of time-mean static pressure

Pope (2003) derives the mean-momentum Reynolds equation in Cartesian coordinate:

$$\frac{\bar{D}<U_j>}{\bar{D}t} = \upsilon\nabla^2 <U_j> - \frac{\partial <u_i u_j>}{\partial x_i} - \frac{1}{\rho}\frac{\partial <p>}{\partial x_j} \qquad \text{(A4.1)}$$

Where the mean substantial derivative is defined as:-

$$\frac{\bar{D}}{\bar{D}t} = \frac{\partial}{\partial t} + <\bar{U}>\cdot\nabla \qquad \text{(A4.2)}$$

The subscript, j, in Eq. A4.1, ranges from 1 to 3 where j=1 denotes the axial direction, j=2 denotes the radial one, and j=3 is the tangential one, hence $x=x_1$, $r=x_2$, and $\theta=x_3$. Following the same convention, the material derivative, $<\bar{U}>\cdot\nabla<\bar{U}>$,where

$\vec{U} = U\hat{i} + V\hat{j} + rW\hat{k}$, can be expanded into the following format in cylindrical coordinate:-

$$< \vec{U} > \cdot \nabla < \vec{U} > = \left(< U > \frac{\partial < U >}{\partial x} + V \frac{\partial < V >}{\partial r} + \frac{< W >}{r} \frac{\partial < W >}{\partial \theta} \right) \hat{i}$$
$$+ \left(< U > \frac{\partial < V >}{\partial x} + < V > \frac{\partial < V >}{\partial r} + \frac{< W >}{r} \frac{\partial < V >}{\partial \theta} - \frac{< W^2 >}{r} \right) \hat{j}$$
$$+ \left(< U > \frac{\partial < W >}{\partial x} + < V > \frac{\partial < W >}{\partial r} + \frac{< W >}{r} \frac{\partial < W >}{\partial \theta} - \frac{< VW >}{r} \right) \hat{k} \qquad \text{(A4.3)}$$

Substituting Eq. A4.2 and A4.3 into Eq. A4.1 with a cylindrical conversion of the right-hand-side (RHS) of Eq. A4.1 (not shown here), then expanding it and the left-hand-side (LHS) yields:-

$$\text{LHS: } \frac{\partial < U >}{\partial t} + < U > \frac{\partial < U >}{\partial x} + < V > \frac{\partial < U >}{\partial r} + \frac{1}{r} < W > \frac{\partial < U >}{\partial \theta} \qquad \text{(A4.4)}$$

$$\text{RHS: } \upsilon \nabla^2 < U > - \frac{1}{\rho} \frac{\partial < p >}{\partial x} - \frac{\partial < u^2 >}{\partial x} - \frac{1}{r} \frac{\partial r < uv >}{\partial r} - \frac{1}{r} \frac{\partial < uw >}{\partial \theta} \qquad \text{(A4.5)}$$

Here is the important part, the following assumptions and simplifications have been made:

$$\begin{aligned} &\frac{\partial}{\partial t} < U > = 0 \\ &\upsilon \nabla^2 < U > = 0 \\ &< W > \frac{\partial < U >}{\partial \theta} = 0 \\ &\frac{\partial < uw >}{\partial \theta} = 0 \end{aligned} \qquad \text{(A4.6)}$$

Where the transient term is assumed negligible, the viscous term is neglected as it is several orders of magnitude smaller than others, and the through-plane component has been neglected. So that the mean-momentum equation in the axial direction (j=1) reduces to:-

$$-\frac{1}{\rho} \frac{\partial < p >}{\partial x} = < U > \frac{\partial < U >}{\partial x} + < V > \frac{\partial < U >}{\partial r} - \frac{\partial < u^2 >}{\partial x} - \frac{1}{r} \frac{\partial r < uv >}{\partial r} \qquad \text{(A4.7)}$$

Taking the radial component of Eq. A4.3 and expanding the counterparts of Equations A4.4 and A4.5 for the radial component yields:-

$$\mathrm{LHS} = \frac{\partial < \mathrm{V} >}{\partial \mathrm{t}} + < \mathrm{U} > \frac{\partial < \mathrm{V} >}{\partial \mathrm{x}} + < \mathrm{V} > \frac{\partial < \mathrm{V} >}{\partial \mathrm{r}} + \frac{1}{\mathrm{r}} < \mathrm{W} > \frac{\partial < \mathrm{V} >}{\partial \theta} - \frac{< \mathrm{W} >}{\mathrm{r}} \tag{A4.9}$$

$$\mathrm{RHS} = -\frac{1}{\rho}\frac{\partial < \mathrm{p} >}{\partial \mathrm{r}} - \frac{\partial < \mathrm{uv} >}{\partial \mathrm{x}} - \frac{1}{\mathrm{r}}\frac{\partial \mathrm{r} < \mathrm{v}^2 >}{\partial \mathrm{r}} - \frac{1}{\mathrm{r}}\frac{\partial < \mathrm{vw} >}{\partial \theta} + \frac{< \mathrm{w}^2 >}{\mathrm{r}} \tag{A4.10}$$

Similar to the axial component, the following assumptions have been made:

$$\begin{aligned} &\frac{\partial}{\partial \mathrm{t}} < \mathrm{V} >= 0 \\ &\upsilon \nabla^2 < \mathrm{V} >= 0 \\ &\frac{< \mathrm{W} >}{\mathrm{r}} \frac{\partial < \mathrm{V} >}{\partial \theta} = 0 \\ &\frac{\partial < \mathrm{vw} >}{\partial \theta} = 0 \end{aligned} \tag{A4.11}$$

So that the mean-momentum equation in the radial direction reduces to:-

$$-\frac{1}{\rho}\frac{\partial < \mathrm{p} >}{\partial \mathrm{r}} = < \mathrm{U} > \frac{\partial < \mathrm{V} >}{\partial \mathrm{x}} + < \mathrm{V} > \frac{\partial < \mathrm{V} >}{\partial \mathrm{r}} - \frac{< \mathrm{W} >^2}{\mathrm{r}} - \frac{< \mathrm{w}^2 >}{\mathrm{r}} + \frac{\partial < \mathrm{uv} >}{\partial \mathrm{x}} + \frac{1}{\mathrm{r}}\frac{\partial \mathrm{r} < \mathrm{v}^2 >}{\partial \mathrm{r}} \tag{A4.12}$$

Appendix 4.3 – Matlab script of RHS of Reynolds averaged momentum equation

```
B1(i,j)=((vx(i+1,j)-vx(i-1,j))/(2*dx))^2;
B2(i,j)=2*((vx(i,j+1)-vx(i,j-1))/(2*dr))*((vr(i+1,j)-vr(i-
1,j))/(2*dx));
B3(i,j)=((vr(i,j+1)-vr(i,j-1))/(2*dr))^2;
B4(i,j)=vr(i,j)^2/r(1,j)^2;
B5(i,j)=(uu(i+1,j)-2*uu(i,j)+uu(i-1,j))/dx^2;
B6(i,j)=2/r(1,j)*(druvdx(i,j+1)-druvdx(i,j-1))/(2*dr);
B7(i,j)=1/r(1,j)*(vv(i,j+1)-vv(i,j-1))/(2*dr)+(vv(i,j+1)-
2*vv(i,j)+vv(i,j-1))/dr^2;
B8(i,j)=-1/r(1,j)*(vz(i,j+1)^2-vz(i,j-1)^2)/(2*dr);
B9(i,j)=-1/r(1,j)*(ww(i,j+1)-ww(i,j-1))/(2*dr);

Btot(i,j)=B1(i,j)+B2(i,j)+B3(i,j)+B4(i,j)+B5(i,j)+B6(i,j)+B7(i,j)+B8(
i,j)+B9(i,j);
```

Appendix 5.1 LES formulation

The spatially filtered transport equations are discretised using the finite volume method. For the momentum equations, spatial derivatives for both convective and diffusive terms are calculated using a second order central differencing scheme. For the scalar transport equation, a central differencing scheme is used for the diffusion term while a second-order TVD scheme has been used for convection discretisation. For all equations solved, the Adams-Bashforth second-order explicit scheme is used for time discretisation, and a fast 3D multi-grid method to obtain the pressure field. A description of numerical tests, which demonstrate the adequacy of the numerical techniques chosen for accurate solution of a conserved scalar equation, are detailed in Dianat et al. (2006).

The simulation is based on a multi block system and the computations are carried out in parallel on four processors. As shown in Fig. A5.1, the solution domain is divided into eight blocks on the axial-radial (x-r) plane. The mesh for each block is generated separately ensuring higher resolutions in the regions of interest such as wall vicinity and shear layers. The meshes are then combined together and rotated through 360° in the tangential θ-direction using 80 uniformly spaced grid to construct a full 3D mesh system of total size 873,600 collapsing to a straight line on the centre-line. Axial and radial mesh numbers were 150 and 80 respectively inside, the combustor; inside the fuel injector these numbers were 50 and 40.

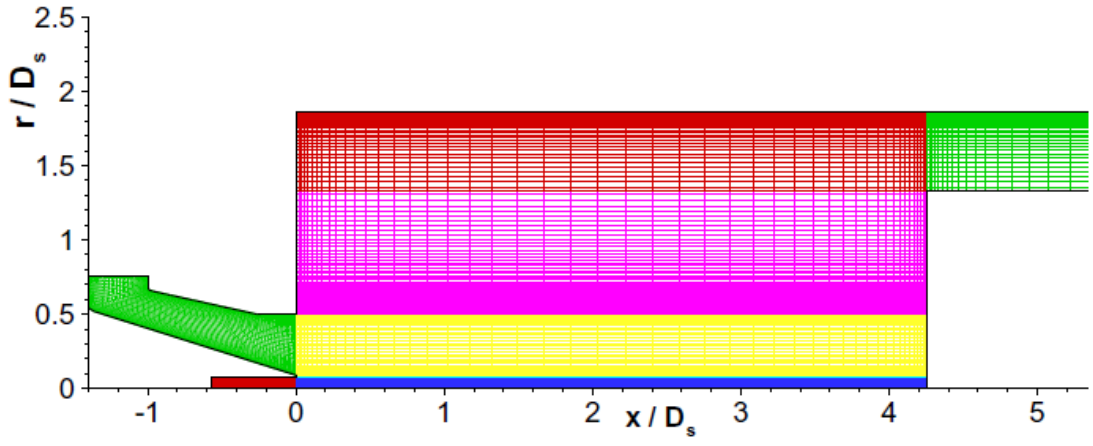

Fig. A5.1 Computational grid and multi-block system

Appendix 5.2 Comparisons between experimental data LES predictions

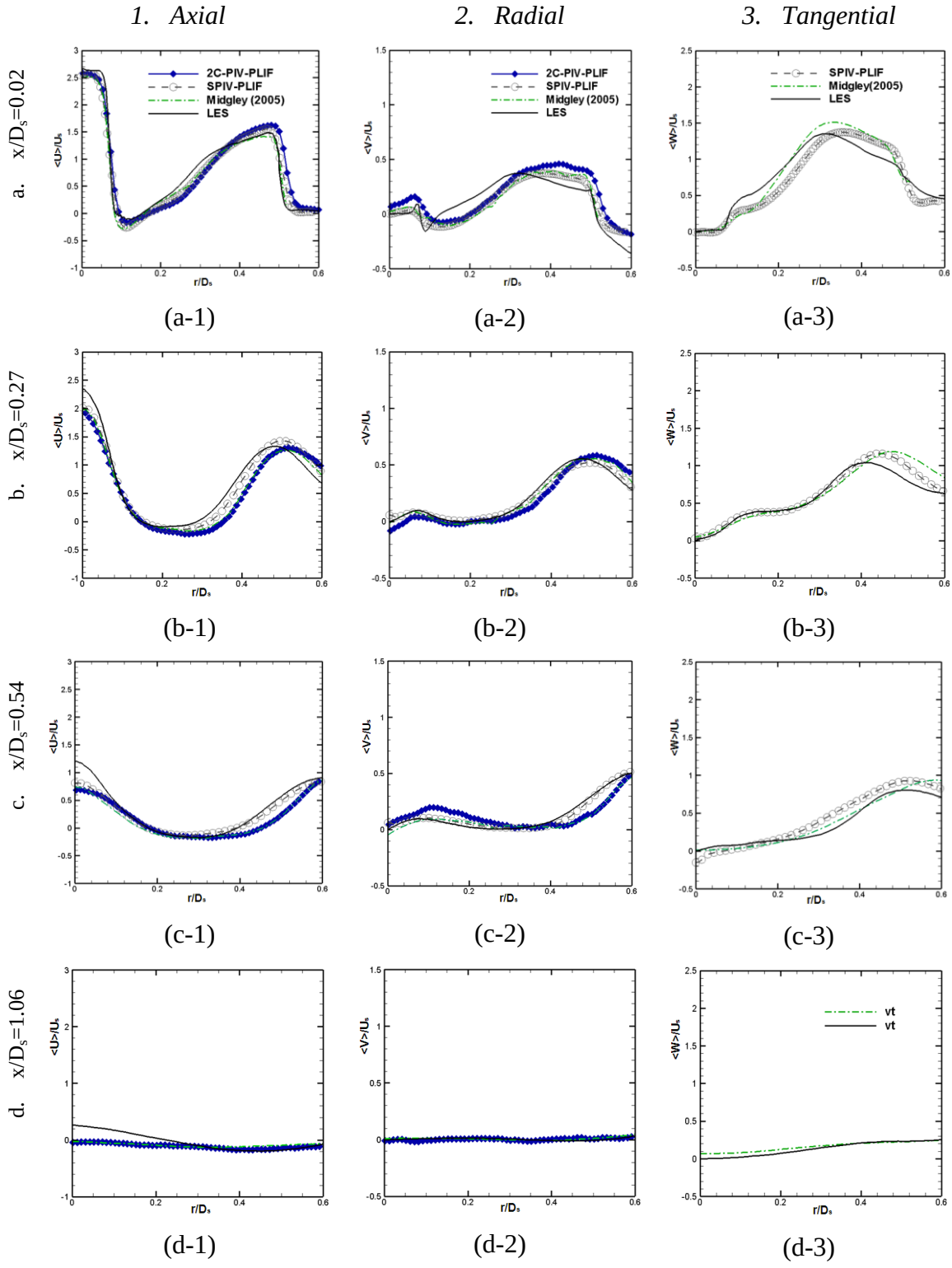

Fig. A5.2 Comparisons of time-mean velocity profiles

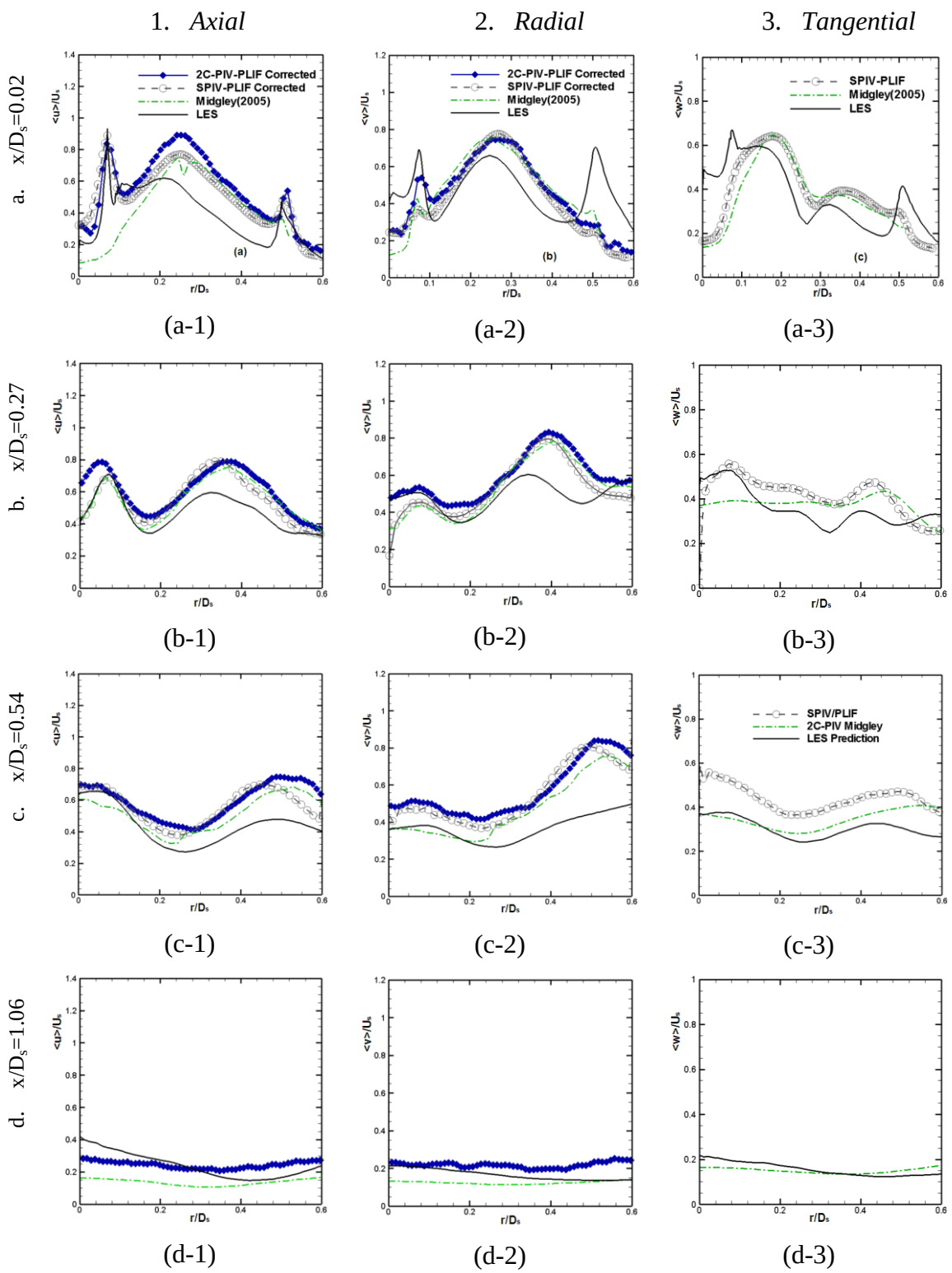

Fig. A5.3 Comparisons of RMS velocity profiles

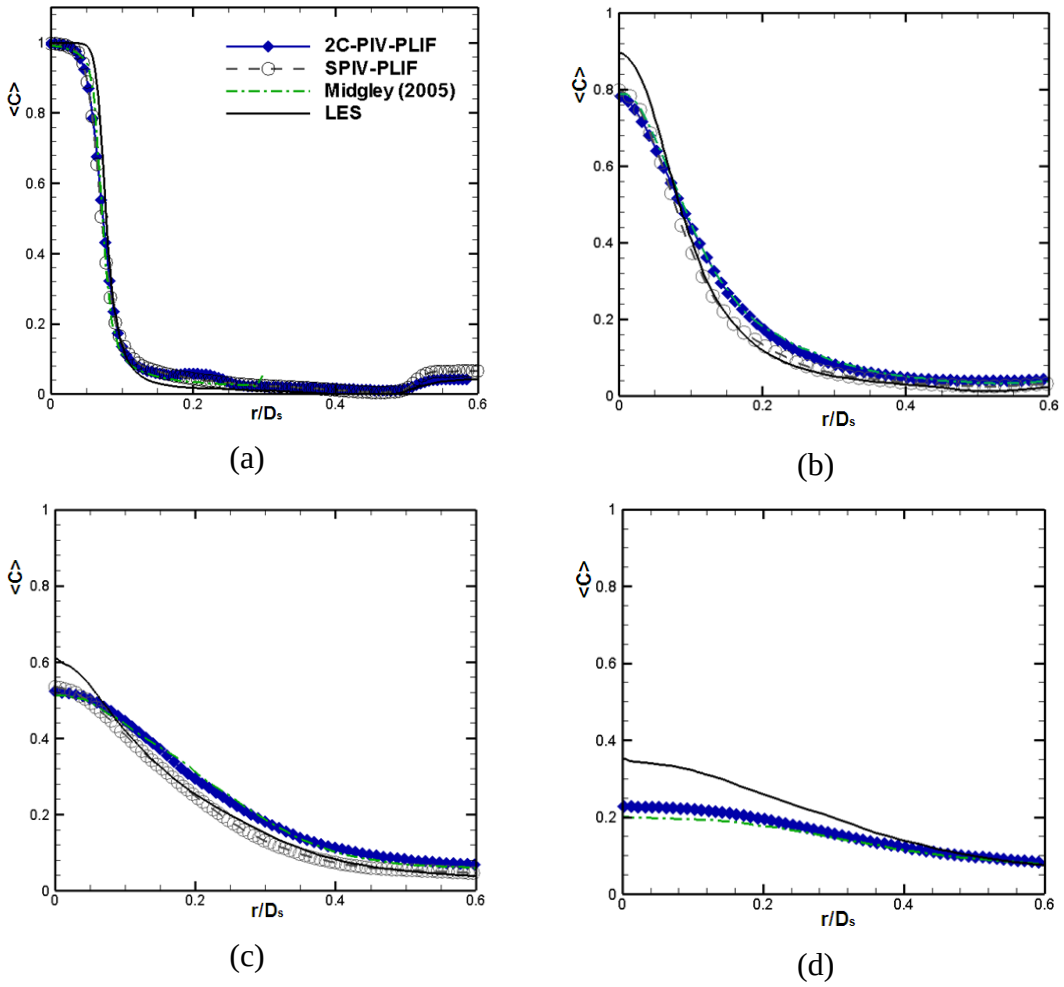

Fig. A5.4 Comparisons of time-mean concentration profiles at (a) x/D_s=0.02, (b) x/D_s=0.27, (c) x/D_s=0.54, and (d) x/D_s=1.06

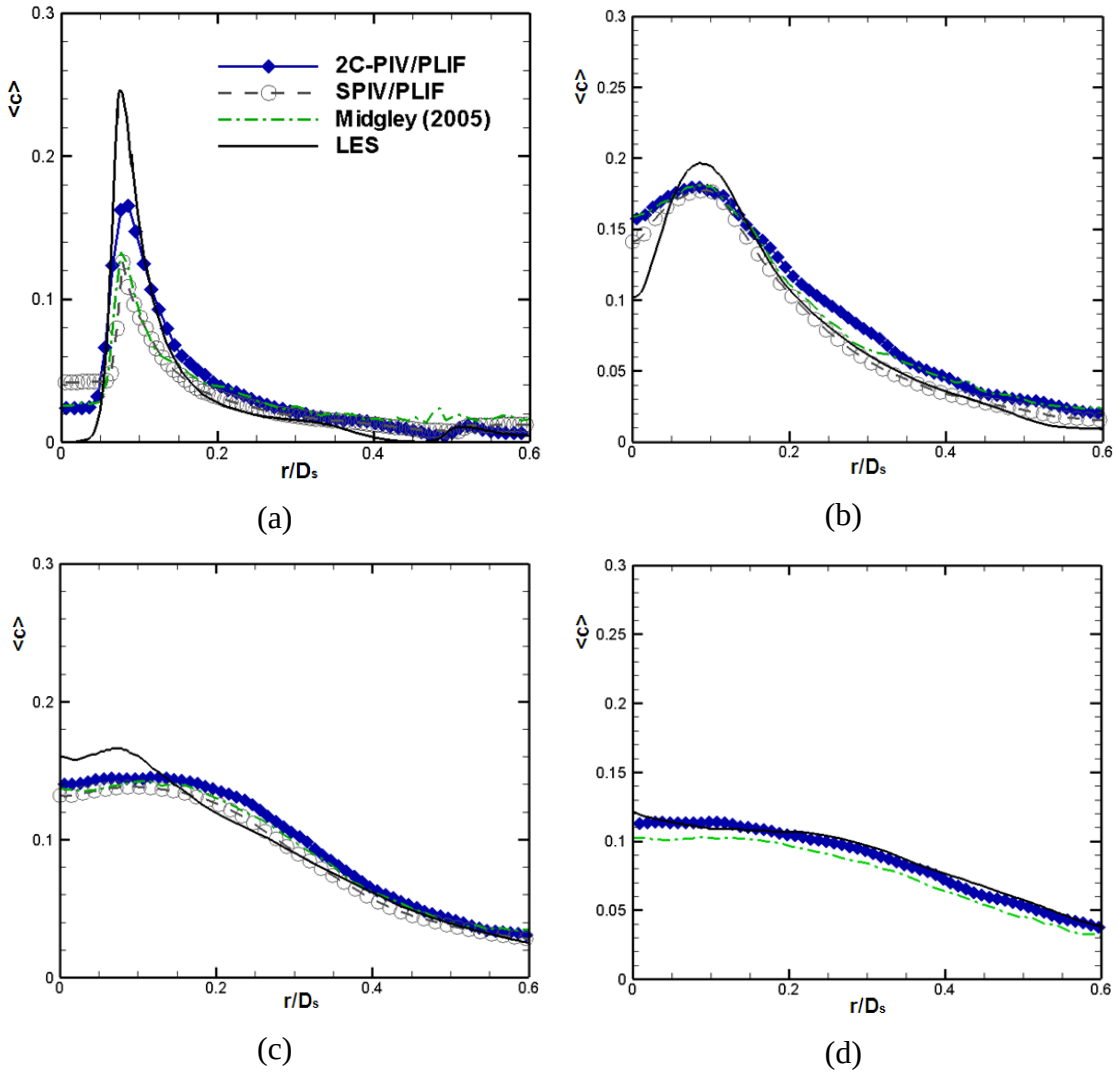

Fig. A5.5 Comparisons of RMS concentration profiles at (a) x/D_s=0.02, (b) x/D_s=0.27, (c) x/D_s=0.54, and (d) x/D_s=1.06

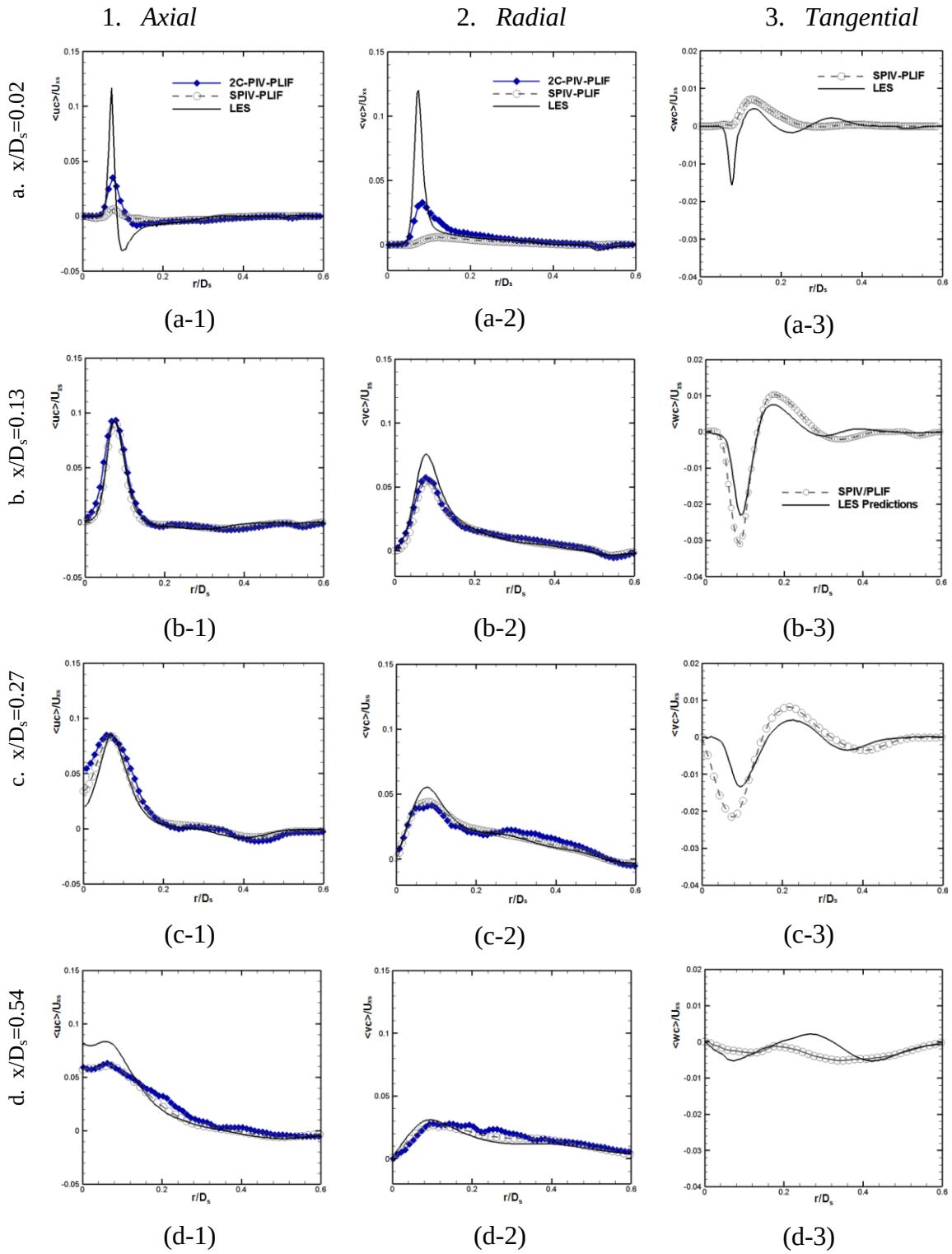

Fig. A5.6 Comparisons of turbulent scalar fluxes

Appendix 5.3 Comparisons of LES filter width with PIV interrogation cell size

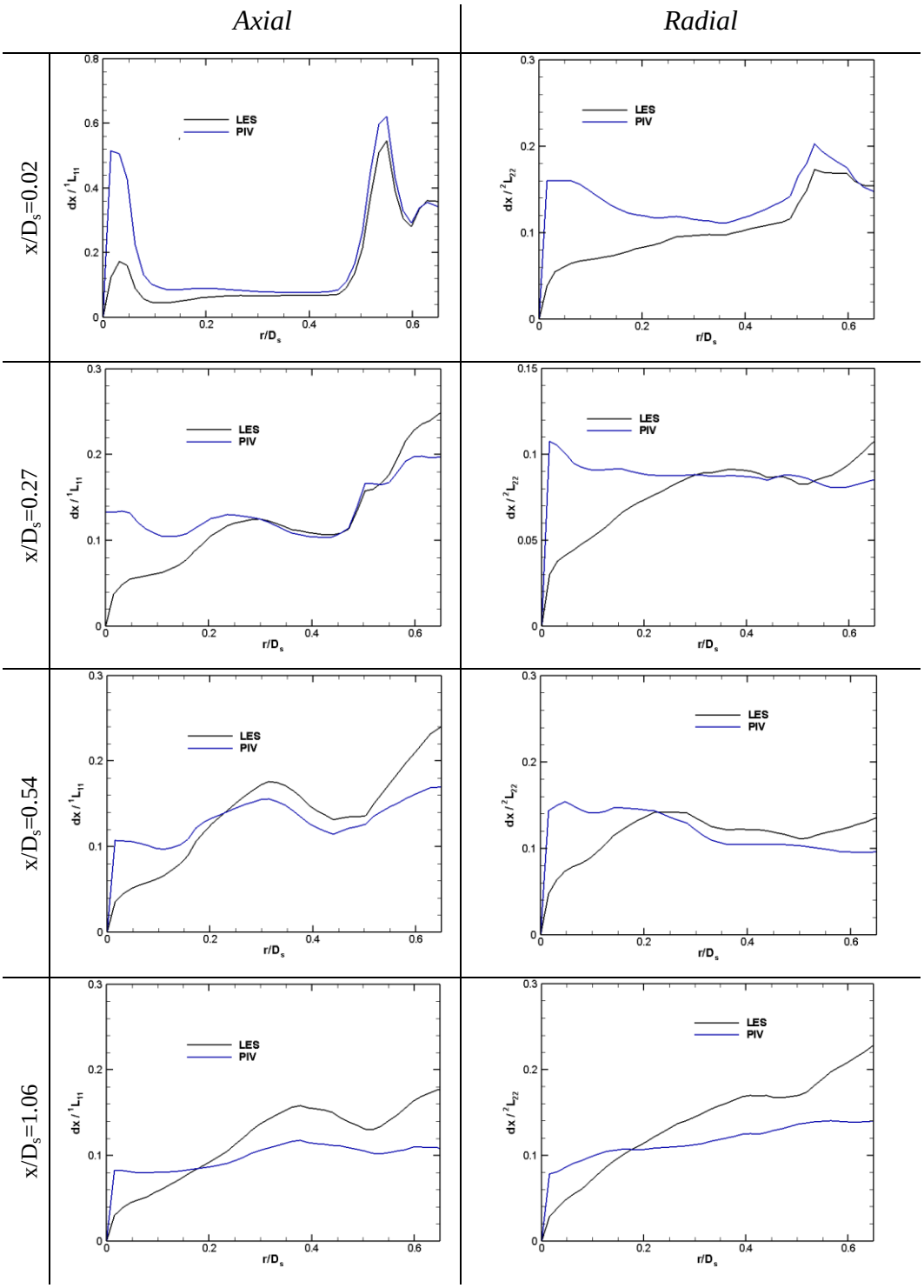

Fig. A5.7 Comparisons of filter width between LES and PIV at four axial stations